



Politecnico
di Bari

Repository Istituzionale dei Prodotti della Ricerca del Politecnico di Bari

Design and fabrication of fiber optic sensors and systems for aerospace applications

This is a PhD Thesis

Original Citation:

Design and fabrication of fiber optic sensors and systems for aerospace applications / Annunziato, Andrea. - ELETTRONICO. - (2024). [10.60576/poliba/iris/annunziato-andrea_phd2024]

Availability:

This version is available at <http://hdl.handle.net/11589/264920> since: 2024-01-18

Published version

DOI:10.60576/poliba/iris/annunziato-andrea_phd2024

Publisher: Politecnico di Bari

Terms of use:

(Article begins on next page)



Department of Mechanics, Mathematics and Management
AEROSPACE SCIENCE AND ENGINEERING
Ph.D. Program
SSD: ING-INF/02–ELECTROMAGNETIC FIELDS

Final Dissertation

Design and Fabrication of Fiber Optic
Sensors and Systems for Aerospace
Applications

by
Andrea Annunziato

Supervisors:

Prof. Francesco PRUDENZANO

Prof.ssa Anna Maria Lucia LANZOLLA

*Coordinator of Ph.D. Program:
Prof. Marco Donato De Tullio*

Course n°36, 01/11/2020-31/10/2023



Department of Mechanics, Mathematics and Management
AEROSPACE SCIENCE AND ENGINEERING
Ph.D. Program
SSD: ING-INF/02-E LECTROMAGNETIC FIELDS

Final Dissertation

Design and Fabrication of Fiber Optic
Sensors and Systems for Aerospace
Applications

by

Andrea Annunziato

Referees:

Prof. Maurizio FERRARI

Prof. Gianluca GALZERANO

Prof. Stefano TACCHEO

Supervisors:

Prof. Francesco PRUDENZANO

Prof.ssa Anna Maria Lucia LANZOLLA

Coordinator of Ph.D. Program:

Prof. Marco Donato De Tullio

Course n°36, 01/11/2020-31/10/2023

Abstract

The rapid evolution of fiber optic technology has revolutionized the field of communication and sensing, enabling unprecedented levels of accuracy, miniaturization, and scalability. This thesis describes the results obtained during my Ph.D. activity and concerning the development of fiber optic sensors, optical fiber components, and light sources tailored to advance the field of aerospace structure monitoring. The work has required the exploration of the research forefront in this field.

The first part of the thesis focuses on the design, fabrication, and characterization of non-conventional fiber optic sensors. These sensors leverage Bragg gratings to detect several physical parameters, including temperature, strain, and bending, matching the stringent requirement of structural health monitoring of Carbon Fiber Reinforced Polymers (CFRP). The findings have been obtained in collaboration with the University of Southampton (Optoelectronic Research Centre - ORC, UK) trying to give a contribution to the ongoing evolution of aerospace sensor technologies.

Bragg gratings are wavelength-selective structures also employed for multiplexing optical signals or for the construction of laser cavities. By considering these aspects and the growing interest in Medium-Infrared (Mid-IR) spectral range, the second part of the thesis delves into the design, fabrication, and characterization of Mid-IR optical fiber components, based on soft glasses, operating between $0.5 \mu m$ and $12 \mu m$. Optical fiber combiners/couplers are essential elements in communication and sensing systems that enable the splitting (or combining) of optical signals into (from) a single optical fiber preserving beam quality. The development of a custom manufacturing procedure for fluoride and chalcogenide glasses, in collaboration with the company Le Verre Fluoré (Bruz, France) made it possible, for the first time, to address the results described in the doctoral thesis.

Moreover, Bragg gratings in combination with these optical fiber components allow the development of all-in-fiber Mid-IR amplifiers, lasers, and wavelength division multiplexing (WDM) systems. In particular, optical fiber lasers,

operating in the Mid-IR spectral range, can be employed for material inspection purposes to assess the integrity and quality of composite materials via Non-Destructive Testing (NDT) techniques. Therefore, the design and optimization of Mid-IR continuous wave (CW) lasers, are reported in the last part of the Ph.D. research work.

Part of the obtained results have been published in International Journals and in the Proceedings of National and International Conferences, as listed at the end of the thesis.

Contents

Introduction	1
1 Optical Sensors Based on Bragg Grating and Mid-IR Optical Systems for Aerospace Applications	4
1.1 Bragg gratings sensors	5
1.1.1 Optical FBG sensors for multiparameter monitoring of CFRP laminates	6
1.1.2 Flexible photonic sensors based on Bragg grating for bending and/or temperature monitoring	9
1.2 Optical fiber devices for combining applications in Mid-IR spectral range	11
1.2.1 Optical fiber taper	12
1.2.2 Optical fiber combiners and couplers	13
1.3 Mid-IR optical fiber sources	16
2 Recall of Theory	18
2.1 Coupled Mode Theory: general formulation	18
2.1.1 CMT applied to FBGs	19
2.2 Opto-mechanical design of Bragg gratings sensors	22
2.2.1 Opto-mechanical properties of silica	22
2.2.2 Refractive index variation due to strain and temperature	25
2.2.3 Refractive index variation due to curvature	27
2.3 Optical fiber coupler and combiner for Mid-IR	30
2.3.1 Symmetric optical fiber coupler: CMT theory and operation principle	30
2.3.2 Brightness principle and adiabatic criterion	32
2.4 Analytical model for fluoroindate glass fiber-based lasers	34
2.4.1 Nd ³⁺ :Ho ³⁺ -doped fluoroindate CW fiber laser	34
2.4.2 Er ³⁺ -doped fluoroindate CW fiber laser	37
3 Optical Gratings for Sensing	41
3.1 Design of Polarization-Maintaining FBGs Using Polyimide Films to Improve Strain-Temperature Sensing in CFRP	42

3.1.1	Optomechanical interaction	42
3.1.2	Simulation approach	44
3.1.3	Validation of composite laminate and FBG models	46
3.1.3.1	Opto-mechanical simulation	47
3.1.4	Performance comparison of FBGs embedded in CFRP laminate	57
3.1.5	Conclusions	61
3.2	Design of Microstructured Flat Optical Fiber for Stress Monitoring in Composite Materials	63
3.2.1	Operation principle and MFOF description	64
3.2.1.1	Design approach	65
3.2.1.2	Model validation	65
3.2.2	Design of the embedded MFOF	68
3.2.3	Results and discussion	73
3.2.4	Conclusion	77
3.3	Effects of Curvature on Flexible Bragg Grating in Off-Axis Core: Theory and Experiment	79
3.3.1	Simulation approach	80
3.3.2	Design and fabrication of the sensor	81
3.3.2.1	Sensor design	81
3.3.2.2	Sensor fabrication and spectrum measurement ..	85
3.3.3	Curvature effect	87
3.3.4	Conclusion	90
3.4	Flexible Photonic Sensors: Exploiting Ratiometric Power in Few-Mode Waveguides for Bending Inference	91
3.4.1	Electromagnetic and mechanical modeling	93
3.4.1.1	Design approach	93
3.4.1.2	Electromagnetic design and modal investigation	94
3.4.1.3	Mechanical investigation: three-point bending test	95
3.4.1.4	Power mode mixing	98
3.4.1.5	Bragg grating spectrum evaluation	99
3.4.2	Fabrication and characterization	100
3.4.2.1	Fabrication and characterization	100
3.4.2.2	Bragg gratings inscription	101
3.4.2.3	Three-point bending test and optical measurement	103
3.4.2.4	Discussion of results	107
3.4.3	Conclusion	108

4 Combining and Coupling of Optical Beams	109
4.1 Fused Optical Fiber Combiner Based on Indium Fluoride Glass: New Perspectives for Mid-IR Applications.....	110
4.1.1 Electromagnetic design and numerical results	110
4.1.1.1 Design approach	110
4.1.1.2 Design of the 3×1 fluoroindate combiner	111
4.1.1.3 Numerical results	113
4.1.2 Fabrication and measurements	116
4.1.2.1 Fabrication challenges	116
4.1.2.2 Fabrication method	117
4.1.2.3 Fabrication results	120
4.1.2.4 Output power measurements	122
4.1.2.5 Output beam measurements	125
4.1.3 Conclusion	126
4.2 Low-Loss Fluoride Optical Fiber Coupler for Mid-Infrared Applications.....	126
4.2.1 Optical fiber coupler design	126
4.2.2 Optical fiber coupler fabrication	130
4.2.3 Optical fiber coupler characterization	132
4.2.4 Conclusion	134
5 Optical Sources for Mid-IR Sensing	135
5.1 Design of a Mid-IR laser based on a Ho:Nd-codoped fluoroindate fiber	135
5.1.1 Energy transfer coefficients recovering	136
5.1.2 Laser design	143
5.1.3 Results discussion	146
5.1.4 Conclusions	148
5.2 Design of a Broadband Erbium-doped Fluoroindate Fiber Laser Emitting up to $3.91\text{ }\mu\text{m}$	148
5.2.1 Laser design	148
5.2.2 Refinement	154
5.2.3 Conclusion	157
Conclusions	159
List of publications	162
References	168

Introduction

In recent decades, a significant increase in the use of composite materials has occurred across various industrial sectors, including aeronautics, aerospace, and wind energy production. In particular, the widespread adoption of CFRP is related to the possibility of increasing reliability, improving safety, enabling lightweight design, and reducing maintenance costs of aerospace crafts. The highly stringent requirement, within the aerospace sector, motivates the research efforts in developing optical sensors and systems for composite materials monitoring.

In the aerospace sector, multiparameter sensors that can be easily embedded in composite laminates with reduced intrusiveness in the mechanical properties of the host material is of paramount importance. Therefore, the exploration of advanced optical sensor technologies for structural health monitoring of CFRP laminates has been one of the main objectives of my Ph.D. research work. The research activity deals with the electromagnetic design, fabrication, and characterization of sensors based on Bragg gratings, recognized as a leading choice in optical sensing. The latter can be used to measure physical quantities such as strain, bending, temperature, and pressure enabling miniaturization, high sensitivity, multiplexing capabilities, and immunity to electromagnetic interference. The Ph.D. research work explores the use of Bragg grating in non-conventional optical platforms such as polarization maintaining optical fibers, flat optical fibers, microstructured flat optical fibers, and all-glass flexible planar platforms for aerospace structure monitoring. The flat optical fiber can be manufactured using typical fiber optic methods, making it cheaper than conventional planar waveguides. On the other hand, the Ph.D. research work developed on all-glass flexible photonic platforms demonstrated the possibility to fabricate ultra-thin and conformable sensors to be applied for bending detection of complex aerospace structures. These novel solutions have been developed in collaboration with the University of Southampton (Optoelectronic Research Centre (ORC), UK), scientific referee Dr. Christopher Holmes.

Bragg gratings are also wavelength-selective structures that can be employed for multiplexing optical signals or for achieving laser cavities. The growing

interest in Mid-IR spectral range and its applications, such as the use of contactless and instantaneous non-destructive testing techniques for the detection of defects in composite material, has moved researchers to swiftly develop optical fiber components and lasers operating above $\lambda = 2 \mu\text{m}$.

Typically, commercial optical fiber components are made of silica glass, and their use is limited in near-infrared (NIR) wavelength range. As an alternative to silica glasses, chalcogenide and fluoride ones, including heavy metal fluoride and halide polycrystals, show a wider transmission window, resulting in excellent candidates for Mid-IR applications. Therefore, during the Ph.D. research activity the design, fabrication, and characterization of Mid-IR optical fiber components has been carried out. A commercial glass workstation Vytran GPX-2400 has been employed to develop an ad-hoc fabrication and normalizing procedure. For the first time, with reference to the state of the art, strong challenges such as the fabrication of low-loss devices and soft-glass processing without surface crystallization are overcome. This research activity has been partially made in collaboration with the French company Le Verre Fluoré (Bruz) and it is within the framework of the European project H2020 “PASSEPARTOUT”. Optical fiber devices, such as combiners/couplers have been designed, fabricated and characterized for combining (or splitting) optical signals into (from) a single optical fiber preserving high optical beam quality. The adoption of these devices eliminates the need for bulk optics and paves the way for the development of all-fiber lasers for Mid-IR applications. A compact system for multiplexing the signals from Bragg grating sensors can be designed with optical fiber combiners and couplers since their operational range spans from NIR to Mid-IR. For instance, the signals delivered by multiple Bragg grating sensors can be combined via an optical fiber combiner. In this manner, a single optical spectrometer can detect simultaneously the sensing signals.

Furthermore, the use of Bragg gratings along with optical fiber combiners and couplers proves valuable in advancing the development of all-fiber Mid-IR amplifiers and lasers. During the doctoral research work I focused also on the design and optimization of CW lasers operating in the Mid-IR wavelength range to be employed in optical communications systems and sensing.

In the end, the research thesis aims to enhance the safety, reliability, and performance of composite structures proposing both innovative Bragg grating sensors and Mid-IR optical systems. The obtained results are illustrated by following this organization:

- (i) Chapter 1 is an introduction to optical Bragg grating sensors, Mid-IR optical devices, and optical fiber laser for aerospace application, with particular reference to the ones that are the object of the thesis.
- (ii) Chapter 2 recalls the theory for the design of: i) Bragg grating sensors, ii) Mid-IR optical fiber components, and iii) Mid-IR optical fiber lasers.
- (iii) Chapter 3 describes optical sensors for aerospace applications. In particular Section 3.1 describes the design of polarization-maintaining Fiber Bragg Gratings (FBGs) using polyimide films to improve strain-temperature sensing in CFRP; Section 3.2 describes the design of a microstructured flat optical fiber for stress monitoring in composite materials; Section 3.3 describes the effects of curvature on flexible Bragg grating in off-axis core, including theoretical and experimental explanations; in Section 3.4 describes the design, fabrication and characterization of flexible photonic sensors which exploits ratiometric power in few-mode waveguides for bending inference.
- (iv) Chapter 4 describes Mid-IR optical components for combining/coupling purposes. In particular, Section 4.1 describes the design, fabrication and characterization of a fused optical fiber combiner based on indium fluoride glass for Mid-IR applications; Section 4.2 describes the design, fabrication and characterization of a low-loss fluoride optical fiber coupler for mid-infrared applications.
- (v) Chapter 5 describes Mid-IR CW optical fiber sources. In particular, Section 5.1 describes the design of a Mid-IR laser based on a Ho:Nd-codoped fluoroindate fiber; Section 5.2 describes the design of a broad-band erbium-doped fluoroindate fiber laser emitting up to $3.91 \mu m$.

1 Optical Sensors Based on Bragg Grating and Mid-IR Optical Systems for Aerospace Applications

The introduction of composite materials brings significant advances in the aerospace field since CFRPs offer excellent mechanical properties such as high stiffness, high fatigue resistance and are particularly suitable in space structures that require force-to-force ratios several times the weight of steel or aluminum. At the same time, the layered nature of composite materials makes them susceptible to delamination, cracks, and hidden voids. Multiparameter optical sensors and Mid-IR optical systems based on laser sources, can be employed to enhance the reliability and safety of aerospace structures. Optical sensors based on Bragg gratings can be embedded in composite materials to exploit real-time monitoring of internal strain during the fabrication process or during the in-service phase. While, prior to deployment, composite structures undergo rigorous quality testing via non-destructive test methods, e.g. by using Mid-IR lasers. For NDT method, the laser beam is focalized on the CFRP laminate under investigation to generate ultrasonic waves and to detect via interferometry the existence of defects. However, optical fiber components operating in Mid-IR, for the development of high beam quality all-in-fiber lasers, are still not widespread on a commercial level since soft glasses processing is challenging.

Finally, in my Ph.D. research activity I have contributed to the design, fabrication and characterization of innovative optical sensing solutions, the identification of well-consolidated fabrication process for Mid-IR components and the design Mid-IR fiber lasers. The main topics of the Ph.D. thesis are summarized in the following:

- (i) Bragg grating sensors based on polarization maintaining optical fibers, flat optical fibers, and flexible planar optical devices for real-time monitoring of unidirectional/tri-axial strains, temperature, and bending in CFRPs;

- (ii) Fluoride/chalcogenide optical fiber-based Mid-IR components, such as couplers and combiners, for beam combining, beam splitting, and WDM applications;
- (iii) Optical sources operating in the Mid-IR wavelength range to be integrated in sensing or optical communication systems.

1.1 Bragg gratings sensors

By solving the Maxwell equation for a dielectric waveguide with, for instance, cylindrical or rectangular shape, it is possible to study the propagation of the electromagnetic field in an optical fiber or in a planar device. The electromagnetic field is confined within the medium with a higher refractive index, namely the core. If a permanent, periodic perturbation of the refractive index is induced within the core, e.g. by exposing it to a laser beam and exploiting the photorefractive effect, it is possible to obtain a Bragg grating. The grating is a wavelength-selective element that filters the light traveling within the waveguide. It reflects a portion of the light centered around a peak wavelength value defined as Bragg wavelength λ_B . Bragg grating couples the light from a forward-propagating mode to a backward one (counter-propagating mode) and the coupling occurs when the resonance condition, e.g. the Bragg condition is verified. The Coupled Mode Theory (CMT) can be used to solve this electromagnetic phenomena. A formal treatise of the CMT will be given in more detail in Section 2.1. For the sake of clarity, a Bragg grating is characterized by a grating period Λ , a refractive index modulation Δn , and length L . Let n_{eff} be the effective refractive index of the guided mode, the Bragg wavelength can be calculated as $\lambda_B = 2n_{eff}\Lambda$. External physical quantities such as strain, pressure or a temperature variation, can alter the grating period Λ , the refractive index n and thus the core effective refractive index n_{eff} (more details in Section 2.2). Consequently, the signal reflected from the grating can experience, depending on the type of external perturbation, a red or blue shift. The optical spectrometer is the most effective solution for measuring the Bragg wavelength shift in order to recover the external perturbations. In Fig. 1.1 is reported the measurement system for Bragg grating sensors developed at the Polytechnic of Bari, Microwave & Optical Engineering (MOE) group laboratory. The main system components are a broadband optical source (SLED), a FBG, and a spectrometer.

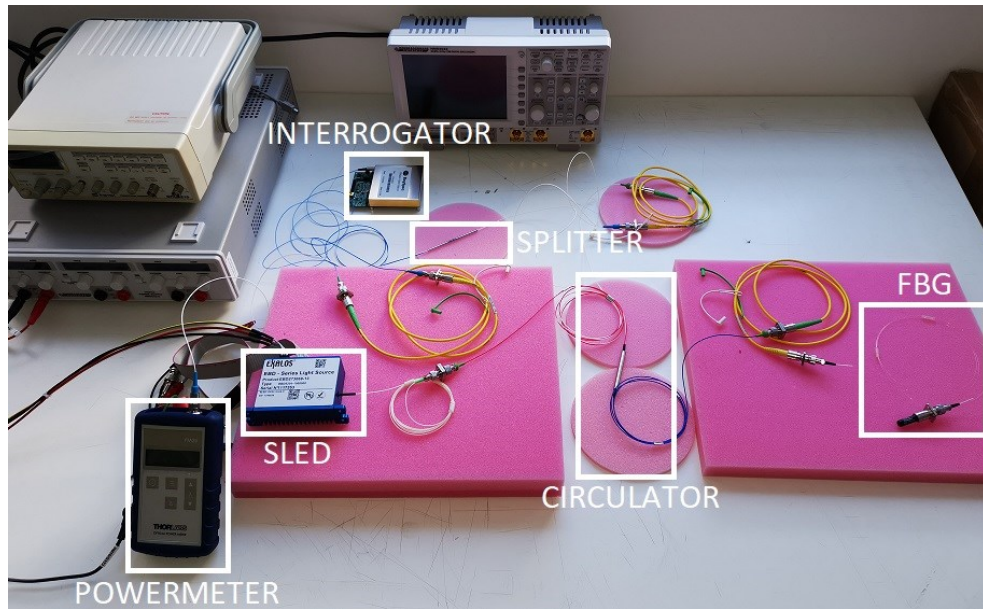


Figure 1.1 Measurement system for optical Bragg grating sensors, developed at Politecnico of Bari, MOE group laboratory.

Typically, Bragg gratings are written in standard optical fibers, thus offering the possibility to retrieve a single external perturbation. Different methods, such as the use of several Bragg grating sensors with different sensitivities or specialized Bragg grating intended to respond to a particular perturbation, have been proposed for multiparameter detection. The main objective of this doctoral thesis has been to design and fabricate novel optical sensors based on Bragg gratings, designed to simultaneously detect multiple physical parameters, while ensuring compact dimensions and simple integration into composite laminates. The research work also focused on the development of miniaturized and conformable flexible sensors to infer bending since aircraft structures are frequently made of composite materials that are curved in shape or exposed to sharp curvature during their use.

In the following paragraphs, are outlined the most interesting approach proposed in literature considering both optical fiber and planar photonic sensors based on Bragg grating, including the findings achieved during the doctoral research activity.

1.1.1 Optical FBG sensors for multiparameter monitoring of CFRP laminates

The use of multiparameter sensors for the real-time monitoring of CFRP has evolved into an indispensable technology for industrial equipment and aircraft.

Composite materials, thanks their exceptional mechanical properties like elevated stiffness, remarkable specific strength, and resistance to fatigue, emphasize the impact of this development. Optical fiber sensor technology can be considered the state-of-the-art solution for monitoring the internal strain state of composite materials as CFRP [1], [2]. At the same time, the employment of a non-destructive sensing approach is crucial to detect failures of the CFRP, such as cracks and delamination [3]–[8]. CFRP tends to be fragile in transverse directions and structural health monitoring (SHM) can be successfully implemented using FBGs [9]. FBGs offer advantages in terms of dimension, weight, immunity to electromagnetic interference, multiplexing, low-cost, high spatial resolution, feasibility in harsh environment [10], [11]. Embedded FBG sensors can detect both static and dynamic strain fields [12]–[14]. The use of embedded optical fiber sensor for the detection of static strain in composite materials can be considered mature for uniaxial load [15]–[19]. Regarding multiparameter detection, in particular with reference to multiaxial strain monitoring, high birefringent FBGs (i.e., microstructured, panda, bow-tie etc.) have been proposed [20], [21]. The birefringence breaks the circular symmetry in the optical fiber, creating two principal transmission axes, known respectively as the fast and slow axes. This determines two reflection peaks of the FBG characterized by two different sensitivities that can be employed to measure two different parameters. Generally, optical fibres are not placed on the surface if not jacketed as they could be easily damaged in-service environments [22]. Polyimide coated optical fibers exhibit very attractive mechanical properties. Polyimide is a high-performance polymer, which allows to operate safely in temperatures up to more than 600 K, allowing the optical fibers to survive in high temperature condition, e.g. after thermally cured embedding processes. For these reasons, polyimide coated optical fibers are an excellent choice for the construction of embedded FBG strain and temperature sensors. Anti-sticky polyimide films (APFs), are typically used to obtain loosely embedded optical fibers in composite materials for strain-free temperature sensing, i.e. for a complete cancellation of stress transfer in all directions [23]. On the other hand, in [24] APFs with high birefringent FBGs are proposed as buffer regions, i.e. stress absorption layers, in order to obtain through a proper design a suitable reduction of transversal stress-transfer between the laminate and the optical fiber. In this way, the temperature and strain measurement decoupling is affected by less uncertainty. Even though high birefringent FBGs are a good choice for multiparameter detection, they requires a precise orientation with respect to the composite material structure, thus errors in orientation assessment can lead to a wrong estimation of the strain field [25],

[26]. Flat optical fiber shape is more appropriate for the embedding process, mitigating both the problems related to resin-rich regions and to orientation. Flat optical fiber is essentially composed of a slab waveguide and a surrounding cladding [27]. In general, it can support multimode propagation in two lateral elliptical core regions, named “eyelets”, and single mode propagation in the central core region due to the presence of a thin and flat core layer [28]. Single mode waveguides can be written, by inducing a further refractive index change, both in the eyelets and in the central core layer through direct UV writing (DUW) or femtosecond laser inscription [27], [29]. Many passive devices have been proposed in flat optical fibers such as gratings, resonators, splitters, interferometers and microfluidic channel [27], [30]. Flat optical fiber sensors can be used for the detection of damages, caused by impact, delamination or debonding, through the comparison of the spectrum before and after their manifestations and the use of detective algorithms for advanced pattern recognition [31]–[34].

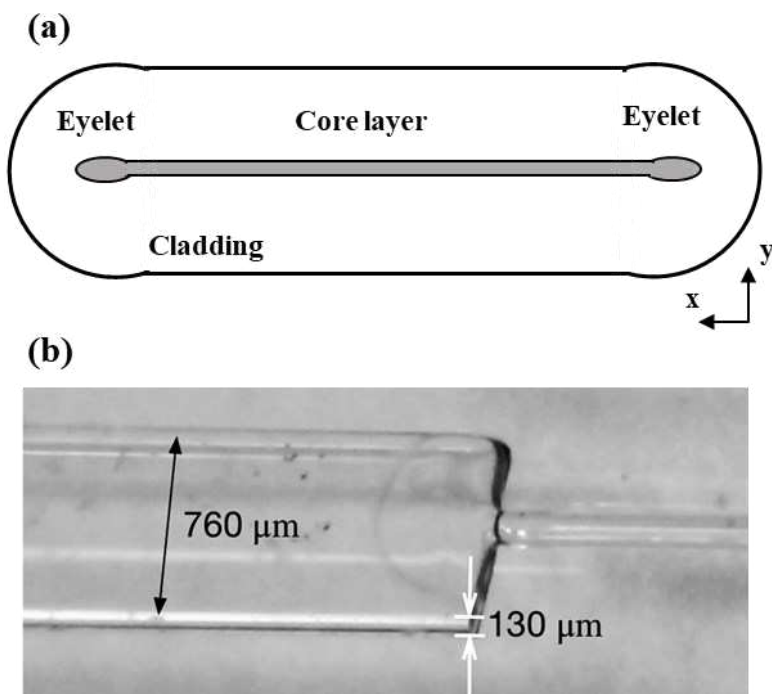


Figure 1.2 (a) Sketch of the cross-section of a flat optical fiber where are clearly evident the core layer and the two eyelets. (b) Flat optical fiber coupled with a standard optical fiber (fabricated at University of Southampton, Optoelectronic Research Center (ORC), UK).

Fig. 1.2 (a) shows schematic representation of the cross-section of a flat optical fiber, while Fig. 1.2 (b) shows a prototype of a flat optical fiber fabricated at the University of Southampton, Optoelectronic Research Center (ORC).

In [35], an innovative microstructured flat optical fiber is designed for multiparameter monitoring. In particular, the sensor is proposed to perform triaxial strain monitoring with high accuracy. To enhance through-thickness strain sensitivity (i.e. strain vector orthogonal to direction of light propagation), other approaches such as external microstructuring or gradual thinning of the cladding region through physical micromachining have been proposed in [36], [37].

1.1.2 Flexible photonic sensors based on Bragg grating for bending and/or temperature monitoring

Curvature sensors have attracted a significant interest during the past ten years, mostly due to the numerous applications. These applications encompass areas such as structural health monitoring, soft robotics, medicine. They can be used to facilitate minimally invasive medical procedures, to enhance soft robotic systems, to detect bending and shape change of composite materials [38]-[44]. Indeed, flexible photonics is a rapidly advancing research field which has opened-up new sensing opportunities, including new monitoring capability of high-value composite materials. Traditional rigid devices in planar optics can be refined through controlled thinning, adding the ability to flex while preserving their essential functionality. Fig. 1.3 (a) shows schematic representation of the cross-section of a flexible photonic platform, while Fig. 1.3 (b) the flexible photonic device which has been fabricated at the Optoelectronic Research Center (ORC) at the University of Southampton and tested employing the measurement set-up (see. Fig. 1.1) at the Polytechnic of Bari.

This innovative class of photonic devices has been successfully fabricated on a number of substrates, as extensively documented in various recent articles. Both organic and inorganic materials used to fabricate devices that can be curved, twisted, or stretched preserving the mechanical and optical performances have been proposed [45]-[47]. In particular, the development of flexible photonic structures and devices using ultrathin glasses, which are mechanically flexible, has provided a new opportunity in addition to the use of polymer-based materials [48]. The maximum curvature depends on the thickness of the glass and the presence of surface defects, which are related to the fabrication process [46].

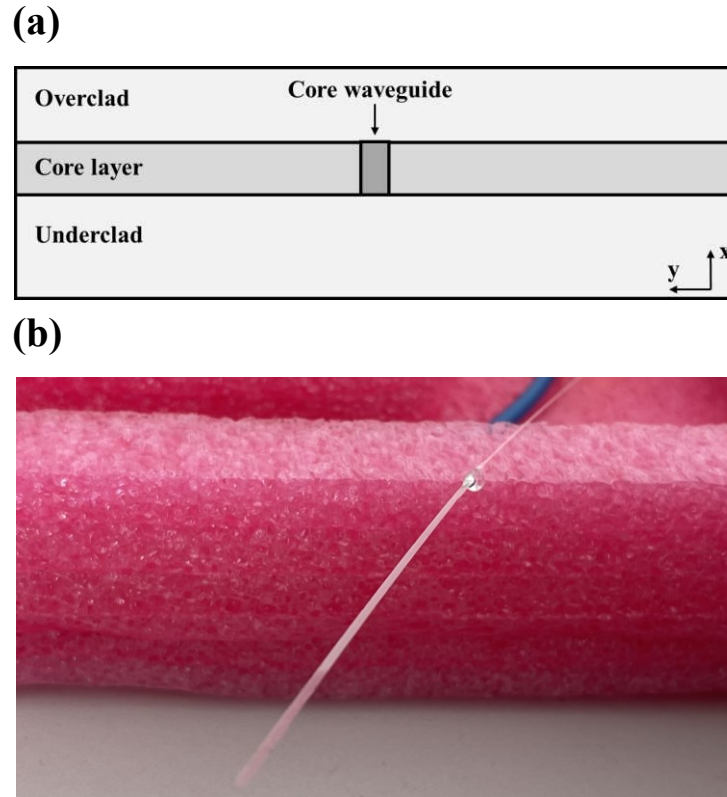


Figure 1.3 (a) Sketch of the cross-section of a flexible photonic device. The overclad, underclad and core layers are clearly evident. At the center the UV written core waveguide. (b) Flexible photonic device (fabricated at University of Southampton, Optoelectronic Research Center (ORC), UK) and tested at the Polytechnic of Bari, MOE group laboratory.

Different operative principles have been proposed to design one-dimensional curvature sensors, including Bragg gratings in off-axis core [38], [49], eccentric Bragg gratings [50], [51], tilted Bragg gratings [52], [53], long period gratings [54]-[57], and in-line interferometers [58]-[60]. Generally, a trade-off between complexity and sensitivity is required. The interferometric scheme benefits from higher sensitivity, but the fabrication cost and complexity could not fully meet the requirements for mass use [38], [39]. Long period gratings have some drawbacks for some specific applications. As an example, the broad resonance that limits the sensor accuracy and their length results in deformation over only a fraction of the sensor when subjected to a sharp, localized curvature [49], [61], [62]. Bragg gratings can be alternative candidates for curvature sensing thanks to fabrication process maturity [38], [58].

Multidimensional curvature monitoring is spreading and multicore fibers play an important role in this context [39], [63]-[67]. Three non-aligned cores, off-axis with respect to the curvature, each of which comprising a Bragg grating, have been exploited to this aim [68], and a redundant number of cores increases the measurement reliability [64]. The overall performance of the shape change monitoring depends on the strain measurements of each Bragg grating [66]. The curvature effect on the reflection spectrum for a few-mode, off-axis core, is also studied in flexible silica planar Bragg grating and reported in [67]. While, a novel approach to monitor the degree of bending via flexible photonics devices, using ratiometric power variation in a few-mode optical waveguide, is proposed [68]. To demonstrate its feasibility, a sensor exploiting three Bragg gratings, approximately aligned to the neutral axis, is designed, fabricated and characterized.

1.2 Optical fiber devices for combining applications in Mid-IR spectral range

Mid-IR spectral range is bringing to light interesting applications and attracting research attention because of its implications in a plethora of applications, such as optical spectroscopy, chemical sensing, thermal imaging, light sources, and comb generation [69]-[72]. Mid-IR is also attracting the research interest in spectroscopy, since the absorption bands of numerous biological substances lies within the wavelengths range $\lambda = [2 - 20] \mu m$. For the abovementioned reasons, it is increasing the need of optical fiber devices for Mid-IR wavelength range [73], [74]. As an alternative to silica glasses optical components, chalcogenide and fluoride ones, including heavy metal fluoride and halide polycrystals, show a wider transmission window, resulting excellent candidates for Mid-IR applications [75]-[77].

The discovery of fluoride glasses dates back to 1974, and since then, they have undergone extensive research and development. Today, fluoride glasses represent a well-established technology capable of transmitting light across a broad spectral range, encompassing the ultraviolet (UV), visible, near-infrared (NIR), and Mid-IR regions [78]. Fluoride optical fibers based on zirconium, indium, barium, or gallium are available on market. Among these, indium fluoride (IFG) optical fibers, also known as fluoroindate fibers, offer a broader transmission window when compared to zirconium fluoride (ZFG) fibers. The transmission range of IFG fibers extends from $\lambda = 0.3 \mu m$ to $\lambda = 5.5 \mu m$. Regarding chalcogenide glasses, they are typically made of arsenic combined with

chalcogen elements such as selenium, sulphur and tellurium. Chalcogenide optical fibers, with respect to fluoroindate ones, exhibit a broader transmission range (up to $\lambda = 20 \mu\text{m}$) and a higher refractive index. Despite their transparency, they suffer of high Fresnel losses at the end-facets. The high technological feasibility of fluoroindate/chalcogenide optical fibers, the need of compact, low cost and all-in fiber lasers, has driven research interest in Mid-IR fused fiber components. The development of fused optical components based on fluoride glass is challenging, due to narrow temperature for processing without surface crystallization. Therefore, the state-of-art lacks of completeness [79]. Some specialized glass processing systems have been proposed for this purpose [80]. In the case of chalcogenide glasses, a few components such as optical couplers and combiners have been developed via custom fusion workstations operating at low melting temperatures [81]-[85].

In the upcoming paragraphs, is reported an overview of recent advancements and the current state of research concerning optical combining components. The main results reported in literature refers to devices made with silica optical fibers but the most recent results on fluoride and chalcogenide optical combining components designed for Mid-IR applications are also reported. This encompass the progress made in this field during the doctoral research, along with a full explanation of the operational principles of the main combining devices [86]. The coupling phenomena occurring in these optical components can be studied by CMT, the formal treatise of the CMT will be given in more detail in Section 2.3.

1.2.1 Optical fiber taper

An optical fiber taper is obtained through a gradual thinning of the cladding diameter, over a specific segment, by applying stretching and heating. The heat source is typically an open flame or a graphite filament, that heat the fiber until the glass reach its softening point. In Fig. 1.4 a schematic representation of an optical fiber taper is reported, highlighting the main regions of a taper, such as down taper $L_{down,t}$, up taper $L_{up,t}$ and waist region L_{waist} .

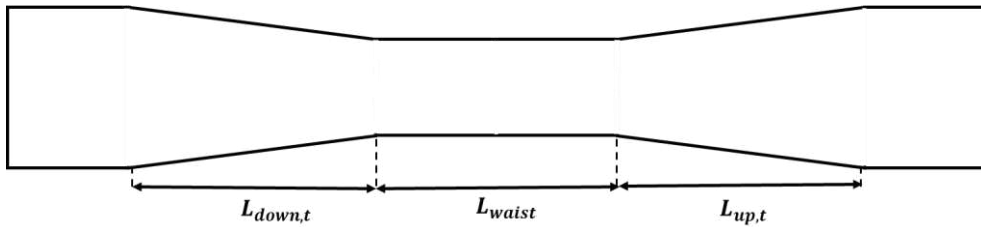


Figure 1.4 Schematic representation of an optical fiber taper.

The fused biconical tapering technique is considered one of the best fabrication approach to fabricate optical fiber combiner or couplers. The devices designed during the Ph.D. activity have been fabricated at the Polytechnic of Bari employing a commercial glass processing system, namely Vytran GPX-2400. In Fig. 1.5 an image captured during the fabrication of an optical fiber taper is reported.

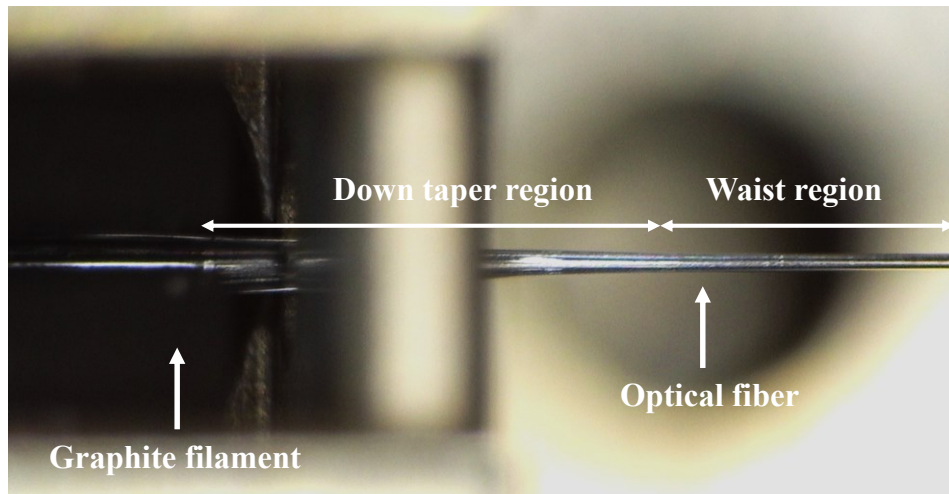


Figure 1.5 Fabrication process of an optical fiber taper via glass processing system Vytran GPX-2400 (at the Polytechnic of Bari).

1.2.2 Optical fiber combiners and couplers

Optical fiber combiners are employed for (a) combining the propagating optical beams from several input optical fibers into one output optical fiber, (b) splitting the propagating optical beam from one input optical fiber into several optical fibers and, (c) coupling the propagating optical beam of a tapered optical fiber, lateral spliced with a signal optical fiber.

Three different categories can be identified to describe the operation of the $N \times 1$ optical fiber combiners: i) end-pump combiners, ii) end-pump and signal combiners, iii) photonic lanterns. The first two categories are used for power delivery in doped optical fibers, while the third category fits well in application in which it is necessary to combine the signal of N single mode fibers into a single multimode output. Figure 1.6 (a) refers to an end-pump combiner. It consists of N pump multimode optical fibers fused together and generally the waist region of the device is spliced with an output multimode optical fiber [84], [86]-[88]. The output multimode optical fiber improves the output beam quality to the expense of device transmission efficiency due to refractive index, numerical aperture and beam size mismatches. High output beam quality is guaranteed if all the input optical fibers are excited simultaneously at the same operating wavelength. Figure 1.6 (b) reports a sketch of an end-pump and signal combiner. It consists of a signal optical fiber surrounded by N pump multimode optical fibers. All the optical fibers are fused together, and the pump power is coupled with the signal optical fiber, obtaining a $(N+1) \times 1$ combiner [89], [90]. Figure 1.6 (c) shows a photonic lantern, where N single mode optical fibers are fused together to obtain a single multimode output. This device is employed for spatial division multiplexing (SDM) [91], [92]. The spatial modes guided in the multimode waist, which is obtained after an adiabatic transition, are exploited to increase the number of data channels in MIMO networks.

The $1 \times N$ optical fiber combiner (Fig. 1.6 (c)) refers also to a photonic lantern. In this case, the signal is launched in the multimode port (output port) and coupled in the several single mode optical fibers (input ports) [93], [94]. This ensures that the optical beam is converted and divided into several single mode optical beams (non-tapered optical fibers). It can be used in astronomy and spectroscopy applications, to perform spectral filtering in single mode optical fibers.

A direct coupling of a pump optical fiber with a signal optical fiber via side power coupling is performed via the device illustrated in Fig. 1.6 (d) [79], [95]. Typically, coreless optical fibers (i.e. optical fiber rods) or thin cladding optical fibers are employed as pump optical fibers. These are pre-tapered and side spliced with the signal optical fiber. The aim is to deliver a high optical power into an active medium.

The 2×2 optical fiber coupler is another fundamental element of most optical fiber systems, typically used for multiplexing/demultiplexing, signal/pump combination, ring cavity, filters, etc. [96], [97]. During 1990s experiments were conducted on couplers using for the first time optical fibers based on soft glasses [98], [99]. Subsequently, investigations predominantly focused on chalcogenide

couplers for broadband, wavelength-dependent, and non-linear applications [81], [82], [100]-[106]. Side-polished bonding and fused biconical tapering techniques have been exploited for the construction of zirconium fluoride couplers [85], [98], [105]-[109]. The fused biconical tapering technique is considered better than side-etching and side-polishing with reference to reliability and repeatability [81].

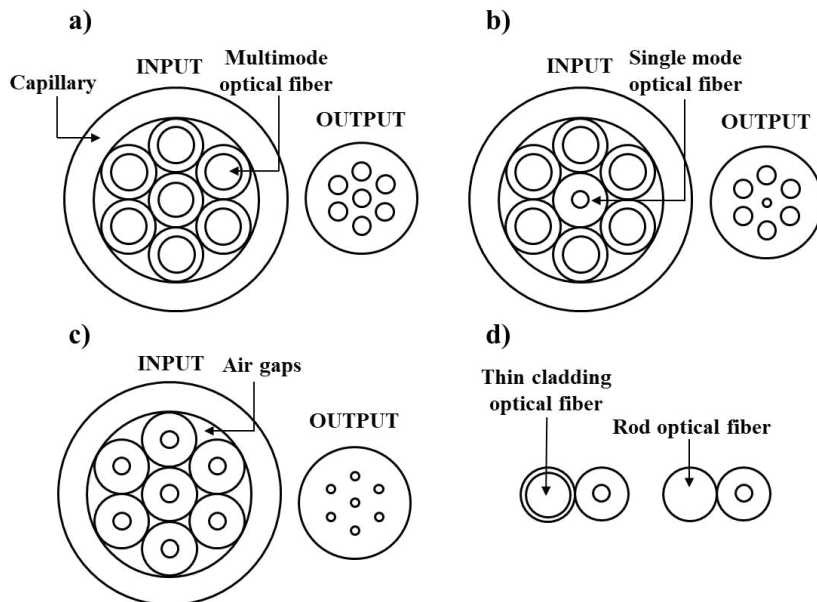


Figure 1.6 Sketch of the input (before tapering) and output cross-section of: (a) end-pump combiner, (b) end-pump and signal combiner, (c) photonic lantern, (d) side-pump combiner.

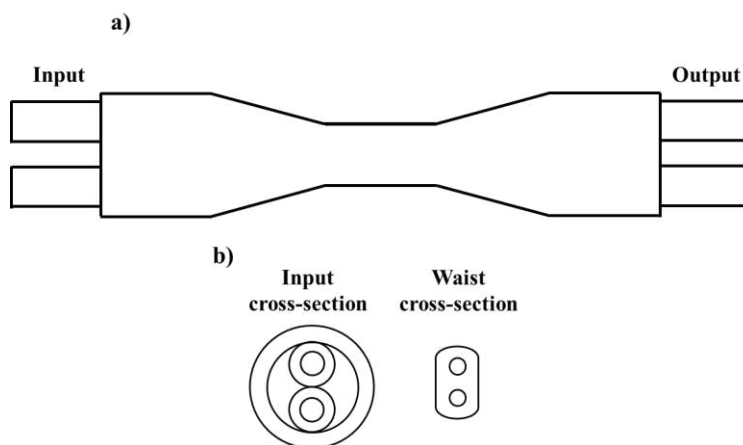


Figure 1.7 (a) Sketch of 2×2 optical fiber coupler, (b) input cross-section and waist cross-section at the center of the device.

1.3 Mid-IR optical fiber sources

The potential applications of Mid-IR emitting sources, particularly for fast optical communications, environmental monitoring, and sensing, have generated a lot of attention in recent years [110]-[115]. Fiber lasers can be customized and fabricated using various types of optical fiber materials, such as chalcogenide and fluoride glasses, which may be doped or co-doped with a variety of rare-earth ions. These ions include thulium, holmium, dysprosium, erbium, neodymium, and praseodymium, enabling the lasers to emit light at different wavelength ranges [116]-[127].

In particular, fluoroindate fibers exhibit high transparency in the $3\text{-}5 \mu\text{m}$ range, where many air pollutants and biomolecules exhibit light absorption peaks. The reduced optical attenuation $\alpha \approx 0.2 \text{ dB/m}$ from ultra-violet (UV) to Mid-IR about $\lambda = 500 \text{ nm}$ to about $\lambda = 4500 \text{ nm}$, and the low phonon energy of fluoroindate glasses make them good candidates for laser construction and exploitation [110], [120], [126]. In addition, they are good rare-earth hosts since contrarily to other glasses, it is possible to incorporate also 10 mol. % of rare earth ions, similarly to fluorozirconate glasses.

Fluoroindate optical fibers can exhibit attenuation much smaller with respect to the fluoride ones at longer wavelength, beyond $\lambda = 3.3/3.5 \mu\text{m}$ [126]. During the last years, rare-earth doped fluoroindate glasses have been spectroscopically investigated with the aim of finding new pumping schemes and operating wavelengths [121]-[125]. Erbium-, dysprosium-, and holmium-doped fluoroindate fibers have attracted particular attention for their emission at $\lambda = 3.5 \mu\text{m}$, $\lambda = 4.2 \mu\text{m}$, and $\lambda = 3.9 \mu\text{m}$, respectively [127]-[129]. Recently, holmium-doped fluoroindate fibers have been characterized [127], [130], [131] and CW lasers emitting at $\lambda_s = 2.875 \mu\text{m}$ [129] and $\lambda_s = 3.92 \mu\text{m}$ [127], pumped at $\lambda_p = 1120 \text{ nm}$ and $\lambda_p = 888 \text{ nm}$ respectively, have been demonstrated. For that pertaining the pulsed laser operation, emissions at the wavelength $\lambda_s = 2.106 \mu\text{m}$ and in the $\lambda_s = 2.95 - 3.015 \mu\text{m}$ range [132], [133] have been obtained.

New spectroscopic investigations on fluoroindate glasses co-doped with holmium-neodymium, holmium-europium, and praseodymium-ytterbium have shown that co-doping can lead to an improvement of the emission efficiency if compared to the employment of a single dopant. In particular, holmium-neodymium co-doping could allow better performance than those of heavily-holmium-doped, $N_{Ho} = 2 \times 10^{27} \text{ ions/m}^3$, fluoroindate fiber lasers [134], [135].

Pulsed lasers in the Mid-IR wavelength range are usually employed as modulators for fast communications. Great research interest was focused on Er^{3+} -

doped fluoride fiber, since emission at about $\lambda = 2.8 \mu m$ and $\lambda = 3.5 \mu m$ allowed to obtain intriguing laser in CW, gain-switched, and *Q*-switched regime [136], [137]. In particular, in [138] a gain-switched fiber laser operating near $\lambda = 3.5 \mu m$ via a dual-wavelength pumping scheme was obtained in an erbium-doped fluorozirconate fiber, with stable pulses with repetition rates ranging between $f_R = 15 \text{ kHz}$ and $f_R = 20 \text{ kHz}$ and laser efficiency of $\eta = 4.7\%$.

In this thesis CW optical sources are designed to work in the Mid-IR range employing commercially available fluoroindate fibers, with the aim to propose new sources for aerospace and optical communication applications.

2 Recalls of Theory

In this chapter, a recall of theory useful for the design of optical sensors, Mid-IR optical devices, and optical sources proposed in this thesis, is briefly reported.

2.1 Coupled Mode Theory: general formulation

CMT is a method to analyze the light propagation in perturbed or weakly coupled waveguides. First of all, the modes of the unperturbed or uncoupled structures are defined and solved. Then, a linear combination of these modes is used as a trial solution to Maxwell's equations for complex perturbed or coupled structures. Here is reported the general expression of Maxwell's equations (2.1) [139]-[141].

$$\begin{aligned}\nabla \times E &= -j\omega\mu H \\ \nabla \times H &= j\omega\varepsilon_0\varepsilon_r E\end{aligned}\tag{2.1}$$

The theory assumes that the electromagnetic field of the coupled structures may be adequately represented by a linear superposition of the modes of the unperturbed structures. This assumption is valid and give to an accurate mathematical description of electromagnetic wave propagation. Assuming a cartesian reference system, the electric field $E(x, y, z)$ and magnetic field $H(x, y, z)$, of a unperturbed (e.g., no periodic perturbation is induced such as a grating) waveguide, can be defined as a linear combination of the ideal modes [139], [140]

$$E(x, y, z) = \sum_{\mu} [A_{\mu}(z) e^{-j\beta_{\mu}z} + B_{\mu}(z) e^{j\beta_{\mu}z}] \cdot E_{\mu}(x, y)\tag{2.2}$$

$$H(x, y, z) = \sum_{\mu} [A_{\mu}(z) e^{-j\beta_{\mu}z} - B_{\mu}(z) e^{j\beta_{\mu}z}] \cdot H_{\mu}(x, y)\tag{2.3}$$

where $A_\mu(z)$ and $B_\mu(z)$ are the slowly varying amplitudes of μ -th mode traveling in the $+z$ and $-z$ directions, β_μ is the propagation constant, $E_\mu(x, y)$ and $H_\mu(x, y)$ are the electric and magnetic field profile of the μ -th mode, respectively. The electric field $E(x, y, z)$ and magnetic field $H(x, y, z)$ are used as a trial solution in the Maxwell's equation. The following Coupled Mode Equations (CMEs), respectively (2.4) and (2.5), can be derived by using the properties of waveguide modes and solved analytically or by numerical methods.

$$A'_\mu = \frac{dA_\mu(z)}{dz} = -j \sum [A_\nu(z)K_{\nu\mu}^t e^{-j(\beta_\nu - \beta_\mu)z} + B_\nu(z)K_{\nu\mu}^t e^{j(\beta_\nu + \beta_\mu)z}] \quad (2.4)$$

$$B'_\mu = \frac{dB_\mu(z)}{dz} = j \sum [A_\nu(z)K_{\nu\mu}^t e^{-j(\beta_\nu + \beta_\mu)z} + B_\nu(z)K_{\nu\mu}^t e^{j(\beta_\nu - \beta_\mu)z}] \quad (2.5)$$

The amplitude of the forward A_μ and backward B_μ mode μ can be calculated by solving the system of linear differential equation.

Based on the direction of the propagating mode, the coupling can be codirectional, in which the modes propagate in the same direction, or contra-directional, in which the modes propagate in opposite directions.

Only the transversal coupling coefficients $K_{\nu\mu}^t$ are considered since their value is generally two orders of magnitude greater than the longitudinal coupling coefficients $K_{\nu\mu}^z$. In (2.6) and (2.7) is reported the general expression for the calculation of transversal $K_{\nu\mu}^t$ and longitudinal $K_{\nu\mu}^z(z)$ coupling coefficients.

$$K_{\nu\mu}^z(z) = \omega \int \int_{-\infty}^{+\infty} \frac{\varepsilon \Delta \varepsilon(x, y, z)}{(\varepsilon + \Delta \varepsilon(x, y, z))} E_{z\nu}(x, y) E_{z\mu}^*(x, y) dx dy \quad (2.6)$$

$$K_{\nu\mu}^t(z) = \omega \int \int_{-\infty}^{+\infty} \Delta \varepsilon(x, y, z) \cdot E_{t\nu}(x, y) \cdot E_{t\mu}^*(x, y) dx dy \quad (2.7)$$

2.1.1 CMT applied to FBGs

The CMT can be used to describe the propagation of light within an optical fibre in the presence of discontinuity induced, for example, by a periodic structure such as a Bragg grating [142] – [144]. It is important to note that, the mathematical treatment reported in the following considers a cylindrical coordinate

reference system. In Fig. 2.1 is reported (a) the cross-section of an optical fiber, (b) the schematic representation of an FBG.

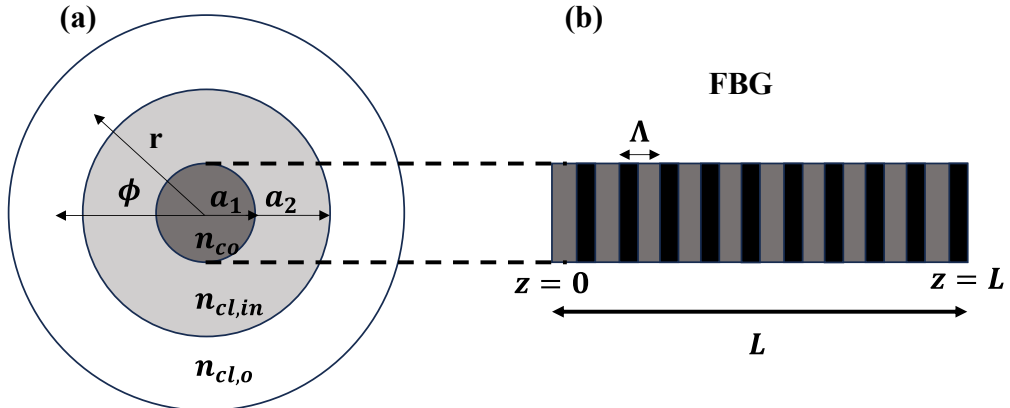


Figure 2.1 (a) Cross-section of an optical fiber, (b) schematic representation of an FBG.

The grating is typically UV written within the core thus the refractive index of the cladding is constant. The following system of equations defines the refractive index in an optical fiber with an inscribed FBG [143]:

$$n(r, z) = \begin{cases} n_{co}(z) = n_{co} \left\{ 1 + \sigma(z) \left[1 + m \cos \left(\frac{2\pi}{\Lambda} z \right) \right] \right\} & r \leq a_1 \\ n_{cl,in} & a_1 < r \leq a_2 \\ n_{cl,o} & r > a_2 \end{cases} \quad (2.8)$$

In the expression (2.8) $n_{cl,in}$ and $n_{cl,o}$ represent the refractive index values of the inner and outer cladding respectively, n_{co} is the refractive index value of the fiber core in the absence of grating, Λ is the period of the grating, m is the fringe modulation of the induced refractive index variation and its value is comprised between $0 \leq m \leq 1$, $\sigma(z)$ is the slowly variable envelope of the grating.

Moreover, by taking into account the equation of the transversal coupling coefficient $K_{v\mu}^t$ (2.7) and expressing it in a cylindrical coordinate, it can be rewritten as follows:

$$K_{\nu\mu}^t(z) = \frac{\omega}{4} \int_0^{2\pi} d\phi \int_0^{+\infty} \Delta\epsilon(r, z) \cdot E_{tv}(r, \phi) \cdot E_{t\mu}^*(r, \phi) r dr \quad (2.9)$$

Since the magnetic permeability of a dielectric medium is practically equal to that of vacuum, we can consider the following approximation:

$$\epsilon = \epsilon_0 n^2 \quad (2.10)$$

Considering small variation in the refractive index, e.g. if $\sigma(z) \cdot m \ll 1$, we can use Taylor's series development till the second term, obtaining

$$\Delta n^2 \approx 2n_{co}\Delta n \quad (2.11)$$

The dielectric constant variation $\Delta\epsilon$ can be calculated as:

$$\Delta\epsilon \approx \epsilon_0 \Delta n^2 \approx 2\epsilon_0 n_{co} \Delta n \quad (2.12)$$

By using the first equation of the system (2.8) it is possible to define

$$\Delta n = n_{co}\sigma(z) \left[1 + m \cos\left(\frac{2\pi}{\Lambda}z\right) \right] \quad (2.13)$$

By substituting (2.12) and (2.13) in (2.9):

$$K_{\nu\mu}^t(z) = \frac{\omega\epsilon_0 n_{co}^2 \sigma(z)}{2} \left[1 + m \cos\left(\frac{2\pi}{\Lambda}z\right) \right] \int_0^{2\pi} d\phi \int_{-\infty}^{+\infty} \Delta\epsilon(r, z) \cdot E_{tv}(r, \phi) \cdot E_{t\mu}^*(r, \phi) r dr \quad (2.14)$$

The (2.14) can be rewritten as follows:

$$K_{\nu\mu}^t = k_{\nu\mu}(z) \left[1 + m \cos\left(\frac{2\pi}{\Lambda}z\right) \right] \quad (2.15)$$

where $k_{\nu\mu}(z)$ includes in its expression the overlap integrals

$$k_{\nu\mu}(z) = \frac{\omega\epsilon_0 n_{co}^2 \sigma(z)}{2} \int_0^{2\pi} d\phi \int_{-\infty}^{+\infty} \Delta\epsilon(r, z) \cdot E_{tv}(r, \phi) \cdot E_{t\mu}^*(r, \phi) r dr \quad (2.16)$$

Since in FBGs the coupling occurs only between counter-propagating modes, in the equation (2.4) the amplitude of the forward mode A_μ can be neglected; whereas, in the equation (2.5), the amplitude of the backward mode B_μ can be neglected. The final CME can be defined as reported in (2.17) and (2.18). The transfer characteristic of a Bragg grating can be analytically determined by solving the obtained system of differential equations and by considering the coupling coefficient expressed in (2.13) [142] – [144].

$$A'_\mu = \frac{dA_\mu(z)}{dz} = -j \sum [B_\nu K_{\nu\mu}^t e^{j(\beta_\nu + \beta_\mu)z}] \quad (2.17)$$

$$B'_\mu = \frac{dB_\mu(z)}{dz} = j \sum [A_\nu K_{\nu\mu}^t e^{-j(\beta_\nu + \beta_\mu)z}] \quad (2.18)$$

To solve the system of differential equation it is necessary to impose appropriate boundary conditions. In the case of contra-directional coupling, the system cannot be solved as an initial value problem (IVP) but as a boundary value problem (BVP). To better explain that, let consider a FBG written in a single-mode optical fiber, having a length L (see Fig. 1 (b)). In this case, to solve the differential equations, we need four boundary conditions, but the known boundary condition are $A_\mu(0) = 1$ and $B_\mu(L) = 0$. These boundary conditions state that the amplitude of the forward propagating mode at the input of the fiber is one (we suppose that all launched power it is associated to the μ -th optical mode), whereas the amplitude of the μ -th backward propagating mode is zero in the after region of the grating. To find the other two boundary conditions, $A_\mu(L)$ and $B_\mu(0)$, it is necessary to solve the system of equations as a BVP.

2.2 Opto-mechanical design of Bragg gratings sensors

In the following, useful concepts to understand what the Bragg wavelength shift originated from are reported. In particular, the opto-mechanical properties of dielectric materials, thus the effects of temperature, strain, curvature on refractive index are described.

2.2.1 Opto-mechanical properties of silica

Dielectric materials, such as the silica, can be influenced by an applied stress e and/or temperature variation T . The physical phenomena related to these

external perturbations are the photo-elastic and thermo-optic effects [145] which can be employed to study the change in the refractive index n . The refractive index n can be expressed, in Cartesian coordinates (xyz), through the use of the following matrix notation:

$$[n] = \begin{bmatrix} n_{xx} & n_{xy} & n_{xz} \\ n_{yx} & n_{yy} & n_{yz} \\ n_{zx} & n_{zy} & n_{zz} \end{bmatrix} \quad (2.19)$$

Given symmetry, it can be represented by making use of six elements:

$$[n] = \begin{bmatrix} n_1 & n_6 & n_5 \\ n_6 & n_2 & n_4 \\ n_5 & n_4 & n_3 \end{bmatrix} \quad (2.20)$$

It is useful to introduce the dielectric impermeability tensor B_i :

$$\begin{aligned} B_i &= \frac{1}{n_i^2} & i &= 1,2,3 \\ B_i &= 0 & i &= 4,5,6 \end{aligned} \quad (2.21)$$

In a material subjected to temperature change ΔT and strain e , the change in the impermeability tensor ΔB is described by:

$$\Delta B_i = Q_i \Delta T + p_{ij} e_j \quad i, j = 1, 2, \dots, 6 \quad (2.22)$$

p_{ij} are the elements of the optical stress tensor, defined as Pockels photoelastic constants. Their values, depends on the specific material taken into account [146], [147].

$$[p] = \begin{bmatrix} p_{11} & p_{12} & p_{12} & 0 & 0 & 0 \\ p_{12} & p_{11} & p_{12} & 0 & 0 & 0 \\ p_{12} & p_{12} & p_{11} & 0 & 0 & 0 \\ 0 & 0 & 0 & \frac{p_{11} - p_{12}}{2} & 0 & 0 \\ 0 & 0 & 0 & 0 & \frac{p_{11} - p_{12}}{2} & 0 \\ 0 & 0 & 0 & 0 & 0 & \frac{p_{11} - p_{12}}{2} \end{bmatrix} \quad (2.23)$$

$$[e] = \begin{bmatrix} e_1 & e_6 & e_5 \\ e_6 & e_2 & e_4 \\ e_5 & e_4 & e_3 \end{bmatrix} \quad (2.24)$$

The constant of proportionality Q_i can be defined as:

$$Q_i = Q'_i - p_{ij}\alpha_j \quad (2.25)$$

where,

$$Q'_i = \left(\frac{d\left(\frac{1}{n_i^2}\right)}{dT} \right) \quad (2.26)$$

In the case of isotropic materials

$$\begin{aligned} Q'_i &= \frac{d}{dT} \left(\frac{1}{n_i^2} \right) = -\frac{2}{n_i^3} \left(\frac{dn_i}{dT} \right) = -\frac{2}{n_i^3} \left(\frac{dn}{dT} \right) & i = 1,2,3 \\ Q'_i &= 0 & i = 4,5,6 \end{aligned} \quad (2.27)$$

$\frac{dn}{dT}$ are constants (typical value $10^{-5} K^{-1}$) and α_j are the coefficients of thermal expansion of the dielectric material (for silica $\alpha = 0.551 \cdot 10^{-6} K^{-1}$). For isotropic materials, the following relationships also apply,

$$\begin{aligned} \alpha_j &= \alpha & i = 1,2,3 \\ \alpha_j &= 0 & i = 4,5,6 \end{aligned} \quad (2.28)$$

By placing equations (2.27) and (2.28) into (2.22):

$$\Delta B_1 = p_{11}e_1 + p_{12}(e_2 + e_3) - \frac{2}{n_1^3} \left(\frac{dn}{dT} \right) \Delta T - (p_{11} + 2p_{12})\alpha\Delta T \quad (2.29)$$

$$\Delta B_2 = p_{11}e_2 + p_{12}(e_1 + e_3) - \frac{2}{n_2^3} \left(\frac{dn}{dT} \right) \Delta T - (p_{11} + 2p_{12})\alpha\Delta T \quad (2.30)$$

$$\Delta B_3 = p_{11}e_3 + p_{12}(e_1 + e_2) - \frac{2}{n_3^3} \left(\frac{dn}{dT} \right) \Delta T - (p_{11} + 2p_{12})\alpha\Delta T \quad (2.31)$$

$$\Delta B_4 = \left(\frac{p_{11}-p_{12}}{2} \right) e_4 \quad (2.32)$$

$$\Delta B_5 = \left(\frac{p_{11}-p_{12}}{2} \right) e_5 \quad (2.33)$$

$$\Delta B_6 = \left(\frac{p_{11} - p_{12}}{2} \right) e_6 \quad (2.34)$$

Given the linear approximation according to which $\Delta B_i = \Delta \left(\frac{1}{n_i^2} \right) = -\frac{2\Delta n_i}{n_i^3}$, equations (2.29):(2.34) can be rewritten:

$$\Delta n_1 = -\frac{n_1^3}{2} (p_{11}e_1 + p_{12}(e_2 + e_3)) + \left(\frac{dn}{dT} \right) \Delta T + \frac{n_1^3}{2} (p_{11} + 2p_{12})\alpha \Delta T \quad (2.35)$$

$$\Delta n_2 = -\frac{n_2^3}{2} (p_{11}e_2 + p_{12}(e_1 + e_3)) + \left(\frac{dn}{dT} \right) \Delta T + \frac{n_2^3}{2} (p_{11} + 2p_{12})\alpha \Delta T \quad (2.36)$$

$$\Delta n_3 = -\frac{n_3^3}{2} (p_{11}e_3 + p_{12}(e_1 + e_2)) + \left(\frac{dn}{dT} \right) \Delta T + \frac{n_3^3}{2} (p_{11} + 2p_{12})\alpha \Delta T \quad (2.37)$$

$$\Delta n_4 = -\frac{n_4^3}{2} \frac{(p_{11} - p_{12})}{2} e_4 \quad (2.38)$$

$$\Delta n_5 = -\frac{n_5^3}{2} \frac{(p_{11} - p_{12})}{2} e_5 \quad (2.39)$$

$$\Delta n_6 = -\frac{n_6^3}{2} \frac{(p_{11} - p_{12})}{2} e_6 \quad (2.40)$$

The equations (2.35):(2.40) make evident how strain and temperature variation can induce optical anisotropy in the material, changing the refractive index. All the mathematical treatments reported before can be easily applied to other kind of optical devices made of silica glass such as planar waveguides.

2.2.2 Refractive index variation due to strain and temperature

As stated before, strain and temperature variations alter the refractive index of an optical fiber, as a direct consequence, the spectrum of Bragg grating it is altered. In the following, we consider a FBG subjected to a uniform temperature change (ΔT) and a strain field with e_1 , e_2 and e_3 , where e_1 lies along the direction of the grating, and e_2 , and e_3 , are the transverse strain components, as shown in Figure 2.2. We are interested in the components of the refractive index along the principal axes which are n_1 , n_2 and n_3 [148]

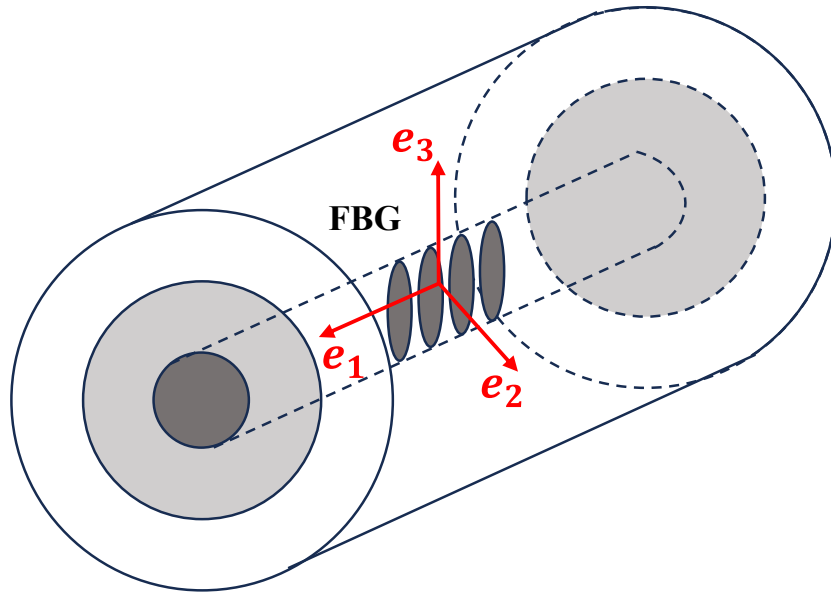


Figure 2.2 Strain field applied to a FBG.

The fundamental mode guided within a single-mode optical fibers respect the principle of weakly guiding since the value of the refractive index of the core n_{co} is similar to that of the cladding $n_{cl,i}$. As well known, a guided mode is related to the effective mode refractive index n_{eff} that satisfies the condition $n_{cl,i} < n_{eff} < n_{co}$. Therefore, the modified value of the effective refractive index for optical fibers subjected to strain components and temperature changes ΔT can be approximated as $n_{eff} \approx n_2$ or $n_{eff} \approx n_3$, where n_2 and n_3 are the cross-sectional components of the refractive index in optical fibers. If $e_2 \neq e_3$, there are two orthogonal guided modes with two effective refractive indices (n_{eff_1} and n_{eff_2}). Substituting n_2 ed n_3 with n_{eff_1} and n_{eff_2} in equations (2.36), (2.37), the changes in the effective refractive index Δn_{eff} of the modes can be expressed as follows

$$\Delta n_{eff_1} = -\frac{n_{eff_1}^3}{2} (p_{11}e_2 + p_{12}(e_1 + e_3)) + \left(\frac{dn}{dT}\right) \Delta T + \frac{n_{eff_1}^3}{2} (p_{11} + 2p_{12})\alpha \Delta T \quad (2.41)$$

$$\Delta n_{eff_2} = -\frac{n_{eff_2}^3}{2} (p_{11}e_1 + p_{12}(e_2 + e_3)) + \left(\frac{dn}{dT}\right) \Delta T + \frac{n_{eff_2}^3}{2} (p_{11} + 2p_{12})\alpha \Delta T \quad (2.42)$$

It is of interest to estimate analytically the resonance wavelength shift (Bragg wavelength) $\Delta\lambda_B$. Indeed, when FBGs are subjected to uniform stretching and

temperature changes, the main effect that occurs is a change in the Bragg wavelength ($\Delta\lambda_B$), which can be expressed in terms of changes in n_{eff} and Λ :

$$\Delta\lambda_B = 2 \left(\Lambda \frac{dn_{eff}}{dl} + n_{eff} \frac{d\Lambda}{dl} \right) \Delta l + 2 \left(\Lambda \frac{dn_{eff}}{dT} + n_{eff} \frac{d\Lambda}{dT} \right) \Delta T \quad (2.43)$$

Which can be rewritten as

$$\Delta\lambda_B = 2(\Lambda\Delta n_{eff} + n_{eff}\Delta\Lambda)_{\Delta T=0} + 2(\Lambda\Delta n_{eff} + n_{eff}\Delta\Lambda)_{e_i=0} \quad (2.44)$$

Where $\Delta\Lambda = e_1\Lambda$. Substituting equations (1.23) and (1.24) into equation (1.28),

$$\begin{aligned} \frac{\Delta\lambda_{B1}}{\lambda_B} &= e_1 - \frac{n_{eff1}^2}{2} (p_{12}e_1 + p_{11}e_2 + p_{12}e_3) + \frac{1}{n_{eff1}} \left(\frac{dn}{dT} \right) \Delta T + \\ &\quad + \frac{n_{eff1}^2}{2} (p_{11} + 2p_{12})\alpha\Delta T \end{aligned} \quad (2.45)$$

$$\begin{aligned} \frac{\Delta\lambda_{B2}}{\lambda_B} &= e_1 - \frac{n_{eff2}^2}{2} (p_{12}e_1 + p_{12}e_2 + p_{11}e_3) + \frac{1}{n_{eff2}} \left(\frac{dn}{dT} \right) \Delta T + \\ &\quad + \frac{n_{eff2}^2}{2} (p_{11} + 2p_{12})\alpha\Delta T \end{aligned} \quad (2.46)$$

The presence of two different Bragg wavelengths peaks at λ_{B1} and λ_{B2} in the reflectivity spectrum of FBGs is called birefringence. Since it is caused by external loads, it is also known as stress-induced birefringence. If the transverse components are equal ($e_2 = e_3$), there is no peak splitting, and equations (2.45), (2.46) can be written as

$$\begin{aligned} \frac{\Delta\lambda_B}{\lambda_B} &= e_1 - \frac{n_{eff}^2}{2} [(p_{11} + p_{12})e_2 + p_{12}e_1] + \frac{1}{n_{eff}} \left(\frac{dn}{dT} \right) \Delta T + \frac{n_{eff}^2}{2} (p_{11} + \\ &\quad + 2p_{12})\alpha\Delta T \end{aligned} \quad (2.47)$$

2.2.3 Refractive index variation due to curvature

A curved optical waveguide, with a cross-sectional refractive index distribution $n(x, y)$ can be mapped into a straight one by using the conformal mapping method. If the curvature radius R is very large with respect to sensor dimension, the equivalent straight optical waveguide is characterized by a modified cross-sectional refractive index distribution $n_s(x, y)$ [62]:

$$n_s(x, y) = n(x, y) \cdot \left(1 + \frac{1}{R} \cdot r \cos(\theta)\right) \quad (2.48)$$

Where $1/R$ is the curvature radius C , while $r \cos(\theta)$ is the projection x_{proj} of each point of the optical waveguide over the plane perpendicular to the neutral plane (see Fig. 2.3 (a)).

By convention, we refer to positive (negative) curvature C when the center of curvature O lies in the negative (positive) semi-axis x , see Fig. 2.3 (a).

Moreover, the curvature C induces strain along the three principal axes, that can be expressed as follows:

$$\varepsilon_x = \varepsilon_y = -\nu \varepsilon_z \quad (2.49)$$

$$\varepsilon_z = C x_{proj} \quad (2.50)$$

where ν is the Poisson's ratio. Therefore, the modified cross-sectional refractive index distribution $n_s(x, y)$ is also influenced by these strain components. Therefore, the cross-sectional refractive index distribution $n(x, y)$ needs to be evaluated by considering the stress-optic relations [62]:

$$n(x, y) = n_0(x, y) + \Delta n = n_0 - \left(\frac{n_0^3}{2}\right) (p_{12} - \nu p_{12} - \nu p_{11}) C x_{proj} \quad (2.51)$$

where $n_0(x, y)$ is the refractive index distribution of the optical waveguide without curvature, p_{11} and p_{12} the components of the photo-elastic tensor [149]. For silica, $p_{11} = 0.121$, $p_{12} = 0.27$, $\nu = 0.16$ [150], [9]. Figure 2.3 (b) shows the 2D-sketch of the straight optical waveguide, in blue colored the off-axis UV written Bragg grating. In Figure 2.3 (c), the 2D-sketches of the curved optical waveguide for positive and negative curvature C are reported. In Fig. 2.3 (c), the strain component along the z-axis ε_z introduces a compression (yellow colored line) along the inner half with respect to the neutral plane, and tension (blue colored line) along the outer half of the device. The neutral plane (red dotted line) is not affected by strain and the refractive index distribution $n(x, y)$ does not change. These tensile and compressive strains modify the cross-sectional refractive index $n_s(x, y)$ according to the relation (2.51). The value of the

refractive index increases with respect to n_0 in the outer half of the device, while decreases in the inner half [151].

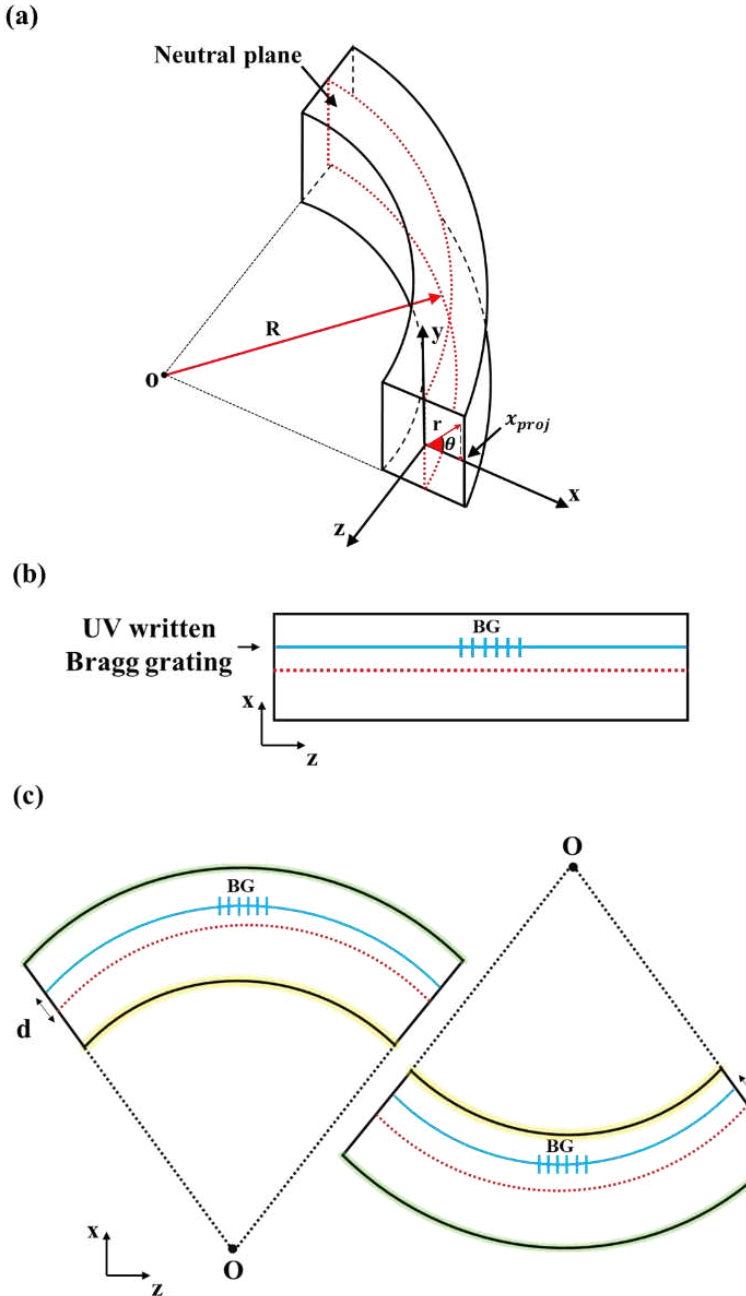


Figure 2.3 (a) 3D-sketch of a curved waveguide; (b) 2D-sketch of the straight optical waveguide; (c) 2D-sketch of the curved optical waveguide with positive (left) and negative (right) curvature C (green colored line for tensile strain, yellow colored line for compressive strain) [67].

In addition, if the Bragg grating is located outside the neutral plane, the nominal Bragg grating pitch Λ_0 changes as $\Lambda = \Lambda_0(1 + \varepsilon_z)$. Generally, for ε_z calculation, x_{proj} corresponds to the distance between the center of the Bragg grating and the neutral plane, defined as core offset d (see Fig. 2.3 (c)) [152]-[154]. This approximation is no longer true when the distance d is comparable or smaller than the core size of the optical waveguide.

2.3 Optical fiber coupler and combiner for Mid-IR

In the following paragraphs, CME to study the coupling in optical fiber couplers and the main design parameters are reported. Moreover, the main criteria to be taken into account for the design of tapered devices, such as optical fiber couplers and combiners are reported.

2.3.1 Symmetric optical fiber coupler: CMT theory and operation principle

Symmetric optical fiber couplers can be fabricated via fused biconical tapering technique, in which two identical optical fibers, are placed in close contact with each other and then heated and stretched over a short distance. The power coupling between the electromagnetic modes occurs in the waist region, i.e. the region with the smallest diameter, see Fig. 2.4, where the well-known periodic exchange of power between the electromagnetic modes is experienced.

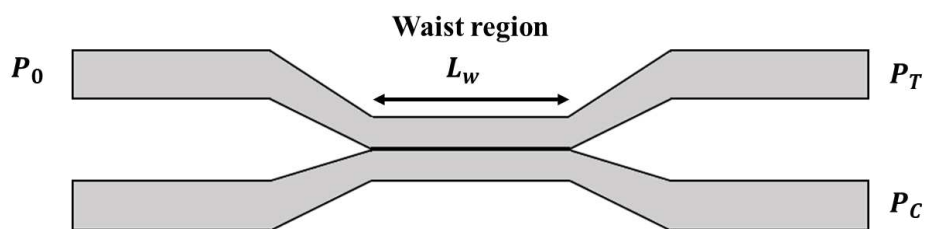


Figure 2.4 Schematic representation of an optical fiber coupler.

Coupled mode theory is usually employed in the electromagnetic design to describe the codirectional coupling for HE_{11} mode [100], [101]. By considering as input of the symmetric optical fiber coupler a low power continuous-wave laser, the nonlinear terms can be neglected and by considering that $\beta_{11} = \beta_{12} = \beta_1$, $\beta_{12} = \beta_{21} = \beta_2$, $K_{12} = K_{21} = K$, thus a simplified form of coupled mode equations, derived from CMT [3], can be written as follows:

$$\frac{\partial A_1(z)}{\partial z} = -jK_{12}A_2(z)e^{-j(\beta_2-\beta_1)z} \quad (2.52)$$

$$\frac{\partial A_2(z)}{\partial z} = -jK_{21}A_1(z)e^{-j(\beta_2-\beta_1)z} \quad (2.53)$$

The solution of these differential equations is

$$A_1(z) = A_0 \cos(Kz) \quad (2.54)$$

$$A_2(z) = A_0 \sin(Kz) \quad (2.55)$$

considering $P_0 \equiv A_0^2$ as input power, the output power at each output port is calculated as

$$P_1 = P_0 \cos^2(Kz) \quad (2.56)$$

$$P_2 = P_0 \sin^2(Kz) \quad (2.57)$$

Equations (2.5) and (2.6) indicate that the input power couples back and forth between the two cores. Considering the specific case of a symmetric coupler, having a waist length L_w , the input power P_0 injected in the input port 1 split between the cross port P_C and the through port P_T , according to [100], [101]:

$$P_C = P_0 \sin^2(\kappa L_w) \quad (2.58)$$

$$P_T = 1 - P_C = P_0 \cos^2(\kappa L_w) \quad (2.59)$$

$$U = r_{co,f} \sqrt{n_{co}^2 k_0^2 - \beta^2} \quad (2.60)$$

$$W = r_{co,f} \sqrt{\beta^2 - n_{cl,i}^2 k_0^2} \quad (2.61)$$

$$K = \frac{K_0 \left(\frac{WD}{r_{co,f}} \right) U^2}{k_0 n_{co} \left(r_{co,f} V K_1(W) \right)^2} \quad (2.62)$$

where the equation parameters are the following: K is the coupling coefficient L_w the waist length, K_0 , and K_1 the zeroth and first order Bessel functions of the second kind (respectively evaluated at $\frac{WD}{r_{co,f}}$ and W), $r_{co,f}$ the core radius in the waist region, D the core-to-core distance in the waist region, n_{co} the core refractive index, $n_{cl,i}$ the cladding refractive index, k_0 the wave number, β the propagation constant, V the normalized frequency. The performance of a 2×2 optical fiber coupler is described by the excess loss E_L and coupling ratio C_R [155].

$$E_L = 10 \log \left(\frac{P_0}{P_T + P_C} \right) \quad (2.63)$$

The coupling ratio C_R is related to the optical power of each output port divided by the sum of the powers at the two output ports [155]:

$$C_{R-T} = \frac{P_T}{P_T + P_C} \quad (2.64)$$

$$C_{R-C} = \frac{P_C}{P_T + P_C} \quad (2.65)$$

The coupling ratio C_R and its spectral dependence are strictly dependent on the geometry of the optical fiber coupler. The excess loss E_L is affected by the quality and the geometry of the transition. To avoid higher order cladding modes coupling, the transition must be adiabatic as described in the following paragraph [156].

2.3.2 Brightness principle and adiabatic criterion

The fabrication of optical fiber combiners can involve the tapering of multimode optical fibers with a much larger core diameter in comparison with single mode fibers, and with a much larger number of excited modes, thus adiabatic criterion and brightness principle should be taken into account. In Fig. 2.5 the schematic representation of an optical fiber taper is reported.

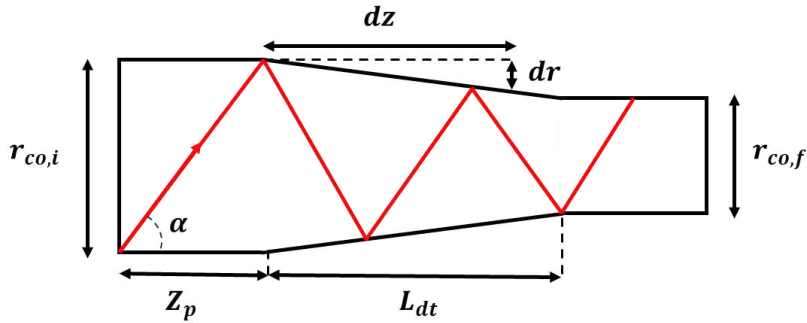


Figure 2.5 Schematic representation of an optical fiber taper.

The taper transition is adiabatic when the core radius r_{co} of the optical fiber slowly decreases along the taper length L_{dt} . In a multimode optical fiber, the radius of the core $r_{co}(z)$, expressed as a function of the propagation direction z , must change by satisfying the following condition:

$$\frac{dr_{co}}{dz} \leq \frac{r_{co}(z)}{Z_p} \quad (2.66)$$

where $Z_p = 2r_{co}/\tan(\alpha)$ is the half period between reflections, $NA = \sin(\alpha)$ is the optical fiber numerical aperture, and α is the ray angle [157], [158]. The minimum taper transition length $L_{dt,min}$ can be calculated from (2.66), according to:

$$L_{dt,min} \geq \frac{2(r_{co,i} - r_{co,f})}{\tan(\alpha)} \quad (2.67)$$

where $r_{co,i}$ and $r_{co,f}$ are the fiber core radii before and after the tapering, respectively.

Moreover, in order to avoid significant losses, the beam brightness, proportional to transmitted optical power, should be preserved [97], [158]. The brightness ratio (BR) parameter allows to estimate the transmission loss of the designed combiner, and it can be defined as follows:

$$BR \approx \frac{(D_{out}^2 NA_{out}^2)}{n D_{in}^2 NA_{in}^2} \geq 1 \quad (2.68)$$

where n defines number of input fibers, NA_{in} and NA_{out} defines numerical apertures of input fibers and output fiber, and D_{out} and D_{in} are the diameters of output and input fibers. If the brightness principle is verified, i.e. $BR > 1$, the beam intensity launched into n input ports is equal to the intensity of the beam at the combiner output. $BR < 1$ means a loss of the beam brightness (beam intensity at the output is lower than at the input), which may be caused by, for example, the leaking of the beam from the structure.

2.4 Analytical model for fluoroindate glass fiber-based lasers

In the following paragraphs, the models for Nd^{3+} : Ho^{3+} -doped and Er^{3+} -doped fluoroindate CW fiber lasers are reported. Mid-IR optical sources are of interest in a wide area of applications, such as communications, environmental monitoring, and sensing.

2.4.1 Nd^{3+} : Ho^{3+} -doped fluoroindate CW fiber laser

A system constituted by 9 energy levels can be employed to model all the ions interactions that occur when a Ho:Nd-codoped fluoroindate fiber is pumped at $\lambda_p = 808 \text{ nm}$ in order to have stimulated emission at $\lambda_s = 3.92 \mu\text{m}$. The complete level scheme, including all the significant ion interactions, is reported in Fig. 2.6. The main phenomena to be taken into account are: i) the pump absorption, ii) the stimulated emission, iii) the radiative and nonradiative decays, and iv) the energy transfers (ET) between Ho^{3+} and Nd^{3+} ions [135].

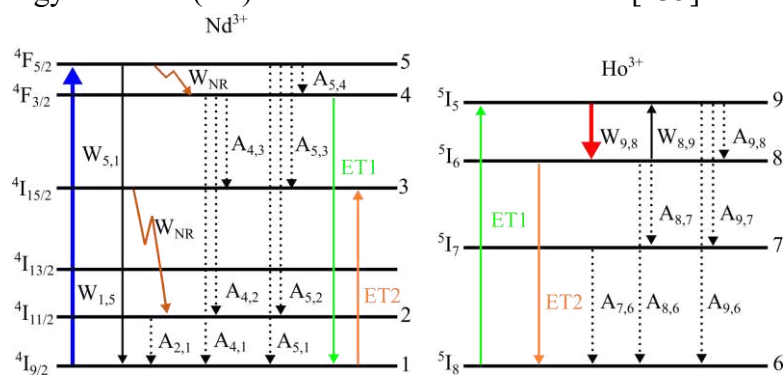


Figure 2.6 Energy level scheme for the 9-level laser, pumped at $\lambda_p = 808 \text{ nm}$, including pump absorption (transition 1-5, bold blue line) stimulated emission at $\lambda_s = 3920 \text{ nm}$ (transition 9-8, bold red line), radiative decays (dotted lines), nonradiative decays (transition 5-4 and transition 3-2, brown lines), and energy transfers (ET) (green and orange solid lines) [74].

The energy level populations N_1, \dots, N_5 of neodymium can be written by the nonlinear system (2.69a)-(2.69j) below by using the rate equations approach [159], [160], [161],

$$\frac{\partial N_1}{\partial t} = -W_{15}N_1 + W_{51}N_5 + A_{51}N_5 + A_{41}N_4 + A_{21}N_2 + K_{ET1}N_6N_4 - K_{ET2}N_8N_1 \quad (2.69a)$$

$$\frac{\partial N_2}{\partial t} = -\frac{1}{\tau_{R2}}N_2 + A_{52}N_5 + A_{42}N_4 + W_{NR}N_3 \quad (2.69b)$$

$$\frac{\partial N_3}{\partial t} = A_{53}N_5 + A_{43}N_4 + K_{ET2}N_8N_1 - W_{NR}N_3 \quad (2.69c)$$

$$\frac{\partial N_4}{\partial t} = -\frac{1}{\tau_{R4}}N_4 + A_{54}N_4 - K_{ET1}N_6N_4 + W_{NR}N_5 \quad (2.69d)$$

$$\frac{\partial N_5}{\partial t} = W_{15}N_1 - W_{51}N_5 - \frac{1}{\tau_{R5}}N_5 - W_{NR}N_5 \quad (2.69e)$$

whereas the energy level populations N_6, \dots, N_9 of holmium can be written as

$$\frac{\partial N_6}{\partial t} = A_{96}N_9 + A_{86}N_8 + A_{76}N_7 - K_{ET1}N_6N_4 + K_{ET2}N_8N_1 \quad (2.69f)$$

$$\frac{\partial N_7}{\partial t} = -\frac{1}{\tau_{R7}}N_7 + A_{97}N_9 + A_{87}N_8 \quad (2.69g)$$

$$\frac{\partial N_8}{\partial t} = W_{98}N_9 - W_{89}N_8 - \frac{1}{\tau_{R8}}N_8 + A_{98}N_9 - K_{ET2}N_8N_1 \quad (2.69h)$$

$$\frac{\partial N_9}{\partial t} = -W_{98}N_9 + W_{89}N_9 - \frac{1}{\tau_{R9}}N_9 + K_{ET1}N_6N_4 \quad (2.69j)$$

where $A_{i,j} = \frac{\beta_{i,j}}{\tau_{Ri}}$ are the radiative decay rates; $\beta_{i,j}$ are the branching ratios; τ_{Ri} are the i -th level lifetimes; K_{ET1} and K_{ET2} are the ET coefficients; W_{NR} are the non-radiative decay rates. The emission/absorption transition rate $W_{i,j}$ for the $i \rightarrow j$ transition is defined as

$$W_{i,j}(z, t) = \frac{\sigma_{i,j}(\lambda_{p/s})}{\frac{hc_0}{\lambda_{p/s}}} [P_{p/s}^\pm(z, t)] \Gamma_{p/s} \quad (2.70)$$

where $\sigma_{i,j}(\lambda_{p/s})$ is the emission/absorption cross section at the wavelength $\lambda_{p/s}$ for the $i \rightarrow j$ (1-5, 5-1 and 8-9, 9-8) transitions; $\lambda_{p/s}$ is the pump/signal

wavelength; h is the Plank constant; c_0 is the light speed in vacuum; P_p^\pm is the forward/backward pump power; P_s^\pm is the forward/backward signal power; Γ_p/Γ_s are the overlap coefficients between the pump/signal beam and the doped area A_d . The conditions $N_1 + N_2 + N_3 + N_4 + N_5 = N_{Nd}$ and $N_6 + N_7 + N_8 + N_9 = N_{Ho}$ are imposed, where N_{Ho} and N_{Nd} are the dopant concentrations.

The power propagation for pump and signal beams is governed by the following partial differential equations

$$\frac{\partial P_p}{\partial z} = [g_p(z) - \alpha]P_p(z) \quad (2.71)$$

$$\frac{\partial P_s^\pm}{\partial z} = \pm[g_s(z) - \alpha]P_s^\pm(z) \quad (2.72)$$

where

$$g_p(z) = [-\sigma_{15}(v_p)N_1(z) + \sigma_{51}(v_p)N_5(z)]\Gamma_p \quad (2.73)$$

$$g_s(z) = [-\sigma_{89}(v_s)N_8(z) + \sigma_{98}(v_s)N_9(z)]\Gamma_s$$

are the gain coefficients for the pump and the signal, respectively, and α is the glass optical background loss.

To solve (2.71) and (2.72), the following boundary conditions are imposed

$$P_p(0) = P_p^{in} \quad (2.74a)$$

$$P_s^+(0) = R_{in}P_s^-(0) \quad (2.74b)$$

$$P_s^-(L) = R_{out}P_s^+(L) \quad (2.74c)$$

where $z = 0$ and $z = L$ represent the ends of the laser cavity, P_p^{in} is the input pump power, R_{in} and R_{out} are the input and output mirror reflectivity, respectively. Initial conditions for level populations are also imposed as follows:

$$N_1(0) = N_{Nd} \quad (2.74d)$$

$$N_6(0) = N_{Ho} \quad (2.74e)$$

$$N_2(0) = N_3(0) = N_4(0) = N_5(0) = N_7(0) = N_8(0) = N_9(0) = 0 \quad (2.74f)$$

2.4.2 Er³⁺-doped fluoroindate CW fiber laser

The pumping scheme for the Er³⁺:IFG system exploits an optical beam at $\lambda_p = 635 \text{ nm}$ to promote electrons from the ground state ${}^4\text{I}_{15/2}$ to the upper laser level ${}^4\text{F}_{9/2}$, as shown in Fig. 2.7. The complete model consists of 5 energy levels [162], including the lower laser level ${}^4\text{I}_{9/2}$ and two intermediate levels (${}^4\text{I}_{13/2}$ and ${}^4\text{I}_{11/2}$). The considered optical transitions are the following: pump absorption (upward solid arrow), pump stimulated emission (downward solid arrow), signal absorption (upward dashed arrow), signal stimulated emission (downward dashed arrow), radiative decays (downward dotted arrows). The employment of a laser transition that does not involve the ground state helps to avoid the phenomenon of signal reabsorption, once the pump is exhausted.

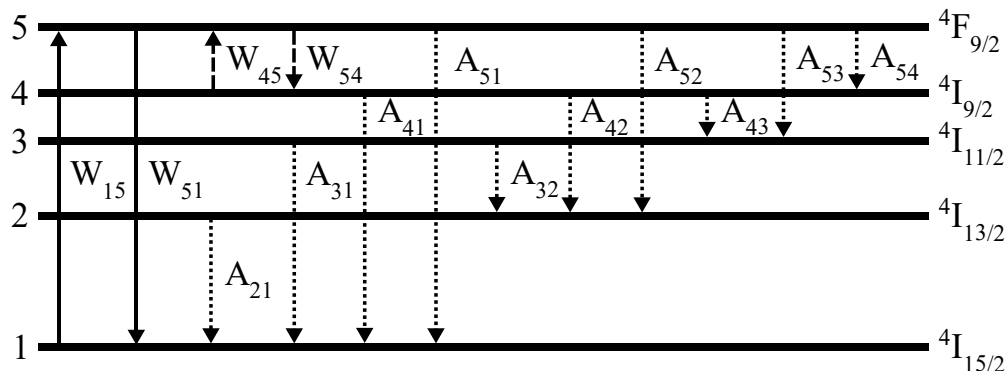


Figure 2.7 Energy levels scheme for the Er³⁺:IFG system [134].

Pump excited state absorption (ESA) occurring between the ${}^4\text{I}_{13/2}$ and the (${}^4\text{F}_{3/2}$, ${}^4\text{F}_{5/2}$) energy levels is neglected since, according to spectroscopic studies [163], the lifetime of the (${}^4\text{F}_{3/2}$, ${}^4\text{F}_{5/2}$) level is rather short and the branching ratio between it and the ground state is over 61 %. This implies that the majority of electrons promoted by pump ESA decay to the ground state and are available again for exciting the upper laser level.

In order to study the population inversion with the aim of obtaining laser emission around $\lambda_s = 3.5 \mu\text{m}$, the following rate equations for the energy levels populations N_1, \dots, N_5 are written:

$$\begin{aligned} \frac{\partial N_5}{\partial t} = & W_{15}N_1 - W_{51}N_5 + W_{45}N_4 - W_{54}N_5 \\ & - (A_{51} + A_{52} + A_{53} + A_{54})N_5 \end{aligned} \quad (2.75a)$$

$$\frac{\partial N_4}{\partial t} = -W_{45}N_4 + W_{54}N_5 + A_{54}N_5 - (A_{43} + A_{42} + A_{41})N_4 \quad (2.75b)$$

$$\frac{\partial N_3}{\partial t} = -(A_{32} + A_{31})N_3 + A_{43}N_4 + A_{53}N_5 \quad (2.75c)$$

$$\frac{\partial N_2}{\partial t} = -A_{21}N_2 + A_{32}N_3 + A_{42}N_4 + A_{52}N_5 \quad (2.75d)$$

$$\frac{\partial N_2}{\partial t} = -A_{21}N_2 + A_{32}N_3 + A_{42}N_4 + A_{52}N_5 \quad (2.75d)$$

$$\begin{aligned} \frac{\partial N_1}{\partial t} = & -W_{15}N_1 + W_{51}N_5 + A_{21}N_2 + A_{31}N_3 \\ & + A_{41}N_4 + A_{51}N_5 \end{aligned} \quad (2.75e)$$

The system (2.75a) - (2.75e) is solved under stationary conditions, i.e. all time derivatives vanish, and by imposing that the sum of the populations is equal to the erbium concentration N_{Er} :

$$N_1 + N_2 + N_3 + N_4 + N_5 = N_{Er} \quad (2.76)$$

The pump and signal transition rates are calculated as follows:

$$W_{15} = \frac{\sigma_{15}(\lambda_p)}{\frac{hc_0}{\lambda_p}} [P_p^+(z) + P_p^-(z)]i_p \quad (2.77)$$

$$W_{51} = \frac{\sigma_{51}(\lambda_p)}{\frac{hc_0}{\lambda_p}} [P_p^+(z) + P_p^-(z)]i_p \quad (2.78)$$

$$W_{45} = \frac{\sigma_{45}(\lambda_s)}{\frac{hc_0}{\lambda_s}} \sum_{k=1}^6 [P_{s,k}^+(z) + P_{s,k}^-(z)]i_{s,k}(x, y) \quad (2.79)$$

$$W_{54} = \frac{\sigma_{54}(\lambda_s)}{\frac{hc_0}{\lambda_s}} \sum_{k=1}^6 [P_{s,k}^+(z) + P_{s,k}^-(z)]i_{s,k}(x, y) \quad (2.80)$$

where c_0 is the speed of light in vacuum, \hbar the Planck constant, λ_p is the pump wavelength, λ_s is the signal wavelength, the cross section at the wavelength λ for the $i \rightarrow j$ transition is denoted by $\sigma_{ij}(\lambda)$, P_p^\pm is the forward (plus sign) and backward (minus sign) pump power, $P_{s,k}^\pm$ is the forward (plus sign) and backward (minus sign) signal power of the k -th guided mode, $i_{s,k}$ is the normalized intensity distribution of the signal for the k -th guided mode. The normalized intensity distribution i_p of the pump is calculated by considering the inner cladding shape of the double D-shaped fiber and assuming that the pump power is uniformly distributed in both the core and the inner cladding:

$$i_p = \frac{1}{A_p} = \left[\frac{d_{cut}}{2} \sqrt{d_{icl}^2 - d_{cut}^2} + \frac{d_{icl}^2}{2} \sin^{-1} \left(\frac{d_{cut}}{d_{icl}} \right) \right]^{-1} \quad (2.81)$$

where d_{icl} is the diameter of the inner cladding, which is cut by two parallel lines at a distance d_{cut} , and A_p is the sum of the core and the inner cladding areas. The radiative decay rate A_{ij} for the $i \rightarrow j$ transition is given by the ratio between the branching ratio β_{ij} of the transition and the lifetime τ_i of the starting energy level:

$$A_{ij} = \frac{\beta_{ij}}{\tau_i} \quad (2.82)$$

The dependence of the pump and signals powers on the longitudinal position along the fiber is given by the power propagation equations [164], [73]. For k guided modes propagating at the signal wavelength, $2 \times k$ equations are needed, taking into account both propagation directions:

$$\frac{dP_p^+}{dz} = [g_p(z) - \alpha(\lambda_p)] P_p^+(z) \quad (2.83a)$$

$$\frac{dP_p^-}{dz} = -[g_p(z) - \alpha(\lambda_p)] P_p^-(z) \quad (2.83b)$$

$$\frac{dP_{s,k}^+}{dz} = [g_{s,k}(z) - \alpha(\lambda_s)] P_{s,k}^+(z) \quad (2.83c)$$

$$\frac{dP_{s,k}^-}{dz} = -[g_{s,k}(z) - \alpha(\lambda_s)] P_{s,k}^-(z) \quad (2.83d)$$

where $\alpha(\lambda)$ is the wavelength-dependent background loss and the gain coefficients are given by the overlap integrals, over the doped core region Ω_d , between the populations and the normalized intensity distributions:

$$\begin{aligned} g_p(z) = & -\sigma_{15}(\lambda_p) \int_{\Omega_d} N_1 i_p dx dy \\ & + \sigma_{51}(\lambda_p) \int_{\Omega_d} N_5 i_p dx dy \end{aligned} \quad (2.84)$$

$$\begin{aligned} g_{s,k}(z) = & -\sigma_{45}(\lambda_s) \int_{\Omega_d} N_4 i_{s,k}(x, y) dx dy \\ & + \sigma_{54}(\lambda_s) \int_{\Omega_d} N_5 i_{s,k}(x, y) dx dy \end{aligned} \quad (2.85)$$

The boundary conditions for the differential equations system (2.86a) - (2.86d) are related to the forward/backward input pump power injected into the fiber and the two FBGs employed as mirrors:

$$P_p^+(0) = P_{p0}^+ \quad (2.86a)$$

$$P_p^-(L) = P_{p0}^- \quad (2.86b)$$

$$P_{s,k}^+(0) = R_1 P_{s,k}^-(0) \quad (2.86c)$$

$$P_{s,k}^-(L) = R_2 P_{s,k}^+(L) \quad (2.86d)$$

where L is the fiber length, P_{p0}^\pm is the forward (plus sign) and backward (minus sign) input pump power, R_1 is input FBG reflectivity and R_2 is the output FBG reflectivity. The output signal power P_{out} of the laser is given by sum of the transmitted powers of each forward signal mode:

$$P_{out} = (1 - R_2) \sum_k P_{s,k}^+(L) \quad (2.87)$$

By exploiting (2.87), it is also possible to evaluate the slope efficiency η_s and the threshold power P_{th} . The developed model is very versatile and can be potentially adapted to simulate amplifiers [165] and pulsed lasers [71], [119], [166], [167] or to be employed in machine learning systems [168] by appropriately modifying the equations and the boundary conditions.

3 Optical Gratings for Sensing

The development of optical sensors based on Bragg gratings has been driven by the need for miniaturized, and cost-effective sensors that can provide real-time, non-invasive, and highly sensitive measurements of several physical parameters. This Chapter illustrates the major results obtained during the Ph.D. research activity with respect to innovative sensors for aerospace applications.

3.1 Design of Polarization-Maintaining FBGs Using Polyimide Films to Improve Strain-Temperature Sensing in CFRP

The simultaneous detection of longitudinal strain and temperature in CFRP laminates can be obtained via uniform FBG sensors based on polarization-maintaining fibers. Indeed, in this Section, Panda, Bow tie and Pseudo-rectangle optical fiber are investigated and accurately designed taking into account three different embedding methods, for each optical fiber. The simulation exactly takes into account that the fibers are embedded in unidirectional CFRP and covered between two adhesive polyimide films. An exhaustive, accurate and robust investigation of the mechanisms originating Bragg wavelength shift is developed by considering a complete multiphysical model including: the propagation modes and their interaction, the birefringence, the optomechanical and thermal behaviour of both the optical fiber and the embedding composite material. For the first time, with reference to the state of the art, the use of polyimide films is investigated to obtain an increase of temperature sensor sensitivity, reducing the stress-transfer, due to thermal expansion, between the composite laminate and the sensing element. The designed FBG sensors are compared and their potential application, for simultaneous strain and temperature measurement of CFRP is discussed. The following paragraphs are organized as follows: in Section 3.1.1, the optomechanical interaction between optical fiber and CFRP; in Section 3.1.2, the simulation approach; in Section 3.1.3 the validation of the model; in Section

3.1.4, the numerical results and performance comparison of the optical fiber sensors embedded in CFRP; in Section 3.1.5, the conclusion.

3.1.1 Optomechanical interaction

Typically, CFRP are made of carbon fibers and thermosetting resin. In Figure 3.1.1 is reported a schematic representation of a CFRP (a) and of its unit cell (b). The carbon fibers (dark grey) and thermosetting resin (soft grey), i.e. the two primary components of composite materials, are used to perform a reinforced matrix construction, contributing to CFRP strength. Carbon fibers carry the load, while resin uniformly distributes the load into the material volume. The unit cell is an elementary cubic volume of CFRP including one carbon fiber segment

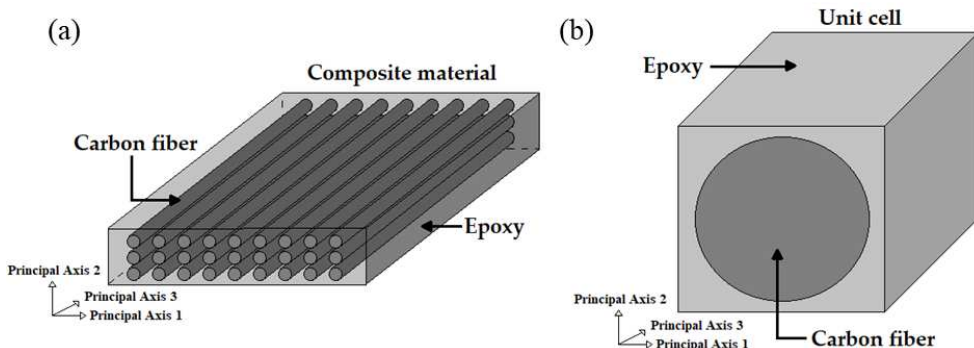


Figure 3.1.1 Schematic representation of CFRP, (b) schematic representation of the unit cell [2].

The identification of the mechanical properties of each carbon fiber in every layer of the laminate is practically unfeasible. For this reason, it is necessary to estimate the homogenized elasticity matrix to model the average mechanical behavior of a single layer. This is possible by performing a micromechanical analysis on a representative unit cell (Fig. 3.1.1 (b)).

The evaluation of the elasticity matrix $[C]_m$ can be obtained through Finite Element Method (FEM) software. The investigation described in the following it is based on COMSOL Multiphysics, which employs an inner mathematical model based on solid mechanics theory. It is important to remember that the Hooke's law, that relates stress and strain and it can be expressed as

$$[e]_m = [C]_m [\sigma]_m \quad (3.1.1)$$

where $[e]_m$ is the strain matrix, $[C]_m$ is the elasticity matrix and $[\sigma]_m$ is the stress matrix. Since the CFRP laminates are constituted by orthotropic material, the

elasticity matrix $[C]_m$ has all terms nonzero depending on the chosen reference system [169].

High birefringence can be induced in the core of the fibers by two Stress Applying Parts (SAPs). For these fibers a stress-induced birefringence occurs. Other PM fibers exhibit birefringence intrinsically induced by their peculiar geometrical shape, which could be microstructured or simply characterized by axial asymmetry in term of refractive index, without exploitation of stress effects obtained during the fabrication. The SAP consists of a material with a thermal expansion coefficient α different from that of the optical fiber cladding which gives rise to a stress field in the optical fiber. The birefringence induced by the elasto-optic effect depends on the constituent material (e.g. level of dopant concentration), the shape and the positions of the SAPs. This leads to a strong difference in the propagation constant of light travelling through the fiber for the two perpendicular polarizations. In other words, the induced birefringence breaks the circular symmetry of the optical fiber, creating two principal transmission axes within the fiber, known as the fast and slow axes of the fiber.

It is worth nothing that a cartesian reference system is taken into account and the coordinate system for the optical fiber is the same of the one employed for the CFRP illustrated in Fig. 3.1.1. The principal axis 1 is parallel to the slow axis, the principal axis 2 to the fast axis and the principal axis 3 to the direction of propagation. As illustrated in Section 2.2, to study the refractive index change of an optical fiber subjected external perturbation it is possible to express the refractive index via matrix notation. In particular, the tensor of the refractive index of an optical fiber is diagonal and defined by the components n_1, n_2, n_3 [170]. By following the mathematical treatment reported in Section 2.2.1 it is possible to determine the variation of the refractive index n due to external strain e , induced by the tensile stress σ , and temperature variation ΔT [171].

It is important to stress that, the thermal expansion coefficient is affected by the presence of the composite structure and it is generally smaller than that of the standalone optical fiber. Therefore, there is a great limitation on the term related to thermal expansion, $\alpha\Delta T$, slightly affecting the temperature sensitivity. Temperature changes cause radial strains within the composite material which differ each other. The grating period variation $\Delta\Lambda$ of the grating as a function of the longitudinal strain is described by $\Delta\Lambda = \Lambda e_3$. The reflection spectra of the Bragg gratings are obtained through the Transfer Matrix Method (TMM) [144]. Each axis in case of PM fibers has a different response to strain Δe_3 and temperature ΔT so that it is possible to solve the following, enabling their discrimination:

$$\begin{pmatrix} \Delta\lambda_{B1} \\ \Delta\lambda_{B2} \end{pmatrix} = \begin{pmatrix} K_{e1} & K_{T1} \\ K_{e2} & K_{T2} \end{pmatrix} \begin{pmatrix} \Delta e_3 \\ \Delta T \end{pmatrix} \quad (3.1.2)$$

where subscripts 1, 2 indicate the slow and fast axis, respectively; $K_{e1}, K_{e2}, K_{T1}, K_{T2}$ are the sensitivities to longitudinal strain e_3 and temperature variation ΔT , $\Delta\lambda_{B1}$ and $\Delta\lambda_{B2}$ are the Bragg wavelength shifts.

3.1.2 Simulation approach

The development and validation of an electromagnetic and mechanical model for FBG sensors embedded in CFRP for structural health monitoring applications using COMSOL Multiphysics is proposed and briefly described in the following. The first part of this approach involves the implementation of a 3D-FEM model of a CFRP laminate with the embedded optical fiber under investigation (in the following indicated as SM3D-FEM), to investigate the thermo-mechanical behaviour when external mechanical and thermal stresses are applied. The proposed SM3D-FEM is based on an accurate micromechanical model of the unit cell in order to evaluate the effective elasticity matrix (equation 3.1.1). This allows to obtain equivalent homogeneous elasticity matrix of the composite layer. In the context of SM3D-FEM, the optical fiber is modeled in three dimensions, considering its mechanical and thermal properties. The optical fiber can be embedded into the composite material, in every position and/or orientation. This model enables a precise simulation of the stress transfer between the composite laminate and the optical fiber. In this way, it is possible to simulate strain distribution inside the optical fiber. The strains evaluated along the three principal axes (longitudinal strain e_3 and the two transverse strains e_1, e_2) via thermal and mechanical simulations are used for the successive modal analysis (2D-FEM) of the optical fiber. The fundamental mode HE_{11} is well confined and, by simulation, the presence of the CFRP can be neglected in the 2D-FEM analysis without significant approximation. Due to the small size of an FBG, we can make the assumption that the stress generated during the composite material cooling phase, following the curing process, remains relatively constant within the FBG region. This just induces a bias of the Bragg wavelength λ_B that does not impact the sensitivity of the sensor [172]. Therefore, in the proposed model this effect originated by fabrication process is neglected according to [172]. The effective refractive indices n_{eff} of the fast and slow propagating modes are found through the 2D-FEM modal analysis. The effective refractive indices n_{eff} are used as

input for the home-made software implementing the TMM. This method is considered for the simulation of the reflection spectra of the gratings and the consequent Bragg wavelength shifts $\Delta\lambda_B$, due to the perturbations applied externally to the system. Fig. 3.1.2 illustrates the simulation approach with a flux diagram of the main calculation blocks.

Lastly, it is important to underline that the proposed method has intrinsic advantages in terms of accuracy and reliability with respect to other ones reported in literature where n_{eff} or $\Delta\lambda_B$ are estimated without modal analyses [173], [20], [174]. Indeed, at first the materials are modelled and then the electromagnetic simulation without approximations is performed.

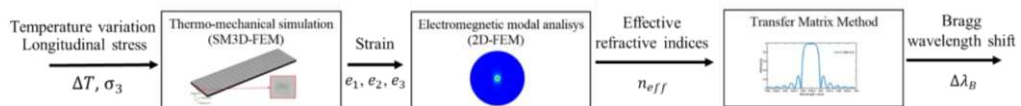


Figure 3.1.2 Flow diagram of the simulation blocks [2].

3.1.3 Validation of composite laminate and FBG models

To validate the SM3D-FEM design approach, experimental data found in the literature related to the tensile mechanical properties of bidirectional carbon fiber composites reinforced with an epoxy matrix have been taken into account [175]. The considered carbon fiber is Toray T620. The composite laminate, investigated in [175], consists of four layers overlapped, each characterized by a thickness $T_L = 0.75\text{ mm}$, a length $L_L = 150\text{ mm}$ and a width $W_L = 20\text{ mm}$. The elasticity matrix $[C]_m$ of a composite layer is evaluated through the micromechanical analysis of the unit cell by considering a carbon fiber-resin volume fraction $v_f = 0.563$. The values of Young's Modulus E , Poisson's ratio ν , Shear modulus G and density ρ , used for the analysis, are reported in Table 3.1.1 [175], [176].

The simulation is in agreement with the experimental results, as depicted in Figure 3.1.3, illustrating the tensile stress σ versus e_3 strain simulated via SM3D-FEM (red dash dotted curve); and measured (blue curve) [175]. It is possible to observe that the experimental curve has an almost linear trend up to a strain value close to $e_3 = 1.7\%$. In the actual behaviour, after the abovementioned value the rupture point of the material is observed.

Table 3.1.1 Mechanical and thermal properties of composite carbon fiber and epoxy resin.

Parameter	Symbol	Value carbon fiber	Value epoxy	Unit
Young's modulus	E	235 (33 direction) 15 (11 direction)	3.1	GPa
Shear modulus	G	50 (31 direction) 50 (12 direction)	-	GPa
Poisson's ratio	ν	0.23 (31 direction) 0.23 (12 direction)	0.35	-
Density	ρ	1770	1130	kg/m^3

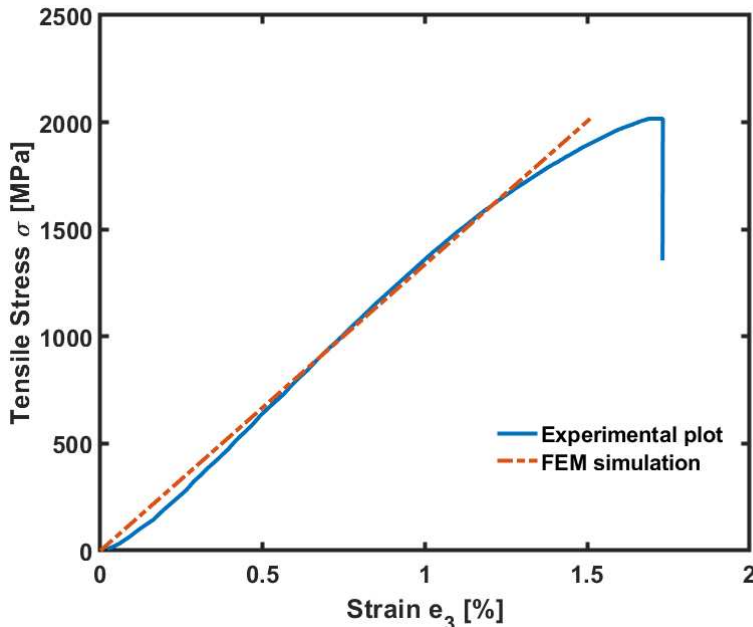


Figure 3.1.3 Simulation via SM3D-FEM solver (red curve); experiment (blue curve) reported in [175], [2].

The simulated stress-strain curve considers only the material elastic behavior, as unidirectional composite laminates typically do not undergo plastic deformation [176], [177].

The developed home-made computer code based on TMM has been validated giving optimum agreement with literature results [178], [179], [144].

3.1.3.1 Opto-mechanical simulation

Three different kinds of PM optical fibers are taken into account, whose geometric and physical parameters employed for the simulation are taken from literature papers [170], [180]-[182]. We investigated Panda, Bow tie and Pseudo-rectangle optical fibers considering three different embedding techniques: i) embedding in CFRP without coating, without APFs, Fig. 3.1.4(a); ii) embedding in CFRP with polyimide coating, without APFs, Fig. 3.1.4(b); iii) embedding in CFRP with polyimide coating and covered between two APFs, Fig. 3.1.4(c) and (d). Therefore, a total of nine cases are investigated.

The optomechanical and electromagnetic investigation exactly takes into account the geometries and physical properties of the abovementioned nine sensors embedded in the CFRP. Fig. 3.1.4 refers only to the case of Panda fiber, to avoid useless repetitions.

The cladding for all the considered optical fibers is made of pure Silica, the core is doped with GeO_2 while the SAPs are doped with B_2O_3 . The physical parameters employed in the simulation are reported in Table 3.1.2 and are taken from literature [171]. In the case of the Pseudo-rectangle fiber, the inner cladding is fluorine doped [180], and has refractive index $n_{icl} = 1.4404$, while the thermal expansion coefficient is $\alpha_{icl} = 5.0 \times 10^{-7} 1/K$. For all the optical fibers, the stress-optical coefficients are $C_1 = 0.757 \times 10^{-12} m^2/N$ and $C_2 = 4.188 \times 10^{-12} m^2/N$. The thermo-optic coefficient is $dn/dT = 9.15 \times 10^{-6} K^{-1}$, the Pockel's coefficients are $p_{11} = 0.121$ and $p_{12} = 0.27$ [181].

For all the three fibers the cladding diameter is $d_{cl} = 125 \mu m$. For the Panda fiber, the distance between the centres of the core and of the SAP is $l_{SAP} = 26.8 \mu m$, SAP has a diameter $d_1 = 35.5 \mu m$ (see Fig. 3.1.5(a)) [182]. For the Bow tie fiber, the position of the SAP is given by $r_1 = 7.5 \mu m, r_2 = 47.5 \mu m, \gamma = 90^\circ$ (see Fig. 3.1.5(b)) [170]. These two fibers have a circular core with diameter $d_{co} = 6 \mu m$. The Pseudo-rectangle fiber has a square core of side $a = 7.5 \mu m, b = 1.25 \mu m, c = 12 \mu m, d = 10 \mu m, f = 18 \mu m, r_3 = 5 \mu m, r_4 = 9 \mu m$ (see Fig. 3.1.5(c)) [180].

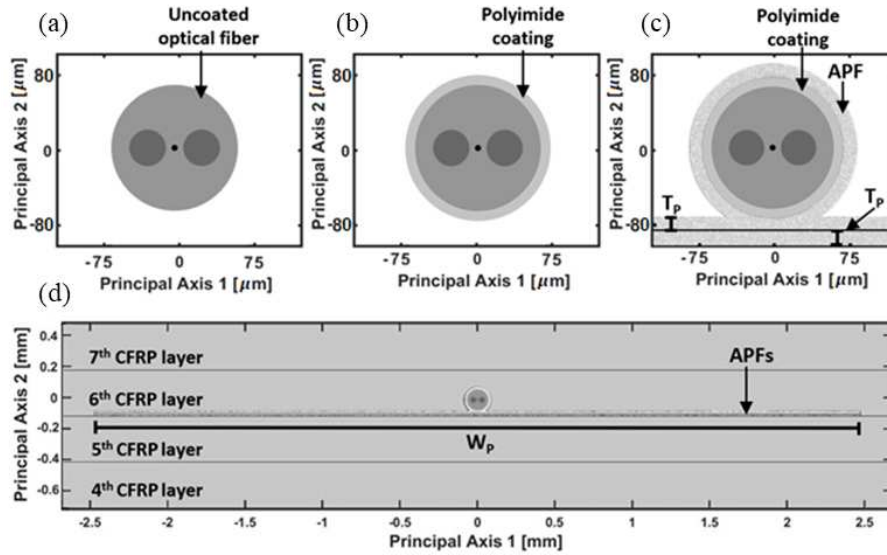


Figure 3.1.4 Cross-section of Panda fiber: (a) without coating, (b) with polyimide coating, (c) with polyimide coating and covered between two APFs, (d) with polyimide coating, covered between two APFs and embedded in the CFRP laminate, $T_p = 0.03\text{ mm}$ and $W_p = 5\text{ mm}$ [2].

The mechanical and thermal characteristics of the composite material employed in the CFRP laminate modelling are detailed in [177] and [183], while the specimen dimensions are compliant to the standard sizes utilized for structural testing.

The carbon fiber-resin volume fraction is $v_f = 0.6$ and the values of Young's Modulus E , Poisson's ratio ν , Shear modulus G and density ρ listed in Table 3.1.3 [183], [184]. The layer thermal expansion coefficient in the carbon fiber direction (principal axis 3) $\alpha_{//} = 3.7249 \cdot 10^{-8}$ and perpendicular to carbon fiber direction (principal axes 1 and 2) $\alpha_{\perp} = 3.4718 \cdot 10^{-5}$ are evaluated considering the layer Poisson's ratio $\nu_{31} = 0.26$. The unidirectional composite laminate has eight layers, each characterized by a thickness $T_L = 0.3\text{ mm}$, length $L_L = 150\text{ mm}$ of and a width $W_L = 40\text{ mm}$.

In all cases, the optical fiber sensor is placed on the sixth layer of the CFRP laminate. Apart from the case of uncoated optical fiber, the polyimide coating has a diameter of $d_{coat} = 145\text{ }\mu\text{m}$. In the case iii), the fiber optic is covered between two APFs, see Fig. 3.1.4(c) and 3.1.4(d). The thickness T_p and the width W_p of both the APFs have been optimized as successively described. The same cases shown in Fig. 3.1.4 for Panda fiber are also investigated for the Bow tie and Pseudo-rectangle optical fibers, i.e. nine different optical sensors are investigated. The mechanical and thermal parameters of carbon fiber, epoxy resin and

polyimide are described in Table 3.1.3. The number of mesh elements is close to $N_E = 317900$ (Fig. 3.1.6).

Table 3.1.2 Common parameters of the simulated optical fibers

Parameter	Symbol	Core	Cladding	SAP	Unit
Refractive index	n	1.448	1.444	1.4384	-
Young's modulus	E	70.7	73.9	50	GPa
Poisson's ratio	ν	0.1708	0.170	0.200	-
Thermal expansion coefficient	α	7.08×10^{-7}	5.6×10^{-7}	20×10^{-7}	1/K

In the stress analysis, we examine a range of tensile stresses ranging from $\sigma = 0 \text{ MPa}$ to $\sigma = 60 \text{ MPa}$, along the principal axis 3 (as depicted in Fig. 3.1.1), using increments of 10 MPa . In the thermal analysis, we investigate a temperature variation from $T = 233.15 \text{ K}$ to $T = 368.15 \text{ K}$, with increments of 15 K .

Figure 3.1.7(a) refers to the case of polyimide coated PM fiber, covered between two APFs and embedded in CFRP subjected to tensile stress σ .

Figure 3.1.7(a) depicts the strain distribution versus the laminate length L_p along the principal axes, evaluated at the center of the optical fiber core for the reference temperature $T_{ref} = 293.15 \text{ K}$ when a tensile stress $\sigma = 30 \text{ MPa}$ is applied. The longitudinal strain e_3 (dashed curve) is related to the transverse strains e_1 (dash dotted curve) and e_2 (dotted curve) through the Poisson's ratio. The strain distributions of Fig. 3.1.7(a) can be practically considered identical for Panda, Bow tie and Pseudo-rectangle fibers since the optical fibers, with same cladding diameter and coating, influence the response of the CFRP laminate to tensile stress σ in a similar way and very slightly. In Fig. 3.1.7(a), as expected, the laminate ends exhibit strain changes/oscillations because of the constraint reaction. The mesh, as illustrated in Figure 3.1.6, exhibits lower resolution along the principal axis 3, making it challenging to determine strain values accurately at the edges of the laminate. However, these values are not within the primary focus, as the FBG sensor is relatively short and positioned in regions where strains remain constant (far away from the laminate edges). Figure 3.1.7(b) shows the strains at temperature $T = 308.15 \text{ K}$ without applying stress $\sigma = 0 \text{ MPa}$, for the case of polyimide coated PM fibers, covered between two APFs and embedded in CFRP. Moreover, Fig. 3.1.7(b) illustrates the strain distribution for the three considered PM fibers. The longitudinal strain e_3 (dashed curve) is close to $0 \mu\epsilon$, so that the length of the laminate L_L does not change significantly.

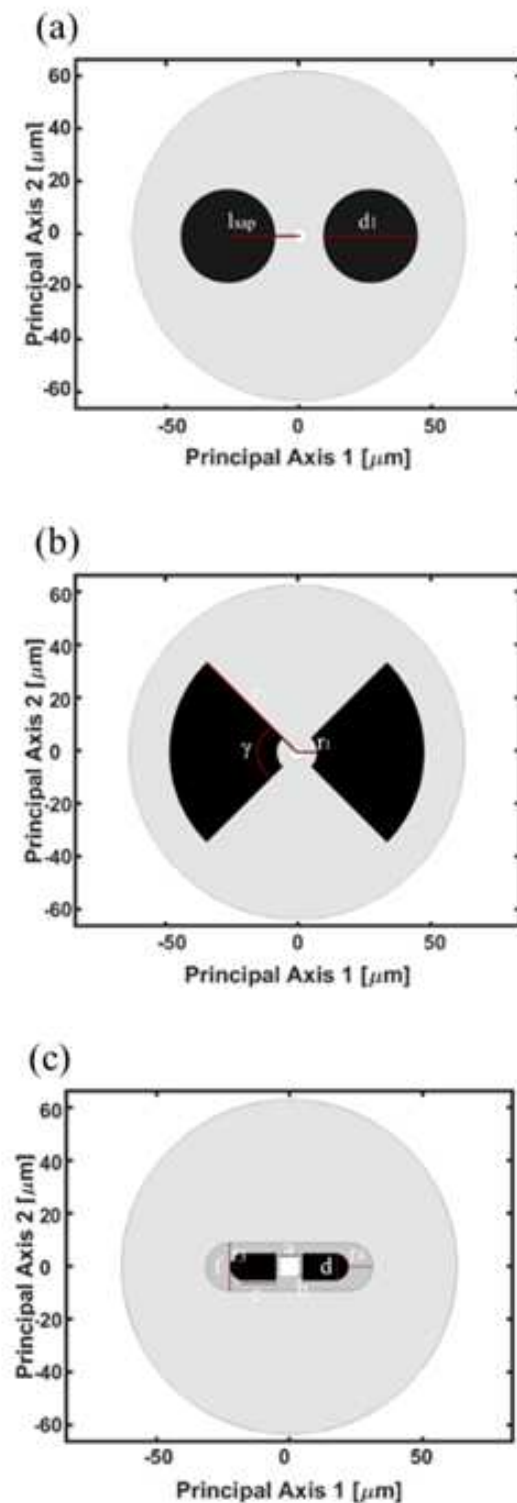


Figure 3.1.5 Cross-sections of the investigated PM fibers: (a) Panda, (b) Bow tie, (c) Pseudo-rectangle [2].

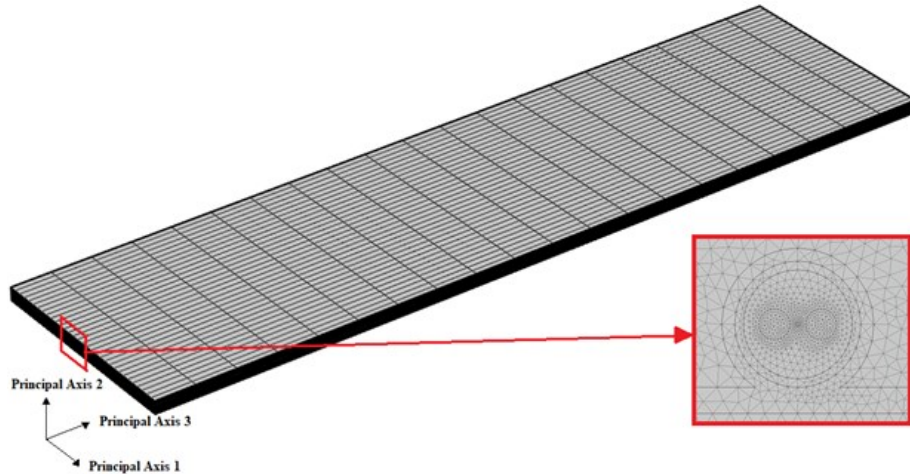


Figure 3.1.6 Mesh of the CFRP laminate and zoom of the mesh cross-section in correspondence of the PM optical fiber [2].

Table 3.1.3 Mechanical and thermal properties of carbon fiber, epoxy resin and polyimide

Parameter	Symbol	Value carbon fiber	Value epoxy	Value polyimide	Unit
Young's modulus	E	230 (33 direction) 15 (11 direction)	4	3.1	GPa
Shear modulus	G	24 (31 direction) 5.03 (12 direction)	-	-	GPa
Poisson's ratio	ν	0.2 (31 direction) 0.07 (12 direction)	0.35	0.35	-
Thermal expansion coefficient	α	-0.6×10^{-6} (/ fiber direction) 8.5×10^{-6} (\perp fiber direction)	55×10^{-6}	60×10^{-6}	1/K
Density	ρ	1800	1100	1300	kg/m ³

The modal analysis is conducted using 2D-FEM, the changes in refractive indices n are simulated by considering the internal stress tensor S . This simulation takes into consideration thermal expansion coefficient α , Young's Modulus E , Poisson's ratio ν according to that described in Section 2.2.1.

The propagating modes are calculated at the wavelength $\lambda = 1550\text{ nm}$. The fictive temperature $T_{fict} = 1273.15\text{ K}$, at which the glass begins to behave elastically and the reference temperature $T_{ref} = 293.15\text{ K}$, in unperturbed condition, both affecting the internal thermal stress, are considered.

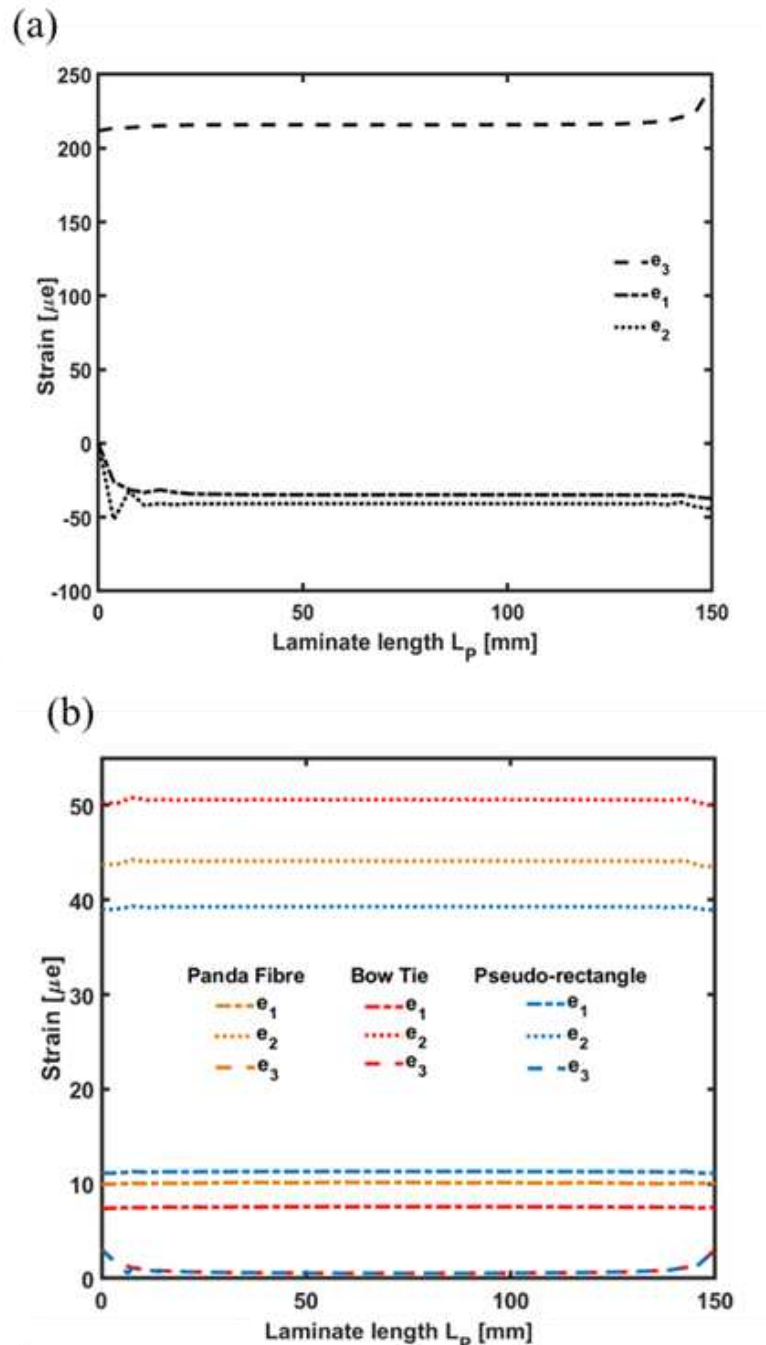


Figure 3.1.7 (a) Strain distribution inside the polyimide coated PM optical fibers, covered between two APFs and embedded in CFRP, versus the laminate length: tensile stress $\sigma = 30 \text{ MPa}$ without temperature variation. (b) Strain distribution inside the polyimide coated PM optical fibers, covered between two APFs and embedded in CFRP, versus the laminate length: temperature $T = 308.15 \text{ K}$ is reached without applying stress [2].

Birefringence B depends on the difference between the fictive temperature T_{fict} and the operation temperature T , the former pertaining to the fabrication process the latter to the operation condition [170], [185], [186].

The fundamental mode exhibits distinct phase velocities for its two polarizations. The effective refractive indices n_{eff} , in absence of external strain fields e and temperature variation ΔT , highlights a higher degree of birefringence B for the Bow tie fiber. Figure 3.1.8 shows the simulated internal stress distributions S_{11} in the Panda, Bow tie and Pseudo-rectangle fibers cross-section in unper- turbed condition (in absence of temperature variation ΔT and tensile stress σ). For all the three kinds of optical fibers considered in Fig. 3.1.8, the SAPs are subjected to a compressive stress (red colour), this means that these regions are shrinking. This happens since the thermal expansion coefficient α of the SAPs is higher than the surrounding cladding. With the exception of the region of the core, that is mainly compressed (red colour), it is also possible to see that the SAPs pull apart and compress, along the principal axis 1, the immediate cladding area around them. Along the principal axis 2, towards the SAPs, the neighboring cladding area is expanded (blue colour). Toward the outer edge of the cladding, the stress intensity tends to $S_{11} = 0 \text{ N/m}^2$, signifying that this region is not strongly compressed or under tension. In Fig. 3.1.9, it is possible to observe that, also in this case, the SAPs region is shrinking but the compression is distributed along the principal axis 2 near the SAPs. Birefringence B is proportional to the difference in stress distributions S_{11} and S_{22} [170]. Observing Fig. 3.1.10, it becomes evident that the Bow tie fiber exhibits a greater degree of birefringence B due to the larger value difference between n_1 and n_2 . Since the dimension of the SAPs of the pseudo rectangle are smaller than the ones of Panda and Bow tie fiber, they slightly affect the Poisson's ratios ν along the slow axis.

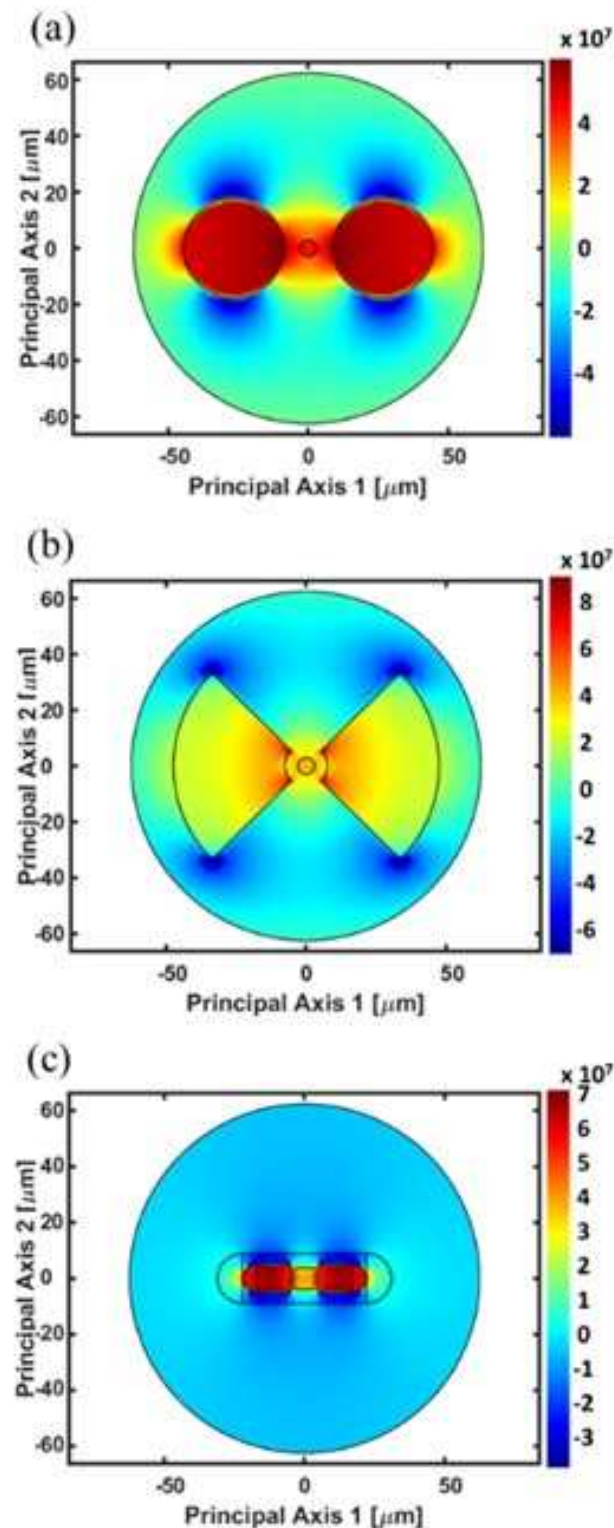


Figure 3.1.8 Simulated internal stress distribution S_{11} [N/m^2] in unperturbed condition: (a) Panda, (b) Bow tie, (c) Pseudo-rectangle [2].

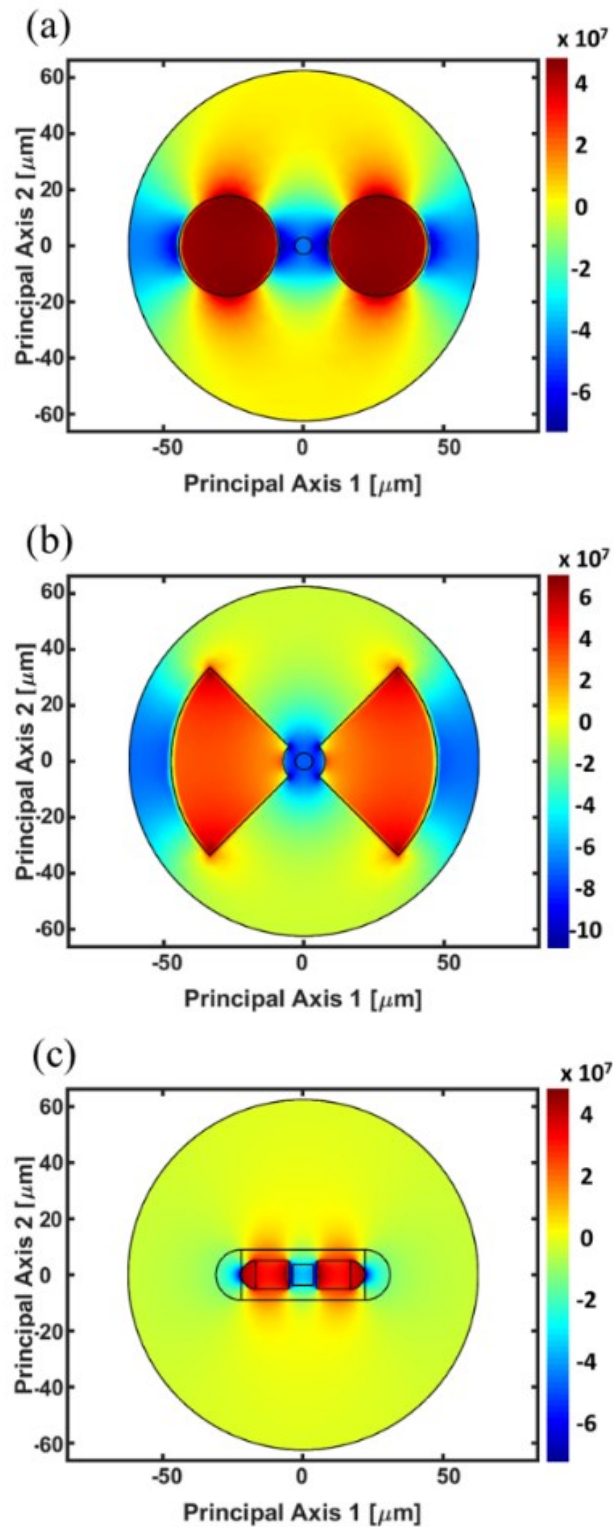


Figure 3.1.9 Simulated internal stress distribution S_{22} [N/m^2] in unperturbed condition: (a) Panda, (b) Bow tie, (c) Pseudo-rectangle [2].

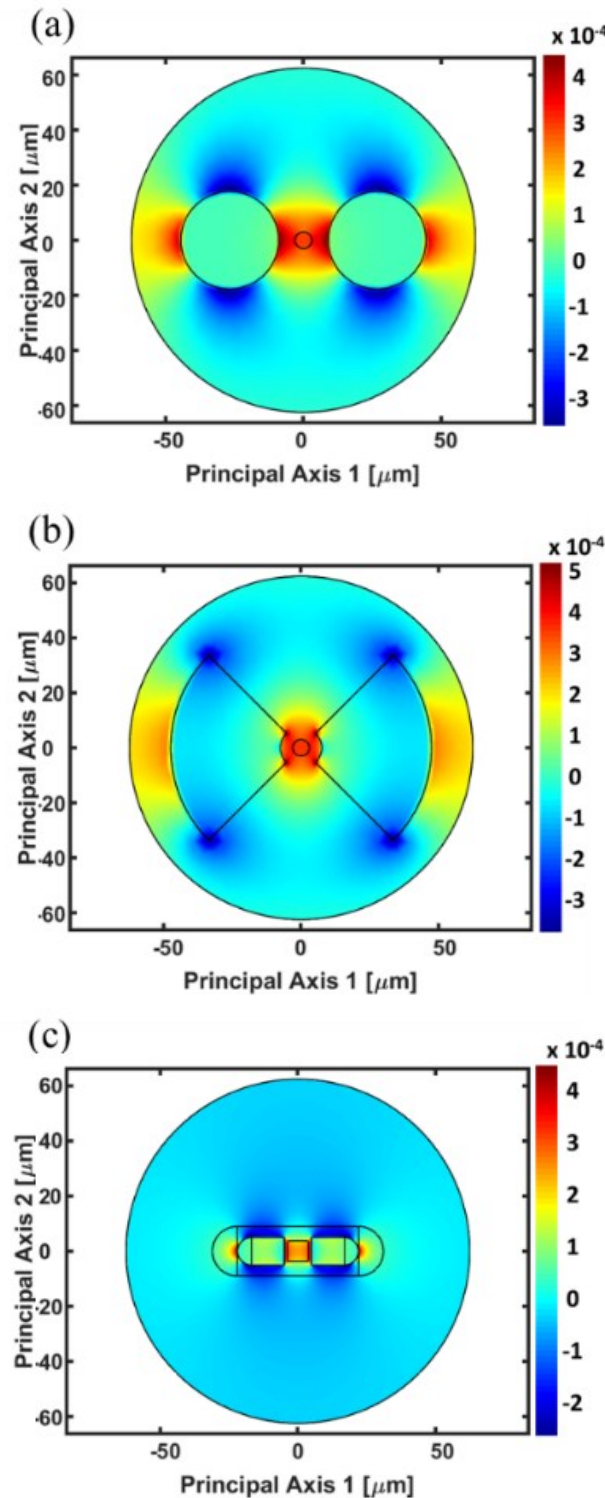


Figure 3.1.10 $n_1 - n_2$ in the optical fiber cross-section in unperturbed condition: (a) Panda, (b) Bow tie, (c) Pseudo-rectangle [2].

This leads to very close slow and fast strain sensitivities if compared with the other two investigated PM optical fibers. This evidences how the design of ad-hoc fiber cross-section, the use of specific dopants and their concentrations allow to hand the stress birefringence. Figure 3.1.10 illustrates the difference between n_1 and n_2 for the PM optical fibers under consideration in unperturbed conditions. The presence of stress anisotropy, due to the stress-optical coefficients, results in refractive index anisotropy [187].

3.1.4 Performance comparison of FBGs embedded in CFRP laminate

The three PM fibers of Fig. 3.1.8-3.1.10, Panda, Bow tie, Pseudo-rectangle, are investigated and compared in the cases of Fig. 3.1.4: i) without coating, ii) with polyimide coating, iii) with polyimide coating and APFs. The nominal parameters of the gratings, i.e. without/before applying external perturbations and at the reference temperature T_{ref} are reported in Table 3.1.4. The amplitude of index modulation m and the length of the grating L ensure good coupling and high reflectivity.

Table 3.1.5 provides the simulated sensitivities for all three PM fibers in both uncoated and polyimide-coated conditions. Furthermore, only the temperature sensitivities are reported, as the presence of polyimide does not impact the strain sensitivity. It can be noticed that its introduction improves the performance of the sensor. The thickness T_P and the width W_P of the two APFs have been optimized via a parametric investigation. The width W_P has been varied from 1 mm to 9 mm with a step of 2 mm. The temperature sensitivity remains almost unchanged by changing the width W_P . Therefore, $W_P = 5$ mm has been chosen because it being a feasible value for an easy implementation and for preventing undesirable crack. Also, the thickness T_P has been optimized. The investigation results regarding the Bow tie fiber are listed in Table 3.1.6. It is evident that by increasing thickness T_P , the sensitivity becomes greater. The drawback is that a too large thickness T_P , could lead to a decreasing of composite material mechanical robustness. We selected $T_P = 0.03$ mm, since it is a good trade-off between sensitivity and probability of failure within the CFRP laminate. The longitudinal strain sensitivity is not affected by variation in APFs size.

Table 3.1.4 Parameters of the simulated uniform FBG for both Panda, Bow tie and Pseudo-rectangle fibers.

Parameter	Symbol	Value	Unit
Grating Period	Λ	0.5365	μm
Amplitude of index modulation	m	7×10^{-4}	-
FBG length	L	2000	μm

Table 3.1.5 Sensitivity to temperature variation ΔT of the simulated FBG written in PM fibers, considering the optical fiber without coating and with polyimide coating.

Parameter	Symbol	Uncoated	Polyimide coating	Unit
Panda sensitivity – slow axis	K_{t1}	7.259	7.952	pm/K
Panda sensitivity – fast axis	K_{t2}	8.647	9.127	pm/K
Bow tie sensitivity – slow axis	K_{t1}	7.237	7.681	pm/K
Bow tie sensitivity – fast axis	K_{t1}	8.720	9.135	pm/K
Pseudo-rectangle sensitivity – slow axis	K_{t1}	7.579	8.219	pm/K
Pseudo-rectangle sensitivity – fast axis	K_{t1}	8.752	9.180	pm/K

Table 3.1.6 Sensitivity to temperature ΔT and thickness T_P variation of the simulated FBG written in polyimide coated Bow tie fiber, covered between two APFs and embedded in CFRP (polyimide width is considered constant and equal to $W_P = 5 mm$).

Parameter	Symbol	Value						Unit
APF thickness	T_P	0.01	0.02	0.03	0.04	0.05	mm	
Sensitivity - slow axis	K_{t1}	7.830	7.950	8.051	8.097	8.160	pm/K	
Sensitivity - fast axis	K_{t2}	9.284	9.402	9.497	9.550	9.608	pm/K	

From this point on, the investigation is focused on the case of the optical fibers coated with polyimide, covered between two APFs and embedded in CFRP. The two APFs have dimensions $T_P = 0.03 mm$ and $W_P = 5 mm$. The three PM fibers exhibit a linear response of the Bragg wavelength λ_B versus the temperature T as evident in Fig. 3.1.11(a) for both slow (blue colour) and fast (red colour) axes of Panda (continuous line), Bow tie (dashed line), Pseudo-rectangle (dotted line) optical fibers.

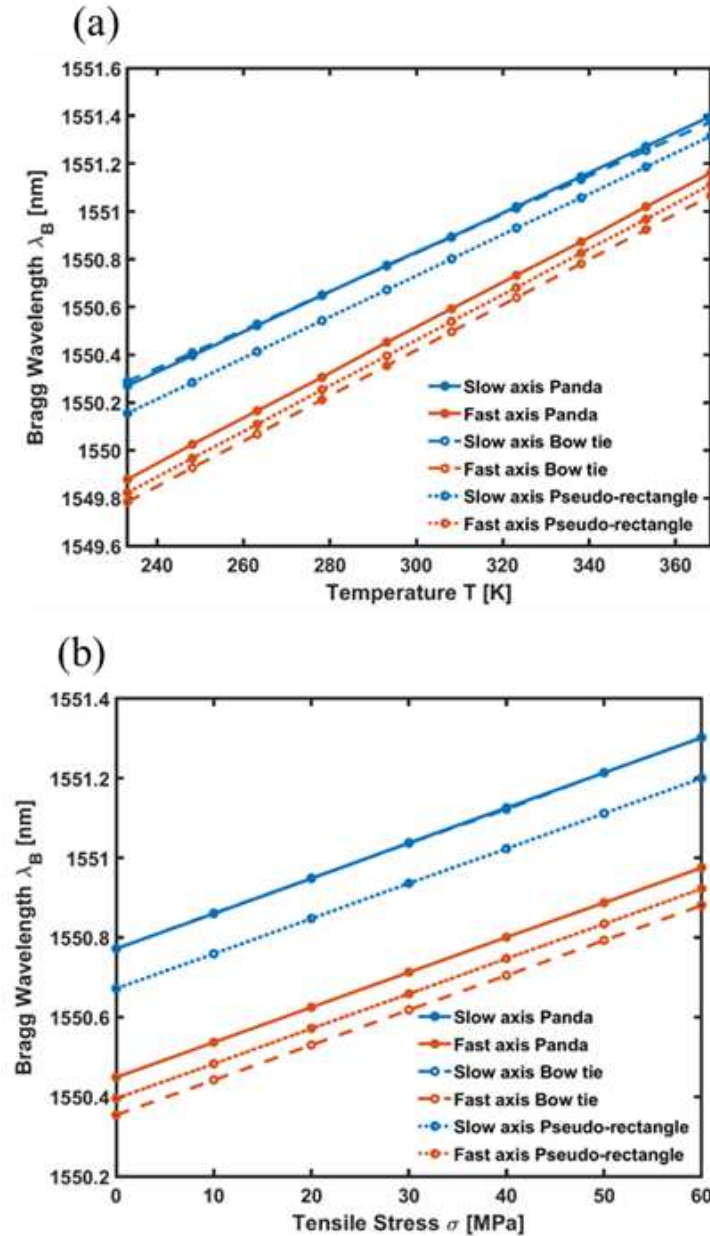


Figure 3.1.11 (a) Bragg wavelength λ_B versus the temperature T simulated for both slow (blue colour) and fast (red colour) axes; Panda (continuous line), Bow tie (dashed line), Pseudo-rectangle (dotted line) coated with polyimide, covered between two APFs and embedded in CFRP. Grating parameter: $\Lambda = 0.5365 \mu m$, $m = 7 \times 10^{-4}$, $L = 2000 \mu m$. (b) Bragg wavelength λ_B versus the tensile stress σ simulated for both slow (blue colour) and fast (red colour) axes; Panda (continuous line), Bow tie (dashed line), Pseudo-rectangle (dotted line) coated with polyimide, covered between two APFs and embedded in CFRP. Grating characteristics: $\Lambda = 0.5365 \mu m$, $m = 7 \times 10^{-4}$, $L = 2000 \mu m$ [2].

In Fig. 3.1.11(a) it is possible to observe that Panda (continuous line) and Bow tie (dashed line) have similar Bragg wavelength in the nominal condition ($T_{ref} = 293.15\text{ K}$) for the slow axis: the characteristics are almost coincident. Similar considerations can be made for Fig. 3.1.11(b), depicting the Bragg wavelength shift $\Delta\lambda_B$ versus the tensile stress σ simulated for both slow (blue colour) and fast (red colour) axes. Table 3.1.7 shows the calculated sensitivity for each axis of each PM fiber analysed. The obtained results highlight that the Bow tie optical fiber shows better performances in terms of decoupling strain and temperature changes, achieving temperature sensitivities of 8.051 pm/K and 9.497 pm/K and strain sensitivities of $1.229\text{ pm}/\mu\epsilon$ and $1.220\text{ pm}/\mu\epsilon$, for the slow and the fast axis respectively. The sensitivity matrix determinant is the highest and thus the system (3.2) is better-conditioned. Furthermore, by using the relation (3.2), it is possible to calculate simultaneously the strain Δe_3 and temperature ΔT changes with a single optical fiber. By comparing uncoated fiber without APFs and polyimide coated fiber with APFs an increase of temperature sensitivity for the Bow tie optical fiber fast and slow axis roughly of 8,9 % and 11,2 % respectively is obtained, as reported in Table 3.1.5 and Table 3.1.7. According to [188], uncertainties on strain and temperature can be computed knowing the interrogator wavelength resolution $\delta\lambda_B$ and sensitivity matrix K_S (3.2). Uncertainty to temperature variation δT and longitudinal strain δe_3 of the simulated FBG written in polyimide coated PM fibers, covered between two APFs and embedded in CFRP is reported in Table 3.1.8 for an interrogator with wavelength resolution of $\delta\lambda_B = 1\text{ pm}$. It is evident by analysing the uncertainties values reported in Table 3.1.8 that the Bow tie fiber is the most suitable for the decoupling. The effect of the polyimide coating and APFs lead to similar percentage increase of temperature sensitivities for all the three simulated optical fibers. Moreover, APFs make simpler the manufacturing process of the composite material, simplifying the alignment of fast and slow axis of PM optical fibers in CFRP layers. They can be readily manufactured through a process that involves the application of a liquid polyimide solution onto the fiber, followed by the placement of a solid polyimide film onto it. There are two main phases, a soft-bake process considering a temperature $T \cong 410\text{ K}$ and a time of curing $t \cong 10'$ followed by a hard-bake process ($T \cong 520\text{ K}$, $t \cong 30'$). As an alternative a spin-coating technique can be employed.

Table 3.1.7 Sensitivity to temperature variation ΔT and longitudinal strain e_3 of the simulated FBG written in polyimide coated PM fibers, covered between two APFs and embedded in CFRP.

Parameter	Symbol	Panda	Bow tie	Pseudo-rectangle	Unit
Sensitivity to strain – slow axis	K_{e1}	1.229	1.229	1.224	$pm/\mu e$
Sensitivity to strain – fast axis	K_{e2}	1.222	1.220	1.220	$pm/\mu e$
Sensitivity to temperature – slow axis	K_{t1}	8.356	8.051	8.596	pm/K
Sensitivity to temperature – fast axis	K_{t2}	9.499	9.497	9.557	pm/K

Table 3.1.8 Uncertainty to temperature variation δT and longitudinal strain δe_3 of the simulated FBG written in polyimide coated PM fibers, covered between two APFs and embedded in CFRP for an interrogator resolution of $\delta\lambda_B = 1 pm$.

Parameter	Matrix K_s	Temperature	Strain
		Uncertainty δT [K]	Uncertainty δe_3 [μe]
Panda with coating and APFs	K_{e1}	1.68	12.20
Bow tie with coating and APFs	K_{e2}	1.32	9.49
Pseudo-rectangle with coating and APFs	K_{t1}	2.02	14.99

3.1.5 Conclusions

In this Section, a comprehensive approach has been developed for the accurate study of three PM fibers (Panda, Bow tie and Pseudo-rectangle) embedded in CFRP. The design of two APFs, covering the fiber optic sensors, is proposed. Numerical results suggest that by adding suitable APFs embedding the polyimide coated optical fibers it is possible to perform a more accurate strain and temperature measurement with respect to uncoated or conventional polyimide coated optical fibers (without APFs). In particular, the temperature sensitivity for both slow and fast axis can be increased of about 10 % for all the investigated optical fibers. By comparing the simulation results obtained for the PM optical fibers polyimide coated and covered between APFs, the Bow tie optical fiber shows the lowest values of uncertainty to temperature variation $\delta T = 1.32 K$ and to longitudinal strain $\delta e_3 = 9.49 \mu e$. We can conclude that, among the other PM fibers, Bow tie allows the best decoupling of the simultaneous temperature and strain measurement. Moreover, the introduction of APFs improve the manufacturing process of composite material, simplifying the alignment of fast and slow axis of PM optical fibers in CFRP layers. The next step will be the

experimental investigation of the simulated results with the construction of the sensor prototypes.

3.2 Design of Microstructured Flat Optical Fiber for Stress Monitoring in Composite Materials

In this Section the design of an innovative Microstructured Flat Optical Fiber (MFOF) to obtain a multiaxial strain sensor for composite material monitoring is described. The sensing regions are a pair of eyelets where Bragg gratings are inscribed. To enable sensing in multiple directions, an appropriate microstructure is designed near just one of the eyelets. The effect of the strain field, evaluated via a 3D-FEM approach, is considered to obtain the change of the refractive index distribution. The electromagnetic modal analysis and the CMT theory are exploited to evaluate the Bragg wavelength shift for the slow and fast axis fundamental modes, guided in the two eyelets and affecting the sensor response. The designed microstructured flat optical fiber is technologically feasible and promises sensing performance higher than that obtainable with the conventional optical fibers. In addition, flat optical fiber can be embedded in composite materials reducing the drawbacks related to both orientation and excess resin. The following paragraphs are organized as follows: in Section 3.2.1, the operation principle, the MFOF description, the simulation approach and the validation of the model; in Section 3.2.2, the geometrical and physical parameters of CFRP and designed MFOF; in Section 3.2.3, the numerical results are outlined and critically discussed with their implications for future works; in Section 3.2.4, the conclusion.

3.2.1 Operation principle and MFOF description

A flat optical fiber has a configuration similar to that of a planar waveguide. It is comprised of a central core layer enclosed by two wider multimode regions, commonly referred to as "eyelets". The outstanding potential of flat optical fiber, can be emphasized as a multiparameter sensor by performing a different design of the two eyelets to alter the strain distribution among them.

The sketch of the proposed flat optical fiber sensor is illustrated in Fig. 3.2.1(a). The figure shows the two eyelets accommodating the DUW waveguides, the central core layer, and a microstructure featuring air holes along the propagation direction. To facilitate comprehension, only the first air hole is presented in a perspective view.

Fig. 3.2.1(b) illustrates a sketch, not in scale, of the uncoated MFOF sensor, embedded on the sixth layer of a CFRP lamina which is made up of eight unidirectional layers.

The sensor can be embedded in every layer being the composite unidirectional. In case of cross-ply configuration, generally, the optical fiber sensor is placed parallel to the carbon reinforcing fiber in order to minimize its intrusive behavior [5]. The use of one sensor demonstrates the ability of the microstructured flat fiber to detect stresses in CFRP. Stresses can potentially be mapped with high spatial resolution taking advantage of the embedding of different flat fibers each featuring a cascade of FBGs.

The fabrication of the proposed flat optical fiber can be achieved through the use of modified chemical vapor deposition (MCVD). Previous fabrication approaches have collapsed the cylindrical preform during the draw process to create the planar format [24]. To create the microstructure, collapse of the preform will need to be conducted prior to the drawing stage. An ultrasonic mill can be used to form the holes directly or, alternatively, it can be achieved through milling an area into the preform and stacking appropriate silica canes. To avoid collapse or tapering of the microstructured holes, a positive gas pressure within air holes can be applied during the fiber draw process. Starting from a few mbar, the pressure can be adjusted to get the required hole dimensions depending on original size of holes and outer preform dimension.

Curing is part of the fabrication process to accomplish a composite material. During curing, a chemical reaction takes place, causing the resin to transition from a liquid to a solid state and establishing cross-links between the initially molten polymer and the carbon fibers. Typically, this process is carried out under a defined time/temperature/pressure profile. In a CFRP lamina, the effects of residual stresses caused by the curing process can be divided in two main kinds: micro-level (difference in material properties leading to debonding or cracks) and macro-level (ply anisotropy, shape change due to temperature gradients) effects. They directly affect the mechanical deterioration of the composite with time [33]. The anisotropic stress related to manufacturing process can alter the spectrum, which is split into two separated Bragg peaks, two for each grating, as if it was a high birefringent fiber in the case of cross-ply configuration [21]. However, in the design, these effects have been neglected since they are not significant with reference to the Bragg wavelength shift and, as a consequence, with reference to the sensitivity [189]. Furthermore, in a composite lamina with a unidirectional layer configuration, like the one under consideration in this

research work, there is no occurrence of Bragg wavelength splitting caused by residual stress.

3.2.1.1 Design approach

The design approach is summarized as follows: i) development of a 3D-FEM (via COMSOL Multiphysics) model of the CFRP lamina with the embedded optical fiber; ii) 2D-FEM mode analysis of the MFOF; iii) transfer matrix method (TMM) to calculate the influence of the strains on reflective spectrum of the gratings.

The 3D-FEM model allows an accurate calculation of the strain transfer from CFRP lamina to the embedded sensor for stresses σ applied along x , y and z axis, see Fig. 3.2.1 (b). The CFRP is modelled considering the micromechanical analysis of the unit cell, leading to the computation of the elasticity matrix $[E]_m$ [2]. The evaluated strains are employed to calculate the refractive index variation Δn of the optical guiding structure [2].

The effective refractive index of fundamental modes n_{eff} guided in the two eyelets can be computed through 2D-FEM mode analysis and used as input data for calculating the Bragg wavelength λ_B shift via TMM [144].

3.2.1.2 Model validation

Through validation, the accuracy as well as reliability of the model used to simulate an optical fiber sensor embedded in a CFRP laminate has been confirmed. In particular, both the mechanical analysis of the composite material lamina and the electromagnetic modal investigation of the MFOF have been validated with literature results [189] for a CFRP lamina Toray T800H/3631 (Toray Industries, Inc) composed of eight layers in cross-ply configuration $[0_2/90_4/0_2]$. Its physical properties are reported in [190]-[193]. A layer of composite lamina is characterized by a thickness $T_L = 0.15 \text{ mm}$, a length $L_L = 120 \text{ mm}$ and a width $W_L = 20 \text{ mm}$. To evaluate the elasticity matrix $[E]_m$ of a layer as in [2], a micromechanical analysis on a single unit cell, made of carbon fiber and resin (carbon fiber-resin volume fraction $v_f = 0.6$), has been performed.

Fig. 3.2.2 shows a comparison between the simulated tensile stress σ_x and the strain ϵ_x represented by the purple dash-dotted curve, and the experimental measurement, indicated by the yellow curve [189].

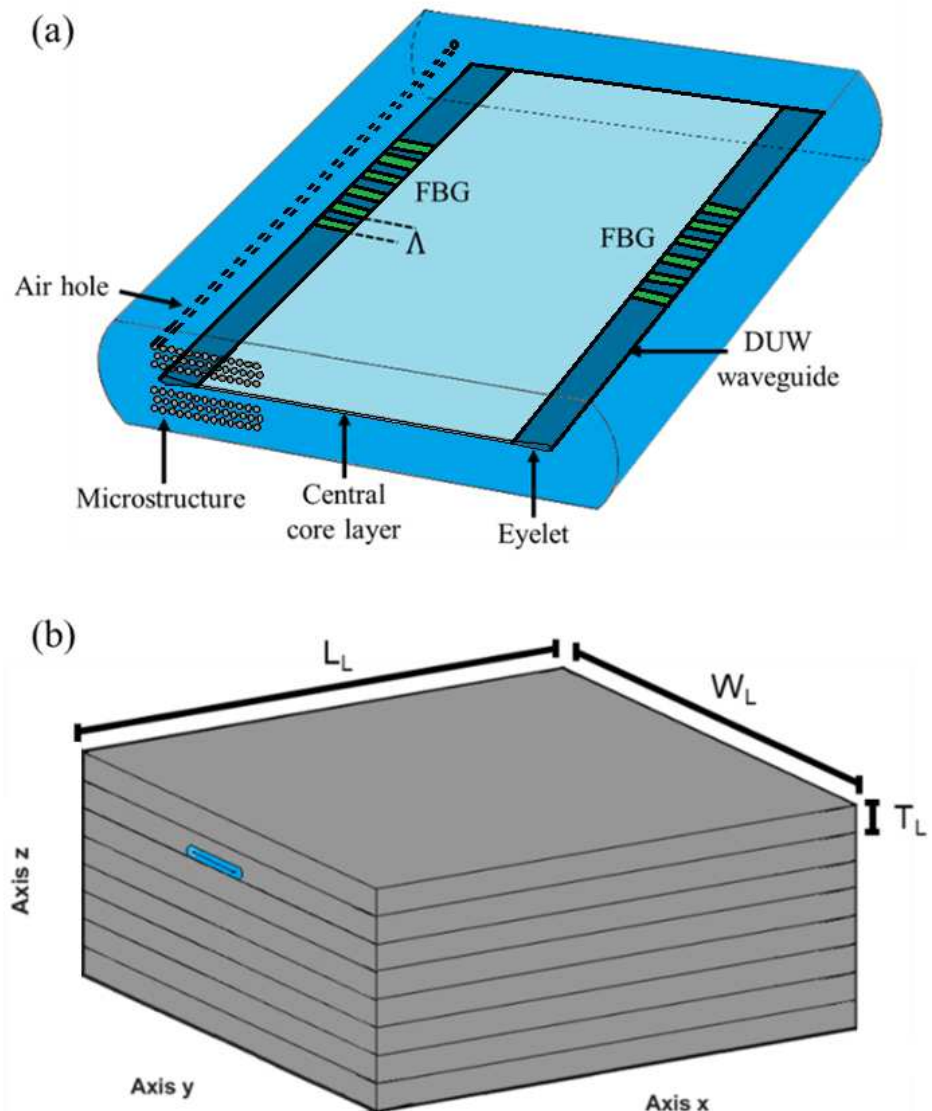


Figure 3.2.1 Sketch of the MFOF with air holes surrounding one eyelet along the x axis (a). Schematic of the simulated CFRP lamina (grey) with MFOF sensor (blue) embedded. The lamina is unidirectional, and it is made of eight layers. Each layer has a thickness T_L , length L_L and a width W_L (b) [35].

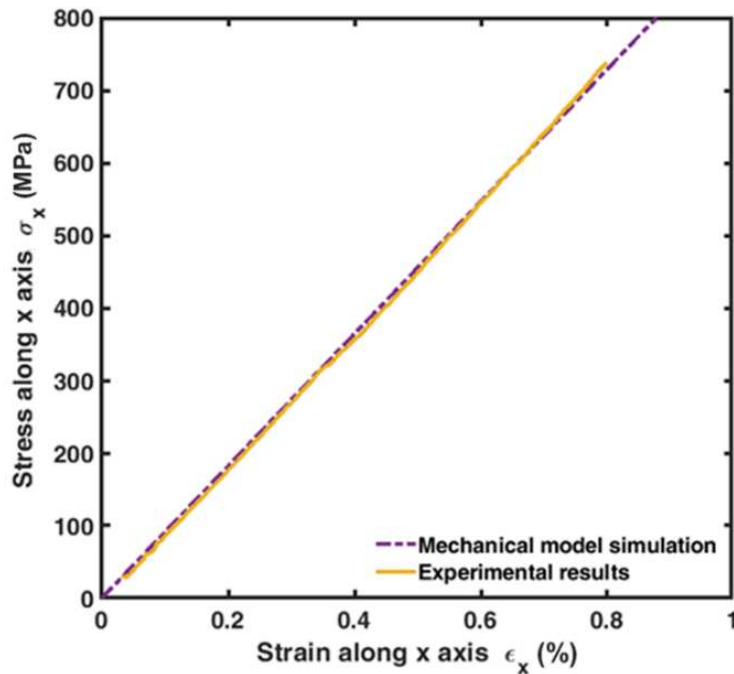


Figure 3.2.2 Tensile stress σ_x versus strain ϵ_x along x axis: simulation via mechanical model (purple dash dotted curve), experimental results (yellow curve) [189], [35].

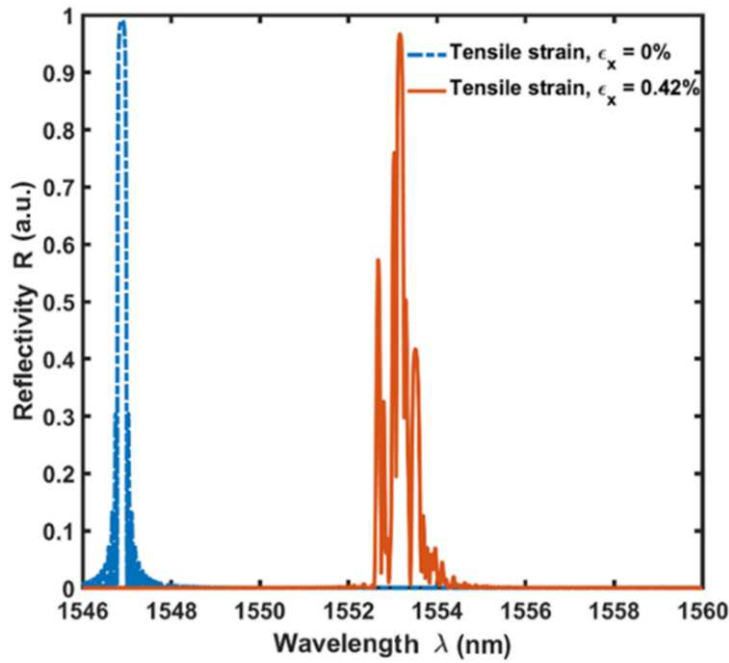


Figure 3.2.3 Simulated reflection spectra in absence of external loading ($\epsilon_x = 0 \%$, dotted blue curve) and in presence of transverse cracks with crack density $\rho = 7 \text{ cm}^{-1}$ ($\epsilon_x = 0.42 \%$, orange curve) of uniform silica FBG characterised by core diameter $d_{co} = 10 \mu\text{m}$, cladding diameter $d_{cl} = 125 \mu\text{m}$ and grating period $\Lambda = 530 \text{ nm}$ [35].

As it is reported in [189] an excellent agreement is obtained. In [189], the stress σ_x as a function of the strain ϵ_x is measured by means of strain gage. In the simulation performed to validate our model, we have considered the presence of the embedded fiber in the CFRP.

Fig. 3.2.3 illustrates the simulated reflection spectra, in absence of external loading ($\epsilon_x = 0\%$, dotted blue curve) and in presence of transverse cracks with crack density $\rho = 7 \text{ cm}^{-1}$ ($\epsilon_x = 0.42\%$, orange curve), of uniform silica FBG with core diameter $d_{co} = 10 \mu\text{m}$, cladding diameter $d_{cl} = 125 \mu\text{m}$ and grating period $\Lambda = 530 \text{ nm}$.

The optical fiber lays on the sixth layer at the interface with the seventh. The obtained results are in excellent agreement with [189]. Consequently, the model and simulation approach have been validated for the scenario concerning an embedded, uncoated FBG subjected to non-uniform uniaxial strain, which is characteristic of situations involving transverse cracks [189].

3.2.2 Design of the embedded MFOF

The electromagnetic and mechanical analysis is carried out to design an embedded sensor taking into account the geometry of the optical fiber and its physical properties in combination with those of the CFRP material. In particular, the parameters regarding the carbon fiber and epoxy resin (carbon fiber-resin volume fraction is $v_f = 0.6$) are reported in Table 3.2.1 and Table 3.2.2 [37].

To effectively perform triaxial strain discrimination using the proposed MFOF sensor for structural health monitoring applications, it is crucial to choose an optimal configuration of air holes along the length of the optical fiber. The sensor response to specific external perturbations can be optimized by varying the diameter, the pitch and the position of the air holes in the MFOF cross-section. It is worth noting that the range of these variations is limited by mechanical robustness consideration.

Regarding the MFOF, the physical properties are reported in Table 3.2.3. The cross-section of MFOF of Fig. 3.2.1(a) is reported in Fig. 3.2.4. The geometrical parameters and the physical properties of the MFOF such as the height of elliptical eyelets H_{eye} , the height of the central layer H_L , the height of the cladding H_{cl} , the length of the cladding D_{cl} are reported in Table 3.2.4 [37]. These geometrical parameters are realistic since they are pertaining to a fabricated flat optical fiber without microstructure [37].

Table 3.2.1 Geometrical parameters of the CFRP lamina.

Parameter	Symbol	Value	Unit
Layer thickness	T_L	0.3	mm
Layer length	L_L	150	μm
Layer width	W_L	40	μm

Table 3.2.2 Physical parameters of the CFRP lamina.

Parameter	Symbol	Value carbon fiber	Value epoxy	Unit
Young's modulus	E	230 (x) 15 (y)	4	GPa
Shear modulus	G	24 (xy) 5.03 (yz)	—	GPa
Poisson's ratio	ν	0.2 (xy) 0.07 (yz)	0.35	—
Density	ρ	1800	1100	kg/m^3

Table 3.2.3 Physical properties of the MFOF [37].

Parameter	Symbol	Value	Unit
Young's modulus	E	78.3	GPa
Poisson's ratio	ν	0.186	—
Pockel's coefficient	ρ_{11}	0.121	—
Pockel's coefficient	ρ_{12}	0.27	—

To prevent light propagation in the central core layer and guide light exclusively through the eyelets, DUW is applied along the length of the flat optical fiber at the positions corresponding to the eyelets. The presence of air holes reduces the total flux of UV light at the fiber core. However, a periodic interference can still be obtained with longer exposure time despite the presence of scattering at the hole-silica interface [1,2].

In particular, the cladding of the flat optical fiber is made of pure silica while the eyelet and the central core layer are doped with germanium and/or boron [25]. The local change of the refractive index in the eyelets with respect to the central core region is $\Delta n_{DUW} = 5 \times 10^{-3}$ [25]. The refractive index values are $n_{eye} = 1.4595$ for the eyelets, $n_{cc} = 1.4590$ for the central core regions and $n_{cl} = 1.4439$ for the cladding at the wavelength $\lambda = 1560 \text{ nm}$. For a flat optical fiber, without microstructure and without any stress external perturbations, having the aforesaid optical and geometrical parameters the simulated effective refractive index of the fundamental mode guided in the eyelet is $n_{eff} = 1.4579$ in perfect agreement with measurement [37].

The primary focus in the design strategy has been on refining the microstructure to achieve the intended sensor response.

It has required the choice of suitable dimensions for the distance between the air holes D_{pitch} , the diameter of the air holes D_{hole} and the vertical distance H_{hole} between the last row and the first row of the upper- and lower-holes distribution. In particular, the optimized microstructure has been obtained through several simulations via a trial-and-error approach, by performing both mechanical and electromagnetic investigations. The main result is that a pattern of air holes, distributed only on an eyelet, with $D_{pitch} = 12.5 \mu\text{m}$, $D_{hole} = 11 \mu\text{m}$ and $H_{hole} = 26 \mu\text{m}$ introduce an optimized strain distribution, very different with respect to that occurring in the eyelet without microstructure.

This can clearly be explained by observing Fig. 3.2.5, that shows the strain distribution ϵ_y (y being the predominant component) in the cross-section of the MFOF embedded in the CFRP lamina, for a tensile stress $\sigma_y = 35 \text{ MPa}$ along the y axis. The presence of the microstructured eyelet results in a more pronounced strain field due to the air holes. Consequently, the designed pattern is well-suited to enhance the birefringence (B) of the microstructured eyelet when it experiences stress along the y -axis (σ_y).

Birefringence B occurs because the two polarizations of the fundamental mode travel at different velocities, being characterized by distinct effective refractive indices n_{eff} . It is possible to define $n_{eff,fast}$ for the mode polarized along the fast axis mode and $n_{eff,slow}$ for the orthogonally polarized mode (i.e. along the slow axis). The spacing $\Delta\lambda_B$ between the two Bragg peaks increases by increasing the birefringence B .

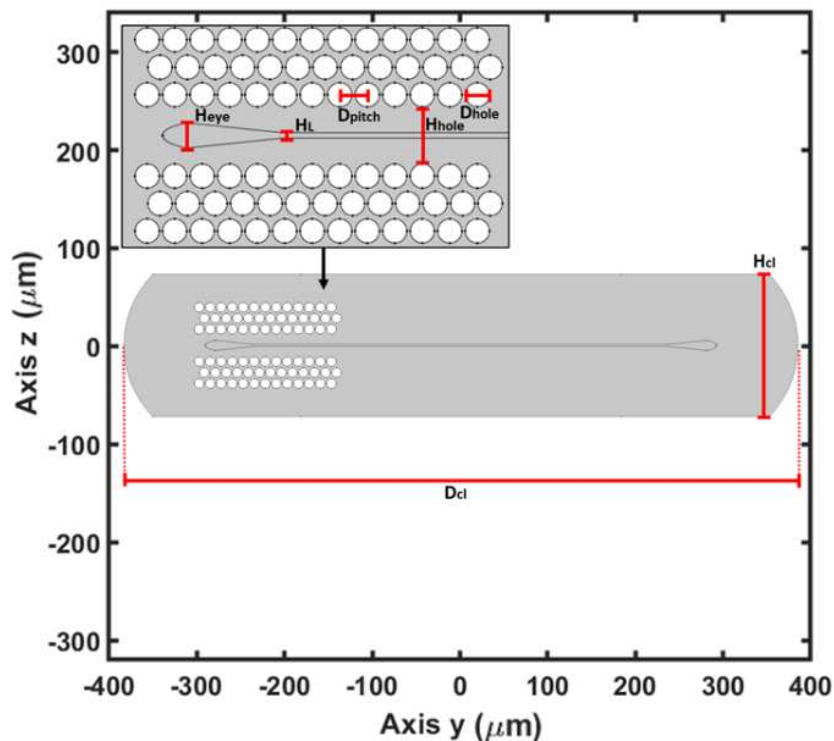


Figure 3.2.4 Cross-section of the MFOF [35].

Table 3.2.4 Physical properties of the MFOF [37].

Parameter	Symbol	Value	Unit
Height of elliptical eyelets	H_{eye}	13.71	\(\mu\text{m}
Height of the central layer	H_L	2.46	\(\mu\text{m}
Height of the cladding	H_{cl}	162.33	\(\mu\text{m}
Length of the cladding	D_{cl}	764.46	\(\mu\text{m}
Distance between the air holes	D_{pitch}	12.5	\(\mu\text{m}
Diameter of the air holes	D_{hole}	11	\(\mu\text{m}
Vertical distance between holes	H_{hole}	26	\(\mu\text{m}

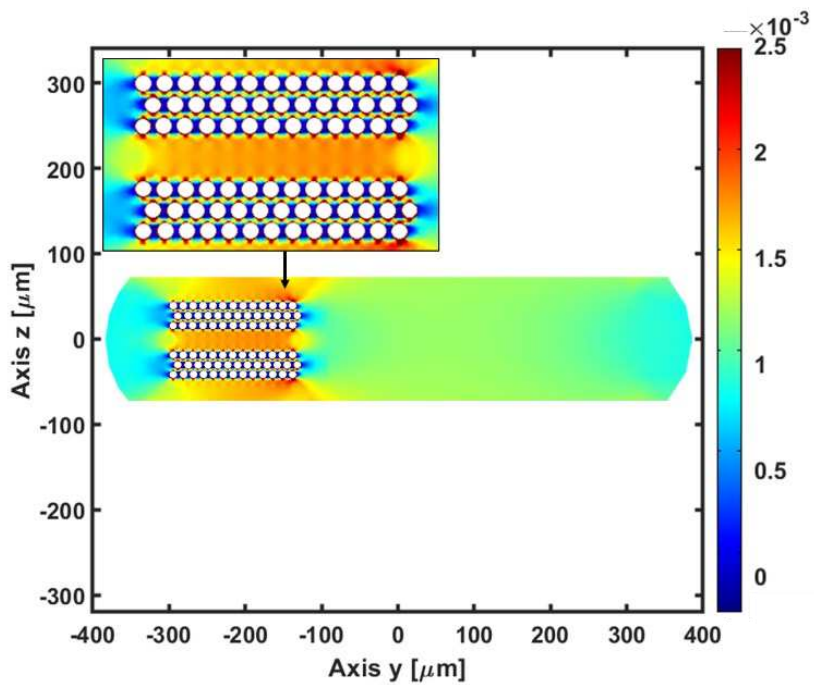


Figure 3.2.5 Strain distribution ϵ_y in the cross-section of the MFOF embedded in the CFRP lamina, for a tensile stress $\sigma_y = 35 \text{ MPa}$ along the y axis [35].

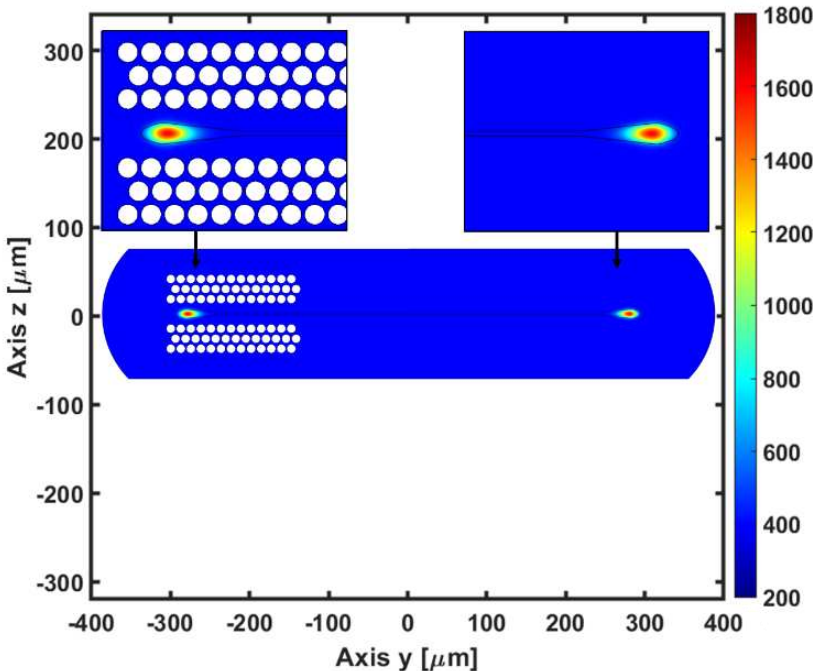


Figure 3.2.6 Electric field norm distribution of the fundamental modes for the micro-structured eyelet and the eyelet without microstructure, at the wavelength $\lambda = 1560 \text{ nm}$ [35].

Conversely, when stress is applied along the z-axis σ_z , the strain field distribution within the microstructured eyelet exhibits reduced magnitudes and consequently leads to a lower birefringence B compared to the scenario where stress is applied to an eyelet without microstructure.

It is worth noting that, in the investigation, for each of mechanical stress component $\sigma_x, \sigma_y, \sigma_z$ all the three principal induced strain components $(\epsilon_x, \epsilon_y, \epsilon_z)$ have been considered.

Fig. 3.2.6 shows the electric field norm distribution of the fundamental modes for the two eyelets at the wavelength $\lambda = 1560 \text{ nm}$; the simulated effective refractive index of the fundamental mode is $n_{eff} = 1.4579$ without external loading.

Uniform FBG with refractive index profile definition $\Delta n_{FBG} = 3 \times 10^{-4}$ is considered in both the eyelets. The nominal parameters of the gratings are listed in Table 3.2.5 (i.e., without/before applying external perturbations).

Table 3.2.5 Characteristics of the FBGs without external loading under isothermal condition.

Parameter	Symbol	Value	Unit
Length of the grating	L	2000	μm
Grating period	Λ	0.5349	μm

3.2.3 Results and discussion

The calculation of the refractive index change resulting from the applied stress has been performed in accordance with the approach reported in [2]. The propagation constants and the electromagnetic field distribution of the propagating modes have been simulated as described in Section 3.2.2.

The reflection spectra as a function of the stress have been evaluated for both the microstructured eyelet and the eyelet without microstructure, for both fast axis and slow axis. Four different sensitivities are calculated by ratio $\Delta\lambda_B/\Delta\sigma_i$ where the subscript $i = x, y, z$ indicates the σ stress direction. They are: i) the fast axis propagation mode of the microstructured eyelet $K_{i,fm}$; ii) the slow axis propagation mode of the microstructured eyelet $K_{i,sm}$; iii) the fast axis propagation mode

of the eyelet without microstructure $K_{i,f}$; iv) the slow axis propagation mode of the eyelet without microstructure $K_{i,s}$.

The longitudinal stress analysis, along the x axis, has been performed in the range from $\sigma_x = 0 \text{ MPa}$ to $\sigma_x = 90 \text{ MPa}$.

In the case of longitudinal stress σ_x , the simulated Bragg wavelength λ_B as a function of stress σ_x reveals four sensitivities that are remarkably comparable. The presence of air holes has a negligible impact in this case. The sensitivities to stress along x axis σ_x are reported in Table 3.2.6.

Fig. 3.2.7 illustrates the Bragg wavelength λ_B as a function of the applied transverse stress along y axis σ_y , for both the microstructured eyelet and the eyelet without microstructure. Specifically, the curves correspond to fast axis propagation mode of the microstructured eyelet (continuous blue), slow axis propagation mode of the microstructured eyelet (orange dashed), fast axis propagation mode of eyelet without microstructure (yellow dash dotted), and slow axis propagation mode of eyelet without microstructure (purple dotted).

The response of the microstructured eyelet slow and fast axes differs from that of the eyelet without microstructure. The pattern of air holes, when transverse stress σ_y is applied, determines a greater transfer of stress between the composite lamina and the FBG sensor. This leads to a significant change in the refractive index, which in turn has a notable impact on the propagation mode characteristics and the Bragg wavelength λ_B .

Fig. 3.2.8 illustrates the Bragg wavelength λ_B as a function of the applied stress along z axis σ_z for the fast axis propagation mode of the microstructured eyelet (continuous blue), slow axis propagation mode of the microstructured eyelet (orange dashed), fast axis propagation mode of eyelet without microstructure (yellow dash dotted), and slow axis propagation mode of eyelet without microstructure (purple dotted). In this case, the sensitivity of the fast and slow axis of the eyelet without microstructure is larger than that of the microstructured eyelet. The sensitivities related to transverse stresses (i.e. σ_y and σ_z), for each polarization of the designed MFOF, are reported in Table 3.2.7 – 3.2.8.

The strong difference of the sensitivity along the transversal directions enables an efficient triaxial stress detection.

The presence of both the double grating and birefringence induced by transverse stresses results in the generation of four peaks or dips in the reflection or transmission spectrum.

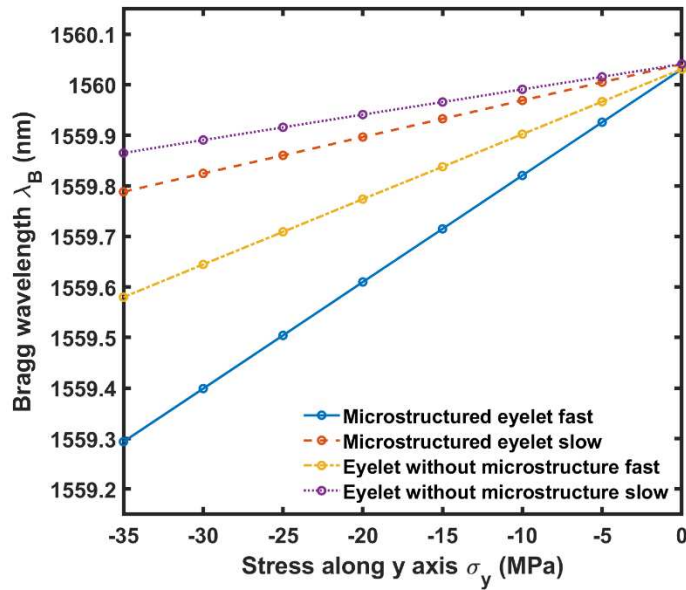


Figure 3.2.7 Simulated Bragg wavelength λ_B versus the transverse stress σ_y : fast axis microstructured eyelet (continuous blue); slow axis microstructured eyelet (orange dashed); fast axis eyelet without microstructure (yellow dash dotted); slow axis eyelet without microstructure (purple dotted). Grating characteristics: $\Lambda = 0.5349 \mu\text{m}$, $\Delta n_{\text{FBG}} = 3 \times 10^{-4}$, $L = 2000 \mu\text{m}$ [35].

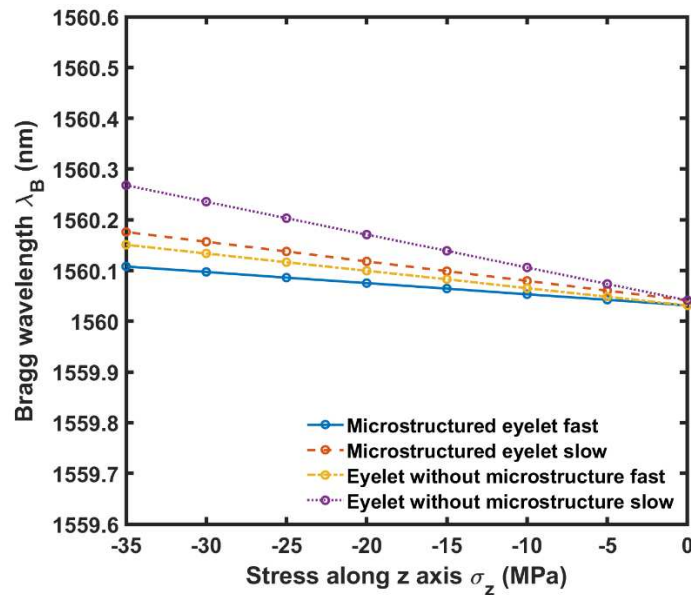


Figure 3.2.8 Simulated Bragg wavelength λ_B versus the transverse stress σ_z : fast axis microstructured eyelet (continuous blue); slow axis microstructured eyelet (orange dashed); fast axis eyelet without microstructure (yellow dash dotted); slow axis eyelet without microstructure (purple dotted). Grating characteristics: $\Lambda = 0.5349 \mu\text{m}$, $\Delta n_{\text{FBG}} = 3 \times 10^{-4}$, $L = 2000 \mu\text{m}$ [35].

In theory, it is possible to measure temperature as well, but the proposed design specifically focuses on isothermal stresses. It is clear that the proposed device exhibits sensitivity to stress in all directions. To perform triaxial stress detection, the linear model proposed in [194], [195] should be exploited. In this way, the stresses in the host material can be effectively derived from measured wavelength shift $\Delta\lambda$ making use of stress transfer matrix and sensitivity matrix [194], [195].

Table 3.2.6 Sensitivity to stress along x axis σ_x .

Parameter	Symbol	Value	Unit
Fast axis eyelet without microstructure	$K_{x,f}$	8.88	pm/MPa
Fast axis microstructured eyelet	$K_{x,sm}$	8.86	pm/MPa
Slow axis eyelet without microstructure	$K_{x,s}$	8.85	pm/MPa
Slow axis microstructured eyelet	$K_{x,sm}$	8.91	pm/MPa

Table 3.2.7 Sensitivity to stress along y axis σ_y .

Parameter	Symbol	Value	Unit
Fast axis eyelet without microstructure	$K_{y,f}$	12.89	pm/MPa
Fast axis microstructured eyelet	$K_{y,sm}$	21.06	pm/MPa
Slow axis eyelet without microstructure	$K_{y,s}$	5.02	pm/MPa
Slow axis microstructured eyelet	$K_{y,sm}$	7.22	pm/MPa

Table 3.2.8 Sensitivity to stress along z axis σ_z .

Parameter	Symbol	Value	Unit
Fast axis eyelet without microstructure	$K_{z,f}$	-3.42	pm/MPa
Fast axis microstructured eyelet	$K_{z,fm}$	-2.19	pm/MPa
Slow axis eyelet without microstructure	$K_{z,s}$	-6.48	pm/MPa
Slow axis microstructured eyelet	$K_{z,sm}$	-3.85	pm/MPa

For a comparison with the state of the art, the longitudinal strain sensitivities along x axis of the sensor proposed in this research work are consistent with literature high performance solutions [194], [196] being equal to $S_x = 1.24 pm/\mu\epsilon$ for both eyelets and slightly higher than those reported in [11].

Generally, triaxial strain sensing reported in literature require complex approaches such as: i) the presence of different sensors embedded in the composite material or different positioning of the sensors for longitudinal, in-plane and out-of-plane monitoring [21]; ii) cascade of two FBGs in a single polarization-maintaining optical fiber, one of which is shielded by a capillary, to reduce transverse strains [196]; iii) use of two cascaded FBGs operating at different wavelengths [194]. In the aforesaid cases, i.e. for high birefringent fibers, the precise control of fiber rotation/mode polarization orientation during embedding process decreases the effective feasibility.

It is worth emphasizing that the importance of the microstructured flat optical fiber illustrated in this Section lies in its capability to utilize just one optical fiber sensor without requiring precise control of its orientation. The flat optical fiber shape mitigates the problem related to resin-rich regions of circular optical fibers. The inscription of a cascade of FBGs enables the possibility to map strains with high spatial resolution, exploiting wavelength division multiplexing. Therefore, the designed microstructured flat fiber paves the way for a feasible multi-axial structural health monitoring.

3.2.4 Conclusion

In this Section a new microstructured flat optical fiber, for multiparameter sensing within CFRP laminates, has been proposed. The microstructured pattern of air holes, positioned at a specific eyelet location, modifies the way strain is transferred between the composite laminate and the guiding region.

The strain-transfer and the electromagnetic modal analysis have led to the calculation of different transverse sensitivities for the two FBGs written in the eyelets. The relevant advantage introduced by the use of the designed microstructure is evident with regard to the slow and fast y axis sensitivities $K_{y,f} = 12.89 \text{ pm/MPa}$, $K_{y,fm} = 21.06 \text{ pm/MPa}$, $K_{y,s} = 5.02 \text{ pm/MPa}$, $K_{y,sm} = 7.22 \text{ pm/MPa}$, yielding to high sensitivity triaxial strain detection. Furthermore, the flat shape of this optical fiber simplifies the embedding process, minimizing the challenges associated with resin-rich areas found in circular optical fibers and the alignment of highly birefringent optical fibers.

Future work shall include testing of microfeatured flat fibers with few holes in order to validate the strain response. In the following, the exploration of more complex microstructures, such as the one examined in this Section, will be the focus of experimental research.

3.3 Effects of Curvature on Flexible Bragg Grating in Off-Axis Core: Theory and Experiment

By using silica glass, a flexible Bragg grating in planar technology is designed, fabricated, and experimentally characterized for high curvature monitoring. Theoretical explanations and experiments explain the mechanism for sensing curvature when the core is slightly off-axis. Conformal mapping, modal analysis, and CMT are employed to investigate the electromagnetic behavior of the proposed sensor. The experimental measurement reveals different sensitivities to positive and negative curvatures. The reflection spectrum of the planar Bragg grating sensor and the relationship between its resonant wavelengths and the curvature is measured for a large curvature range up to $1/R = \pm 33m^{-1}$. The interest toward off-axis core on planar flexible platform for curvature monitoring is due to the lateral stiffness and low Young's modulus of the substrate. The following paragraphs are organized as follows: in Section 3.3.1, the simulation approach; Section 3.3.2, the sensor design, fabrication, and spectrum measurement; Section 3.3.3, the comparison between numerical and experimental results; Section 3.3.4, the prospects, and conclusion.

3.3.1 Simulation approach

In general, standard optical FBG sensors exhibit low sensitivity to curvature. However, when non-symmetrical configurations are introduced, such as an off-axis core, the spectral response of the Bragg grating is notably influenced by curvature. The curvature induces a stress distribution within an optical waveguide, a variation of its refractive index distribution (due to the stress-optic effects) and a shift of the electromagnetic mode field profile. These effects together lead to changes in the interaction between the optical modes coupled by the Bragg grating. According to Section 2.2.3, conformal mapping and the well-known CMT can be used to study the interaction between the propagating modes. The modified refractive index distribution n_s is employed to calculate the electromagnetic fields distributions of the fundamental and high order propagating modes, via 2D-FEM. The transversal electromagnetic field distributions are calculated both for the straight and curved waveguide. As a result, the transversal electromagnetic field profile of the propagating modes, within the curved optical waveguide, shifts toward the region with higher refractive index [9]. The link between the Bragg grating's spectral response and the curvature C can be

explained using the CMT. Before solving the CME, the transversal coupling coefficients $K^t(z)$ are calculated for all the propagating modes travelling in the positive $+z$ and negative $-z$ direction [9]:

$$K_{\pm}^t(z) = \frac{w}{4} \iint_{core} \Delta\epsilon(x, y, z) E_{\pm}^t(x, y, z) \overline{E_{\mp}^t}(x, y, z) dx dy \quad (3.3.1)$$

where w is the angular frequency of the propagating light and $\Delta\epsilon(x, y, z)$ is the dielectric perturbation which is dependent on curvature C , and related to the imposed refractive index modulation [197]; $E^t(x, y, z)$ is the transversal electromagnetic field profile depending on curvature C . The CMT longitudinal coupling coefficients $K^z(z)$, are two orders of magnitude smaller than transversal ones $K^t(z)$, therefore they are neglected. Finally, the CMT equations can be solved.

Moreover, if the Bragg grating is located outside the neutral plane, the nominal Bragg grating pitch Λ_0 changes as $\Lambda = \Lambda_0(1 + e_z)$. Generally, for e_z calculation, x_{proj} corresponds to the distance between the center of the Bragg grating and the neutral plane, defined as core offset d (more details in Section 2.2.3) [152]-[154]. When the distance d is equal to or less than the core size of the optical waveguide, this approximation is no longer valid. In this instance, the mode coupling calculation must take into account the shifting of the electromagnetic field profile of the propagating modes toward the region with greater refractive index. [198], [143], [152]-[154]. The simulation approach employed for the design is summarized as follows: i) conformal mapping in order to describe the curved waveguide with an equivalent one, ii) 2D-FEM to compute the electromagnetic mode analysis of the equivalent waveguide, iii) calculation of the coupling coefficient $K_{\pm}^t(z)$ [140], iv) implementation of the CMT as a boundary value problem to evaluate counter-propagating modes powers. The procedure is repeated for each wavelength λ in the range of interest, with a defined wavelength step $\Delta\lambda$, and for each curvature value C . The method used is precise, and adaptable to any type of multimode optical waveguide. Approximated investigations use simplified equations without CMT or take into account a Gaussian beam with a closed form equation [51], [62], [199], [198].

3.3.2 Design and fabrication of the sensor

3.3.2.1 Sensor design

The aim of the design is to investigate a curvature sensor's response by employing a slightly off-axis core. To avoid the orientation issue, common in unidirectional curvature sensing with cylindrical optical fiber, the planar technology was adopted. It is possible to realize the geometrical and physical properties of the proposed device by using physical machining and flame hydrolysis deposition [200]. In order to make more evident the effect of electromagnetic modes profile shift, a few-mode waveguide is chosen. Figure 3.3.1 reports a not to scale sketch of the designed planar Bragg grating sensor. The core thickness $t_c = 19.5 \mu\text{m}$ is larger than the core width $w_c = 14.5 \mu\text{m}$, leading to great electromagnetic modes shift along the x axis, see Fig. 3.3.1. The other geometrical parameters are width $w_p = 1 \text{ mm}$, thickness $t_p = 57 \mu\text{m}$, core offset $d = 1.2 \mu\text{m}$. The thickness t_p is thin enough to reduce surface stresses and thick enough to avoid evanescent field exposure.

The underclad and overclad silica glass regions have identical composition with a refractive index $n_{clad} = 1.444$ at the wavelength $\lambda = 1570 \text{ nm}$. Step-index profile is assumed for both the core layer and the waveguide. In particular, the refractive index of the core layer is $n_{core,l} = 1.4633$ and of the waveguide is $n_w = 1.4713$ at the wavelength $\lambda = 1570 \text{ nm}$. The wavelength dispersion is modelled via proper Sellmeier equation [201]. The effective refractive indices of all propagating modes and electromagnetic field profiles are modelled using FEM and taken into account in the CMT equations. The effective refractive index of the fundamental mode, simulated via FEM, is $n_{eff} = 1.4712$ at the wavelength $\lambda = 1570 \text{ nm}$ when the sensor is not subjected to curvature C .

The designed uniform Bragg grating has a sinusoidal modulation with an amplitude $\Delta n_{BG} = 2 \times 10^{-4}$ and a length $L = 12 \text{ mm}$. The nominal grating period Λ_0 , when the planar sensor is not subjected to curvature C , is $\Lambda_0 = 0.534 \mu\text{m}$. This value is designed to obtain the mode matching between the forward and backward fundamental mode around the wavelength $\lambda = 1570 \text{ nm}$.

The curvature C determines a shift of the electromagnetic field of the propagating modes towards the waveguide region with higher refractive index, as discussed in Section 3.3.1. As an example, Fig. 3.3.2 reports the shift of electric field norm E of the fundamental mode for curvature $C = [0 \text{ m}^{-1}, \pm 33 \text{ m}^{-1}]$.

The simulation is carried out in the wavelength range λ from 1565 nm to 1574 nm with a wavelength step $\Delta\lambda = 5 \text{ pm}$.

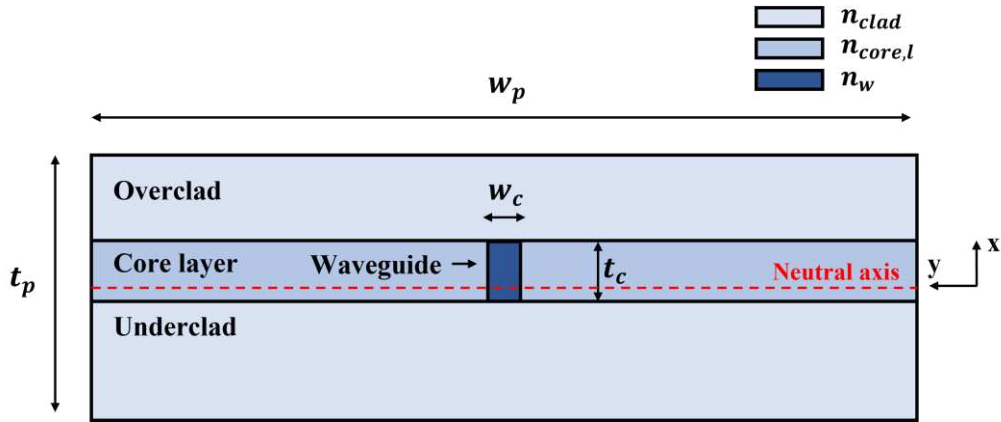


Figure 3.3.1 Sketch of the designed planar Bragg grating sensor. The waveguide in which the grating is inscribed (blue colored) is written in the central core layer and it is slightly off-axis with respect to the neutral axis [67].

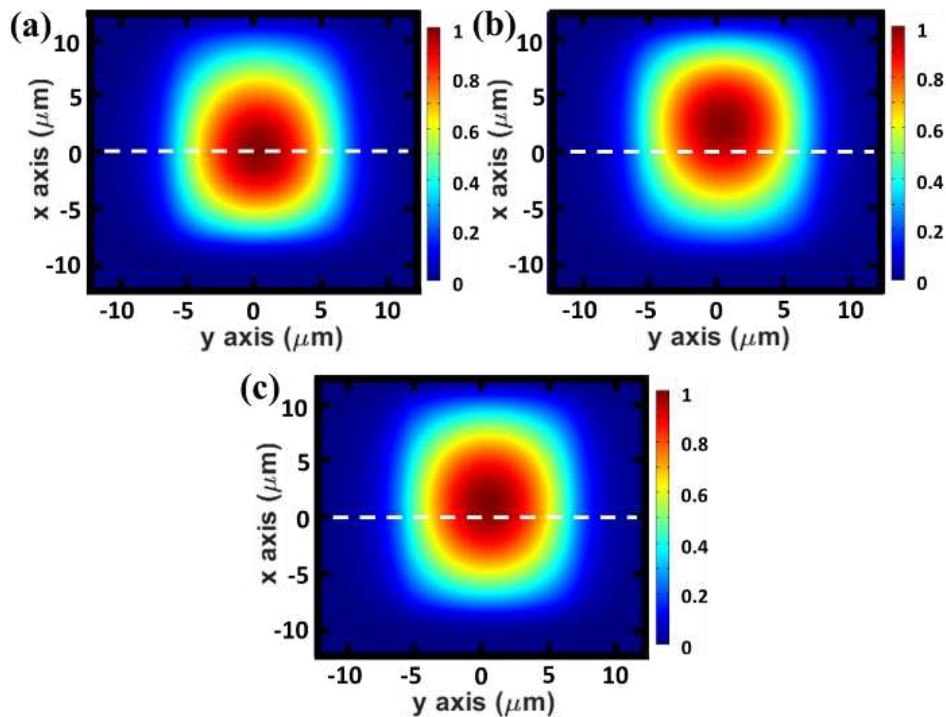


Figure 3.3.2 Norm of the electric field E of the fundamental mode for: (a) curvature $C = -33 \text{ m}^{-1}$, (b) curvature $C = 33 \text{ m}^{-1}$, (c) curvature $C = 0 \text{ m}^{-1}$ [67].

The simulated reflection spectrum when the planar Bragg grating is not curved is reported in Fig. 3.3.3. The UV written waveguide is few-mode. The spatial modes are classified as E_{lm} modes, where l and m depends on the number of

maxima and minima of the electric field distributions along the y axis and x axis of the rectangular core [202].

Four propagating modes interacts with the Bragg grating inducing multiple resonant wavelengths, marked as P1, P2, P3, P4, corresponding to the spatial modes E_{11} , E_{21} , E_{31} , E_{32} , respectively. For the sake of simplicity, the inset of Fig. 3.3.3, shows only one of the nearly degenerate orthogonal polarizations, E_{lm}^y .

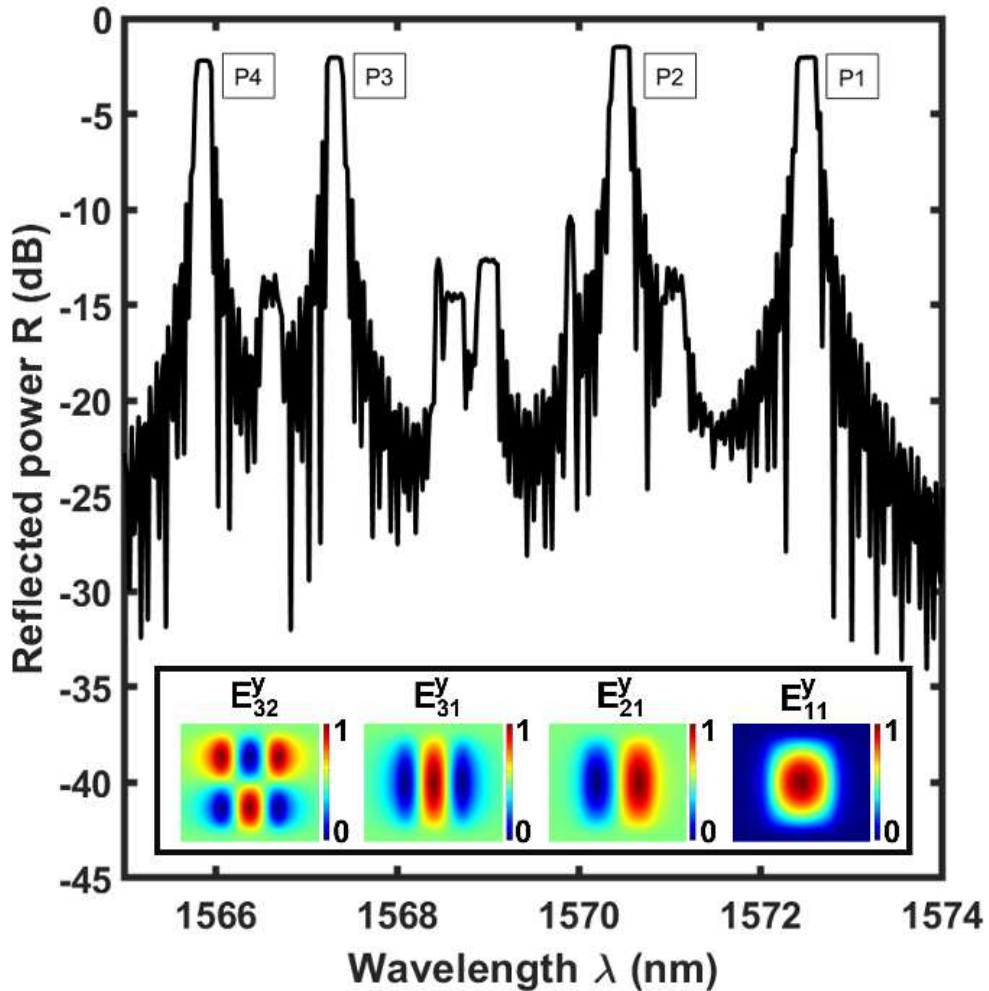


Figure 3.3.3 Simulated reflection spectrum of the planar Bragg grating sensor when no curvature C is applied; length of the Bragg grating $L = 1.2\text{ mm}$, refractive index modulation of the Bragg grating $\Delta n_{BG} = 2 \times 10^{-4}$. In the inset, the y component of the electric field for y polarized modes E_{11}^y , E_{21}^y , E_{31}^y , E_{32}^y [67].

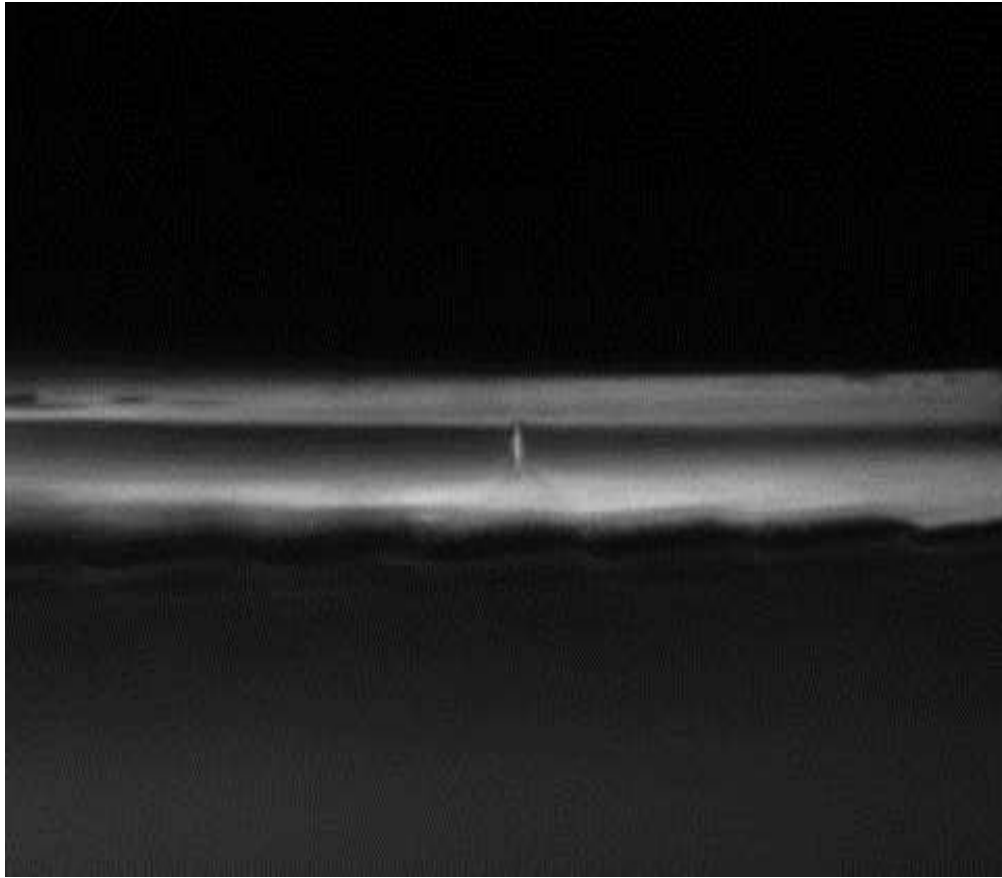


Figure 3.3.4 Enlargement of the cross section of the planar Bragg sensor captured via CCD camera [67].

3.3.2.2 Sensor fabrication and spectrum measurement

Flame Hydrolysis Deposition (FHD) is made upon a sacrificial p-doped [1 0 0] silicon wafer with diameter $d_{Si} = 152\text{ mm}$. Three doped silica layers: overclad, core and underclad are deposited and the silicon is later removed through physical machining, leaving a flexible glass substrate with a nominal thickness $t_p = 57\text{ }\mu\text{m}$. Figure 3.3.4 shows an image of the cross-section of the planar sensor captured through a CCD camera.

The overclad, core and underclad are clearly distinguishable. Due to the physical machining used to remove the silicon wafer, underclad does not have a constant thickness.

Direct UV writing is employed to inscribe the few-mode waveguide and the uniform Bragg grating in the core layer.

The planar sensor is coupled to a cylindrical optical fiber using UV-curable adhesive, as shown in Fig. 3.3.6. The planar Bragg grating reflection spectrum was evaluated using an optical spectrum analyzer. Four resonant wavelengths are

apparent in Fig. 3.3.5 due to the few guided modes. The different reflected powers depend mainly on i) the mode power distribution in the few-mode waveguide; ii) the corresponding coupling coefficients $K_{\pm}^t(z)$. Furthermore, an unwanted Bragg grating chirping is evident, induced by UV writing. The simulated and measured resonant peaks are in good agreement.

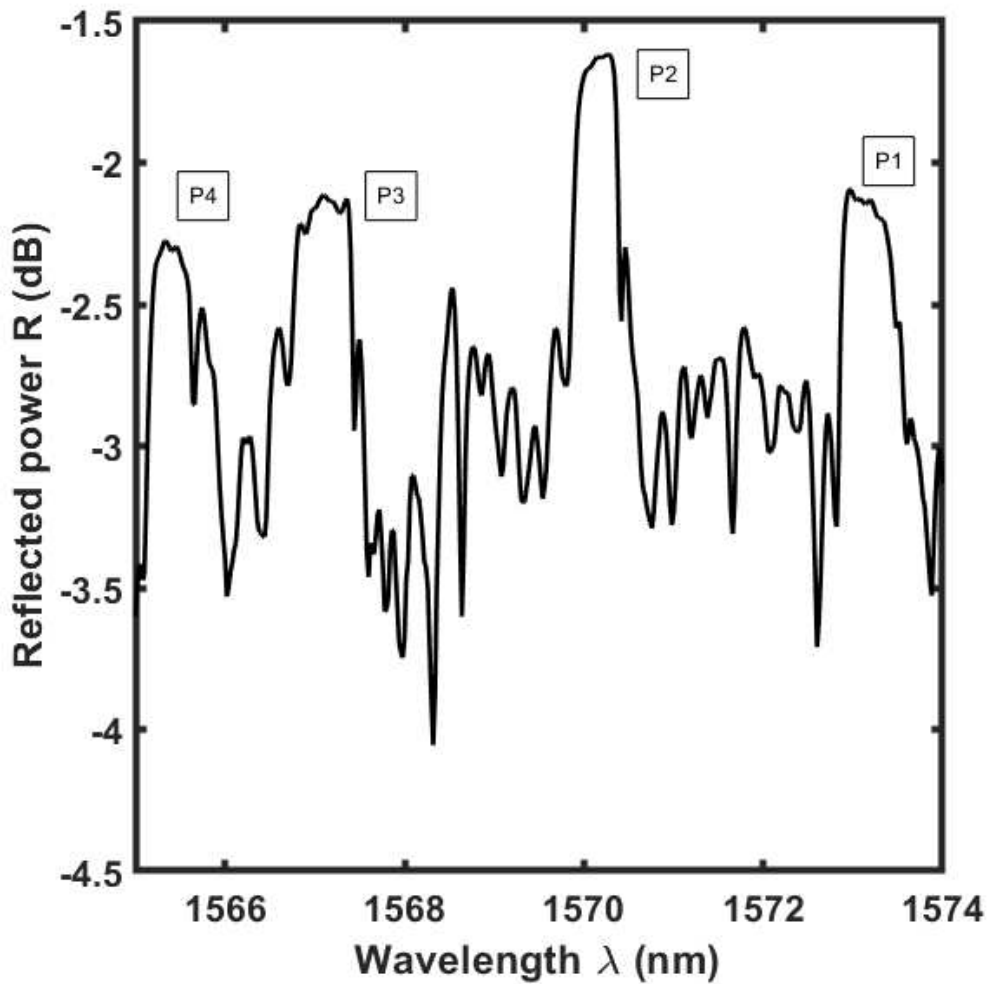


Figure 3.3.5 Measured reflection spectrum of the planar Bragg grating sensor when no curvature C is applied; length of the Bragg grating $L = 1.2 \text{ mm}$, refractive index modulation of the Bragg grating $\Delta n_{BG} = 2 \times 10^{-4}$ [67].

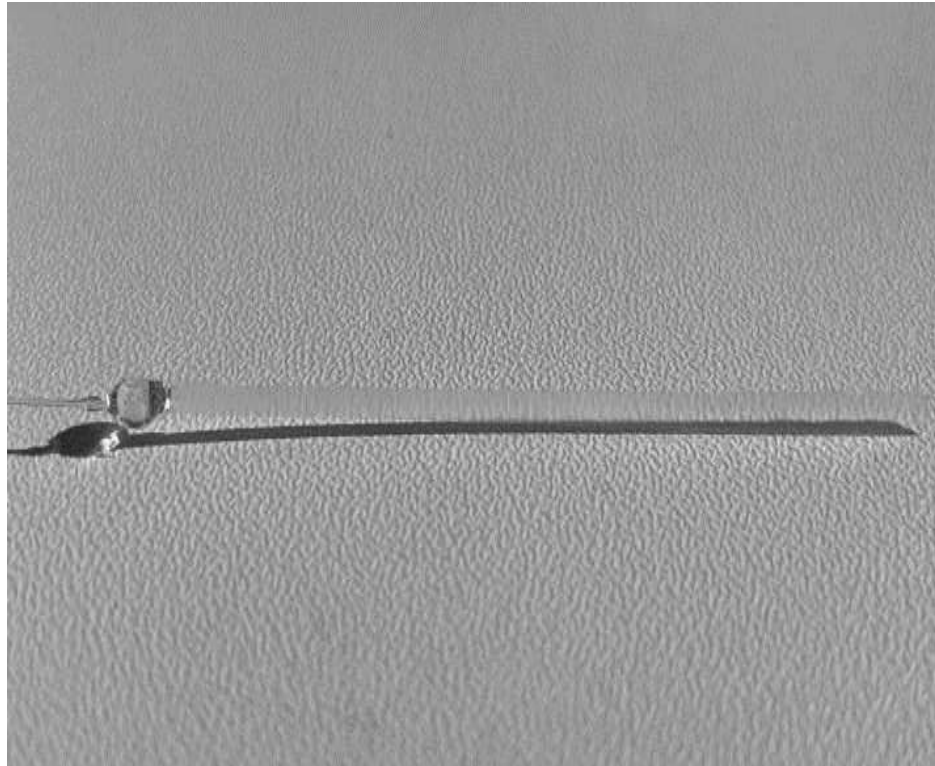


Figure 3.3.6 Planar Bragg sensor butt-coupled to a cylindrical optical fiber through UV curable adhesive [67].

3.3.3 Curvature effect

Different values of curvature C have been taken into account while accounting for both positive and negative curvature orientations. For comparison between simulation and experiment, the considered curvature values are: $C = 0 \text{ m}^{-1}, \pm 8.5 \text{ m}^{-1}, \pm 16 \text{ m}^{-1}, \pm 23 \text{ m}^{-1}, \pm 28 \text{ m}^{-1}, \pm 33 \text{ m}^{-1}$. In order to characterize the sensor response to curvature C , it is important to vanish the influence of cross-sensitivities induced by temperature and/or spurious strain not directly related to curvature C . The measurements are done in a temperature-controlled environment to achieve this goal. A mount and a motorized stage are employed to perform curvature C measurement and particular attention is paid to avoid that the clamping could affect the planar Bragg grating spectral characteristics. Furthermore, the use of mount and motorized stage suppresses any unintentional twisting effect.

The Bragg wavelength shift $\Delta\lambda_B$ is measured as the difference between the resonance peak when the sensor is subjected to curvature C and the resonance peak when the sensor is not curved in order to account for any effects of temperature. High resolution measurements are performed with a Bayspec FBGA

optical spectrometer rather than an optical spectrum analyzer. The spectrometer allows the detection of peaks P3 and P4 ensuring a minimum detectable wavelength change of $r = \pm 1 \text{ pm}$. A sketch of the adopted experimental set-up is reported in Fig. 3.3.7. The measured Bragg wavelength shift $\Delta\lambda_B$ (black squares) as a function of curvature C are reported in Fig. 3.3.8 for peak P3 and in Fig. 3.3.9 for peak P4 showing good agreement with numerical results. Both the characteristics of Fig. 3.3.8 and Fig. 3.3.9 show an almost linear characteristic for positive curvature C values.

In particular, for positive values of curvature C , the electromagnetic field shifts toward the outer half of the planar Bragg grating sensor. It is mainly subjected to tensile strain ϵ_z , which linearly increases with curvature C . The linearized sensitivity for positive values of curvature C is $S_{P3}^+ = 5.9 \text{ pm/m}^{-1}$ for the peak P3 and $S_{P4}^+ = 5.2 \text{ pm/m}^{-1}$ for the peak P4. The reason for the dissimilar values of linearized sensitivity S^+ is due to the difference in the effective refractive indices between the straight and curved planar Bragg grating sensor for each mode. The difference in the effective refractive indices for peak P3 is greater than for peak P4, causing the Bragg wavelength shift of the peak P3 to be larger than that of the peak P4. This is directly influenced by the mode profile being considered. Decreasing the value of curvature C , the electromagnetic field shifts in the opposite direction toward the centre of the planar sensor. In particular, when the curvature C is slightly negative, the electromagnetic field is affected by the compressive strain ϵ_z effect. By further decreasing the curvature C , the electromagnetic field intercepts the neutral plane, where no strains along the principal axes occur, and the sensitivity becomes zero, around $C = -23 \text{ m}^{-1}$. As the curvature C becomes more negative, the electromagnetic field marginally extends beyond the neutral plane and tensile strain ϵ_z is experienced. Therefore, the combined effect of cross-sectional refractive index change and tensile strain ϵ_z on the grating period Λ , leads to a reversal of the slope.

In conclusion, with positive curvature C values, the electromagnetic field gradually moves toward the device's outer half, where more tensile strain e_z occurs;

for negative values of curvature C , the electromagnetic field shifts from the inner half, where the compressive strain e_z occurs, toward the outer half of the device, where there is a tensile strain e_z .

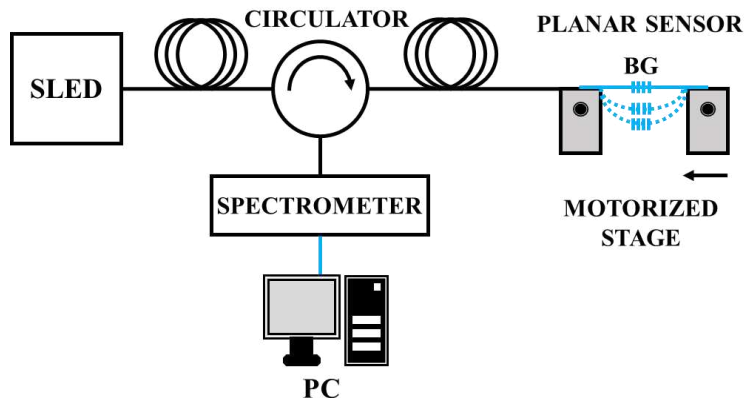


Figure 3.3.7 Experimental set-up adopted for the curvature measurement of the planar Bragg grating [67].

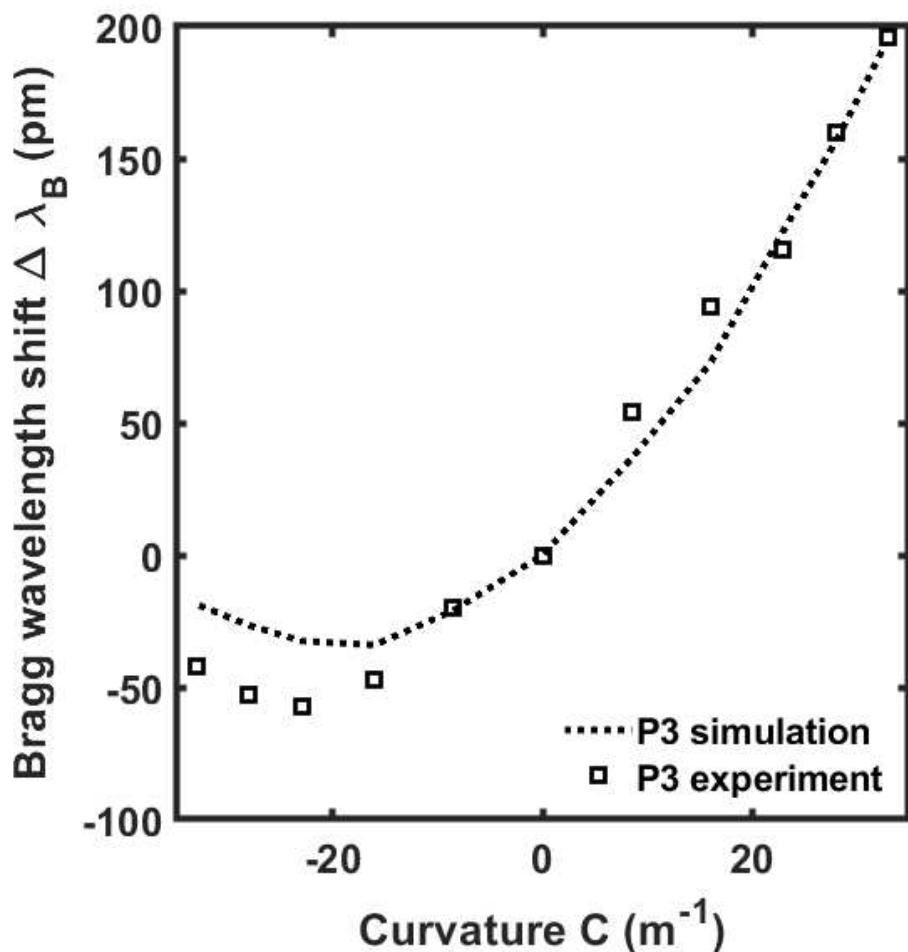


Figure 3.3.8 Simulated (dotted line) and measured (square markers) Bragg wavelength shift $\Delta\lambda_B$ of the resonance peak P3 for curvature $C = 0 \text{ } m^{-1}, \pm 8.5 \text{ } m^{-1}, \pm 16 \text{ } m^{-1}, \pm 23 \text{ } m^{-1}, \pm 28 \text{ } m^{-1}, \pm 33 \text{ } m^{-1}$ [67].

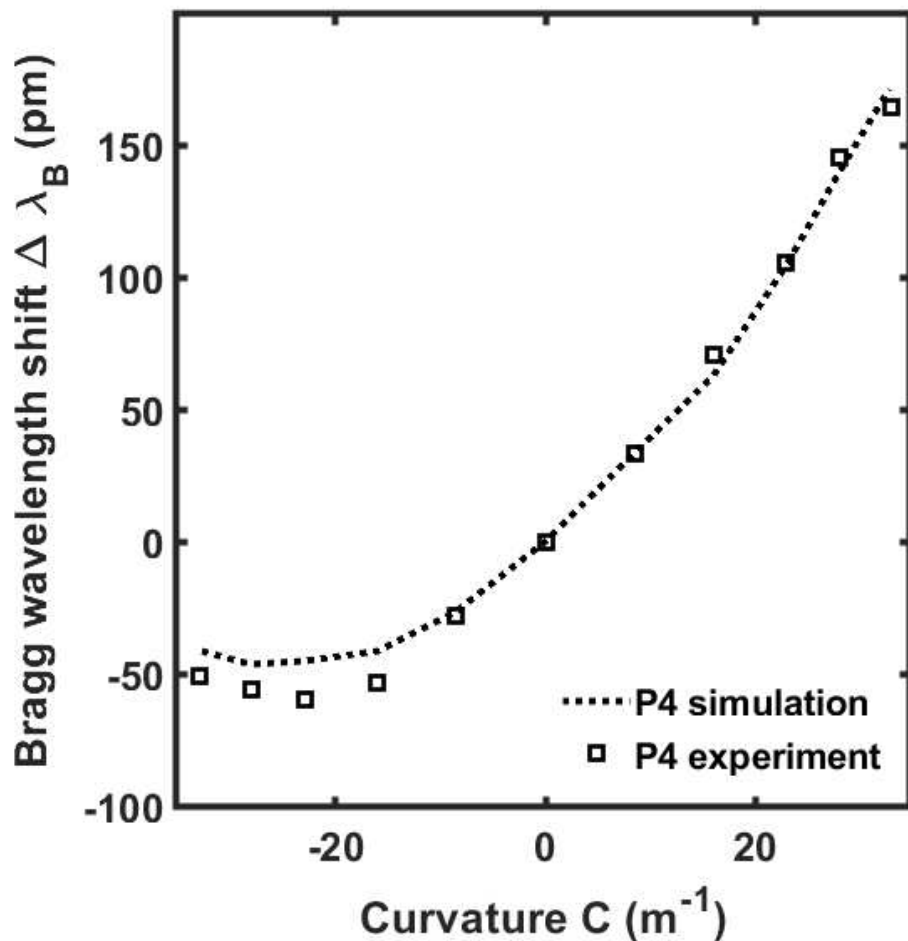


Figure 3.3.9 Simulated (dotted line) and measured (square markers) Bragg wavelength shift $\Delta\lambda_B$ of the resonance peak P4 for curvature $C = 0 \text{ m}^{-1}, \pm 8.5 \text{ m}^{-1}, \pm 16 \text{ m}^{-1}, \pm 23 \text{ m}^{-1}, \pm 28 \text{ m}^{-1}, \pm 33 \text{ m}^{-1}$ [67].

3.3.4 Conclusion

For the first time, an ultra-thin, flexible silica planar Bragg grating-based high curvature sensor is designed, fabricated, and experimentally characterized. The shift of the resonant wavelength for different curvatures are explained by means of CMT-based code. The experimental results agree with simulation and are reported for high curvature up to $\pm 33 \text{ m}^{-1}$, showing an excellent mechanical robustness also with respect to the optical fiber solution. The device exhibits different sensitivities when positive and negative curvatures are applied. This is theoretically explained with a discussion on the longitudinal strain to which the Bragg grating is subjected. This concept finds applications also in curvature

direction and radius sensing in multicore optical fibers. Future sensors and reconstruction algorithm can be engineered taking into account the demonstrated principle, leading to a better shape reconstruction. The chosen planar photonic platform is suitable for a novel generation of photonic sensing devices due to the ability to change the geometry and the position of the waveguides as well as the absence of orientation issues typical of cylindrical optical fiber.

3.4 Flexible Photonic Sensors: Exploiting Ratiometric Power in Few-Mode Waveguides for Bending Inference

In this Section, the use of ratiometric power change in a few-mode optical waveguide is proposed as a distinctive method to measure the degree of bending via flexible photonics devices. To demonstrate its feasibility, a sensor exploiting a Bragg grating, approximately aligned to the neutral axis, is designed, fabricated and characterized. The optical confinement requirements are the only factor limiting the proposed planar photonic sensor's reduced thickness, allowing for an extremely thin and highly flexible planar device built on an all-glass substrate. FEM, Beam Propagation Method and CMT are employed in the design to model the electromagnetic and mechanical phenomena occurring during the three-point bending test. The experiment demonstrates that the planar device withstands tight curvature without mechanical failure. The device shows that by increasing the bending the reflected power from the fundamental mode decreases but the reflected power from the higher order mode increases. The measured ratiometric power sensitivity versus displacement is $K_{P_R} = -0.78 \text{ dB/mm}$ with negligible variation over a 40°C thermal range. The proof of concept of the flexible photonic bend sensor is reported in Fig. 3.4.1. The suggested sensor can be used for multiparameter sensing applications, such as simultaneous temperature and curvature monitoring, by utilizing both the Bragg wavelength shift and the mode optical power change. The following paragraphs are organized as follows: Section 3.4.1 illustrates the electromagnetic design and mechanical performance investigation of the sensor; Section 3.4.2 describes the sensor fabrication and the comparison between numerical and experimental results; Section 3.4.3 provides the conclusions and the discussion on the future prospects.



Figure 3.4.1 Flexible planar photonic chip in doped silica fabricated through Flame Hydrolysis Deposition [68].

3.4.1 Electromagnetic and mechanical modeling

3.4.1.1 Design approach

Using the COMSOL Multiphysics® Wave Optics module, a 2D-FEM electromagnetic modal analysis is used for the design of the flexible photonic sensor. In order to simulate the three-point bending test, a 3D-FEM model of the flexible photonic sensor is made using the COMSOL Multiphysics® Structural Mechanics module. The optical response of the Bragg grating, under three-point bending, is investigated through electromagnetic and mechanical analyses. The mechanical analysis allows to determine the maximum displacement, the curvature profile, and the strain distribution. The calculated curvature profile is used in the 3D-BPM modeling (Beam Propagation Method, BeamProp®-RSOFT Design®) to assess power mode mixing in addition to the CMT. It is well known that in multimode waveguides, bending induces mode coupling and optical power exchange amongst other phenomena. The strain distribution, the electromagnetic field profile, and the powers of the propagating modes are employed as inputs to an in-house MATLAB® code based on CMT [144]. This combines the influence of the bending on refractive index distribution, grating period, and coupling

coefficients. CMT is exploited to compute the reflection spectra and the Bragg wavelength shift of the gratings [67].

Following the aforementioned approach, three Bragg gratings, namely #G1, #G2, and #G3, are designed. An exhaustive electromagnetic investigation is focused on the Bragg grating #G2, constituting the flexible sensor, which is subjected to an almost constant curvature along the entire grating length. The numerical findings support the experiment and provide an explanation for the optical response of #G2 and the other two Bragg gratings, #G1 and #G3, which were designed and fabricated exclusively to better understand the sensor behavior.

3.4.1.2 Electromagnetic design and modal investigation

By exploiting an off-axis core and detecting the Bragg wavelength shift, FBGs may be used to infer the degree of bending. A channel waveguide with two propagating modes is fabricated to investigate the capability of the sensor for the monitoring of two parameters, such as the temperature and curvature. The electromagnetic design of the flexible photonic sensor with a slight off-axis core is carried out. Figure 3.4.2 shows a not-to-scale sketch of the flexible sensor cross-section. The total thickness is $t_{fp} = 60 \mu\text{m}$ and the total width is $w_{fp} = 1 \text{ mm}$. The thickness t_{fp} is chosen as a trade-off, to provide both a low level of surface stress and a suitable electromagnetic field confinement when the sensor is bent. The sensor is multi-layered, comprising overclad, core, and underclad. The core layer is offset by $1.5 \mu\text{m}$ from the central neutral axis of the sensor, with the underclad thickness being slightly larger than the overclad. The channel waveguide is rectangular, and it is written within the core layer. Its width is $w_{wg} = 7 \mu\text{m}$ and its thickness is identical to the one of the core layer, $t_{co} = t_{wg} = 9 \mu\text{m}$. The underclad and overclad layers are made of identical silica glass composition and uniform refractive index distribution $n_{cl} = 1.4452$ at the wavelength $\lambda = 1553 \text{ nm}$. The core layer refractive index is $n_{co} = 1.4645$ at the wavelength $\lambda = 1553 \text{ nm}$. At the same wavelength, the channel waveguide refractive index is $n_{wg} = 1.4695$, obtainable by adopting direct UV Writing (DUW) manufacturing technique. Both the core layer and the channel waveguide have a step-index profile distribution. A suitable Sellmeier equation is employed to model the refractive index wavelength dispersion [201]. The norm of the electric field E of the fundamental and high (second) order mode, i.e. the spatial modes E_{11}, E_{21} , is reported in Fig. 3.4.3.

3.4.1.3 Mechanical investigation: three-point bending test

The multi-layered glass platform described in Section 3.4.1.2 and having a length $L_{fp} = 60$ mm, see Fig. 3.4.4 (a), is 3D-modeled in order to quantitatively examine the sensor response to the three-point bending test.

The employed mechanical parameters, such as Poisson's ratio $\nu = 0.17$ and Young's modulus E_{cl} , have been measured through nano-indentation tests [9]. The underclad and overclad compositions are identical, with Young's modulus $E_{cl} = 40$ GPa. The core layer is stiffer than the cladding layers and its Young's modulus is $E_{co} = 62$ GPa. According to the schematic in Fig. 3.4.4 (a), (b), the 3D-FEM model's boundary conditions and applied forces are set. The three Bragg gratings, designated as #G1, #G2, and #G3, as well as the location where the force F is applied, are shown in a schematic of the set-up in Fig. 3.4.4 (b). A fixed constraint condition is applied on the left boundary of the flexible photonic sensor, while, on the right, a simply supported boundary condition is imposed. The force F acts perpendicularly to the longitudinal axis (z-axis), at the centre of the Bragg grating #G2. A free tetrahedral mesh is employed, consisting of $M_{3D-FEM} = 168442$ domain elements. Three-point bending test is simulated by considering the force values $F_i = [0 \text{ mN}, 3.3 \text{ mN}, 6.6 \text{ mN}, 9.8 \text{ mN}, 12 \text{ mN}]$ with $i = 1 \rightarrow 5$.

The simulated maxima displacements d_{sim} , for each force value F_i , are respectively $d_{sim} = [0 \text{ mm}, 3 \text{ mm}, 6 \text{ mm}, 9 \text{ mm}, 11 \text{ mm}]$. Figure 3.4.5 plots the simulated displacement of the flexible photonic sensor versus its length L_{fp} due to the force F_5 , i.e. the maximum applied force value. Moreover, Fig. 3.4.5 shows the curvature sign according to the convention used. The displacement d_{sim} obtained from the 3D-FEM model (black solid curve) perfectly agrees with that obtained by classical beam theory (red dotted markers) [203]. The 3D-FEM approach allows a multiphysics investigation including the internal strain calculation. Figure 3.4.6 illustrates the curvature radius C_R as a function of the cumulative arc length S , for the case of maximum displacement $d_{sim} = 11 \text{ mm}$. The curvature radius is evaluated by considering the curvature equation $C_R = |(1 + \dot{y}^2)^{\frac{3}{2}}/\ddot{y}|$ where \dot{y} and \ddot{y} are the first and second order derivative of the displacement profile function. The values of the curvature radius C_R , are then used for 3D-BPM modeling.

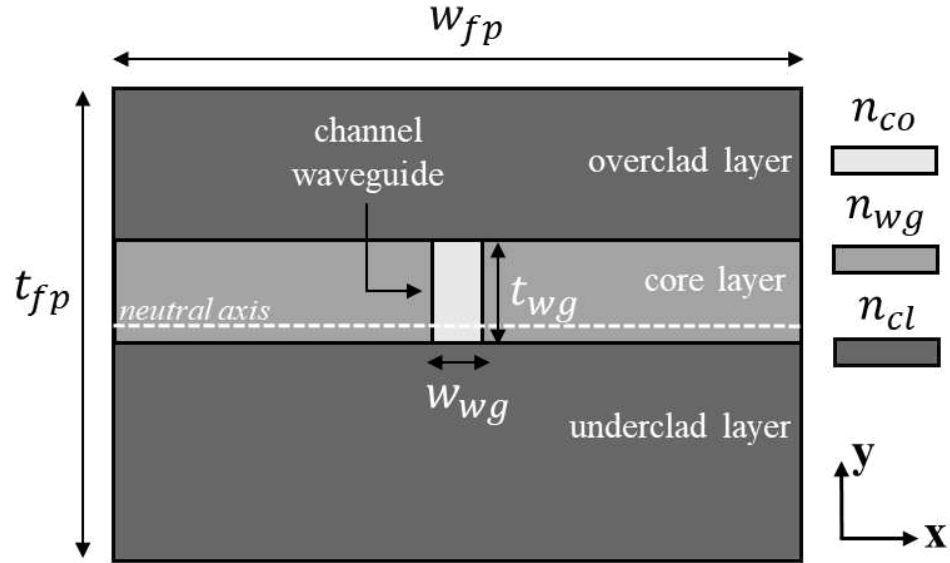


Figure 3.4.2 Sketch of the flexible sensor. The channel waveguide (light gray colored), in which the gratings are inscribed, is written in the central core layer and it is slightly off-axis with respect to the neutral axis [68].

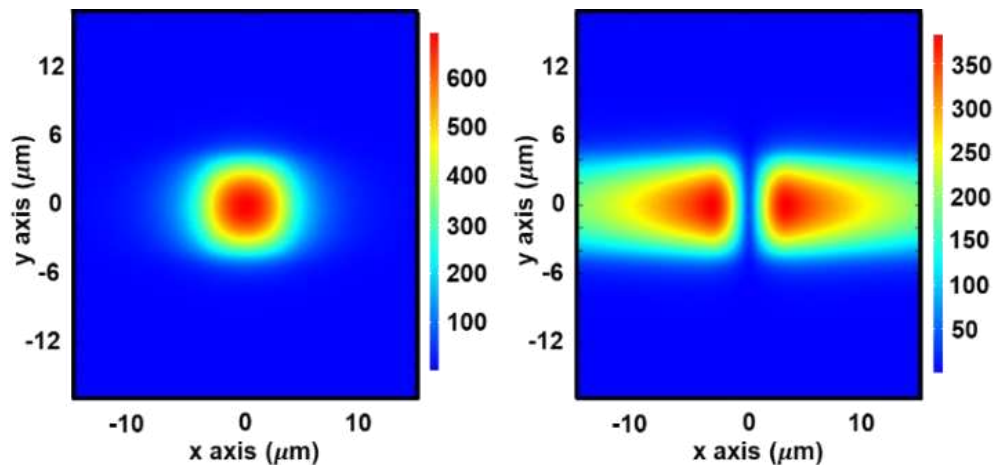


Figure 3.4.3 Norm of the electric field E of the fundamental E_{11} and high order mode E_{21} . The coordinates (0; 0) refer to the center of the waveguide [68].

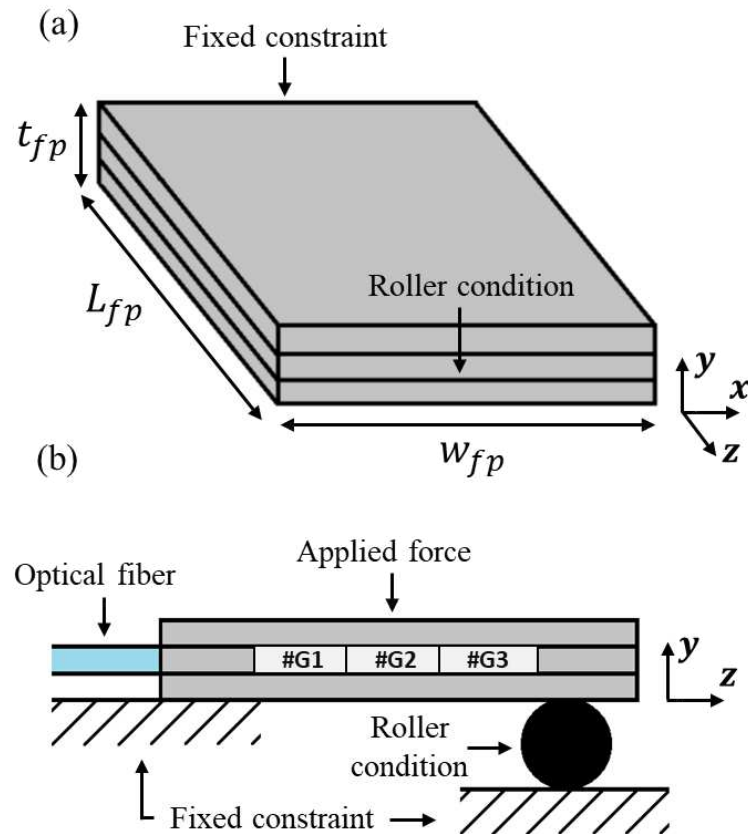


Figure 3.4.4 (a) Sketch of the boundary conditions and applied forces to the 3D-FEM modeled flexible photonic sensor for three-point bending test simulation; (b) schematic representation of the set-up and Bragg grating locations [68].

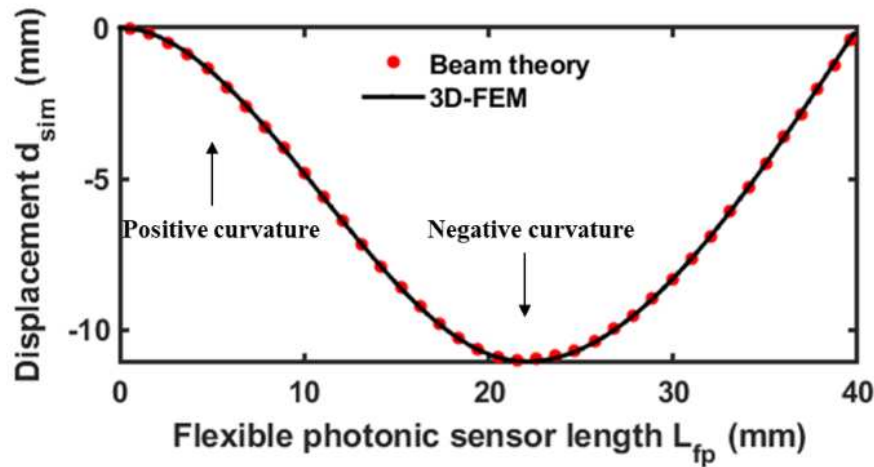


Figure 3.4.5 Displacement profile as a function of the flexible photonic sensor length L_{fp} considering the applied force F_5 [68].

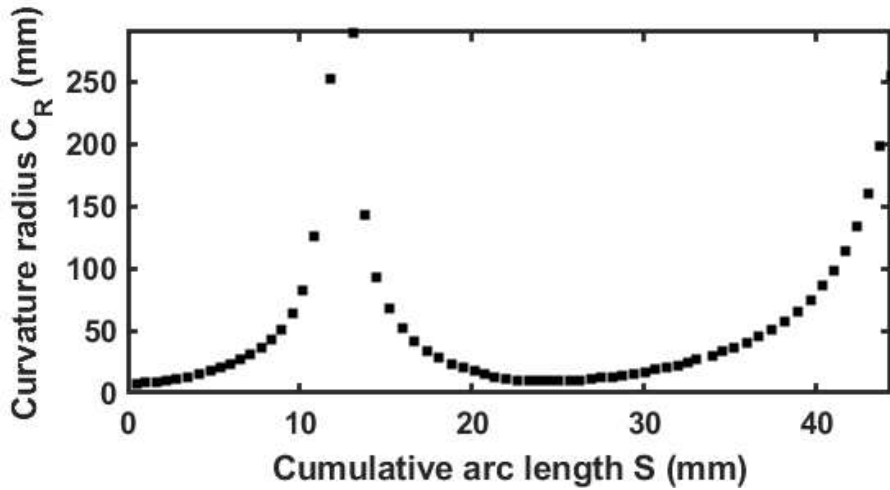


Figure 3.4.6 Curvature radius C_R vs cumulative arch length S considering the applied force F_5 [68].

3.4.1.4 Power mode mixing

Using 3D-BPM, which makes use of the conformal mapping technique, the optical power exchange between the propagating modes in a bent optical fiber/waveguide is examined [62]. The conformal mapping is used to map the cross-sectional refractive index n_c of a curved optical waveguide, into a straight one. If the size of the flexible photonic sensor is very small compared to the applied curvature radius C_R , a straight equivalent waveguide, with a novel cross-sectional refractive index $n_m = n_c (1 + x_p/C_R)$, can be modeled [62], [204]. The distance from the optical waveguide centre is indicated with x_p , while, n_c is the cross-sectional refractive index when the sensor is unperturbed, i.e. not bent. 3D-BPM approach does not consider the effect caused by the strain field on the refractive index n_c . When evaluating the Bragg grating spectra in Section 3.4.1.5, stress-optic relations are used to account for this additional effect [206]. For each value of d_{sim} , the curvature radius C_R versus the cumulative arc length S is exploited by 3D-BPM to calculate the cross-sectional refractive index n_m and to assess the power mode mixing. A Gaussian beam profile is taken into consideration as an input optical field to model the butt coupling with a single mode optical fiber. The grid resolution of the simulation is $M_{BPM,t} = 0.1 \mu\text{m}$ and $M_{BPM,l} = 0.25 \mu\text{m}$ respectively for transverse (x-y axis) and longitudinal direction (z axis). By considering the maximum displacement $d_{sim} = 11 \text{ mm}$, the power mode mixing investigation for the grating #G2 demonstrates (as it will be shown in the following Section) that the simulated peak power $P_{s,hom}$ of the high order mode increases of $\Delta P_{s,hom} = 3.4 \text{ dBm}$ at the expense of the peak power $P_{s,fun}$ of the fundamental mode.

3.4.1.5 Bragg grating spectrum evaluation

The 2D-FEM modal analysis is carried out by using the stress-optic relations and the strain distribution within the flexible photonic sensor, derived from the 3D-FEM mechanical investigation. To solve CMT, the transversal coupling coefficients $K^t(z)$ are calculated considering the effective refractive indices n_{eff} and the electromagnetic field profiles E of the two modes propagating along the z axis (along both positive and negative directions) [144]:

$$K_{\pm}^t(z) = \frac{w_f}{4} \iint_{core} \Delta\epsilon(x, y, z) E_{\pm}^t(x, y, z) \overline{E^t}(x, y, z) dx dy \quad (3.4.1)$$

where w_f is the angular frequency, $E^t(x, y, z)$ is the transversal electromagnetic field profile, $\Delta\epsilon(x, y, z)$ is the dielectric perturbation which relies on refractive index modulation. The 3D-BPM is employed to calculate the input power of the two guided modes in CMT model [144]. To compute the reflection spectrum of grating #G2, the approach is executed for each displacement d_{sim} ; the wavelength range is from $\lambda = 1514$ nm to $\lambda = 1520$ nm with a wavelength step $\Delta\lambda_{step} = 5$ pm. The effective refractive index of the fundamental mode is $n_{eff,fun} = 1.46618$ and that of the second order mode is $n_{eff,hom} = 1.46291$ at the wavelength $\lambda = 1553$ nm. The designed uniform Bragg grating has a sinusoidal modulation with an amplitude $\Delta n_{BG} = 2 \times 10^{-4}$ and a length $L = 12$ mm. When the sensor is not curved, the nominal grating period of #G2 is $\Lambda_{#G2} = 0.51774$ μm . This value is selected to obtain the mode matching between the forward and backward fundamental mode around the wavelength $\lambda = 1519$ nm. For completeness, the grating period of Bragg grating #G1, and #G3 were selected to obtain the resonant wavelengths of the fundamental mode at $\lambda_{#G1} = 1528$ nm and $\lambda_{#G3} = 1588$ nm.

Figure 3.4.7 reports the simulated reflection spectrum when grating #G2 is unperturbed and when a displacement $d_{sim} = 11$ mm is applied, respectively. Two resonant wavelengths are obtained as a result of the propagating modes' interactions with the Bragg grating #G2. Additionally, Fig. 3.4.7 demonstrates how the applied bending results in a blue shift of the resonant wavelengths as well as a power exchange between the two modes. The results demonstrate a variation of the Bragg wavelength for both the fundamental and high order mode, reaching the maximum Bragg wavelength shift $\Delta\lambda_{s,fun} = -250$ pm and $\Delta\lambda_{s,hom} = -240$ pm, respectively.

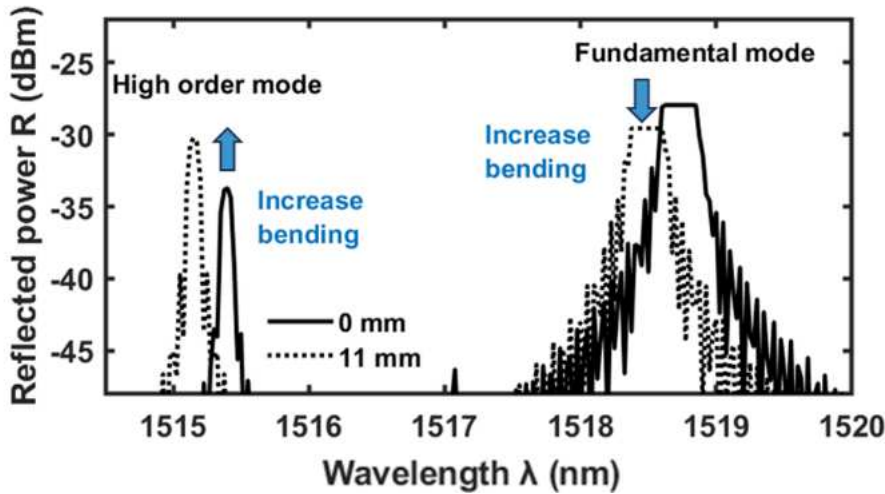


Figure 3.4.7 Simulated reflection spectrum of the Bragg grating #G2, unperturbed (solid curve) and with displacement $d_{sim} = 11$ mm (dotted curve); length of the Bragg grating $L = 12$ mm, refractive index modulation of the Bragg grating $\Delta n_{BG} = 2 \times 10^{-4}$ [68].

3.4.2 Fabrication and characterization

3.4.2.1 Fabrication and characterization

The flexible glass substrate is fabricated via FHD. On a stiff sacrificial silicon wafer, three doped silica layers (overclad, core, and underclad) are sequentially deposited (diameter $d_{sw} = 152$ mm, thickness $t_{sw} = 1$ mm, p-doped [1 0 0]). The silicon had a thermally grown wet oxide layer, of thickness $t_{wo} = 6 \mu\text{m}$, used to avoid chemical reaction between the deposited doped silica layers and the silicon substrate. By using equivalent compositions for the underclad and overclad, the stress differentials on both the sides of the flexible substrate are balanced. This latter reduces intrinsic bend when released from the sacrificial substrate. The underclad and overclad layers are processed with flow rates of SiCl_4 at 137 sccm, BCl_3 at 70 sccm and PCl_3 at 31 sccm through a hydrogen-oxygen flame with flow rate 6.5 l/min and 1.5 l/min, respectively. The fabrication of the core layer is made with flow rates of SiCl_4 at 123 sccm, GeCl_4 at 130 sccm, BCl_3 at 16 sccm through a hydrogen-oxygen flame with flow rate 5.4 l/min and 2.7 l/min. After each FHD layer, the deposited soot requires high temperature consolidation. This was achieved within a furnace, flowing O_2 at rates of 1.9 l/min and consolidating at temperatures $T_{co} = 1360^\circ\text{C}$ and $T_{cl} = 1250^\circ\text{C}$, for the core layer and cladding layers respectively. The flexible photonic platform is created by removing the rigid silicon substrate through a physical machining process in the final processing step [200]. Figure 3.4.8 (a) shows

the cross-section of the fabricated device, captured via microscope camera. The flexible photonic sensor has a measured width of $w_{fp,meas} \sim 1$ mm, thickness $t_{fp,meas} \sim 58$ μm and length $L_{fp,meas} \sim 60$ mm. The thickness of the underclad is greater than that of the overclad. A key feature of the design is that the core layer is not centred on the neutral axis but it is offset.

The measured core layer thickness $t_{co,meas}$ differs slightly with respect to the desired t_{co} , due to dopant diffusion induced by the high temperature process involved. Figure 3.4.8 (b) shows the flexible photonic sensor coupled via UV-cured optical adhesive with a single mode polarization maintaining (PM) optical fibre. The refractive indices are measured, through a prism coupler, at the wavelength $\lambda = 1553$ nm. The underclad and overclad layers have a measured refractive index $n_{cl} = 1.445$, while the core layer has a measured refractive index $n_{co} = 1.469$.

3.4.2.2 Bragg gratings inscription

The three Bragg gratings and the channel waveguide can both be simultaneously inscribed onto the UV photosensitive core layer using the DUW method [205]. According to Fig. 3.4.4 (b), the Bragg gratings are written at different locations along the length of the device. They have a length $L = 12$ mm and a uniform apodization

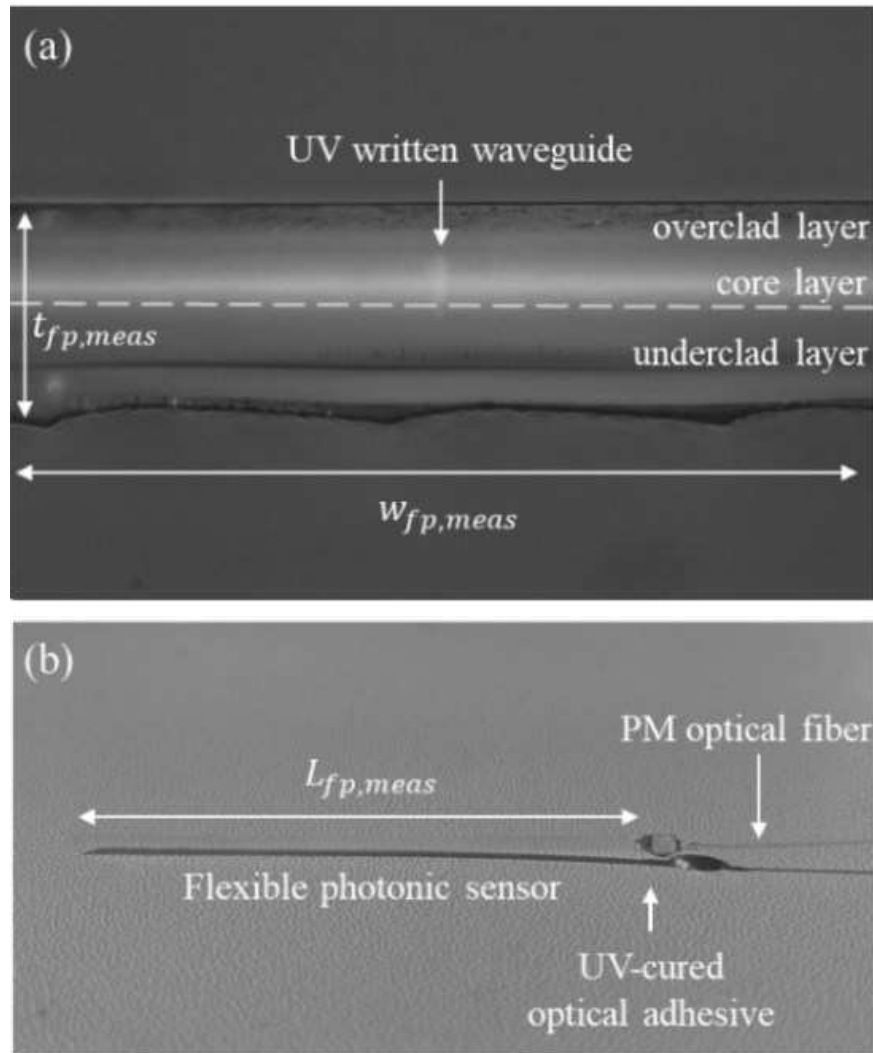


Figure 3.4.8 (a) Cross-section of the flexible photonic sensor captured via microscope camera; (b) flexible photonic sensor coupled to a polarization maintaining optical fiber via UV-cured optical adhesive [68].

profile, refractive index modulation of the Bragg grating $\Delta n_{BG} = 2 \times 10^{-4}$. Moreover, they are pseudo-randomly ordered, such that the spectral sequence does not correlate with spatial sequence. The measured resonant wavelengths of the fundamental mode are $\lambda_{\#G1} = 1528$ nm, $\lambda_{\#G2} = 1519$ nm and $\lambda_{\#G3} = 1588$ nm. The reflected power versus the wavelength for the three unperturbed Bragg gratings is shown in Fig. 3.4.9. Since each grating has two resonant peaks, the waveguide supports two modes of propagation according to the electromagnetic design.

3.4.2.3 Three-point bending test and optical measurement

To examine the optical response when subjected to significant deflections, the flexible photonic sensor was inserted into a mechanical test equipment. To apply three-point bending, an Instron E1000 electromechanical test machine is employed. The fixture comprises three steel rollers having a diameter $d_{roll} = 6$ mm, each separated by a distance $s = 20$ mm. The upper roller is used to apply the displacement and was attached to the actuator as shown in Fig. 3.4.10. To reduce the impact of optical fiber movement, the side that is optically connected to the fiber (the device left side in Fig. 3.4.10) is secured with tape.

The flexible photonic sensor was subjected to an incremental displacement d , from $d = 0$ mm (i.e. unperturbed) to $d = 11$ mm. The optical measurements were conducted during the three-point bending test using the setup depicted in Fig. 3.4.11. A negative Bragg wavelength shift in the pm range was obtained [67]. Grating #G2 is positioned at the loading point where the displacement and the strains are the largest and it is subjected to a curvature with negative concavity (see Fig. 3.4.5). Therefore, compared with the other gratings, it produces the greatest wavelength shifts. The maximum measured Bragg wavelength shift $\Delta\lambda_m$, for the fundamental and high order mode, are $\Delta\lambda_{m,fun} = -264$ pm and $\Delta\lambda_{m,hom} = -223.5$ pm, respectively. There is an increase of the measured peak power $\Delta P_{m,hom} = +4$ dBm for the high order mode, for a displacement $d = 11$ mm. The optical measurements of all the grating optical responses, for increasing displacement $d = [0 - 11]$ mm of the central roller, are reported in Fig. 3.4.12 and Fig. 3.4.13. Figures 3.4.12 (a) and (b) illustrate the measured Bragg wavelength shifts $\Delta\lambda_m$, of the fundamental mode (triangle markers) and high order mode (cross markers) for the gratings #G1 and #G3. Figures 3.4.12 (c) and (d) report the comparison between the simulated (dotted line) and measured Bragg wavelength shifts $\Delta\lambda$, of the fundamental mode (triangle markers) and high order mode (cross markers), of the grating #G2. As previously underlined, the grating #G2 constitutes the sensor, the gratings #G1 and #G3 are considered for a critical discussion of the obtained results. It is clear that the numerical calculations and the experimental data are in perfect agreement. By analysing the wavelength shifts reported in Fig. 3.4.12, all the gratings and both the propagating modes, show a shift of the resonant peaks towards smaller wavelengths. Since grating #G2 lies along the region of maximum and constant negative curvature, the Bragg wavelength shift $\Delta\lambda_m$ is negative with a linear trend that is larger than that of the gratings #G1 and #G3. Regarding the grating #G1, it is positioned in a region where two curvatures with opposite signs are present.

This provides an explanation for the wavelength shift reaching $\Delta\lambda_{m,fun} = -38 \text{ pm}$, $\Delta\lambda_{m,hom} = -20.6 \text{ pm}$ at the maximum central displacement $d = 11 \text{ mm}$. The flexible photonic sensor's right end is not joined, this causes a negative curvature on the grating #G3.

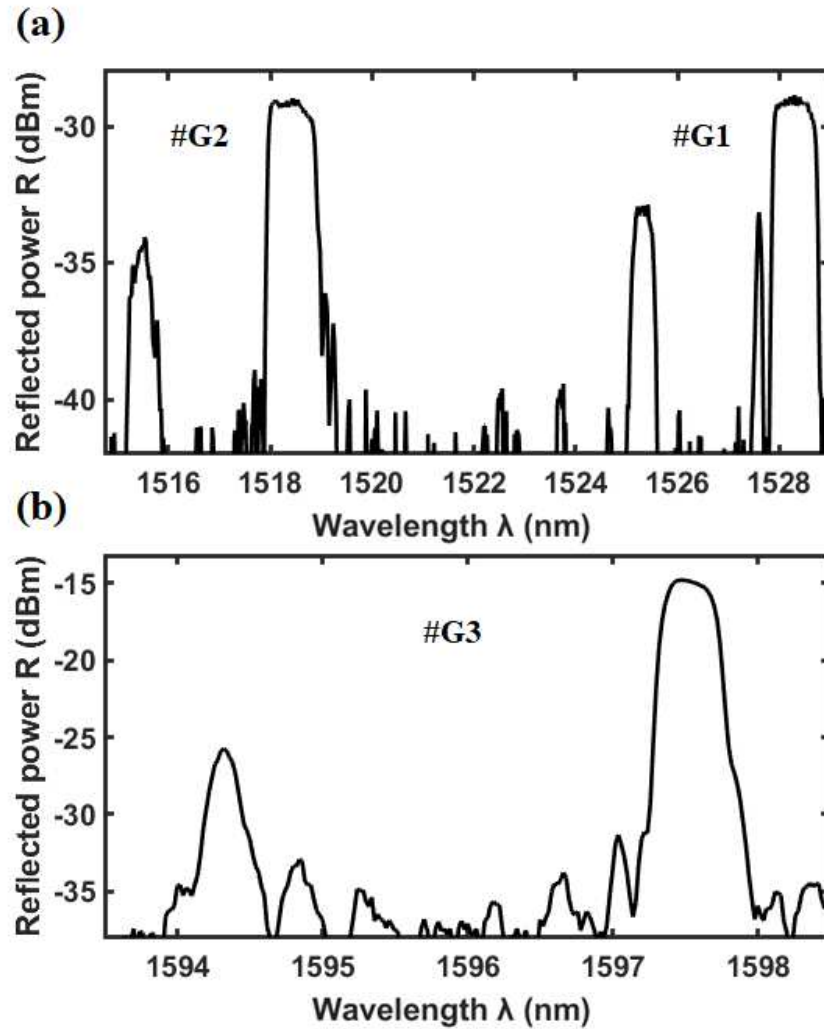


Figure 3.4.9 Measured reflection spectra of the unperturbed Bragg gratings (a) #G1, #G2 and (b) #G3; length of the Bragg grating $L = 12 \text{ mm}$, refractive index modulation of the Bragg grating $\Delta n_{BG} = 2 \times 10^{-4}$ [68].

In this case, the displacement and strains are lower than those occurring at the loading point where grating #G2 is situated. The maximum measured Bragg wavelength shift for the grating #G3 is $\Delta\lambda_{m,fun} = -95.2 \text{ pm}$, $\Delta\lambda_{m,hom} = -112 \text{ pm}$. Ultimately, the grating #G2, subjected to curvature, provides Bragg wavelength shift sensitivities $K_{\lambda,fun} = -2.4 \text{ pm/m}^{-1}$, $K_{\lambda,hom} = -2.1 \text{ pm}/$

m^{-1} . Figure 3.4.13 illustrates the measured peak power change $\Delta P_{m,hom}$ for the high order mode of the grating #G1 (triangle markers), #G2 (cross markers) and #G3 (circle markers) as a function of the displacement d . The simulated peak power change $\Delta P_{s,hom}$ of the high order mode of the grating #G2 (dotted line) is in good agreement with the measured value. The power trend of the high-order mode of gratings #G1 and #G3, which are symmetrically positioned about the loading point, exhibits comparable changes in power, but with opposite directions. Both the gratings reach the maximum peak power change $\Delta P_{m,hom}$ at a displacement of $d = 6 \text{ mm}$.

The power exchange between the two propagating modes can be utilized to deduce the degree of bending of grating #G2 by employing ratiometric power P_R . Where P_R is defined as the ratio between the peak power reflected by the fundamental mode $P_{m,fund}$ and the high order mode $P_{m,hom}$. In Fig. 3.4.14 the measured ratiometric power P_R of the grating #G2 versus the displacement d (cross markers) is reported. The red dashed line is the linear fit of the experimental curve.

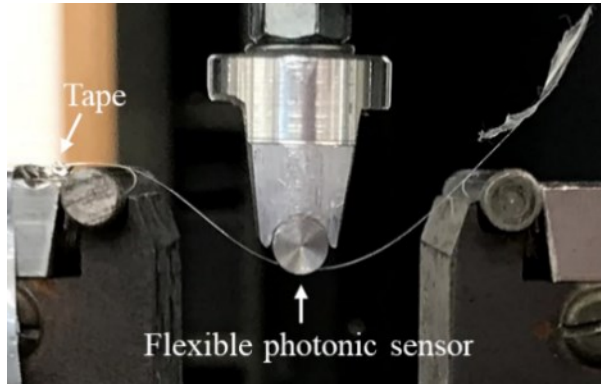


Figure 3.4.10 Photograph of the experimental set-up. Centre-to-centre separation of rollers $s = 20 \text{ mm}$, diameter of rollers $d_{roll} = 6 \text{ mm}$ [68].

The sensor exhibits a linear response between $d = 2 \text{ mm}$ and $d = 10 \text{ mm}$ with a ratiometric power sensitivity being $K_{P_R} = -0.78 \text{ dB/mm}$. The almost flat response between $d = 0 \text{ mm}$ and $d = 2 \text{ mm}$, can be addressed to an unwanted initial deflection of the sensor. It is worth noting that, over a $40 \text{ }^\circ\text{C}$ thermal range, power change shows negligible variation, thus it is not affected by environment temperature. The measured thermo-optic Bragg shift sensitivity is approximately $K_T = 11.5 \text{ pm/K}$.

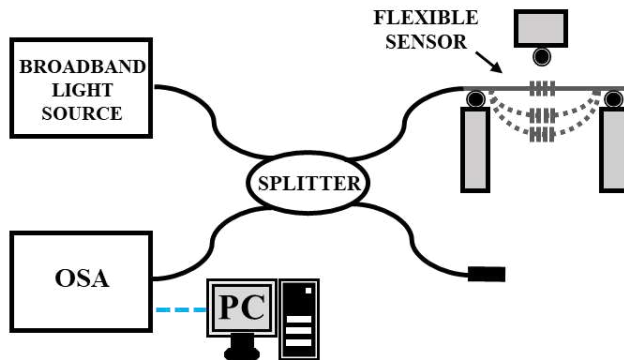


Figure 3.4.11 Experimental set-up employed for spectra measurements [68].

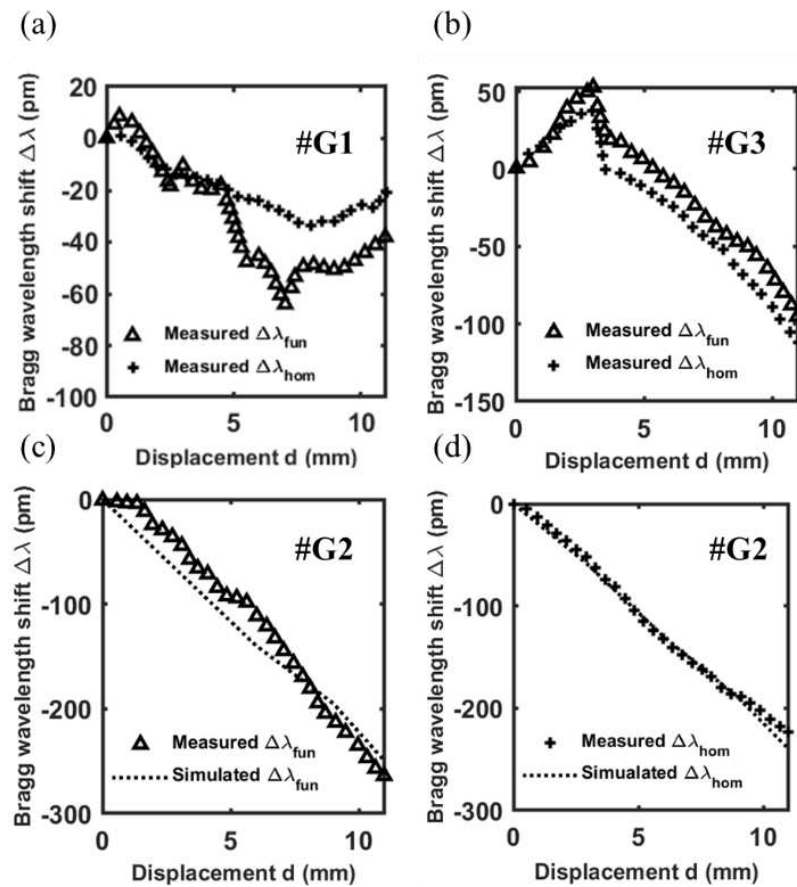


Figure 3.4.12 Measured Bragg wavelength shifts $\Delta\lambda_m$, of the fundamental mode (triangle markers), high order mode (cross markers) for (a) the gratings #G1 and (b) #G3. (c) Comparison between the simulated (dotted curve) and measured (triangle markers) Bragg wavelength shift $\Delta\lambda_{fun}$ of the fundamental mode, (d) comparison between the simulated (dotted curve) and measured (cross markers) Bragg wavelength shift $\Delta\lambda_{hom}$ of the high order mode, for the grating #G2 [68].

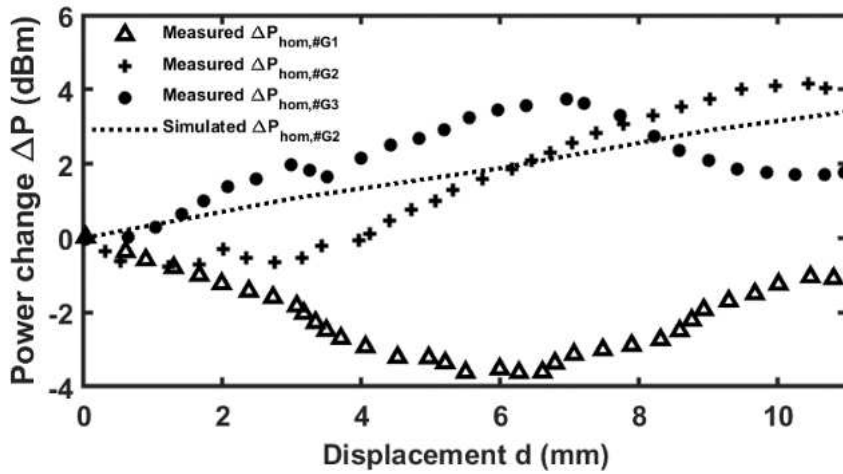


Figure 3.4.13 Measured peak power change $\Delta P_{m,hom}$ versus the displacement d for the high order mode of the grating #G1 (triangle markers), #G2 (cross markers), #G3 (circle markers) and simulated peak power change $\Delta P_{s,hom}$ for the grating #G2 (dotted curve) [68].

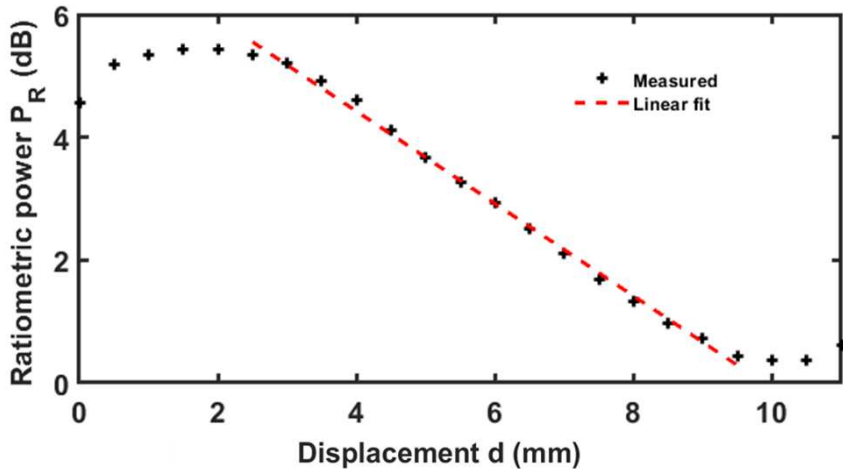


Figure 3.4.14 Ratiometric power P_R versus the displacement d for the grating #G2 (cross markers). The red dashed line is the linear fit of the curve [68].

3.4.2.4 Discussion of results

The focus of this research work is the demonstration of a novel approach to infer level of bending, based on ratiometric power change, between the peak power reflected by fundamental and high order mode.

Table 3.4.1 reports a comparison with other Bragg curvature sensors which exhibit very high performances and include different approaches: multimode interference [60], embedding in silicone substrate [38], polymeric optical fibers with eccentric core [50], multicore optical fibers [63], or tilted FBGs [206]. In particular, multimode interference [60] requires a more sophisticated measurement

approach, with excitation of a number of modes; embedded in silicone sensor [38] exhibits higher thickness; polymeric optical fibers [50] show higher confinement losses due to lower refractive index changes [63], [206] show high sensitivities but smaller measurement range.

The proposed proof of concept shows the following strength points: i) the minimum thickness, ii) the maximum curvature, iii) exploitation of the ratiometric power which is immune to temperature variation, iv) immunity to power fluctuation of light source, due to the intrinsic compensation of the measurement technique, v) simultaneous measurement of bending and temperature. The refining of the design and fabrication of further devices based on the same approaches is encouraged by these outcomes.

Table 3.4.1 State-of-art comparison between flexible sensors.

Reference	Thickness	Maximum curvature	K_λ	K_{P_R}	K_T	T compensation
[60]	125 μm	—	—	2.1 dB/mm	—	no
[38]	5 mm	80 m^{-1}	1.64 pm/ m^{-1}	—	—	no
[50]	230 μm	22.7 m^{-1}	63 pm/ m^{-1}	—	—	no
[63]	150 μm	11 m^{-1}	59.47 pm/ m^{-1}	—	—	yes
[206]	—	15.5 m^{-1}	—	0.74 dB/ m^{-1}	—	yes
This work	58 μm	110 m^{-1}	2.4 pm/ m^{-1}	0.78 dm/mm	11.5 pm/K	yes

3.4.3 Conclusion

A novel approach for curvature monitoring through flexible photonics is introduced, taking into account both the ratiometric power between the peak power reflected by the fundamental and higher-order modes and the Bragg wavelength shift. A sensor is fabricated to validate the approach. In particular, a comprehensive optomechanical design and characterization of the flexible photonic sensor is reported. The suggested approach reduces the overall thickness of the substrate in comparison to conventional fiber optic curvature sensors, allowing for greater degrees of bending. The results indicate that the wavelength shift depends on the sign of applied curvature. The experiments agree with simulations and show that the proposed flexible sensor can withstand very high curvatures up to 110 m^{-1} . The grating #G2 provides Bragg wavelength shift sensitivities $K_{\lambda,fun} = -2.4 \text{ pm}/\text{m}^{-1}$, $K_{\lambda,hom} = -2.1 \text{ pm}/\text{m}^{-1}$ and ratiometric power sensitivity $K_{P_R} = -0.78 \text{ dB}/\text{mm}$. Regarding thermal characterization of the sensor, negligible variation over a 40°C range has been observed in terms of power change.

The thermo-optic sensitivity is approximately $K_T = 11.5 \text{ pm/K}$. A novel class of multiparameter sensors, for simultaneous temperature and curvature detection, could be developed by utilizing the values of the Bragg wavelength shift and temperature-independent ratiometric optical power change.

4 Combining and Coupling of Optical Beams

As the demand for Mid-IR technologies continues to grow in fields such as environmental monitoring, healthcare, and industrial process control, the development of optical components has become paramount. This Chapter illustrates the major results obtained during the Ph.D. research activity with respect to Mid-IR optical components for combining and coupling optical beams.

4.1 Fused Optical Fiber Combiner Based on Indium Fluoride Glass: New Perspectives for Mid-IR Applications

A 3×1 fused fiber combiner based on multimode step-index fluoroindate optical fibers (InF_3) has been designed, fabricated and characterized for the first time, to the best of my knowledge. Due to the low melting point and mechanical properties of fluoroindates fibers, several attempts to reach a well-consolidated manufacturing and normalization protocol have been required. Fabrication results demonstrate repeatability and absence of crystallization. Therefore, the described fabrication process paves the way for manufacturing fluoroindate devices. The electromagnetic design of the combiner is carried out through modal investigation and beam propagation method by computing the transmission efficiency. The experimental results agree with the simulation and demonstrate the device feasibility to operate in the Mid-IR spectral range. The following paragraphs are organized as follows: Section 4.1.1 reports the 3×1 fluoroindate combiner description and the electromagnetic design; Section 4.1.2, the fabrication challenges, the developed fabrication process and the experimental characterization; Section 4.1.3, prospects and conclusion.

4.1.1 Electromagnetic design and numerical results

4.1.1.1 Design approach

For beam combining applications over the Mid-IR spectral range, the design of the 3×1 fluoroindate combiner is performed. The adiabatic taper requirement and the beam brightness principle are the primary restrictions to take into account for the design of an optical combiner, as detailed in Section 2.3.2 [157], [158]. In particular, the electromagnetic design is carried out through i) a preliminary modal investigation, considering both the untapered and tapered cross-sections, see Fig. 4.1.1 (a) and Fig. 4.4.1 (b); and ii) the Beam Propagation Method (BPM) for evaluating the electromagnetic power propagation/coupling. The geometrical parameters have been chosen a) to ensure the electromagnetic field confinement in a single core, over the entire wavelength range from $\lambda = 1.00 \mu\text{m}$ to $\lambda = 5.00 \mu\text{m}$, when only one of the three optical fibers is excited; b) to fulfill the adiabatic taper criterion [49, 50]. Additionally, the BPM has been employed to simulate the net transmission efficiency $\eta_{s,\text{net}}(z) = P_p(z)/P_{in}$, defined as the ratio between the power along the propagation direction $P_p(z)$, i.e. along the z -axis direction of the combiner, and the power launched in one of the three input fibers P_{in} ($z = 0$), excited one at a time, for different wavelengths λ and different waists B_w of the input gaussian beam.

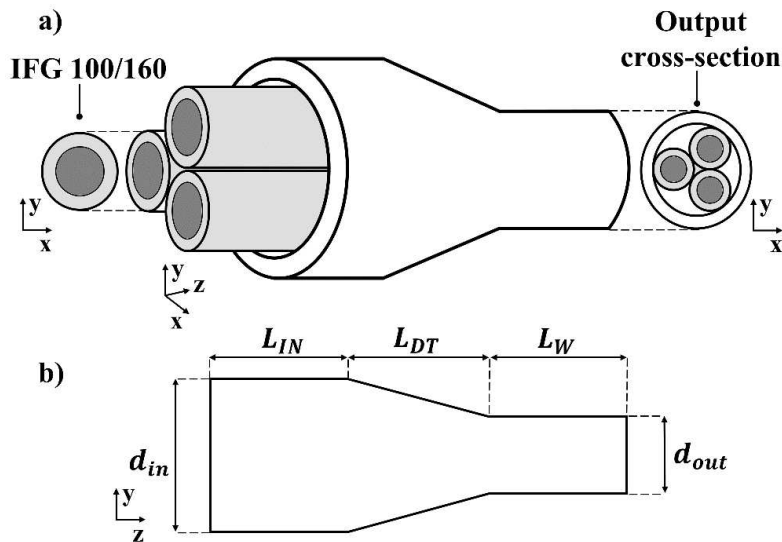


Figure 4.1.1 a) 3×1 fluoroindate combiner sketch; b) longitudinal section in the y - z plane of the 3×1 fluoroindate combiner with linear down-taper [86].

4.1.1.2 Design of the 3×1 fluoroindate combiner

A low-index fluoroindate capillary surrounds three multimode step-index fluoroindate optical fibers that are positioned at the vertices of an equilateral

triangle to form the 3×1 fluoroindate combiner. A 3D schematic of the device is presented in Fig. 4.1.1 (a). Both optical fibers and capillary are manufactured by the company Le Verre Fluoré, France [126]. The fluoroindate optical fibers IFG MM (0.30) 100/160 have a core diameter $d_{co} = 100 \mu\text{m}$ and a cladding diameter $d_{cl} = 160 \mu\text{m}$. The capillary has an internal diameter of $d_{inner,cap} = 360 \mu\text{m}$ and an external diameter of $d_{outer,cap} = 580 \mu\text{m}$. The material used for core and cladding is InF_3 glass with different stoichiometries. The core and cladding refractive index, at the wavelength $\lambda = 1.55 \mu\text{m}$, are respectively $n_{co} = 1.504$ and $n_{cl} = 1.474$, resulting in a numerical aperture $NA \sim 0.30$. The capillary is not commercially available and it is ad-hoc designed and fabricated to have a refractive index $n_{cap} = 1.472$ lower than cladding refractive index n_{cl} . The simulations take into account the real dispersion curves of fluoroindate glasses as shown in Fig. 4.1.2 and supplied by Le Verre Fluoré.

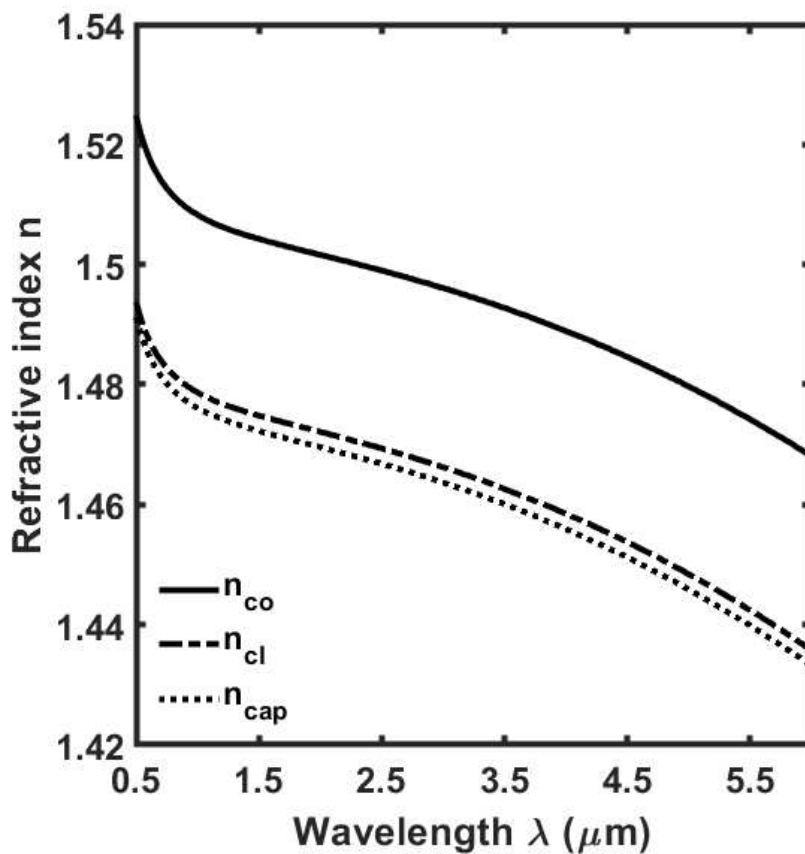


Figure 4.1.2 Refractive index n as a function of the wavelength λ ; core refractive index n_{co} (solid line), cladding refractive index n_{cl} (dotdash line), capillary refractive index n_{cap} (dotted line) [86].

In Fig. 4.1.1 (b), the sketch of the longitudinal section of the 3×1 combiner is reported. The straight input section has length $L_{IN} = 1\text{ cm}$, the linear down-taper section has length $L_{DT} = 1.5\text{ cm}$ while, the waist section has length $L_W = 2.5\text{ cm}$. The total length of the combiner can be defined as $L_{out} = L_{IN} + L_{DT} + L_W = 5\text{ cm}$. The structure, having a diameter $d_{in} = d_{outer,cap} = 580\text{ }\mu\text{m}$ is tapered with a scaling factor $SF = 5$. This corresponds to an output diameter $d_{out} = d_{outer,cap}/SF = 116\text{ }\mu\text{m}$.

Several double cladding fibers are characterized by an inner cladding diameter which correspond to the waist diameter dimension d_{out} . Therefore, to enhance the beam quality and provide a better delivery of the overall power, the combiner output can be spliced with a double-cladding fiber. In Fig. 4.1.3, the refractive index profile distribution at the output cross-section of the combiner (i.e. $z = L_{out}$) is reported.

The outer low-index capillary (white colored) surrounds both the cladding (light grey colored) and the core (dark grey colored) of the three optical fibers.

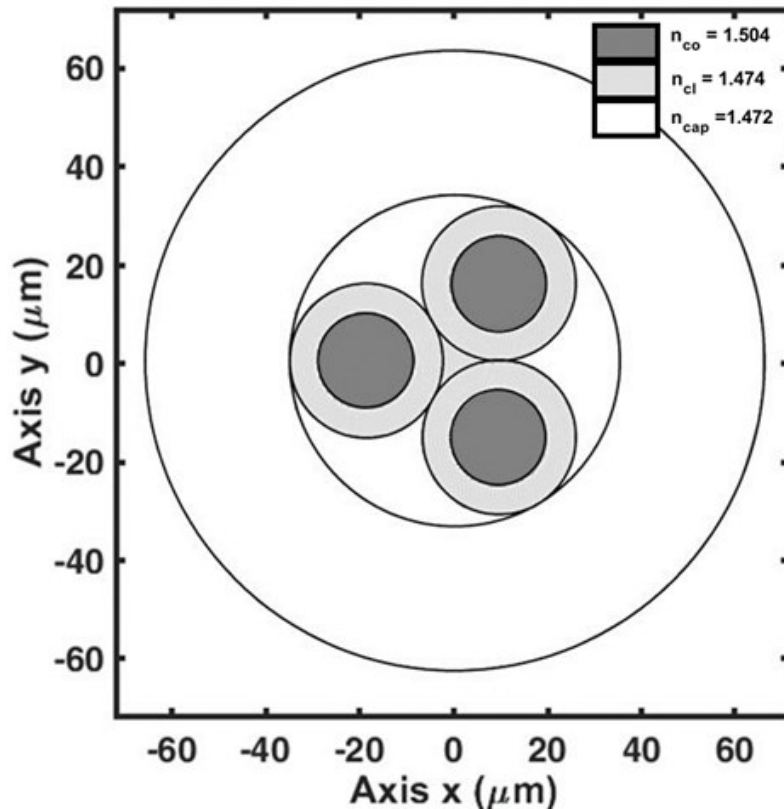


Figure 4.1.3 Refractive index distribution, greyscale, of the simulated 3×1 fluoroindate combiner at the output cross-section ($z = L_{out}$) at the wavelength $\lambda = 1.55\text{ }\mu\text{m}$ (x-y plane) [86].

4.1.1.3 Numerical results

The numerical investigation of the 3×1 fluoroindate combiner, from NIR to Mid-IR, for the wavelengths $\lambda = \{1.00, 1.55, 3.20, 5.00\} \mu m$ and for a beam waist $B_W = 70.0 \mu m$ has been performed. The beam waist $B_W = 70.0 \mu m$ is chosen to highlight the device performance by considering a suitable excitation condition, which is a trade-off for maximizing the net transmission efficiency $\eta_{s,net}$ at the four wavelengths of interest. In addition, for a comparison/validation with the experimental results, the 3×1 fluoroindate combiner operation at the wavelength of $\lambda = 1.55 \mu m$ is simulated by considering a beam waist $B_W = 10.4 \mu m$. The net transmission efficiencies $\eta_{s,net}$, simulated with BPM, at the wavelength $\lambda = 1.55 \mu m$ for beam waist $B_W = 10.4 \mu m$ and $B_W = 70.0 \mu m$, are reported in Fig. 4.1.4. The beam waist $B_W = 10.4 \mu m$ is typical of Corning SMF-28 silica optical fiber and it corresponds to the one employed in the experiment at NIR wavelength. Table 4.1.1 illustrates the net simulated transmission efficiencies $\eta_{s,net}(z)$ fluoroindate, at the output section of the 3×1 fluoroindate combiner e.g., $z = L_{out}$, for the aforementioned wavelength λ . The obtained findings demonstrate compliance with the multimode fiber tapering adiabatic requirement [207]. The simulations emphasize the possibility to obtain a device with high net transmission efficiency $\eta_{s,net}(L_{out})$ over a wide range of wavelength from NIR to Mid-IR. The power losses over the wavelength λ given by the taper are negligible. Table 4.1.1 suggests a flat behavior of net transmission efficiency $\eta_{s,net}(L_{out})$. This is explained by the normalized frequency V value of each optical fiber, constituting the 3×1 fluoroindate combiner. At the output cross-section, the core diameter of each optical fiber is $d_{co,t} = d_{co}/SF = 20 \text{ cm}$ with numerical aperture $NA = 0.3$. Therefore, at the upper bound of the wavelength range (i.e. $\lambda = 5 \mu m$), the normalized frequency is $V \sim 3.77$, high enough to support not only the fundamental mode but also a few higher order modes. The simulation shows that there is power coupling between the optical fibers, but it is minimal since there is only a small amount of optical tunneling [87]. It is in agreement with the modal analysis results.

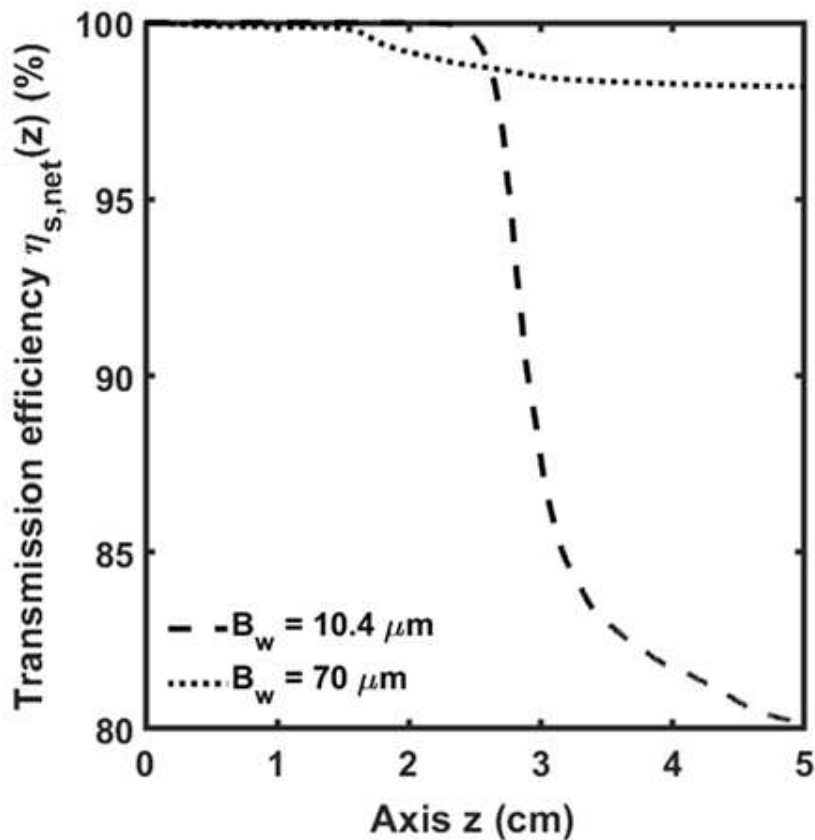


Figure 4.1.4 BPM simulation of transmission efficiency $\eta_{sim}(z)$ along the propagation direction (z-axis), for beam waist $B_W = 10.4 \mu\text{m}$ (dashed line) and $B_W = 70 \mu\text{m}$ (dotted line) at the wavelength $\lambda = 1.55 \mu\text{m}$ [86].

Table 4.1.1 Simulated transmission efficiencies $\eta_{s,net}(L_{out})$ of the 3×1 fluoroindate combiner.

Wavelength $\lambda [\mu\text{m}]$	Beam waist $B_w [\mu\text{m}]$	Simulated transmission efficiency $\eta_{s,net}(L_{out}) [\%]$
1.55	10.4	80.1
1.00	70.0	98.2
1.55	70.0	98.2
3.20	70.0	98.2
5.00	70.0	98.1

4.1.2 Fabrication and measurements

4.1.2.1 Fabrication challenges

The optical fibers and capillaries are provided by Le Verre Fluoré, detailed in Section 4.1.1 and employed to obtain the structure of the 3×1 fluoroindate combiner. It is fabricated through fusion technique by employing Vytran® GPX-2400 glass filament processing system at Politecnico di Bari. Due to the fragility of the material and its thermal characteristics [208], such as its low melting temperature, narrow glass transition, and steep viscosity/temperature characteristic, the processing of fluoroindate glass is challenging. Figure 4.1.5 shows the typical viscosity/temperature of fluoroindate glass. The steep profile justifies the need for strict temperature control [80].

A fine temperature monitoring is necessary to avoid geometric inhomogeneities and surface crystallization. To reach a precise temperature control during combiner manufacture, an ad-hoc normalization procedure of the Vytran® GPX-2400, making use of fluoride glass, is developed. In addition, parameters such as filament power, applied tension, pull velocity of the translation stage and argon flow rate have been optimized by carrying out several tests. The manufacturing of high quality fluoroindate optical components is strictly dependent on these crucial aspects. Ultimately, a reliable and controlled fabrication process is obtained.

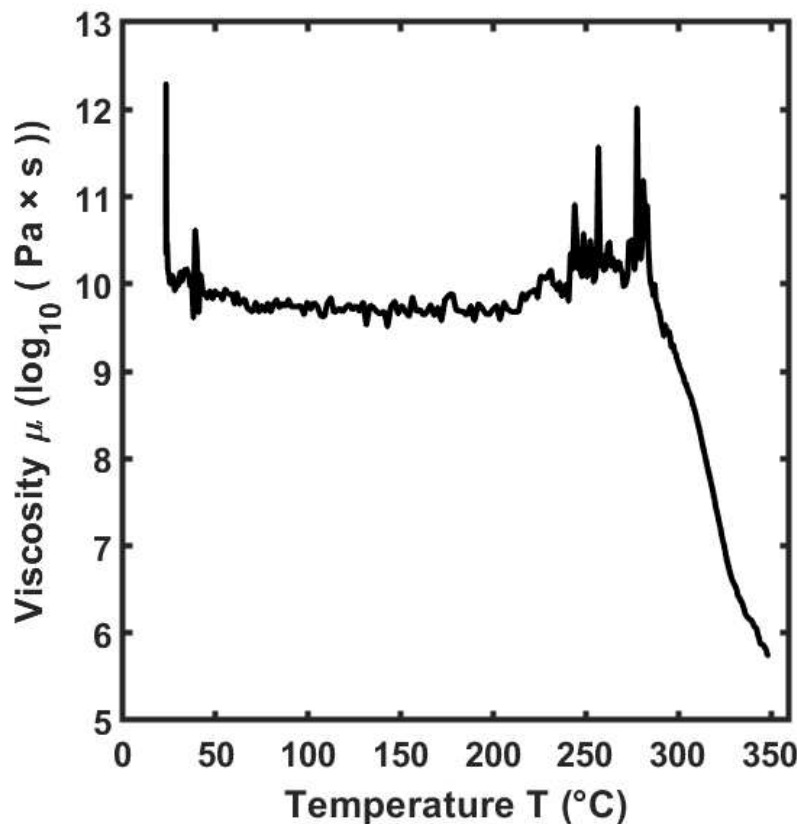


Figure 4.1.5 Viscosity μ of fluoroindate glass versus temperature T [86].

4.1.2.2 Fabrication method

The optical fibers are manually inserted into the capillary after being manually cleaned with isopropyl alcohol and stripped of their polymer coating using a particular stripping gel. To avoid refractive index inhomogeneities and additional losses, during the tapering process great attention is devoted toward many aspects. No dust or coating residuals are left onto the fibers and within the capillary. Generally, to facilitate fibers insertion, the capillary has an internal diameter higher than the needed one and is pre-tapered before inserting fibers. In the case of fluoroindate glasses, this procedure is to be avoided since the repetition of the tapering procedure can easily lead to glass surface crystallizations. For this reason, the inner capillary size, i.e. diameter $d_{inner,cap}$, is identified as an opportune trade-off. It is large enough to permit a manual threading of the three fibers but, at the same time, an arrangement without significant air gaps is ensured. In order to operate at a softening point near to the glass transition temperature $T_g = 275^\circ\text{C}$ (determined by differential thermal analysis at $10^\circ\text{C}/\text{min}$), a

commercial FTAT3 graphite filament is utilized as the heating source and properly normalized.

During the whole fabrication process, the glass has to be accurately maintained at the softening point. The main consequences of an excessive amount of heat transmitted to the combiner under construction are surface crystallization, waist diameter smaller than the desired one or completely fused waist. On the contrary, an amount of heat lower than that required to reach the softening point of the glass, leads to larger waist diameter or capillary breaking.

The diameter of the combiner under construction tends to decrease due to the tapering process. Therefore, the amount of heat provided by the filament during the manufacturing process must decrease as well (via a reduction of the filament power along the taper process) to keep the softening glass temperature. As an alternative, a non-constant fiber holding block pull velocity v_{block} can be imposed. A larger (smaller) fiber holding block pull velocity v_{block} results in smaller (larger) amount of heat absorbed by the combiner under fabrication. However, the use of non-constant fiber holding block pull velocity v_{block} can lead to low quality taper. Therefore, a constant fiber holding block pull velocity $v_{block} = 0.5 \text{ mm/s}$ is exploited and the initial filament power $P_f \sim 12 \text{ W}$ is reduced during the process. The initial filament power P_f should be finely tuned since it is slightly dependent on ambient temperature when working with fluoroindate optical fibers. The pull velocity v_{block} is controlled with a repetition time $\Delta t = 0.1 \text{ s}$. The structure is clamped between the two translation fiber holders. Before starting the fusion process i) the entire structure is pre-tensioned, moving one fiber holding block, to approximately $L = 15 \text{ g}$, ii) an argon flow is employed to purge the fusion region, to prevent the glass crystallization and extend the graphite filament lifetime, iii) any excess of isopropyl alcohol is removed through the vacuum pump Linicon LV-125A. Before the fabrication process it is necessary to purge the filament for a pre-purge duration time $t_{pp} = 20 \text{ s}$ considering a pre-purge flow rate $F_{pp,R} = 0.80 \text{ L/min}$. The argon flow rate during the process, dependent on the adopted filament and kind of glass, is $F_R = 0.35 \text{ L/min}$.

During the tapering process, the vacuum pump is also employed to encourage capillary collapse and, consequently, a homogeneous cross-section without trapped air [92]. The tension was monitored during the tapering using Vytran® GPX-2400 built-in sensor. The tension monitor is a useful tool to understand how to set the parameters of the manufacturing process. In particular, if the tension L goes to large negative values, i.e. the glass is heated over the softening

temperature, the filament power P_f should be decreased or the fiber holding block pull velocity v_{block} increased. If the tension L goes to large positive values, the glass has not reached the softening temperature. In this case, the filament power P_f should be increased or the fiber holding block pull velocity v_{block} decreased. Figure 4.1.6 shows the tension varying during the automatic tapering and drawing process. The trend of the tension indicates that no issues occurred during the process [92]. Figure 4.1.7 shows a picture taken during the fabrication process using a Dino-Lite camera (digital microscope camera).

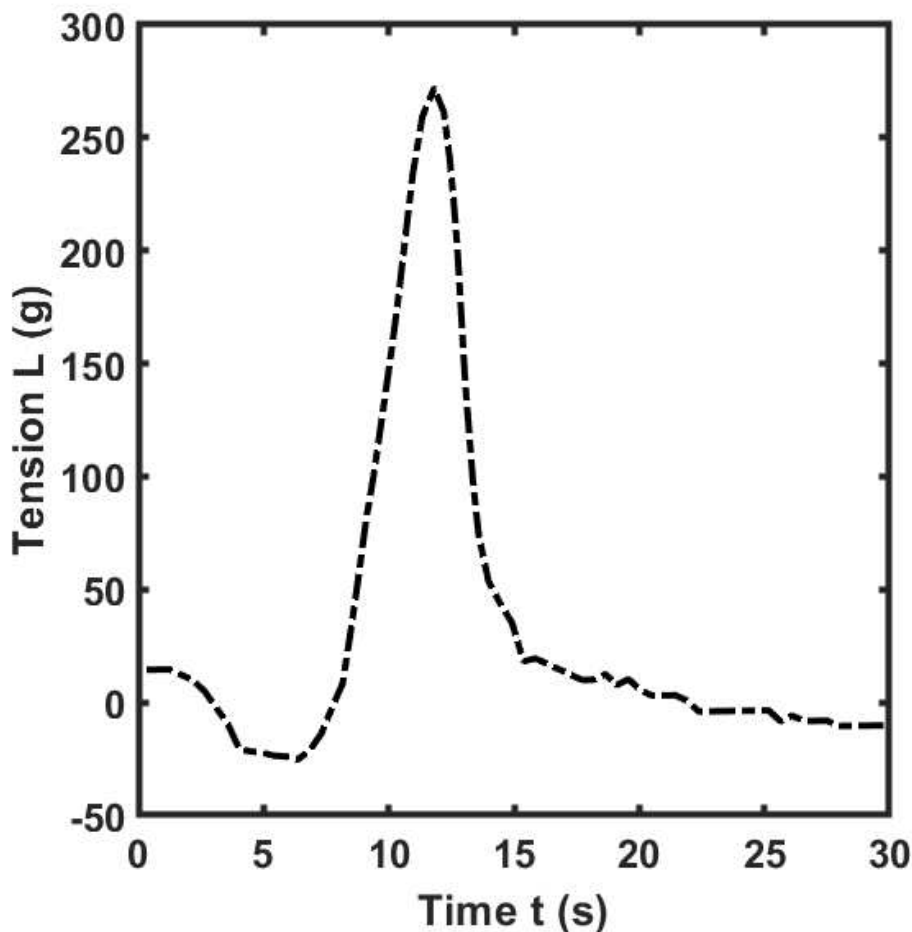


Figure 4.1.6 Tension monitor measured during combiner manufacturing using Vytran® GPX-2400 sensor [86].

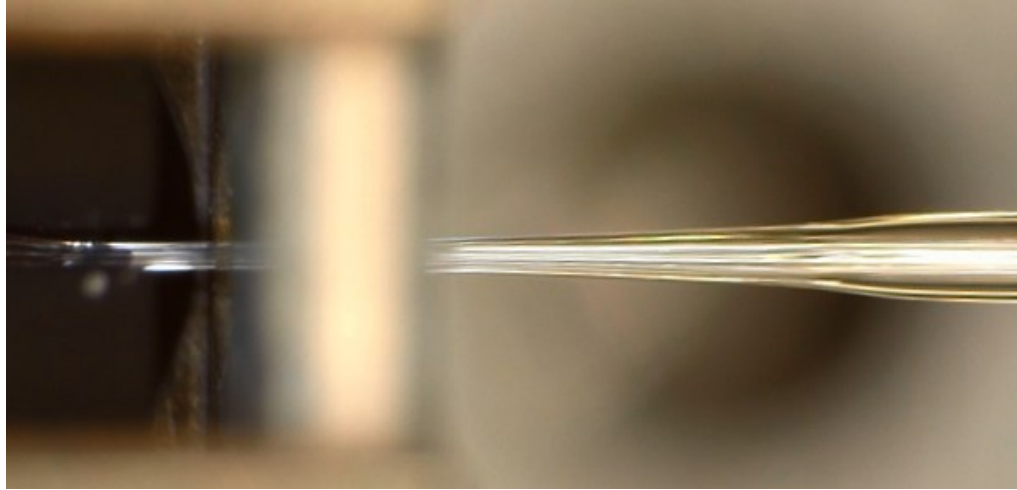


Figure 4.1.7 Longitudinal view of the 3×1 fluoroindate combiner, captured with Dino-Lite camera, during a stage of the fabrication process. At left, the FTAT3 graphite filament of the Vytran® GPX-2400 workstation [86].

4.1.2.3 Fabrication results

Using Vytran® GPX-2400 microscope camera, the final 3×1 fluoroindate combiner's dimensions, longitudinal view, and output cross-section were captured and measured. The device was cleaved at the center of the waist region via Vytran® cleaver LDC-400.

Figure 4.1.8 shows the combiner output cross-section. The obtained results show that the use of a fluoroindate capillary with a melting temperature lower than that of the optical fibers and the use of vacuum pump during the process helps to obtain a homogeneous output cross-section.

In Fig. 4.1.9, the microscope images of the longitudinal view of the 3×1 fluoroindiate combiner, at different stages of the tapering process, are shown. The down taper transition of the combiner has a length $L_{DT} = 1.5\text{ cm}$ while the waist has a length $L_W = 2.5\text{ cm}$.

The desired combiner dimensions have been obtained ensuring high glass quality (e.g. without surface crystallization), long adiabatic transition and a scaling factor $SF = 5$. By varying the filament power and pulling rates, different tapering ratios and transition lengths may be achieved.

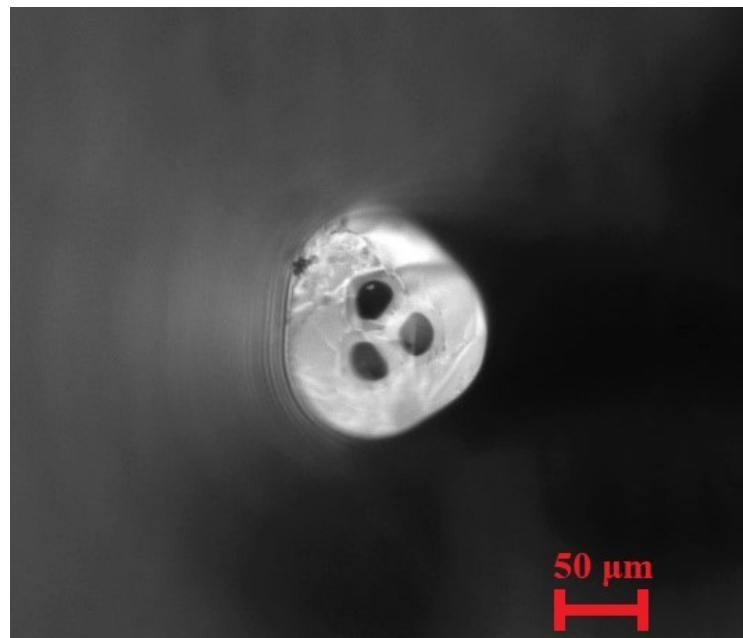


Figure 4.1.8 Output cross-section of the 3×1 fluoroindate combiner, captured with Vytran® GPX-2400 microscope camera [86].

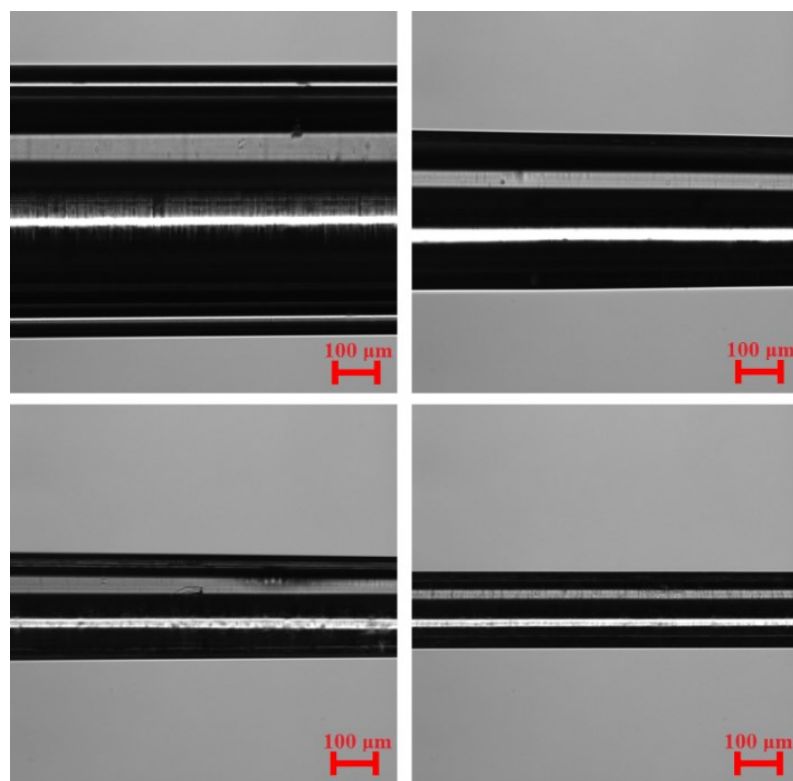


Figure 4.1.9 Longitudinal view of the 3×1 fluoroindate combiner, captured with Vytran® GPX-2400 microscope camera, at different stages of the tapering process [86].

4.1.2.4 Output power measurements

In order to assess the performance of the 3×1 fluoroindate combiner in the NIR and Mid-IR spectral region, two distinct experimental setups are developed. The first set-up, sketched in Fig. 4.1.10, is constituted by a light source Exalos SLED EBD-5200 which emits a signal having wavelength around $\lambda = 1.55 \mu\text{m}$, a silica single-mode 50:50 coupler and two power meters (Newport, Optical Power Meter, Model 840). The two arms of the silica single-mode 50:50 coupler are joined to the fluoroindate optical fibers using bare fiber terminators (BFTs). This set-up is employed to characterize the combiner in terms of per-port net transmission efficiency $\eta_{m,\text{net}}$ at the wavelength $\lambda = 1.55 \mu\text{m}$. The net transmission efficiency $\eta_{m,\text{net}} = P_{\text{out,comb}}/P_{\text{probe,IFG}}$ is defined as the ratio between the power measured at the output section of the combiner $P_{\text{out,comb}}$ and the power at the output section of a probe IFG 100/160 optical fiber $P_{\text{probe,IFG}}$; $P_{\text{probe,IFG}}$ being equal to the power launched in the IFG 100/160 optical input fiber of the combiner. Since both 3×1 IFG 100/160 fluoroindate input fibers of the combiner and the probe IFG 100/160 optical fiber are connectorized by using bare fiber terminators (BFTs), the transmission efficiency $\eta_{m,\text{net}}$ is net, i.e. evaluated without the coupling losses introduced by temporary connectors. The measured power levels by injecting the light at the different input ports P_i with $i = \{1 \div 3\}$ and the net transmission efficiencies $\eta_{m,\text{net}}$ are reported in Table 4.1.2. The measured net transmission efficiency $\eta_{m,\text{net}}$ for a gaussian input beam with waist $B_W = 10.4 \mu\text{m}$ at the wavelength $\lambda = 1.55 \mu\text{m}$ is in excellent agreement with the simulated one $\eta_{s,\text{net}}(L_{\text{out}})$. The measurements from NIR to Mid-IR are performed by employing the set-up sketched in Fig. 4.1.11, with the aim to investigate the combiner operation over the wavelength range from $\lambda = 1.00 \mu\text{m}$ to $\lambda = 5.00 \mu\text{m}$.

In the second setup, a halogen light, a Horiba iHR550 monochromator to choose the wavelength λ , and an In-Sb-detector working in combination with a lock-in amplifier are employed. A number of 3×1 fluoroindate combiner have been fabricated and exhibited similar characteristics, proving a high repeatability. As an example, the characterization of the 3×1 fluoroindate combiner shown in Fig. 4.1.8, performed by exciting one of the input fibers, is reported. They are affected by coupling losses due to the axial/angular misalignment and due to the beam-quality degradation. Ultimately, the set-up in Fig. 4.1.11, differently from the one reported in Fig. 4.1.10, is not compensated and allows to measure the overall transmission efficiency $\eta_{m,\text{overall}}$. The overall transmission efficiency $\eta_{m,\text{overall}} = P_{\text{out,comb}}/P_{\text{in}}$ is defined as the ratio between the power measured

at the output section of the combiner $P_{out,comb}$ and the input power P_{in} delivered by the IFG 100/160 optical fiber, free space coupled with the optical source.

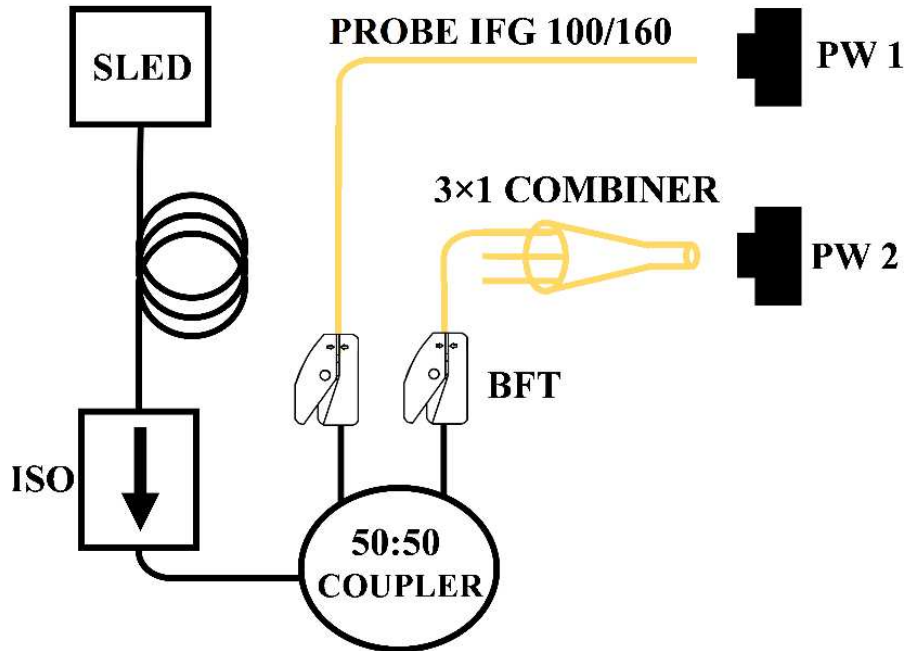


Figure 4.1.10 Sketch of the experimental set-up used to characterize 3×1 fluoroindate combiner transmission efficiency $\eta_{m,net}$ at the wavelength $\lambda = 1.55 \mu\text{m}$. The silica optical fibers are represented in black, the fluoroindate optical fibers in yellow [86].

Table 4.1.2 Measured power levels and 3×1 combiner transmission efficiencies at $\lambda = 1.55 \mu\text{m}$

Parameter	Value [mW]	Measured transmission efficiency $\eta_{m,net}$ [%]	Simulated transmission efficiency $\eta_{s,net}(L_{out})$ [%]
P_1	1.513	78.4	80.1
P_2	1.555	80.6	80.1
P_3	1.497	77.6	80.1

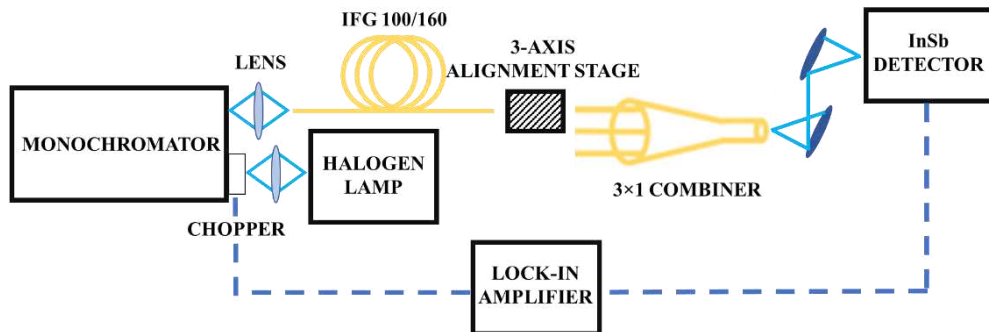


Figure 4.1.11 Schematic of the experimental set-up used for 3×1 fluoroindate combiner characterization from NIR to Mid-IR [86].

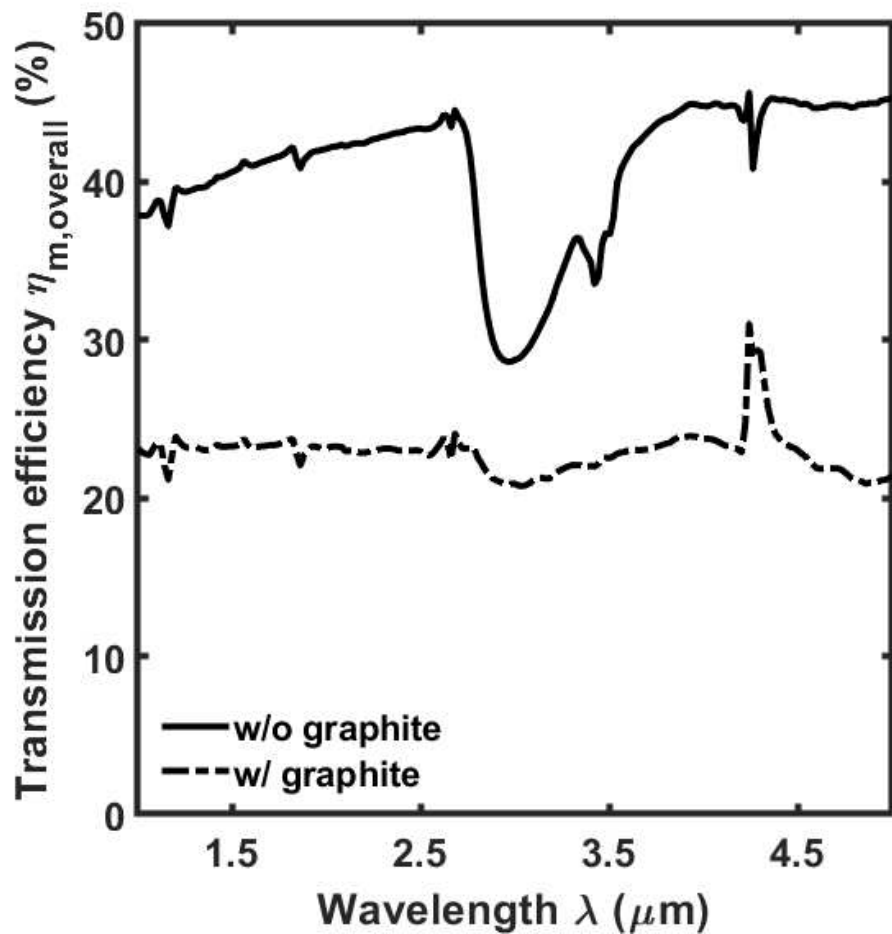


Figure 4.1.12 Overall transmission efficiency $\eta_{m,\text{overall}}$ measured in the Mid-IR wavelength range; 3×1 fluoroindate combiner without graphite covering (solid line), with graphite covering (dotdash line) [86].

While the net transmission efficiency $\eta_{m,net}$ provides the actual performances of the 3×1 fluoroindate combiner the overall transmission efficiency $\eta_{m,overall}$ includes both the transmission losses of the combiner and those introduced by free propagation coupling. Despite these drawbacks, the qualitative measurement in Mid-IR is significant to demonstrate the 3×1 fluoroindate combiner operation over the entire wavelength range.

It is important to measure the power at the output section of the combiner, $P_{out,comb}$, without taking into account the capillary-guided power. As a result, a graphite adhesive, alcohol-based solution serving as an absorber is applied to the combiner in order to dissipate the light power led by the capillary (at the air-capillary contact, as no coating was put to the combiner).

The overall transmission efficiency $\eta_{m,overall}$ with (dotdash line) and without graphite covering (solid curve) are illustrated in Fig. 4.1.12. It is worth noting that the measured overall transmission efficiencies $\eta_{m,overall}$ with graphite covering has an almost flat behavior from NIR to Mid-IR wavelength range. The same can be asserted for the net transmission efficiency $\eta_{m,net}$. Indeed, the overall transmission efficiency $\eta_{m,overall}$ is the net transmission efficiency $\eta_{m,net}$ reduced by the coupling losses.

I conclude that the actual net transmission efficiency $\eta_{m,net}$ exhibits, as expected by simulations of Table 4.1.1 for larger beam waist $B_W = 70 \mu\text{m}$, an almost flat behavior from $\lambda = 1 \mu\text{m}$ to $\lambda = 5 \mu\text{m}$. The mean value of this net transmission efficiency is expected to be larger than $\eta_{m,net} = 80.6 \%$, which is the value accurately measured in the worst case of beam waist $B_W = 10.4 \mu\text{m}$ at the wavelength $\lambda = 1.55 \mu\text{m}$ via a balanced/compensated system.

In other words, the measurement with the broadband source proves a net transmission efficiency flat from NIR to Mid-IR reasonably close to the simulated value $\eta_{s,net} \sim 98 \%$.

4.1.2.5 Output beam measurements

To perform a far-field measurement of the beam at the output of the 3×1 fluoroindate combiner, an Ophir Pyrocam IV beam profiler has been employed. One of the three input optical fibers have been excited with an SLED source operating at the wavelength $\lambda = 1.55 \mu\text{m}$. A calibration is performed to compensate the ambient light intensity. Figure 4.1.13 a) reports the far-field measurement of the captured beam at the output of the combiner. Figure 4.1.13 b) reports near-field measurement of the beam at the output of 3×1 fluoroindate

combiner, captured, at the wavelength $\lambda = 0.635 \mu m$, by the CCD microscope camera of the Vytran[®], for the same input optical fiber of Fig. 4.1.13 a).

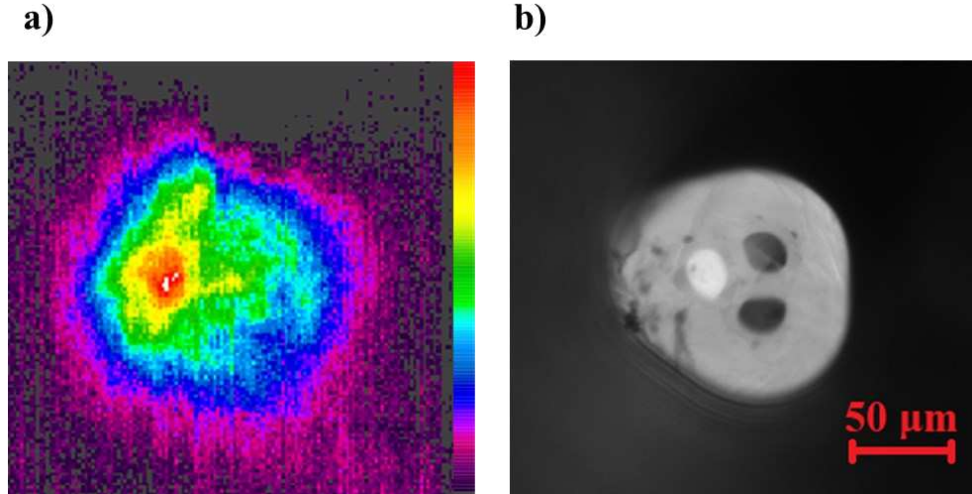


Figure 4.1.13 a) Far-field measurement of the beam at the output of the 3×1 fluoroindate combiner captured with the camera beam profiler Ophir Pyrocam IV at the wavelength $\lambda = 1.55 \mu m$; b) Near-field measurement of the beam at the output of the 3×1 fluoroindate combiner captured, at the wavelength $\lambda = 0.635 \mu m$, by the CCD microscope camera of the Vytran[®] GPX-2400 [86].

4.1.3 Conclusion

The design and fabrication of a 3×1 fluoroindate combiner for the Mid-IR wavelength range is made for the first time, also with reference to the state of the art. By employing a Vytran[®] GPX-2400 glass processing workstation, a customized manufacturing and normalizing process has been developed. This result constitutes a first important step towards reliable further fused glass components based on fluoroindate (InF_3) optical fibers. The characterization at the wavelength $\lambda = 1.55 \mu m$ demonstrates a maximum per-port net transmission efficiency of $\eta_{m,net} = 80.6\%$ in agreement with simulations. The measurement with the broadband source proves a net transmission efficiency flat from NIR to Mid-IR reasonably close to the $\eta_{s,net} \sim 98\%$. The use of commercial glass workstations and these findings open the way for the manufacture of high-quality and low-loss fluoroindate fiber combiners, enabling wavelength and power scaling and eliminating the requirement for bulk optics components and free-space optical setups.

4.2 Low-Loss Fluoride Optical Fiber Coupler for Mid-Infrared Applications

A 2×2 optical fiber coupler made of indium fluoride optical fibers is designed via CMT, fabricated by fused biconical tapering, and then characterized in the Mid-IR spectral region. A conventional glass processing system, Vytran® GPX-2400, is employed for the 2×2 optical fiber coupler fabrication, overcoming the main limitation related to the narrow temperature range for indium fluoride optical fiber processing. Moreover, the fabricated device exhibits negligible surface crystallizations. The experimental results are in optimum agreement with the simulations, demonstrating that reproducible manufacturing of low-loss fused optical fiber components for the Mid-IR spectral range is possible. In particular, the fabricated 2×2 optical fiber coupler is characterized by a measured coupling ratio $CR = 72.2:27.8$ at the wavelength $\lambda = 3.34 \mu m$, with low excess loss $E_L = 0.88 dB$. The following paragraphs are organized as follows: Section 4.2.1, the electromagnetic design of the optical fiber coupler; Section 4.2.2, the fabrication process via commercial glass processing system; Section 4.2.3, the characterization of the device in the Mid-IR spectral range; Section 4.2.4, the conclusion and the prospects.

4.2.1 Optical fiber coupler design

CMT is used to electromagnetic design the 2×2 indium fluoride optical fiber coupler and to estimate the through and cross port powers for various waist geometries [139], [209]. A schematic of an optical fiber coupler is reported in Fig. 4.2.1. More theoretical details and fiber coupler operating principle can be found in Section 2.3.1. The designed optical fiber coupler is made of two step-index indium fluoride fibers IFG MM (0.20) 28/100 from Le Verre Fluoré (Bruz, France), having core diameter $d_{co,i} = 28 \mu m$ and cladding diameter $d_{cl,i} = 100 \mu m$. The cladding diameter is smaller than that of the typical optical fibers (i.e. $d_{cl,i} = 125 \mu m$) to assist the mode coupling in the waist region. The optical fibers are inserted within a capillary with low refractive index. The capillary allows the close contact of the optical fibers, makes the optical fiber coupler robust, and facilitates the fusion process, since the larger cross-sectional area allows to make less demanding the control of the fabrication parameters. The inner

capillary diameter is $d_{in-cap,i} = 360 \mu m$, the output capillary diameter is $d_{out-cap,i} = 550 \mu m$.

The refractive index of the core and of the cladding, at the wavelength $\lambda = 3.34 \mu m$, are respectively $n_{co} = 1.4774$ and $n_{cl} = 1.4638$, resulting in a numerical aperture $NA \sim 0.20$. The capillary refractive index is $n_{cap} = 1.4618$ at the same wavelength $\lambda = 3.34 \mu m$. Figure 4.2.2 reports the measured refractive index dispersion of the core refractive index n_{co} (solid line) and of the cladding refractive index n_{cl} (dotted line) as a function of the wavelength λ , interpolated via a proper Sellmeier equation to perform realistic simulation. The effect of eventual glass component interdiffusion is neglected, so that the waist region is just a scaled-down version of the non-tapered geometry.

Finite element method (FEM) simulation results show that the effective refractive index of the mode guided in the waist region of each optical fiber, in the absence of the other optical fiber, is $n_{eff} \sim 1.4647$ at the wavelength $\lambda = 3.34 \mu m$. The electric field norm of the supermode guided in the waist region (i.e. related to the linear combination of the HE_{11} mode guided in each optical fiber), having practically the same effective refractive index $n_{eff} \sim 1.4647$, is reported in Fig. 4.2.3 and shows the field overlapping. The desired coupling ratio $C_R = 70:30$ can be obtained considering the waist length $L_W = 21.25 mm$ and the scaling factor $SF = 4.3$. Therefore, the designed core radius in the waist region is $r_{co,f} = r_{co,i}/SF = 14 \mu m/4.3 = 3.26 \mu m$ and the core-to-core distance in the waist region is $D = d_{cl,i}/SF = 100 \mu m/4.3 = 23.26 \mu m$. The optical fibers are single mode in the waist region. Down-taper and up-taper have the same length $L_{dt} = L_{ut} = 15 mm$; adiabatic transitions are designed to avoid losses related to higher order modes coupling [139].

Figure 4.2.4 reports the spectral dependence of the normalized output power of the through port P_T (solid line) and of the cross port P_C (dotted line).

Figure 4.2.5 reports the normalized output power of the through port P_T (solid line) and of the cross port P_C (dotted line), for different waist length L_w , at the wavelength $\lambda = 3.34 \mu m$. The 3D-BPM (Beam-Prop, RSoft Design Group) is also used to validate the design. The input optical fiber is excited with a gaussian beam with beam waist $B_W = 31 \mu m$. Coincident coupling ratio CR is obtained.

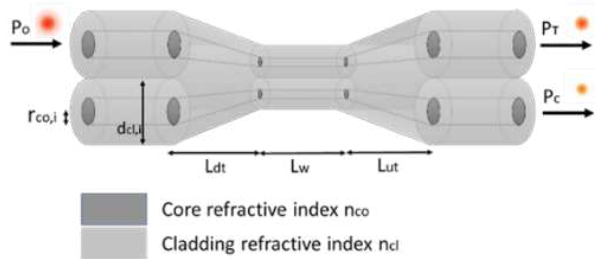


Figure 4.2.1 Sketch of an optical fiber coupler fabricated via fused biconical tapering technique; the input power P_0 is split among the through and the cross port, according to the physical and geometrical properties of the waist/coupling region, long L_W .

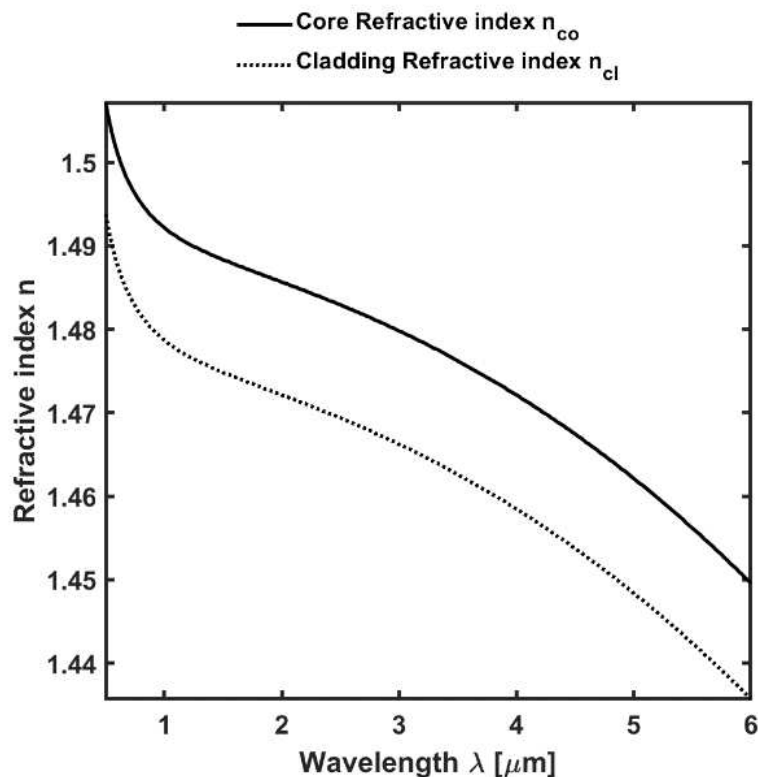


Figure 4.2.2 Dispersion of the core refractive index n_{co} (solid line) and of the cladding refractive index n_{cl} (dotted line) as a function of the wavelength λ .

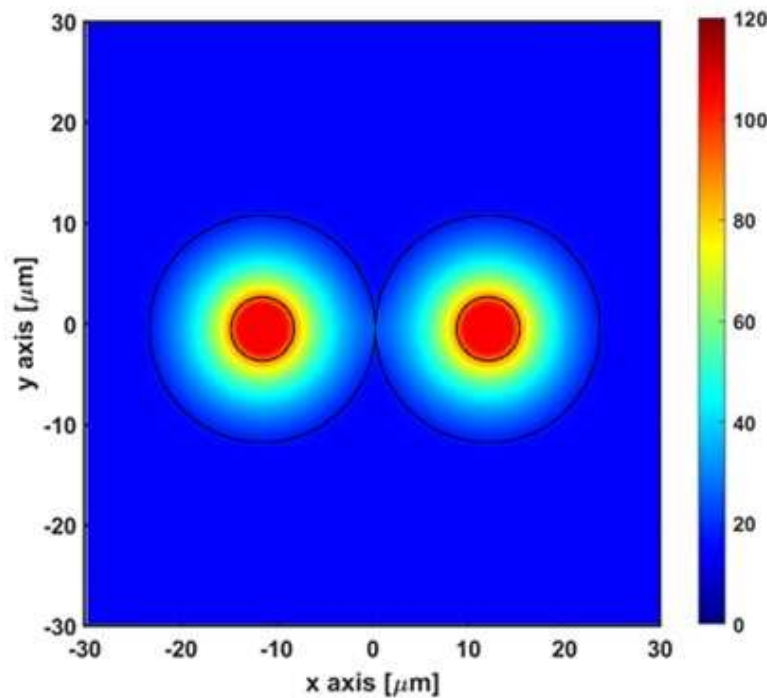


Figure 4.2.3 Electric field norm E of the supermode guided in the waist region; scaling factor $SF = 4.3$, supermode effective refractive index $n_{eff} \sim 1.4647$, at the wavelength $\lambda = 3.34 \mu m$.

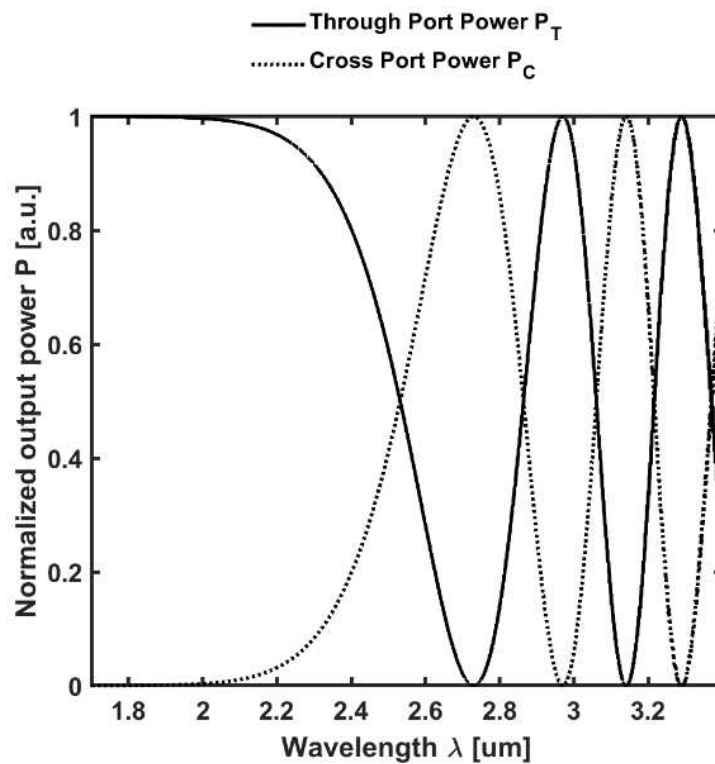


Figure 4.2.4 Normalized output power of the through port P_T (solid line) and of the cross port P_C (dotted line) as a function of the wavelength λ .

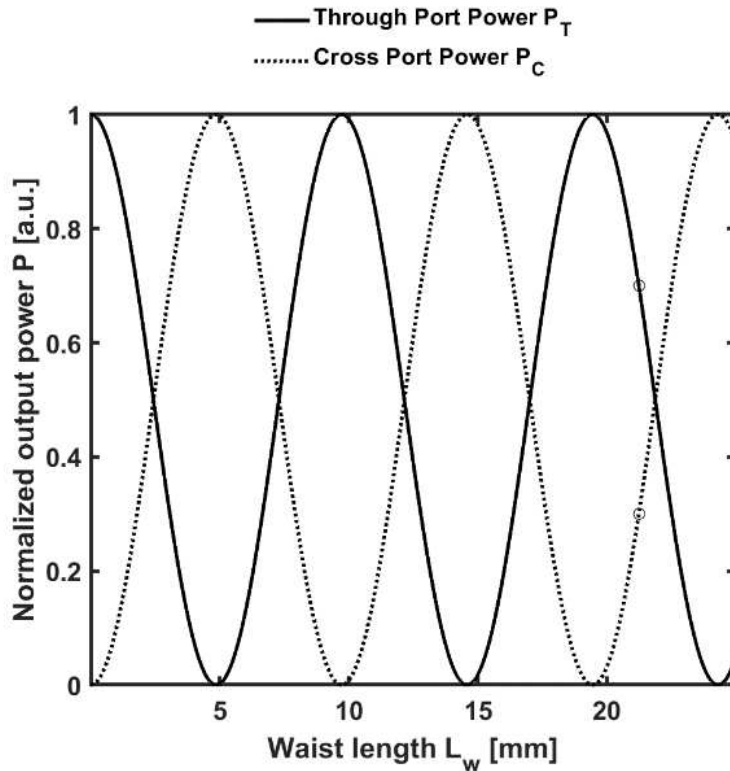


Figure 4.2.5 Normalized output power of the through port P_T (solid line) and of the cross port P_C (dotted line) as a function of the waist length L_w , at the wavelength $\lambda = 3.34 \mu\text{m}$.

4.2.2 Optical fiber coupler fabrication

Vytran® LDC-400 optical fiber cleaver is used to cleave two segments of IFG MM (0.20) 28/100. To avoid having scratches on the optical fiber end-facets, the cross-sections are examined under a microscope. The optical fiber segments are inserted in the low-index capillary, with the help of isopropyl alcohol. Alcohol excesses are then removed by the vacuum pump Linicon LV-125A. The optical fibers are not twisted to avoid eventual bend loss. The structure is clamped in the fiber holding blocks of the Vytran® GPX-2400 glass filament processing system. The room temperature is $T_r \sim 20^\circ\text{C}$, the room humidity is $RH \sim 30\%$.

Mechanical fragility, physical behavior dependent on ambient temperature and humidity, surface oxidation, glass viscosity, and interdiffusion of core, cladding, and capillary material are some of the disadvantages of indium fluoride glass [80]. Some of these downsides can be mitigated making sure that the graphite filament operates near the glass transition temperature $T_g \sim 275^\circ\text{C}$ for the entire

fabrication process and the heating is performed under controlled environment (i.e. argon flow) [86]. The main parameters pertaining the fabrication via Vytran® GPX-2400 glass filament processing system are identified through trial-and-error technique and reported in Table 4.2.1.

The quality of the optical fiber coupler transitions, the consistency of the imposed and measured dimensions, and the drawing tension behavior during the fabrication process are all taken into account for the accurate identification of the fabrication parameters. For a fixed value of the fiber holding block pull velocity v_{FHB} , a high filament power P may lead to surface crystallization, small waist diameter, or impossibility of completing the fused biconical taper. Otherwise, a low filament power may lead to big waist diameter, or capillary/optical fibers breaking. Figure 4.2.6 shows the drawing tension T during the fabrication time t , useful to identify the correct value for the initial filament power P , for the fiber holding block pull velocity v_{FHB} reported in Table 4.2.1. In particular, if the peak is negative, or close to 0 g, the glass is over softened or melted, leading to visible surface crystallization.

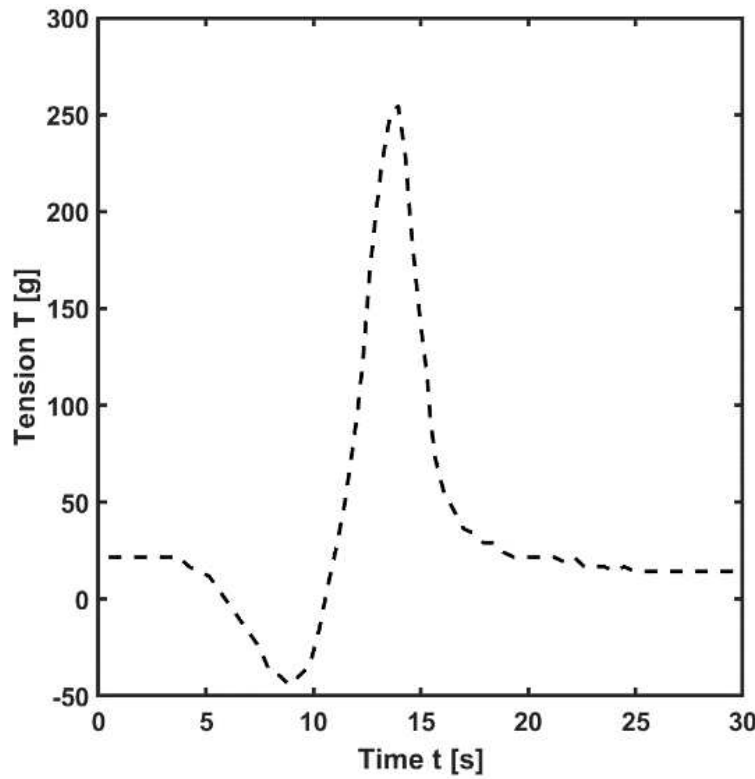


Figure 4.2.6 Drawing tension T as a function of the fabrication time t .

Table 4.2.1 Main Parameters for Vytran GPX-2400 Processing System [36].

Parameter	Value	Description
P	12.1 W	Initial filament power
v_{FHB}	500 $\mu\text{m}/\text{s}$	Fiber holding block pull velocity
T_0	19 g	Initial tension
F_{Ar}	0.35 L/min	Argon flow rate during the process

On the contrary, if the peak is too high, the initial filament power P must be increased since the glass has not reached the softening temperature T_g .

The measured waist length is $L_W \sim 21 \text{ mm}$, the capillary cross-section in the waist region is elliptical, characterized by semi-axes $a \sim 70 \mu\text{m}$ and $b \sim 90 \mu\text{m}$. The length of the semi-axes b , which is the most significant, is in good agreement with the imposed scaling factor $SF = 4.3$, i.e. $(b = 2 \times d_{cl,i} + d_{out-cap,i} - d_{in-cap,i})/SF = 90.70 \mu\text{m}$. In Fig. 4.2.7, a montage of the longitudinal micrographs captured by Vytran® GPX-2400 CCD camera is reported. Surface crystallization is very limited, indicating low excess loss E_L .

4.2.3 Optical fiber coupler characterization

In Figure 4.2.8 the schematic of the experimental set-up is reported. The fabricated device is tested via an ICL, Nanoplus Nanosystems and Technologies GmbH (Wurzburg, Germany), emitting at $\lambda = 3.34 \mu\text{m}$. The ICL has been pigtailed with indium fluoride optical fiber IFG (0.30) 9.5/125, Le Verre Fluoré (Bruz, France). The mode electromagnetic field diameter of the IFG (0.30) 9.5/125 optical fiber is $MFD = 9.7 \mu\text{m}$.

The power injected in the input optical fiber of the coupler is $P_0 = 4.4 \text{ mW}$, measured by cut-back method before the down-taper region. The excitation is performed with free-space coupling, by means of groove and Thorlabs MAX313D/M 3-axis stage.

The through P_T and cross P_C port powers are read by two thermal power sensors, i.e. PW 1 and PW 2, connected to Thorlabs PM100D console.

The fabricated coupler waist length is slightly shorter than the designed one. As a consequence, the measured coupling ratio is $C_R = 72.2 : 28.8$, very close but not coincident with the nominal $C_R = 70 : 30$. The excess loss is $E_L = 0.88 \text{ dB}$ and takes into account also the losses induced from the reduction of the modes number in the down-taper transition [210]. Indeed, the untapered optical fiber is few-mode, and the waist/coupling region just guides the fundamental mode.

Indeed, the starting geometry is a few-mode optical fiber and only the fundamental mode is guided in the waist/coupling region. Better excess loss E_L could be obtained by exploiting single-mode optical fibers. However, the achieved performance is remarkably high also with reference to the state of the art, as it can be inferred by Table 4.2.2.

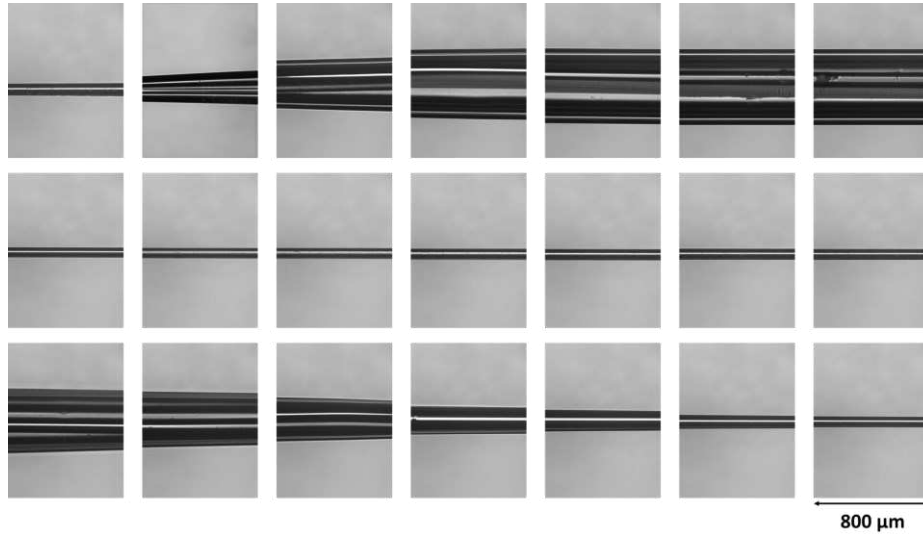


Figure 4.2.7 Montage of longitudinal micrographs (starting from top right, finishing to bottom left) of the fabricated 2×2 indium fluoride optical fiber coupler, captured via CCD camera. Each micrograph covers a length of 800 μm . Micrographs are reported with a sampling step of 1600 μm .

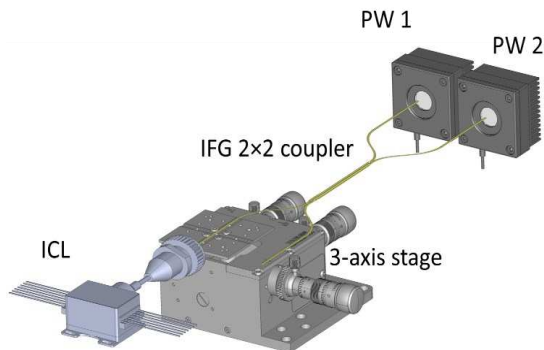


Figure 4.2.8 Sketch of the experimental set-up adopted to characterize the fabricated 2×2 indium fluoride optical fiber coupler. The ICL power is coupled in the input optical fiber of the coupler via Thorlabs MAX313D/M 3-axis stage. The cross port power P_C and the through port power P_T are measured with two thermal power sensors, i.e. PW

4.2.4 Conclusion

The design, fabrication, and characterization of a low-loss optical fiber coupler based on indium fluoride optical fibers within the Mid-IR spectral range is proposed. The measured coupling ratio is $CR = 72.2 : 27.8$, while the excess loss is $E_L = 0.88 \text{ dB}$ at the wavelength $\lambda = 3.34 \mu\text{m}$. The experimental results are in optimum agreement with the simulation. The 2×2 coupler promotes and supports research on all-in-fiber Mid-IR applications, such as high-power all-in-fiber lasers and in-band pumped Mid-IR amplifiers.

Table 4.2.2 Performance comparison between fluoride optical fiber couplers.

Ref.	Glass	Operation	Wavelength λ	Coupling Ratio C_R	Excess Loss E_L
[106]	Zirconium fluoride	Multimode	$2.00 \mu\text{m}$	50: 50	3.0 dB
[107]	Zirconium fluoride	Single mode	$2.20 \mu\text{m}$	14: 86	1.8 dB
[108]	Zirconium fluoride	Single mode	$2.70 \mu\text{m}$	61: 39	4.3 dB
[109]	Zirconium fluoride	Single mode	$2.73 \mu\text{m}$	41: 59	2.5 dB
Thesis work	Indium fluoride	Few mode	$3.34 \mu\text{m}$	72.2: 27.8	0.88 dB

5 Optical Sources for Mid-IR Sensing

Mid-IR fiber lasers have found a wide range of applications across various fields such as spectroscopy, non-destructive testing, and industrial process control. This Chapter describes the design of innovative Mid-IR CW optical fiber lasers that can be used for sensing applications.

5.1 Design of a Mid-IR laser based on a Ho:Nd-codoped fluoroindate fiber

Applications for optical sources in the Mid-IR wavelength range include laser surgery, high-speed communications, imaging, and atmospheric contamination monitoring. In this Section, a novel Mid-IR CW laser, based on a fluoroindate fiber co-doped with holmium and neodymium, is designed to emit at $\lambda_s = 3.92 \mu m$, when pumped at $\lambda_p = 808 nm$. The model of the laser takes into account a nine-level system, by taking into account experimental spectroscopical parameters. Since the energy transfer coefficients are unknown, they have been evaluated starting from the measured emission spectra of the bulk glass, reported in literature, and comparing their ratio with respect to the ratio between the simulated signal gain coefficients. When compared to holmium-heavily doped fibers, the developed laser offers improved slope efficiency and a lower power threshold. having same fiber section geometry, same refractive indices and pumped at $\lambda_p = 888 nm$. Slope efficiency $\eta = 16.67\%$ and input power threshold $P_{th} = 0.2 W$ are obtained for the fiber length $L_{fiber} = 0.4 m$, dopants concentrations $N_{Ho} = 8 \times 10^{26} ions/m^3$ and $N_{Nd} = 1 \times 10^{26} ions/m^3$, and output mirror reflectivity $R_{out} = 60\%$. This result encourages the fabrication of a continuous wave laser based on a Ho:Nd-codoped fluoroindate fiber. The following paragraphs are organized as follows: Section 5.1.1, the energy

transfer coefficients recovering; Section 5.1.2, the laser design; Section 5.1.3, results discussion; Section 5.1.4, the conclusions.

5.1.1 Energy transfer coefficients recovering

A step-index double-cladding fluoroindate (InF_3) glass fiber, doped with Ho^{3+} and Nd^{3+} ions is considered. The cross-section of the fiber is shown in Fig. 5.1.1. The core diameter is $d_{co} = 16 \mu\text{m}$. The cladding is 2-D shaped, obtained with circular diameter $d_{cl1} = 100 \mu\text{m}$ truncated by two parallel planes at a distance $d = 90 \mu\text{m}$, to enhance cladding pump absorption. The second cladding, made of low index resin, has diameter $d_{cl2} = 155 \mu\text{m}$. The inner and outer numerical apertures are $NA_1 = 0.2$ and $NA_2 = 0.5$, respectively. The optical losses are conservatively considered $\alpha = 0.2 \text{ dB/m}$ for both pump and signal wavelengths, according to the measurement reported in [126]. This kind of double cladding fiber doped with holmium is produced by Le Verre Fluoré [126], [127]. In the following, the co-doping with Ho^{3+} and Nd^{3+} ions is supposed. The pump and signal wavelengths are $\lambda_p = 808 \text{ nm}$ and $\lambda_s = 3920 \text{ nm}$, respectively. The pump wavelength is attainable with industrial pigtailed semiconductor lasers, therefore it is feasible.

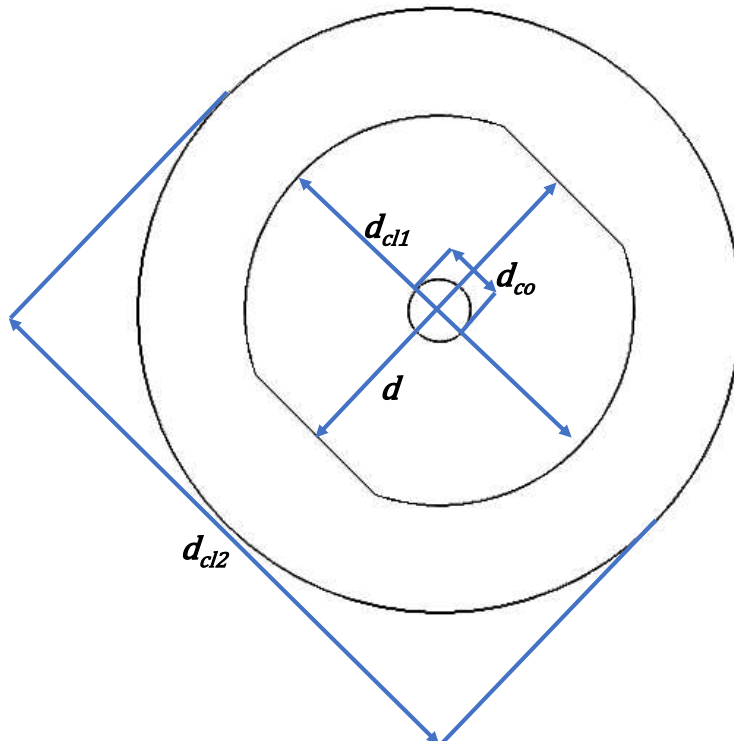


Figure 5.1.1. Transverse section of the employed double cladding fiber [74].

A commercial Finite Element Method (FEM) solver has been employed to perform the electromagnetic investigation, has shown that the fiber is slightly multimode at the normalized frequency number $V = 2.56$ of the signal wavelength. However, the second order mode can be neglected in the laser operation since its overlapping coefficient Γ_s is less than a half of the one of the fundamental mode; its contribution in the laser operation is not considered without significant error, as confirmed by preliminary simulation performed without any approximation [161]. The simulation employs the spectroscopic parameters that are listed in Table 5.1.1. They are taken from [211]-[215], [163], [164]. The ion rate equations and the power propagation equations are implemented in a home-made computer code to simulate the optical gain and the laser behavior. Since energy transfer (ET) coefficients K_{ET1} and K_{ET2} are not available from literature, they have been evaluated starting from measured emission spectra from [213] of the bulk glass and comparing their ratio with respect to the gain coefficient ratio simulated for the fiber laser, as reported below. This approach was proposed in a previous work [216]. The aforesaid comparison is feasible in the linear region of the laser characteristic.

Fig. 5.1.2 shows the measured emission spectra intensities $s_{sn}(\lambda)$ for different Ho^{3+} concentrations [213], normalized with respect to $s_{s1}(\lambda)$ for a better reading; the Nd^{3+} concentration is set to $N_{Nd} = 2 \times 10^{26} \text{ ions}/\text{m}^3$ (1 mol.%). In particular, $s_{s1}(\lambda)$ is the normalized emission spectrum intensity for $N_{Ho} = 2 \times 10^{26} \text{ ions}/\text{m}^3$ (1 mol.%) (blue curve), $s_{s2}(\lambda)$ for $N_{Ho} = 1 \times 10^{26} \text{ ions}/\text{m}^3$ (0.5 mol.%) (red curve), and $s_{s3}(\lambda)$ for $N_{Ho} = 4 \times 10^{25} \text{ ions}/\text{m}^3$ (0.2 mol.%) (yellow curve). The ratios R_n between measured emission spectra at $\lambda_s = 3920 \text{ nm}$ are defined as in Table 5.1.2. The signal gains coefficients $g_{s1}(\lambda_s)$, $g_{s2}(\lambda_s)$, and $g_{s3}(\lambda_s)$ refer to $N_{Ho} = 2 \times 10^{26} \text{ ions}/\text{m}^3$ (1 mol.%), $N_{Ho} = 1 \times 10^{26} \text{ ions}/\text{m}^3$ (0.5 mol.%), and $N_{Ho} = 4 \times 10^{25} \text{ ions}/\text{m}^3$ (0.2 mol.%), respectively. The ratios RG_n are defined as follows $RG_1 = g_{s1}(\lambda_s)/g_{s3}(\lambda_s)$; $RG_2 = g_{s1}(\lambda_s)/g_{s2}(\lambda_s)$; $RG_3 = g_{s2}(\lambda_s)/g_{s3}(\lambda_s)$.

Table 5.1.1 Spectroscopic parameters of co-doped Ho:Nd fluoroindate glass fiber.

Symbol	Value	Description
$\sigma_{15}(\lambda_p)$	$3.51 \times 10^{-24} m^2$ [163]	Absorption cross section $Nd: I_{9/2} \rightarrow F_{5/2}$
$\sigma_{51}(\lambda_p)$	$3.51 \times 10^{-24} m^2$ [163]	Emission cross section $Nd: F_{5/2} \rightarrow I_{9/2}$
$\sigma_{98}(\lambda_s)$	$3.4 \times 10^{-25} m^2$ [212]	Absorption cross section $Ho: I_6 \rightarrow I_5$
$\sigma_{89}(\lambda_s)$	$3.4 \times 10^{-25} m^2$ [212]	Emission cross section $Ho: I_5 \rightarrow I_6$
τ_{R2}	$\approx 0.01 ms$ [164]	$Nd: I_{11/2}$ radiative lifetime
τ_{R4}	$0.943 ms$ [163]	$Nd: F_{3/2}$ radiative lifetime
τ_{R5}	$0.315 ms$ [163]	$Nd: F_{5/2}$ radiative lifetime
τ_{R7}	$9.09 ms$ [211]	$Ho: I_7$ radiative lifetime
τ_{R8}	$3.66 ms$ [213]	$Ho: I_6$ radiative lifetime
τ_{R9}	$0.29 ms$ [213]	$Ho: I_5$ radiative lifetime
β_{21}	100% [163]	$Nd: I_{11/2} \rightarrow I_{9/2}$ branching ratio
β_{41}	63.7% [163]	$Nd: F_{3/2} \rightarrow I_{9/2}$ branching ratio
β_{42}	36.3% [163]	$Nd: F_{3/2} \rightarrow I_{11/2}$ branching ratio
β_{43}	$\approx 0\%$ [163]	$Nd: F_{3/2} \rightarrow I_{15/2}$ branching ratio
β_{51}	62.6% [163]	$Nd: F_{5/2} \rightarrow I_{9/2}$ branching ratio
β_{52}	37.4% [163]	$Nd: F_{5/2} \rightarrow I_{11/2}$ branching ratio
β_{53}	$\approx 0\%$ [163]	$Nd: F_{5/2} \rightarrow I_{15/2}$ branching ratio
β_{54}	$\approx 0\%$ [163]	$Nd: F_{5/2} \rightarrow F_{3/2}$ branching ratio
β_{76}	100% [212]	$Ho: I_7 \rightarrow I_8$ branching ratio
β_{86}	94.0% [212]	$Ho: I_6 \rightarrow I_8$ branching ratio
β_{87}	6.00% [212]	$Ho: I_6 \rightarrow I_7$ branching ratio
β_{96}	55.7% [212]	$Ho: I_5 \rightarrow I_8$ branching ratio
β_{97}	43.0% [212]	$Ho: I_5 \rightarrow I_7$ branching ratio
β_{98}	1.30% [212]	$Ho: I_5 \rightarrow I_6$ branching ratio
W_{NR}	$\approx 10^8 s^{-1}$ [214][215]	Non-radiative rates $Nd: F_{5/2} \rightarrow F_{3/2}$ and $Nd: F_{15/2} \rightarrow F_{11/2}$

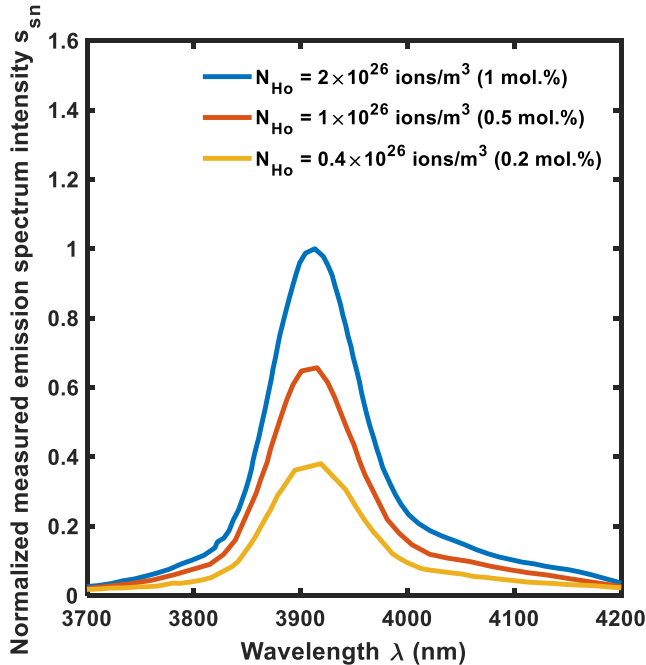


Figure 5.1.2 Normalized measured emission spectra intensities s_{sn} as a function of the wavelength λ , for different Ho^{3+} concentrations; Nd^{3+} concentration is set to $N_{Nd} = 2 \times 10^{26} \text{ ions}/\text{m}^3$ (1 mol.%) [213], [74].

Table 5.1.2 Emission spectra ratios.

Symbol	Expression	Description
R_1	$s_{s1}(\lambda_s)/s_{s3}(\lambda_s)$	Ratio between the normalized emission spectra at signal wavelength for $N_{Ho} = 2 \times 10^{26} \text{ ions}/\text{m}^3$ and $N_{Ho} = 4 \times 10^{25} \text{ ions}/\text{m}^3$
R_2	$s_{s1}(\lambda_s)/s_{s2}(\lambda_s)$	Ratio between the normalized emission spectra at signal wavelength for $N_{Ho} = 2 \times 10^{26} \text{ ions}/\text{m}^3$ and $N_{Ho} = 1 \times 10^{26} \text{ ions}/\text{m}^3$
R_3	$s_{s2}(\lambda_s)/s_{s3}(\lambda_s)$	Ratio between the normalized emission spectra at signal wavelength for $N_{Ho} = 1 \times 10^{26} \text{ ions}/\text{m}^3$ and $N_{Ho} = 4 \times 10^{25} \text{ ions}/\text{m}^3$

Fig. 5.1.3(a), Fig. 5.1.3(b), and Fig. 5.1.3(c) show the colormaps of the percentage difference between the ratios $(R_n - RG_n)/R_n$ as a function of the trial energy transfer coefficients K_{ET1} and K_{ET2} .

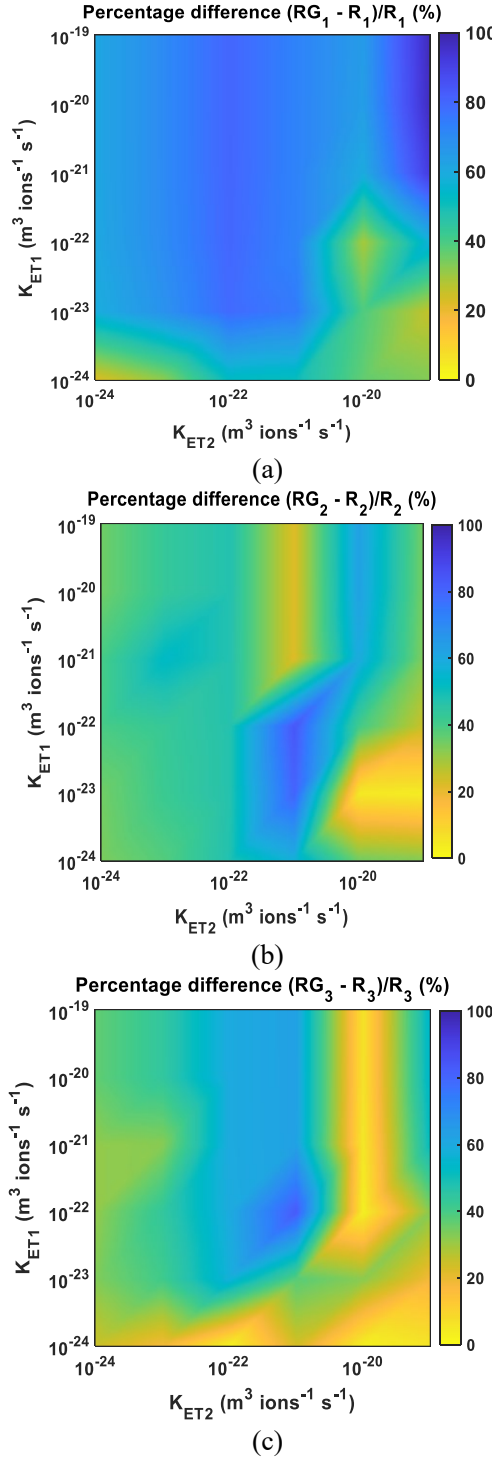


Figure 5.1.3 (a) Percentage difference $(RG_1 - R_1)/R_1$, (b) percentage difference $(RG_2 - R_2)/R_2$, and (c) percentage difference $(RG_3 - R_3)/R_3$ as a function of energy transfer coefficients K_{ET1} and K_{ET2} [74].

These three percentage differences must be contemporarily minimized. This condition is obtained for $K_{ET1} = 4 \times 10^{-22} m^3 ions^{-1} s^{-1}$ and $K_{ET2} = 6 \times 10^{-21} m^3 ions^{-1} s^{-1}$, for which $(R_1 - RG_1)/R_1 = 8\%$, $(R_2 - RG_2)/R_2 = 1\%$, and $(R_3 - RG_3)/R_3 = 0.7\%$. Table 5.1.3 reports the simulated signal gain coefficient ratios RG_n for the recovered $K_{ET1} = 4 \times 10^{-22} m^3 ions^{-1} s^{-1}$ and $K_{ET2} = 6 \times 10^{-21} m^3 ions^{-1} s^{-1}$ compared to the measured emission spectra ratios R_n . The signal gain coefficient ratios RG_n are obtained considering the same average pump energy of [213], i.e., $P_p = 0.4 W$, neodymium concentration $N_{Nd} = 2 \times 10^{26} ions/m^3$ (1 mol.%), and holmium concentrations $N_{Ho} = 2 \times 10^{26} ions/m^3$ (1 mol.%), $N_{Ho} = 1 \times 10^{26} ions/m^3$ (0.5 mol.%), and $N_{Ho} = 0.4 \times 10^{26} ions/m^3$ (0.2 mol.%). This allows a proper comparison with R_n .

Table 5.1.3 Emission spectra and signal gain coefficient ratios comparison.

Emission spectra ratio R_n	Signal gain coefficient ratio RG_n
$R_1 = 2.63$	$RG_1 = 2.42$
$R_2 = 1.54$	$RG_2 = 1.51$
$R_3 = 1.62$	$RG_3 = 1.61$

These results have been validated since the global $Ho:I_5$ level lifetime τ'_{R9} and the global $Ho:I_6$ level lifetime τ'_{R8} have been simulated and compared with the experimental ones taken from literature [213], for different holmium concentrations N_{Ho} . The lifetimes have been simulated solving the rate equations (2.17a)-(2.17j) as a function of time, pumping the system until the ion populations steady-state condition. Therefore, the pump power is turned off, setting $P_p = 0 W$, and the simulated population exponential decays are observed. The level lifetimes are calculated as the time constants of the obtained exponential curves.

Fig. 5.1.4 shows the $Ho:I_5$ level lifetime τ'_{R9} and the $Ho:I_6$ level lifetime τ'_{R8} simulated (blue) and measured (red) [213] as a function of the holmium concentration N_{Ho} . The good accordance confirms that the recovered energy transfer coefficients K_{ET1} and K_{ET2} are correct.

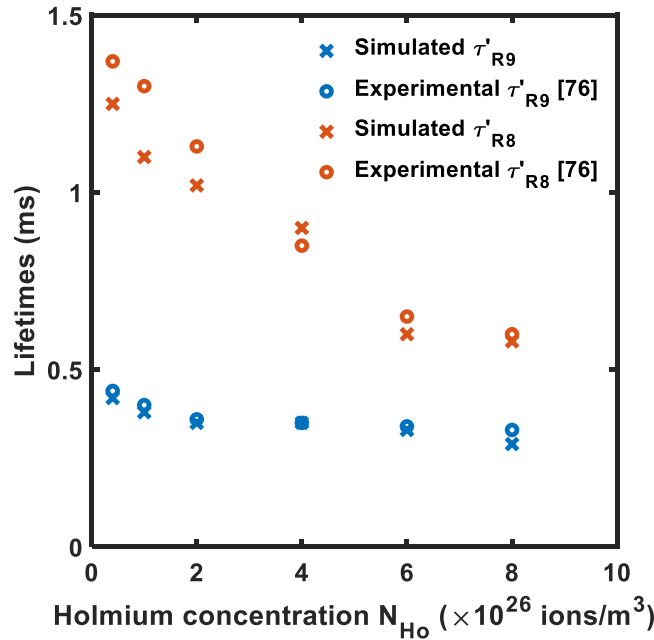


Figure 5.1.4 $Ho:I_5$ level lifetime τ'_R9 and the $Ho:I_6$ level lifetime τ'_R8 as a function of the holmium concentration N_{Ho} , comparing simulated (blue) and measured [213] (red) values; $N_{Nd} = 2 \times 10^{26}$ ions/m³ (1 mol.%) [74].

5.1.2 Laser design

The design of the laser has been conducted via a deep investigation of the laser output signal power P_s versus: i) the laser fiber length L_{fiber} ; ii) the dopants concentration N_{Nd} and N_{Ho} ; iii) the output mirror reflectivity R_2 is carried out, in order to identify the configuration allowing the maximum slope efficiency η and the minimum threshold power P_{th} .

Fig. 5.1.5 shows the output power P_s as a function of the input pump power P_p , for different values of the fiber length L_{fiber} . The characteristics show a discontinuity with a sawtooth shape in all cases. The reason behind this behavior will be deeply investigated in Section 5.1.3. The discontinuity shifts towards higher pump power as the fiber length L_{fiber} increases. Moreover, the slope efficiency η slightly decreases, while the input pump threshold is close to $P_{th} = 0.5 W$ in all cases. It is worthy to observe that experiments in literature suggest avoiding input power larger than $P_p = 6 W$ in typical fluoroindate fibers [127]. In a lightly doped fiber higher pumping levels could be potentially employed. Therefore, a different cavity optimization could be required. A good trade-off length is $L_{fiber} = 0.4 m$, for which the discontinuity occurs be-

yond the realistic range of power, i.e., for $P_p = 8 W$, and for which the efficiency $\eta = 8.47\%$ is obtained. The slope efficiency is calculated after the threshold, between $P_p = 1 W$ and $P_p = 1.5 W$.

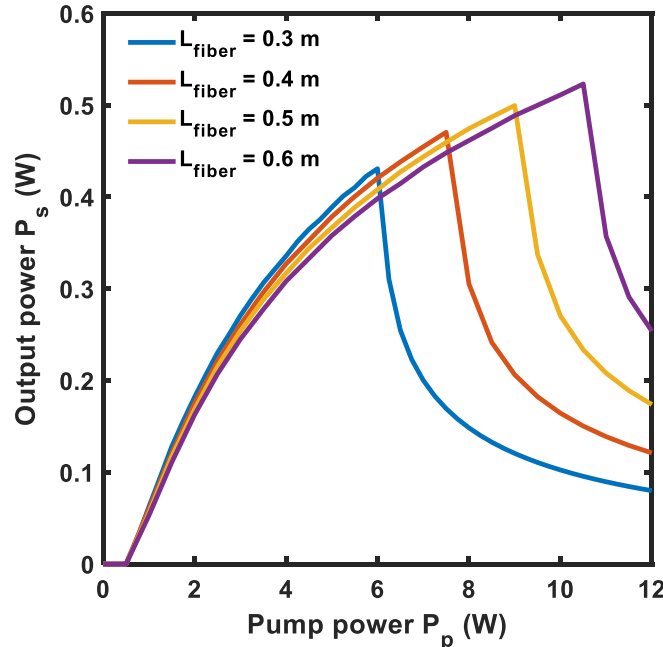


Figure 5.1.5 Output power P_s as a function of the input pump power P_p , for different values of the fiber length L_{fiber} . Holmium concentration $N_{Ho} = 2 \times 10^{26} \text{ ions}/m^3$ (1 mol.%), neodymium concentration $N_{Nd} = 2 \times 10^{26} \text{ ions}/m^3$ (1 mol.%), input mirror reflectivity $R_{in} = 99\%$, output mirror reflectivity $R_{out} = 70\%$ [74].

Fig. 5.1.6 shows the output power P_s as a function of the input pump power P_p , for different values of the holmium concentration N_{Ho} . As the concentration increases, the slope efficiency η also increases and the discontinuity shifts to higher input pump powers. The input pump threshold decreases to $P_{th} = 0.1 W$. The optimal holmium concentration is the maximum considered in the simulations $N_{Ho} = 8 \times 10^{26} \text{ ions}/m^3$ (4 mol%) (purple curve). Generally, higher holmium concentrations are not used in practice to avoid second order phenomena, such as cross-relaxation or up-conversion.

Fig. 5.1.7 shows the output power P_s as a function of the input pump power P_p , for different values of neodymium concentration N_{Nd} . As the concentration increases, the slope efficiency η slightly increases until $N_{Nd} = 1 \times 10^{26} \text{ ions}/m^3$ (0.5 mol%) (yellow curve), while the input pump threshold P_{th} always decreases. The value $N_{Nd} = 1 \times 10^{26} \text{ ions}/m^3$ (0.5 mol%) can be considered as optimized, allowing the highest efficiency and a good input pump threshold $P_{th} = 0.15 W$.

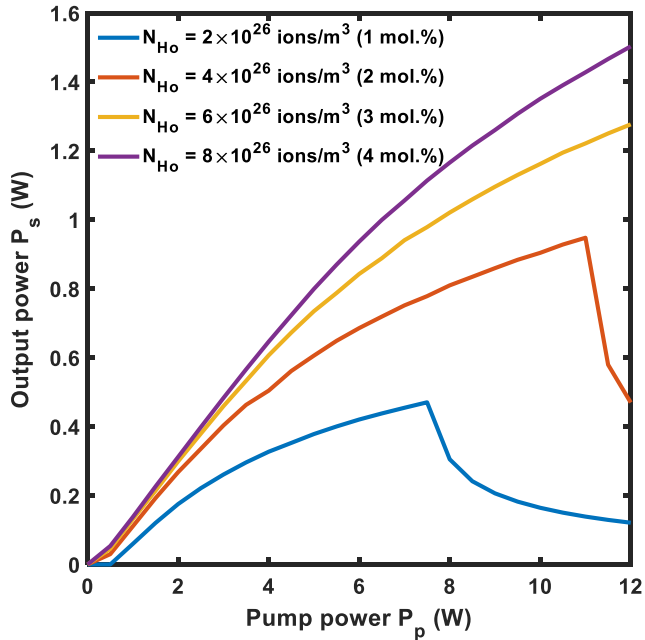


Figure 5.1.6 Output power P_s as a function of the input pump power P_p , for different values of the holmium concentration N_{Ho} . Fiber length $L_{fiber} = 0.4\text{ m}$, neodymium concentration $N_{Nd} = 2 \times 10^{26}\text{ ions}/\text{m}^3$ (1 mol.%), input mirror reflectivity $R_{in} = 99\%$, output mirror reflectivity $R_{out} = 70\%$.

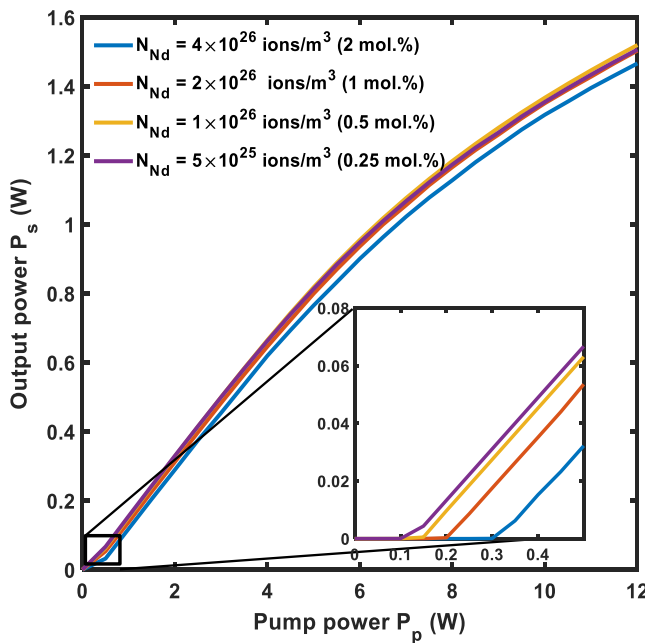


Figure 5.1.7 Output power P_s as a function of the input pump power P_p , for different values of the neodymium concentration N_{Nd} . Fiber length $L_{fiber} = 0.4\text{ m}$, holmium concentration $N_{Ho} = 8 \times 10^{26}\text{ ions}/\text{m}^3$ (4 mol.%), input mirror reflectivity $R_{in} = 99\%$, output mirror reflectivity $R_{out} = 70\%$ [74].

Fig. 5.1.8 shows the output power P_s as a function of the input pump power P_p , for different values of output mirror reflectivity R_{out} . The slope efficiency η increases as the output mirror reflectivity R_{out} decreases until $R_{out} = 60\%$, while the input pump threshold P_{th} decreases from $P_{th} = 0.3\text{ W}$ to $P_{th} = 0.05\text{ W}$.

The optimal laser configuration is obtained for fiber length $L_{fiber} = 0.4\text{ m}$, holmium concentration $N_{Ho} = 8 \times 10^{26}\text{ ions/m}^3$, neodymium concentration $N_{Nd} = 1 \times 10^{26}\text{ ions/m}^3$, and output mirror reflectivity $R_{out} = 60\%$, allowing the slope efficiency $\eta = 16.67\%$ and the input pump threshold $P_{th} = 0.2\text{ W}$. These simulated performances are better than those typical of CW lasers obtained with heavily-holmium-doped fiber with the same geometry, pumped at $\lambda_p = 888\text{ nm}$, showing $\eta = 10.2\%$ and input pump threshold $P_{th} = 4.3\text{ W}$ [127].

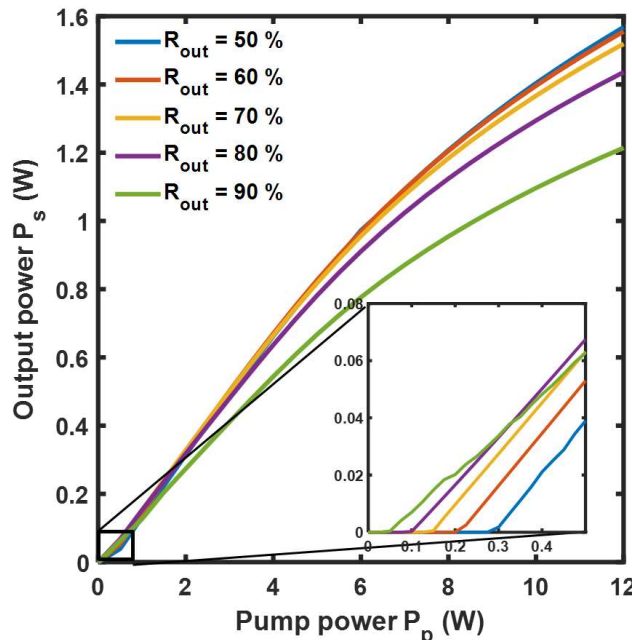


Figure 5.1.8 Output power P_s as a function of the input pump power P_p , for different values of the output mirror reflectivity R_{out} . Fiber length $L_{fiber} = 0.4\text{ m}$, holmium concentration $N_{Ho} = 8 \times 10^{26}\text{ ions/m}^3$ (4 mol.%), neodymium concentration $N_{Nd} = 1 \times 10^{26}\text{ ions/m}^3$ (0.5 mol.%), input mirror reflectivity $R_{in} = 99\%$ [74].

5.1.3 Results discussion

By the inspection of the energy level diagram of Fig. 9.4, for each ion couple involved in the ET2 transition an energy loss equal to the energy difference $\Delta E = 1.7 \times 10^3\text{ cm}^{-1}$ [213] between level 8 and level 3 occurs, due to the 1-3

and 8-6 transitions. This energy leakage could be the cause of the sawtooth. Indeed, simulating the system without ET2 effect, by putting null K_{ET2} , the laser shows the typical characteristic with a pump threshold $P_{th} = 0.6\text{ W}$, a slope efficiency $\eta = 0.2\%$, and a saturation power $P_{ss} = 4.3\text{ W}$, without any sawtooth.

Fig. 5.1.9 shows the output power P_s (blue curve) and the output residual pump power P_{res} at the end of the fiber (red curve) as a function of the input pump power P_p . The output residual pump power P_{res} steeply increases when the output signal P_s shows the discontinuity, close to $P_p = 7.5\text{ W}$. For larger values of the input pump power P_p , a large amount is not absorbed, reaching about the 50 % for $P_p = 12\text{ W}$. This is plausibly caused by a too large depopulation of level 1 ($Nd: I_{9/2}$), reducing ET2 effect. By simulation, the N_1 ion population at the end of the fiber steeply decreases for pump power higher than $P_p = 7.5\text{ W}$. Therefore, few ions can be promoted from level 1 to level 3 ($Nd: I_{15/2}$) and the related transition 8-6 does not occur efficiently. Accordingly with this phenomenon, for pump power larger than $P_p = 7.5\text{ W}$, the N_8 ion population steeply increases affecting the laser population inversion. This could be a further cause of the sawtooth.

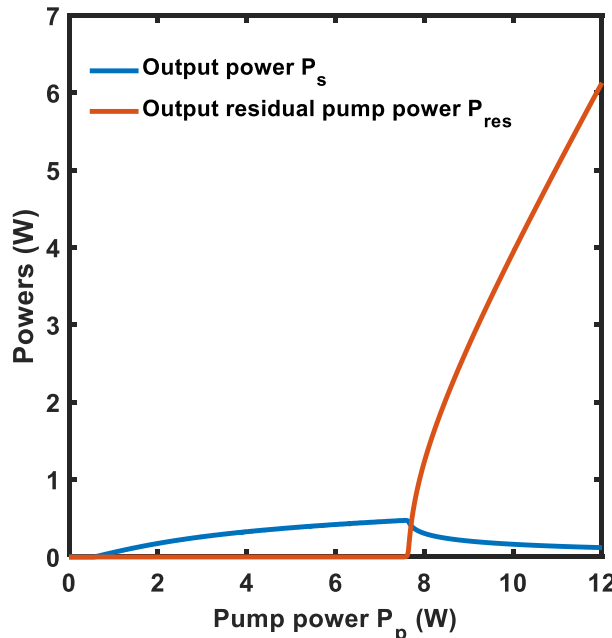


Figure 5.1.9 Output power P_s (blue curve) and output residual pump power P_{res} (red curve) as a function of the input pump power P_p . Fiber length $L_{fiber} = 0.4\text{ m}$, holmium concentration $N_{Ho} = 2 \times 10^{26}\text{ ions/m}^3$ (1 mol.%), neodymium concentration $N_{Nd} = 2 \times 10^{26}\text{ ions/m}^3$ (1 mol.%), input mirror reflectivity $R_{in} = 99\%$, output mirror reflectivity $R_{out} = 70\%$ [74].

5.1.4 Conclusions

By using measured and recovered spectroscopic parameters, a CW laser emitting at $\lambda_s = 3.92 \mu m$, based on a fluorinated glass fiber co-doped with holmium and neodymium, is designed for the first time, to the best of my knowledge.

By considering an input pump power at the wavelength $\lambda_p = 808 nm$, a fiber length $L_{fiber} = 0.4 m$, an holmium concentration $N_{Ho} = 8 \times 10^{26} ions/m^3$ (4 mol.%), a neodymium concentration $N_{Nd} = 1 \times 10^{26} ions/m^3$ (0.5 mol.%), and an output mirror reflectivity $R_{out} = 60 \%$, a slope efficiency $\eta = 16.67 \%$ and an input pump threshold $P_{th} = 0.2 W$ can be obtained. If compared to the efficiency achievable with fiber doped with holmium, this finding is interesting.

5.2 Design of a Broadband Erbium-doped Fluorodate Fiber Laser Emitting up to 3.91 μm

An home-made code is developed to carry out to design and optimization of an erbium-doped fluoroindate fiber laser pumped at 635 nm and emitting up to $3.91 \mu\text{m}$. The used fiber has a double D-shaped geometry and is provided by Le Verre Fluoré. Continuous-wave laser emission is obtained thanks to the population inversion between the $^4\text{F}_{9/2}$ and $^4\text{I}_{9/2}$ energy levels. The model takes into account measured spectroscopic parameters for the absorption, stimulated emission and spontaneous decay processes. The device performance is investigated by varying several parameters, such as the input pump power, the fiber length, the dopant concentration, the output mirror reflectivity and the signal wavelength. The proposed device is very versatile and is optimized for different scenarios, including: the shortest fiber, the highest output power and the lowest threshold. Simulation results show that the best performance in terms of emission bandwidth is obtained for the laser with the lowest threshold, i.e. only 25 mW , predicting a broadband coherent emission in the $3.25 - 3.91 \mu\text{m}$ wavelength range and paving the way to the fabrication of a low-cost and easy-to-pump Mid-IR fiber laser. The following paragraphs are organized as follows: Section 5.2.1, the laser design; Section 5.2.2, the laser refinement; Section 5.2.3, the conclusions.

5.2.1 Laser design

The laser scheme is reported in Fig. 5.2.1 by considering an erbium-doped fiber produced by Le Verre Fluoré and characterized by a double D-shaped geometry. In particular, the core diameter is $d_{co} = 16 \mu\text{m}$ and the inner cladding diameter is $d_{icl} = 100 \mu\text{m}$. The distance at which the inner cladding is cut is $d_{cut} = 90 \mu\text{m}$. The total area calculated as described in Section 2.4.2 is $A_p = 7560 \mu\text{m}^2$, leading to a normalized pump intensity distribution $i_p = 132.3 \mu\text{W}/\mu\text{m}^2$.

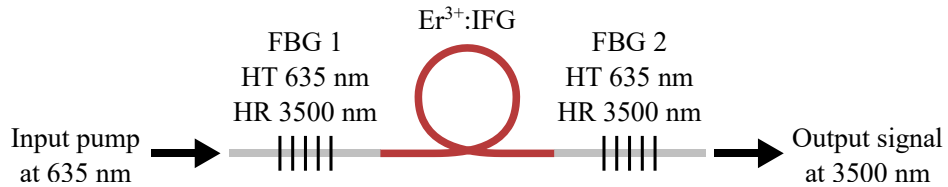


Figure 5.2.1 Schematic of the device.

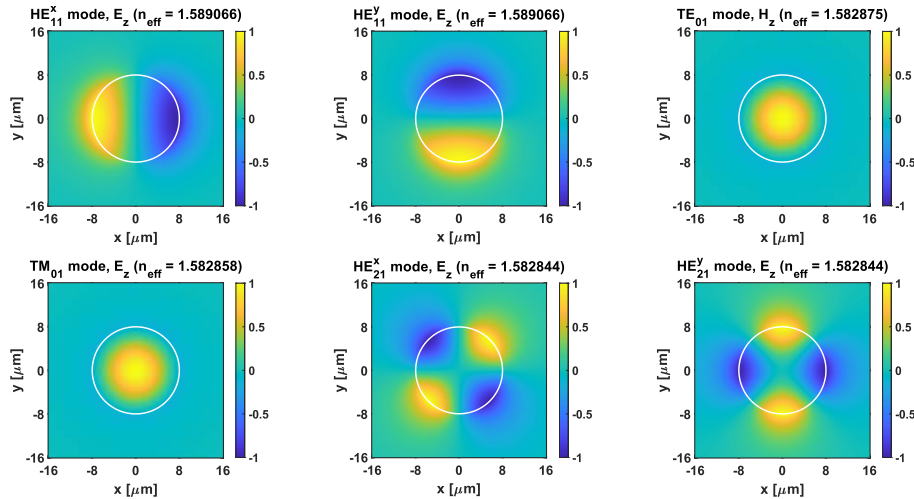


Figure 5.2.2 Longitudinal components E_z/H_z and effective mode indices for the six guided optical modes of the double D-shaped fluoroindate fiber at the signal wavelength $\lambda_s = 3500 \text{ nm}$. The fiber core is represented by the white circle.

The glass refractive index is close to $n_{IFG}(\lambda_s) = 1.5$ at the signal wavelength $\lambda_s = 3.5 \mu\text{m}$ and $n_{IFG}(\lambda_p) = 1.51$ at the pump wavelength $\lambda_p = 635 \text{ nm}$ [86]. The core/inner cladding and the inner/outer claddings numerical apertures are $NA_1 = 0.2$ and $NA_2 = 0.5$, respectively. The background losses at the pump and signal wavelengths are $\alpha(\lambda_p) = 0.25 \text{ dB/m}$ and $\alpha(\lambda_s) = 0.0045 \text{ dB/m}$, respectively. Fig. 5.2.2 shows the longitudinal field components and the effective mode indices for the guided modes inside the core of the fluoroindate fiber at the signal wavelength $\lambda_s = 3.5 \mu\text{m}$, obtained through a FEM analysis.

The spectroscopic parameters for the erbium ions in the fluorindate glass are reported in Table 5.2.1 and were taken from the literature [162], [163], [217]. The pump absorption cross section is assumed equal to emission cross section. The design of the laser is performed by studying the output signal power, when the dopant concentration increases from a low to a high value in the range $N_{Er} = 2 \times 10^{25} - 8 \times 10^{25} \text{ ions/m}^3$ (see Figs. 5.2.3-5.2.5). The input mirror

reflectivity is kept fixed to $R_1 = 99\%$, in agreement with the recent advances on inscription of FBGs in fluoroindate fibers [218]. Co-directional pumping is considered with an input pump power equal to $P_{p0}^+ = P_{p0}^- = 1 \text{ W}$. It is worth noting that a positive optical gain was achieved only for the fundamental mode HE_{11} , even with input pump powers up to $P_{p0} = 10 \text{ W}$, thanks to its higher overlap coefficient compared with those of the higher order modes. In the following, step sizes equal to $\Delta L = 10 \text{ cm}$ and $\Delta R_2 = 2\%$ are assumed for discretizing the fiber length L and the output mirror reflectivity R_2 , respectively. Fig. 5.2.3 shows the output signal power P_{out} as a function of the fiber length L and the output mirror reflectivity R_2 , for a low dopant concentration $N_{Er} = 2 \times 10^{25} \text{ ions/m}^3$. Output powers of at least $P_{out} = 1 \text{ mW}$ are obtained for $L = 0.5 \text{ m}$ and $R_2 = 97\%$. Similar output powers can be achieved when the fiber length is increased while the reflectance is decreased. The value of L and R_2 should both be increased for better results. The maximum output power $P_{out} = 10 \text{ mW}$ is achieved only for very long fibers, i.e. $L > 4.6 \text{ m}$, requiring an output mirror reflectivity around $R_2 \approx 90\%$.

Fig. 5.2.4 shows the output signal power P_{out} as a function of the fiber length L and the output mirror reflectivity R_2 , for an intermediate dopant concentration $N_{Er} = 5 \times 10^{25} \text{ ions/m}^3$. In this case, thanks to the higher optical gain, similar output powers are obtained with shorter fibers and smaller reflectivities. It is also apparent that, for lengths greater than $L = 4 \text{ m}$, the signal power is almost independent of the fiber length value. The shortest fiber length providing at least $P_{out} = 1 \text{ mW}$ is close to $L = 0.2 \text{ m}$, again with $R_2 = 97\%$. The maximum output power $P_{out} = 14 \text{ mW}$ is achieved for the fiber length $L = 3.2 \text{ m}$, with an output mirror reflectivity around $R_2 \approx 88\%$.

The output signal power P_{out} as a function of the fiber length L and the output mirror reflectivity R_2 , for a high dopant concentration $N_{Er} = 8 \times 10^{25} \text{ ions/m}^3$ is reported in Fig. 5.2.5. Although an even higher concentration improves the overall efficiency, the benefit is marginal. In fact, the achievable power levels are very close to the previous case and saturation already occurs for lengths greater than $L = 2.5 \text{ m}$. The maximum output power increases by only one mW, reaching $P_{out} = 15 \text{ mW}$ when the fiber length is $L = 2.4 \text{ m}$ and the output reflectivity is $R_2 = 97\%$. To avoid the occurrence of concentration quenching phenomena and detrimental nonlinear effects the dopant concentration has been kept at the intermediate value of $N_{Er} = 5 \times 10^{25} \text{ ions/m}^3 \approx 0.26 \text{ mol \%}$.

Table 5.2.1 Spectroscopic parameters for the erbium-doped fluoroindate glass

Parameter	Value	Description
λ_p	635 nm	Pump wavelength
λ_s	3.5 μm	Signal wavelength
λ_c	4.2 μm	Fiber cut-off wavelength
$\sigma_{15}(\lambda_p)$	$1.1547 \times 10^{-24} \text{ m}^2$	Pump absorption cross section
$\sigma_{51}(\lambda_p)$	$1.1547 \times 10^{-24} \text{ m}^2$ [163], [217]	Pump emission cross section
$\sigma_{45}(\lambda_s)$	$4.6058 \times 10^{-26} \text{ m}^2$ [162]	Signal absorption cross section
$\sigma_{54}(\lambda_s)$	$4.8468 \times 10^{-26} \text{ m}^2$ [162]	Signal emission cross section
τ_2	12.57 ms [162]	${}^4\text{I}_{13/2}$ energy level lifetime
τ_3	10.49 ms [162]	${}^4\text{I}_{11/2}$ energy level lifetime
τ_4	8.33 ms [162]	${}^4\text{I}_{9/2}$ energy level lifetime
τ_5	1.04 ms [162]	${}^4\text{F}_{9/2}$ energy level lifetime
β_{21}	100 % [162]	${}^4\text{I}_{13/2} \rightarrow {}^4\text{I}_{15/2}$ branching ratio
β_{32}	14.23 % [162]	${}^4\text{I}_{11/2} \rightarrow {}^4\text{I}_{13/2}$ branching ratio
β_{31}	85.77 % [162]	${}^4\text{I}_{11/2} \rightarrow {}^4\text{I}_{15/2}$ branching ratio
β_{43}	0.53 % [162]	${}^4\text{I}_{9/2} \rightarrow {}^4\text{I}_{11/2}$ branching ratio
β_{42}	22.80 % [162]	${}^4\text{I}_{9/2} \rightarrow {}^4\text{I}_{13/2}$ branching ratio
β_{41}	76.67 % [162]	${}^4\text{I}_{9/2} \rightarrow {}^4\text{I}_{15/2}$ branching ratio
β_{54}	0.21 % [162]	${}^4\text{F}_{9/2} \rightarrow {}^4\text{I}_{9/2}$ branching ratio
β_{53}	4.38 % [162]	${}^4\text{F}_{9/2} \rightarrow {}^4\text{I}_{11/2}$ branching ratio
β_{52}	4.99 % [162]	${}^4\text{F}_{9/2} \rightarrow {}^4\text{I}_{13/2}$ branching ratio
β_{51}	90.43 % [162]	${}^4\text{F}_{9/2} \rightarrow {}^4\text{I}_{15/2}$ branching ratio

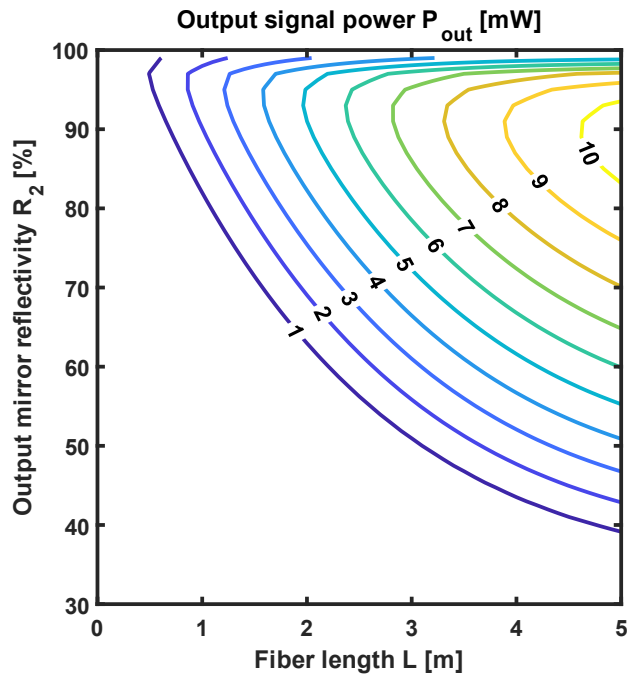


Figure 5.2.3 Output signal power P_{out} as a function of the fiber length L and the output mirror reflectivity R_2 . Input pump power $P_{p0} = 1\text{ W}$, dopant concentration $N_{Er} = 2 \times 10^{25}\text{ ions/m}^3$, input mirror reflectivity $R_1 = 99\%$.

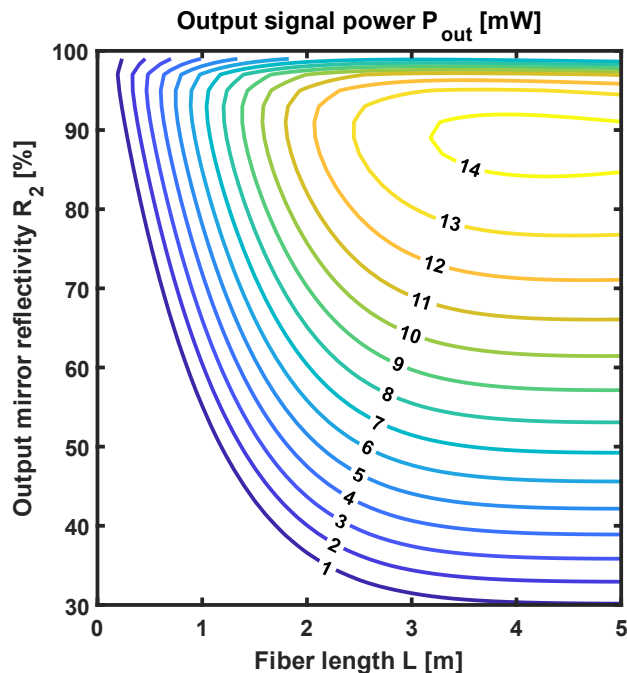


Figure 5.2.4 Output signal power P_{out} as a function of the fiber length L and the output mirror reflectivity R_2 . Input pump power $P_{p0} = 1\text{ W}$, dopant concentration $N_{Er} = 5 \times 10^{25}\text{ ions/m}^3$, input mirror reflectivity $R_1 = 99\%$.

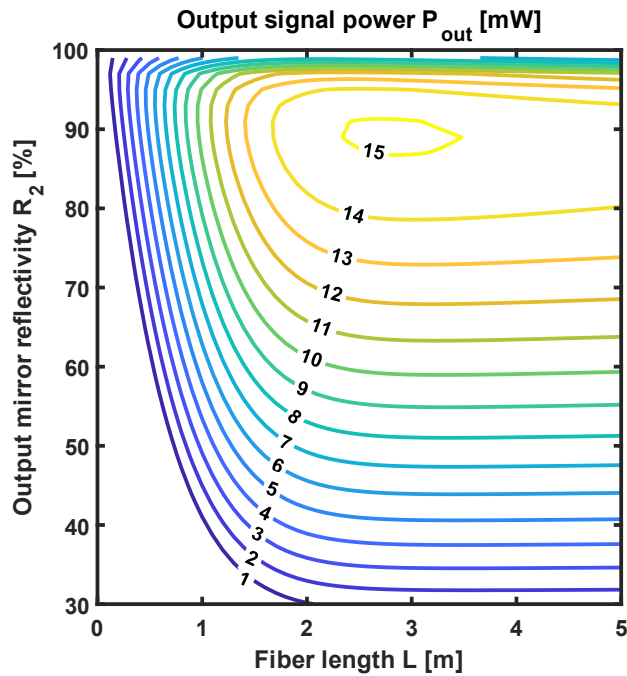


Figure 5.2.5 Output signal power P_{out} as a function of the fiber length L and the output mirror reflectivity R_2 . Input pump power $P_{p0} = 1 \text{ W}$, dopant concentration $N_{Er} = 8 \times 10^{25} \text{ ions/m}^3$, input mirror reflectivity $R_1 = 99\%$.

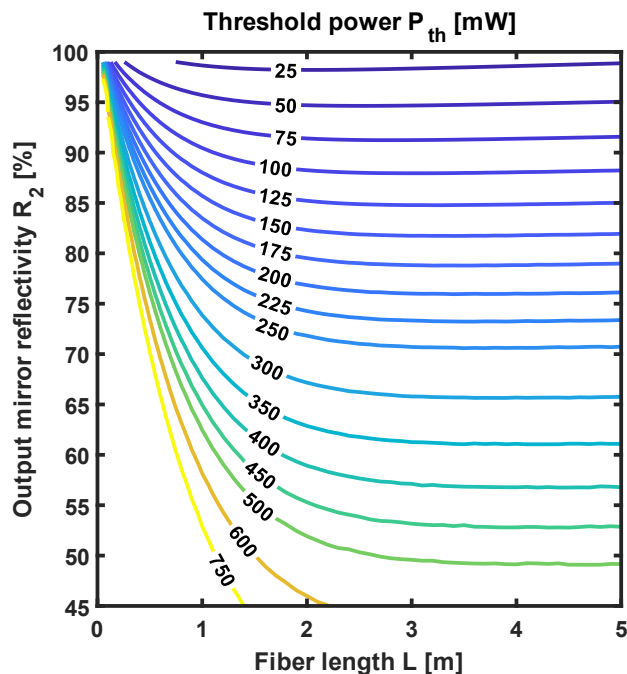


Figure 5.2.6 Threshold power P_{th} as a function of the fiber length L and the output mirror reflectivity R_2 . Dopant concentration $N_{Er} = 5 \times 10^{25} \text{ ions/m}^3$, input mirror reflectivity $R_1 = 99\%$.

By using an Er^{3+} concentrations up to 9 mol % as reported in [162] no quenching in the $\lambda = 3.5 \mu\text{m}$ emission spectrum was observed. Moreover, another important feature for a laser is the threshold power P_{th} , here defined as the input pump power value required to obtain a signal power of at least $P_{out} = 10 \mu\text{W}$.

Fig. 5.2.6 shows the threshold power P_{th} as a function of the fiber length L and the output mirror reflectivity R_2 . The threshold power strongly depends on the output reflectivity, but becomes almost insensitive to the length for fibers longer than $L = 2.5 \text{ m}$. Similar thresholds are obtained by simultaneously increasing the fiber length and reducing the output reflectivity. The mirror reflectivity must be kept higher than $R_2 = 86 \%$ if threshold powers less than $P_{th} = 100 \text{ mW}$ are desired. On the other hand, if the mirror reflectivity is less than $R_2 = 49 \%$, at least half a watt of pump is needed to achieve lasing.

5.2.2 Refinement

The results reported in the previous Section show that obtaining an exclusive laser configuration that delivers the maximum output power and the lowest threshold power at the same time is not feasible. Moreover, no information regarding the laser bandwidth can be inferred. To overcome these issues, three different scenarios are considered for optimizing the device: (I) shortest fiber, (II) highest output power and (III) lowest threshold. In the first scenario, the goal is to shorten the fiber as much as possible in order to obtain a coherent light source in the Mid-IR which is very compact and, hence, affordable. It was accomplished by selecting, in Fig. 5.2.4, the curve corresponding to the shortest fiber, i.e. $L = 19.3 \text{ cm}$, still proving an output power of $P_{out} = 1 \text{ mW}$. The required mirror reflectivity is $R_2 = 97\%$. In the second instance, the objective is to maximize the signal power for a given input pump power in order to obtain laser emission with the highest output power while using the greatest amount of pump power. It was accomplished by selecting, in Fig. 5.2.4, the point at the center of the region bounded by the yellow contour line, having coordinates $L = 4.3 \text{ m}$ and $R_2 = 88.5 \%$ and yielding the maximum signal power $P_{out} = 14.25 \text{ mW}$. In the last scenario, the goal is to decrease the threshold power as much as possible in order to obtain a device which is easy to pump with low-cost red laser diodes. It was accomplished by selecting, in Fig. 5.2.6, the curve corresponding to the lowest threshold power, i.e. $P_{th} = 25 \text{ mW}$, with a decent trade-off between the fiber length, equal to $L = 2.1 \text{ m}$, and the mirror reflectivity, equal to $R_2 = 98.2 \%$.

Fig. 5.2.7 shows the output signal power P_{out} as a function of the input pump power P_{p0} for the three aforementioned optimization scenarios. It allows for evaluating the slope efficiency η_s and the threshold power P_{th} for each configuration. In particular, the slope efficiencies for the optimization scenarios (I), (II) and (III) are rather low, respectively $\eta_s = 0.2\%$, $\eta_s = 1.6\%$ and $\eta_s = 1\%$. On the other hand, the threshold powers are $P_{th} = 127\text{ mW}$, $P_{th} = 97\text{ mW}$ and $P_{th} = 25\text{ mW}$, respectively.

The final investigation is related to the laser bandwidth, which was investigated by changing the signal wavelength. The dependence of the background loss on the wavelength is taken into account even if it is typically lower than $\alpha(\lambda_s) = 0.009\text{ dB/m}$ and could be neglected.

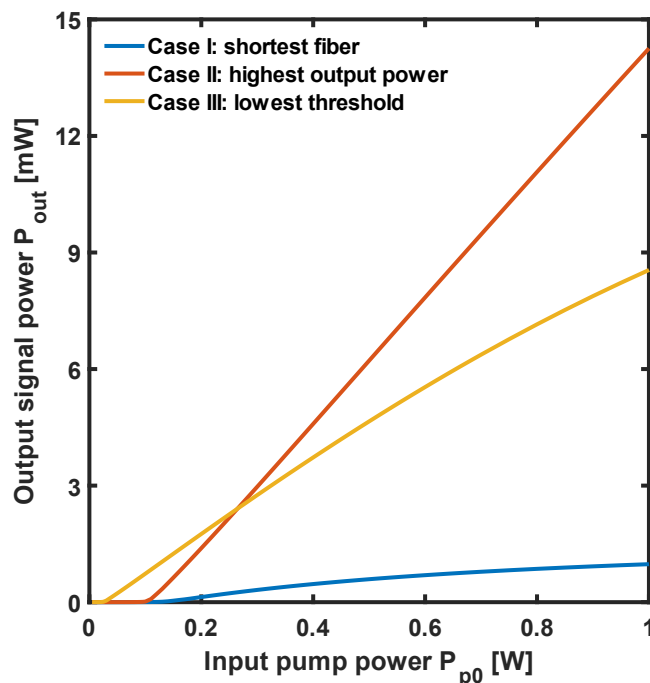


Figure 5.2.7 Output signal power P_{out} as a function of the signal wavelength λ_s for three optimization scenarios: (I) shortest fiber, (II) highest output power and (III) lowest threshold. Input pump power $P_{p0} = 1\text{ W}$, dopant concentration $N_{Er} = 5 \times 10^{25}\text{ ions/m}^3$, input mirror reflectivity $R_1 =$

Fig. 5.2.8 the output signal power P_{out} as a function of the signal wavelength λ_s , again for the three optimization scenarios. The device optimized for the scenario (I) exhibits the lowest output power $P_{out} = 1.1\text{ mW}$ at the wavelength $\lambda_s = 3.62\text{ }\mu\text{m}$. This was to be expected, since a short fiber limits the overall optical gain. However, this configuration provides the flattest spectral response, with a 10-dB bandwidth of $BW = 440\text{ nm}$. The device optimized for the

scenario (II) exhibits the highest output power $P_{out} = 22.5 \text{ mW}$ at the wavelength $\lambda_s = 3.73 \mu\text{m}$, with an apparent benefit. The 10-dB bandwidth increases to $BW = 545 \text{ nm}$. Lastly, the optimized for the scenario (III) exhibits an intermediate output power $P_{out} = 15.5 \text{ mW}$ at the wavelength $\lambda_s = 3.8 \mu\text{m}$.

The widest 10-dB bandwidth $BW = 659 \text{ nm}$ is obtained with this configuration, covering the spectral range $\lambda = 3255 - 3913 \text{ nm}$. This is because a lower threshold power makes it easier to obtain a positive net gain at wavelengths far from the central wavelength. It is also worth noting that single-mode operation still occurred for all three optimization scenarios in the entire wavelength range. Table 5.2.2 summarizes in a compact form the results exposed in this Section.

Table 5.2.2 Spectroscopic parameters for the erbium-doped fluoroindate glass

Param.	Optimization Scenario I	Optimization Scenario II	Optimization Scenario III	Description
L	19.3 cm	4.3 m	2.1 m	Fiber length
N_{Er}	$5 \times 10^{25} \text{ ions/m}^3$	$5 \times 10^{25} \text{ ions/m}^3$	$5 \times 10^{25} \text{ ions/m}^3$	Dopant
R_1	99%	99%	99%	Input mirror reflectivity
R_2	97%	88.5%	98.2%	Output mirror reflectivity
λ_s	$3.62 \mu\text{m}$	$3.73 \mu\text{m}$	$3.8 \mu\text{m}$	Central wavelength
P_{out}	1.1 mW	22.5 mW	15.5 mW	Output power (at central wavelength)
BW	440 nm	545 nm	659 nm	10-dB bandwidth
η_s	0.2%	1.6%	1%	Slope efficiency (at $\lambda_s = 3.5 \mu\text{m}$)
P_{th}	127 mW	97 mW	25 mW	Threshold power (at $\lambda_s = 3.5 \mu\text{m}$)

For a comparison, in [219] a CW erbium-doped ZBLAN fiber laser pumped at $\lambda_p = 658 \text{ nm}$ emitted up to $P_{out} = 203 \text{ mW}$ at $\lambda_s = 3462 \text{ nm}$ by employing a much higher input pump power $P_{p_0} = 8.6 \text{ W}$. The fiber was $L = 2.15 \text{ m}$ long, with a pretty high erbium concentration $N_{Er} = 7 \text{ mol \%}$. The measured slope efficiency was about $\eta_s = 3.8 \%$, with a threshold power of about $P_{th} = 3.4 \text{ W}$. Even though the device here proposed exhibits a slightly worse slope efficiency ($\eta_s = 1.6 \%$ for the Optimization Scenario II), numerical simulations predict much better threshold powers (only $P_{th} = 25 \text{ mW}$ for the Optimization Scenario III) with very low doping levels ($N_{Er} = 5 \times 10^{25} \text{ ions/m}^3 \approx 0.26 \text{ mol \%}$).

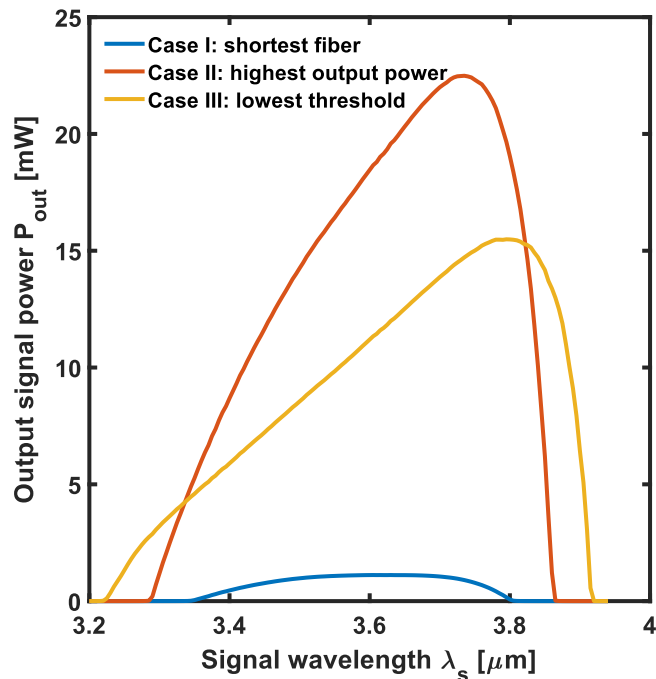


Figure 5.2.8 Output signal power P_{out} as a function of the signal wavelength λ_s for three optimization scenarios: (I) shortest fiber, (II) highest output power and (III) lowest threshold. Input pump power $P_{p_0} = 1 \text{ W}$, dopant concentration $N_{Er} = 5 \times 10^{25} \text{ ions/m}^3$, input mirror reflectivity $R_1 = 99\%$.

5.2.3 Conclusion

With reference to the state of the art, this is the first accurate design and optimization of a CW erbium-doped fluoroindate fiber laser emitting in the Mid-IR. Its performance was deeply investigated by studying the output signal power, the threshold power, the slope efficiency and the emission bandwidth. Among the three optimized configurations, the one with the lowest threshold power offers

the widest 10-dB bandwidth of 659 nm , emitting 15.5 mW of optical power at 3800 nm and covering the spectral range from 3255 nm to 3913 nm . Despite the low slope efficiency, the obtained results are promising and encourage the fabrication of the proposed fiber laser, which could find applications in environmental monitoring, remote sensing, biomedicine and optical communications. The developed laser is appealing because it employs a commercial Le Verre Fluoré optical fiber and is simple to pump at 635 nm using inexpensive red laser diodes.

Conclusions

This Ph.D. thesis reports innovative optical fiber sensors, Mid-IR optical fiber components, and optical fiber sources, designed, fabricated and characterized to address the specific needs and challenges of the aerospace field.

The most salient results regarding the developed non-conventional fiber optic sensors based on Bragg gratings to detect physical quantities such as strain, temperature and bending, can be summarized as follows:

- (i) a comprehensive optomechanical simulation approach has been developed for the design of three polarization maintaining optical fibers (Panda, Bow tie and Pseudo-rectangle) embedded in CFRP. Moreover, the design of two APFs, covering the fiber optic sensors, is proposed to enhance the temperature sensitivity of about 10 % for all the investigated sensors. Low values of uncertainty to temperature variation $\delta T = 1.32 \text{ K}$ and to longitudinal strain $\delta e_3 = 9.49 \mu\text{e}$ have been obtained.
- (ii) a microstructured flat optical fiber, for multiparameter sensing within CFRP laminates, has been designed. The relevant advantage introduced by the use of the designed microstructure is evident with regard to the slow and fast y axis sensitivities $K_{y,f} = 12.89 \text{ pm/MPa}$, $K_{y,fm} = 21.06 \text{ pm/MPa}$, $K_{y,s} = 5.02 \text{ pm/MPa}$, $K_{y,sm} = 7.22 \text{ pm/MPa}$, yielding to high sensitivity triaxial strain detection. The use of a flat fiber minimizes the embedding challenges associated with standard circular optical fibers.
- (iii) an ultra-thin, flexible silica planar Bragg grating-based sensor is designed, fabricated, and experimentally characterized for high curvature monitoring. The shift of the resonant wavelength for different curvatures are explained by means of CMT-based code. The experimental results agree with simulations showing good sensor sensitivity to bending and an excellent mechanical robustness, reaching curvature values up to $\pm 33 \text{ m}^{-1}$.

- (iv) a novel approach for bending monitoring through flexible photonics Bragg grating-based sensor is theoretically and experimentally investigated. The approach takes into account both the ratiometric power between the peak power reflected by the fundamental and higher-order modes and the Bragg wavelength shift. The experiments agree with simulations and show that the proposed flexible sensor can withstand very high curvatures up to 110 m^{-1} with Bragg wavelength shift sensitivities $K_{\lambda,fun} = -2.4 \text{ pm/m}^{-1}$, $K_{\lambda,hom} = -2.1 \text{ pm/m}^{-1}$ and ratiometric power sensitivity $K_{P_R} = -0.78 \text{ dB/mm}$.

The main results regarding the design, fabrication, and characterization of Mid-IR optical fiber components based on soft glasses applicable for optical signal multiplexing, laser cavities, communication and sensing systems are reported in the following:

- (i) the design, fabrication and characterization of a 3×1 fluoroindate combiner for the Mid-IR wavelength range is made for the first time via Vytran® GPX-2400 glass processing workstation. A customized manufacturing and normalization process has been developed. The characterization at the wavelength $\lambda = 1.55 \mu\text{m}$ demonstrates a maximum per-port net transmission efficiency of $\eta_{m,net} = 80.6 \%$ in agreement with simulations. The net transmission efficiency is flat from NIR to Mid-IR and it is reasonably close to the $\eta_{s,net} \sim 98 \%$.
- (ii) the design, fabrication, and characterization of a low-loss optical fiber coupler based on indium fluoride optical fibers within the mid-infrared spectral range is reported. The measured coupling ratio is $CR = 72.2 : 27.8$, while the excess loss is $E_L = 0.88 \text{ dB}$ at the wavelength $\lambda = 3.34 \mu\text{m}$.

The design and optimization of Mid-IR CW lasers have been an essential part of this research since they can be potentially applied for non-destructive material inspection and quality assessment of composite materials. The most relevant results are summarized in the following:

- (i) the design of a CW laser emitting at $\lambda_s = 3.92 \mu\text{m}$ based on a holmium and neodymium co-doped fluoroindate glass fiber is reported, by using measured and recovered spectroscopic parameters. By employing an input pump power at the wavelength $\lambda_p = 808 \text{ nm}$, a fiber length $L_{fiber} = 0.4 \text{ m}$, an holmium concentration $N_{Ho} = 8 \times 10^{26} \text{ ions/m}^3$ (4 mol.%), a neodymium concentration $N_{Nd} = 1 \times 10^{26} \text{ ions/m}^3$ (0.5 mol.%), and an output mirror reflectivity

$R_{out} = 60\%$, a slope efficiency $\eta = 16.67\%$ and an input pump threshold $P_{th} = 0.2\text{ W}$ can be obtained.

- (ii) the design and optimization of a CW erbium-doped fluoroindate fiber laser emitting in the middle infrared. Among the three optimized configurations, the one with the lowest threshold power offers the widest 10-dB bandwidth of 659 nm , emitting 15.5 mW of optical power at 3800 nm and covering the spectral range from 3255 nm to 3913 nm . The developed laser is appealing because it employs a Le Verre Fluoré optical fiber that is commercial and is simple to pump at 635 nm using inexpensive red laser diodes.

As listed at the end of the thesis, the results obtained have been published in International Journals and presented at National and International Conferences, providing a valuable contribution to the field of fiber optics and aerospace structure monitoring.

List of publications

International Journals:

- [j1] A. Annunziato, F. Anelli, J. Gates, C. Holmes and F. Prudenzano, “Design of Polarization Maintaining FBGs Using Polyimide Films to Improve Strain-Temperature Sensing in CFRP Laminates,” in IEEE Photonics Journal, vol. 13, no. 2, pp. 1-15, April 2021, Art no. 7100315, doi: 10.1109/JPHOT.2021.3063172.
- [j2] F. Anelli, A. Annunziato, A. Erario, C. Holmes, C. Ciminelli and F. Prudenzano, “Design of Microstructured Flat Optical Fiber for Multi-axial Strain Monitoring in Composite Materials,” in IEEE/OPTICA Journal of Lightwave Technology, vol. 40, no. 17, pp. 5986-5994, 1 Sept.1, 2022, doi: 10.1109/JLT.2022.3186912.
- [j3] A. Annunziato, F. Anelli, P. Le Pays Du Teilleul, S. Cozic, S. Poulain and F. Prudenzano, “Fused Optical Fiber Combiner Based on Indium Fluoride Glass: New Perspectives for Mid-IR Applications,” in OPTICA Optics Express, Vol. 30, Issue 24, 30, pp. 44160-44174, 2022, doi: 10.1364/OE.471090.
- [j4] A. M. Loconsole, M. C. Falconi, A. Annunziato, S. Cozic, S. Poulain, F. Prudenzano, “Design of a Mid-IR Laser Based on a Ho:Nd-codoped Fluoroindate Fiber,” in IEEE/OPTICA Journal of Lightwave Technology, pp. 1-7, November 2022, doi: 10.1109/JLT.2022.3218190.
- [j5] F. Anelli, A. Annunziato, M. Godfrey, A. M. Loconsole, C. Holmes and F. Prudenzano, “Effects of Curvature on Flexible Bragg Grating in Off-Axis Core: Theory and Experiment,” in IEEE/OPTICA Journal of Lightwave Technology, pp. 1-7, January 2023, doi: 10.1109/JLT.2023.3238427.
- [j6] M. C. Falconi, A. M. Loconsole, A. Annunziato, S. Cozic, S. Poulain and F. Prudenzano, “Design of a Broadband Erbium-doped Fluoroindate Fiber Laser Emitting up to $3.91\text{ }\mu\text{m}$,” in IEEE/OPTICA Journal of Lightwave Technology, doi: 10.1109/JLT.2023.3275168.

- [j7] A.M. Loconsole, V. Portosi, V. V. Francione, F. Anelli, A. Annunziato, M. C. Falconi, F. Prudenzano, "Optimization of a wideband antipodal Vivaldi antenna with metalenses," in International Journal of Microwave and Wireless Technologies, pp. 1-8, 2023. doi:10.1017/S1759078723001022
- [j8] A. Annunziato, M. Godfrey, F. Anelli, J. D. Barton, C. Holmes, F. Prudenzano, "Flexible Photonic Sensors: Exploiting Ratiometric Power in Few-Mode Waveguides for Bending Inference," submitted to OPTICA Optics Express, September 2023 (Under Review).
- [j9] F. Anelli, A. Annunziato, A. Maria Loconsole, V. Portosi, S. Cozic, P. L. P. du Teilleul, S. Venck, S. Poulain, F. Prudenzano, "Low-Loss Fluoride Optical Fiber Coupler for Mid-Infrared Applications," IEEE/OPTICA submitted to Journal of Lightwave Technology, August 2023 (Under Review).
- [j10] A. M. Loconsole, V. V. Francione, A. Annunziato, F. Anelli, and F. Prudenzano, "Design of a High Performance Mid-IR Fiber Laser Based on Pr³⁺-doped Fluoroindate Glass," submitted to IEEE/OPTICA Journal of Lightwave Technology, September 2023 (Under Review).

Proceedings of SPIE:

- [sp1] A. M. Loconsole, M. C. Falconi, A. Annunziato, S. Cozic, S. Poulain and F. Prudenzano, "Feasibility Investigation Of Ho:Nd Codoped Inf3 Fibers Pumped at 808 nm Wavelength," in Proceedings SPIE 12142, Fiber Lasers and Glass Photonics: Materials through Applications III, Strasbourg, France, 25 May 2022, 1214210, doi: 10.1117/12.2622232.
- [sp2] M. C. Falconi, A. M. Loconsole, A. Annunziato, S. Cozic, S. Poulain and F. Prudenzano, "Design of an Er³⁺: InF₃ fiber laser pumped with red light," in Proceedings SPIE 12142, Fiber Lasers and Glass Photonics: Materials through Applications III, Strasbourg, France, 25 May 2022, 121420Z, doi: 10.1117/12.2622148.

Proceedings of International Conferences:

- [c1] F. Anelli, A. Annunziato, V. Portosi, S. Cozic, S. Poulain, P. Le Pays Du Teilleul, F. Prudenzano, "Multimode Fluoroindate Optical Fiber Coupler," in Proceedings of the IEEE, Conference on Lasers and Electro-Optics, CLEO Europe 2023, Munich, 26-30 June 2023.

- [c2] C. Holmes, S. Zahertar, B. Moog, M. Godfrey, T. Lee, A. Annunziato, F. Anelli, B. Shi, M. Beresna, M. Whitaker, F. Prudenzano, R. Day, And J. Barton, "Fabrication of Externally Microstructured Flat Optical Fibre for In-process Monitoring of Laminated Composite Structures," in Proceedings of the IEEE, Conference on Lasers and Electro-Optics, CLEO Europe 2023, Munich, 26-30 June 2023.
- [c3] A. Annunziato, A. Erario, F. Anelli, G. Abbate, M. Godfrey, S. L. Jantzen, J. Gates, C. Holmes, C. Ciminelli and F. Prudenzano, "Structural Health Monitoring of Composite Laminae for Aerospace Applications via Embedded Panda Fiber Bragg Grating," in Proceedings of the IEEE, ICTON 2020, 22nd International Conference on Transparent Optical Networks (ICTON), Bari, 19-23 July 2020, pp. 1-5, doi: 10.1109/ICTON51198.2020.9203011.
- [c4] A. Annunziato, F. Anelli, M. Godfrey, J. M. Barton, C. Holmes and F. Prudenzano, "Design of Flat Optical Fiber Sensor for Triaxial Strain Monitoring in Composite Laminates," in Proceedings of the IEEE, 2021 AEIT International Annual Conference (AEIT), Milan, 04-08 October 2021, pp. 1-6, doi: 10.23919/AEIT53387.2021.9626867.
- [c5] A. M. Loconsole, M. C. Falconi, V. Portosi, A. Annunziato, S. Taccheo and F. Prudenzano, "Incoherent Multi-Wavelength Emission in the Wavelength Range 1500-2100 nm," in Proceedings of the IEEE, 2021 AEIT International Annual Conference (AEIT), Milan, 04-08 October 2021, pp. 1-6, doi: 10.23919/AEIT53387.2021.9627051.
- [c6] A. Annunziato, F. Anelli, A. M. Loconsole, M. C. Falconi, V. Portosi, V. V. Francione, F. Prudenzano, "Optical Combining in Medium Infrared Wavelength Range and its Applications," (INVITED) in Proceedings of the IEEE, ICTON 2023, 23nd International Conference on Transparent Optical Networks (ICTON), Bucarest, 2-6 July 2023.
- [c7] F. Anelli, A. Annunziato, A. M. Loconsole, V. Portosi, V. V. Francione, M. C. Falconi, P. Le Pays Du Teilleul, S. Cozic, S. Poulaing, Francesco Prudenzano, "Fabrication of Tapered Devices with Fluoride and Chalcogenide Optical Fibers for Mid-IR Applications," in Proceedings of the IEEE, ICTON 2023, 23nd International Conference on Transparent Optical Networks (ICTON), Bucarest, 2-6 July 2023.
- [c8] A. M. Loconsole, A. Annunziato, F. Anelli, V. V. Francione, V. Portosi, M. C. Falconi, F. Prudenzano, "Design of a Pr³⁺:InF₃ fiber laser pumped in near-IR and emitting at 4 micron wavelength," in

Proceedings of the IEEE, ICTON 2023, 23nd International Conference on Transparent Optical Networks (ICTON), Bucarest, 2-6 July 2023.

International Conferences:

- [i1] M. C. Falconi, A. M. Loconsole, A. Annunziato, F. Anelli, Yuchen Wang, G. Galzerano, and F. Prudenzano, "Simulation of a Dy³⁺:ZBLAN fiber laser passively Q-switched with a SESAM," in Photoluminescence in Rare Earths:Photonic Materials Workshop (PRE'22-Poland), Szczawnica, Poland 11-14 September 2022.
- [i2] M. C. Falconi, A. M. Loconsole, A. Annunziato, F. Anelli, Yuchen Wang, G. Galzerano, and F. Prudenzano, "Numerical investigation of an Er³⁺ :IFG fiber for lasing at 3.5 μm," in Photoluminescence in Rare Earths:Photonic Materials Workshop (PRE'22-Poland), Szczawnica, Poland 11-14 September 2022.
- [i3] A. Annunziato, F. Anelli, V. Portosi, V. V. Francione, A. M. Loconsole, M. C. Falconi And F. Prudenzano, "Optical Fiber Couplers Based on Indium Fluoride Optical Fibers," in C-PASS 2023, Conference on Photonics for Advanced Spectroscopy and Sensing (C-PASS), Castellaneta Marina, 3-8 September 2023.
- [i4] F. Anelli, A. Annunziato, A. M. Loconsole, M. C. Falconi, V. Portosi, V. V. Francione and F. Prudenzano, "Fabrication of Mid-IR Tapered Devices Using Fluoride and Chalcogenide Optical Fibers," in Conference on Photonics for Advanced Spectroscopy and Sensing (C-PASS), Castellaneta Marina, 3-8 September 2023.
- [i5] A. M. Loconsole, M. C. Falconi, A. Annunziato, F. Anelli, V. Portosi, V. V. Francione And F. Prudenzano, "Investigation on a 4-μm emitting laser based on a fluoroindate fiber doped with praseodymium," in Conference on Photonics for Advanced Spectroscopy and Sensing (C-PASS), Castellaneta Marina, 3-8 September 2023.
- [i6] C. Holmes, S. Zahertar, B. Moog, M. Godfrey, T. Lee, A. Annunziato, F. Anelli, B. Shi, M. Beresna, M. Whitaker, F. Prudenzano, R. Day, J. Dulieu-Barton, "Flexible Glass Photonics and Applications for Aerospace," in 3rd International Conference on Dielectric Photonic Devices and System Beyond Visible, D-Photon 2023, Bari, 11-13 July 2023.
- [i7] A. Annunziato, F. Anelli, V. V. Francione, V. Portosi, A. M. Loconsole, C. Holmes, M. Godfrey, J. Dulieu-Barton, F. Prudenzano, "Flexible Photonic Sensor For Bending Monitoring," in D-Photon 2023, 3rd

International Conference on Dielectric Photonic Devices and System Beyond Visible, Bari, 11-13 July 2023.

- [i8] F. Anelli, A. Annunziato, V. Portosi, P. Le Pays Du Teilleul, S. Cozic, S. Poulain, F. Prudenzano, "Indium Fluoride Optical Fiber Coupler For Mid-Infrared Applications," in D-Photon 2023, 3rd International Conference on Dielectric Photonic Devices and System Beyond Visible, Bari, 11-13 July 2023.
- [i9] A. M. Loconsole, A. Annunziato, M. C. Falconi, F. Anelli, V. V. Francione, V. Portosi, F. Prudenzano, "Investigation On A Mid-Ir Laser Based On A Praseodymium-Doped Fluoroindate Fiber," in D-Photon 2023, 3rd International Conference on Dielectric Photonic Devices and System Beyond Visible, Bari, 11-13 July 2023.
- [i10] F. Anelli, V. Portosi, A. M. Loconsole, V. V. Francione, A. Annunziato, F. Prudenzano, "A Wideband Inkjet-Printed Antenna On Flexible Pet Substrate," in D-Photon 2023, 3rd International Conference on Dielectric Photonic Devices and System Beyond Visible, Bari, 11-13 July 2023.
- [i11] A. Annunziato, F. Anelli, V. V. Francione, A. M. Loconsole, V. Portosi, F. Prudenzano, "Mid-IR Optical Combiners For All-In-Fiber Laser," in D-Photon 2023, 3rd International Conference on Dielectric Photonic Devices and System Beyond Visible, Bari, 11-13 July 2023.
- [i12] F. P. Pallotta, V. Portosi, A. M. Loconsole, V.V. Francione, F. Anelli, A. Annunziato, A. Crudele, F. Prudenzano, "A Metalens For Non-Invasive Microwave Hyperthermia In Cancer Treatment," in D-Photon 2023, 3rd International Conference on Dielectric Photonic Devices and System Beyond Visible, Bari, 11-13 July 2023.

Proceedings of National Conferences:

- [p1] A. M. Loconsole, M. C. Falconi, A. Annunziato, V. Portosi and F. Prudenzano, "Design of a Ho:Nd-codoped fluoroindate fiber for Mid-IR laser emission" in Italian Conference on Optics and Photonics (ICOP), Trento, June 15-17, 2022.
- [p2] M. C. Falconi, A. M. Loconsole, A. Annunziato, F. Anelli and F. Prudenzano "Design Of An Erbium-Doped Fluoroindate Fiber Laser Pumped at 635 nm," in Italian Conference on Optics and Photonics (ICOP), Trento, June 15-17, 2022.

National Conferences:

- [n1] M. C. Falconi, A. M. Loconsole, A. Annunziato, F. Anelli, Y. Wang, G. Galzerano and F. Prudenzano: “Modeling of a Sesam-Based Dysprosium-Doped Zblan Fiber Laser Operating in Q-Switching Regime,” in XXIV RiNEm, XV Riunione Nazionale di Elettromagnetismo, Catania, 18-21 September 2022.
- [n2] A. M. Loconsole, V. Portosi, F. Anelli, A. Annunziato, V. V. Francione, M. C. Falconi and F. Prudenzano: “Low-Profile Antipodal Vivaldi Antenna (Ava) for Ground Penetrating Radar Applications,” in XXIV RiNEm, XV Riunione Nazionale di Elettromagnetismo, Catania, 18-21 September 2022.

References

- [1] C. Sonnenfeld et al., “Microstructured optical fiber sensors embedded in a laminate composite for smart material applications,” *Sensors*, vol. 11, no. 3, pp. 2566–2579, 2011, doi:10.3390/s110302566.
- [2] A. Annunziato, F. Anelli, J. Gates, C. Holmes, F. Prudenzano, “Design of polarization-maintaining fbg’s using polyimide films to improve strain-temperature sensing in cfrp laminates,” *IEEE Photonics J.*, vol. 13, no. 2, pp. 1–15, 2021, doi:10.1109/JPHOT.2021.3063172.
- [3] T. Vella et al., “Full-spectrum interrogation of fiber bragg gratings at 100 khz for detection of impact loading,” *Meas. Sci. Technol.*, vol. 21, no. 9, 2010, doi:10.1088/0957-0233/21/9/094009.
- [4] H.-P. Wang, Y.-Q. Ni, J.-G. Dai, M.-D. Yuan, “Interfacial debonding detection of strengthened steel structures by using smart cfrp-fbg composites,” *Smart Mater. Struct.*, vol. 28, no. 11, 2019, doi: 10.1088/1361-665X/ab3add.
- [5] S. Takeda, Y. Okabe, N. Takeda, “Monitoring of delamination growth in cfrp laminates using chirped fbg sensors,” *J. Intell. Mater. Syst. Struct.*, vol. 19, no. 4, pp. 437–444, 2008, doi:10.1177/1045389X06074085.
- [6] S. Takeda, Y. Okabe, N. Takeda, “Delamination detection in cfrp laminates with embedded small-diameter fiber bragg grating sensors,” *Compos. - A: Appl. Sci. Manuf.*, vol. 33, no. 7, pp. 971–980, 2002, doi:10.1016/S1359-835X(02)00036-2.
- [7] A. Rajabzadeh, R. Heusdens, R. C. Hendriks, R. M. Groves, “Characterisation of Transverse Matrix Cracks in Composite Materials Using Fibre Bragg Grating Sensors,” *J. Light. Technol.*, vol. 37, no. 18, pp. 4720-4727, 15 Sept.15, 2019, doi: 10.1109/JLT.2019.2919339.
- [8] P. Zhu, P. Liu, Z. Wang, C. Peng, N. Zhang, M. A. Soto, “Evaluating and Minimizing Induced Microbending Losses in Optical Fiber Sensors Embedded Into Glass-Fiber Composites,” *J. Light. Technol.*, vol.

- 39, no. 22, pp. 7315-7325, 15 Nov.15, 2021, doi: 10.1109/JLT.2021.3112484.
- [9] C. Holmes, M. Godfrey, D. J. Bull, J. Dulieu-Barton, “Real-time through-thickness and in-plane strain measurement in carbon fibre reinforced polymer composites using planar optical bragg gratings,” *Opt. Lasers Eng.*, vol. 133, 2020, doi: 10.1016/j.optlaseng.2020.106111.
 - [10] G. Pereira, C. Frias, H. Faria, O. Frazão, A. Marques, “On the improvement of strain measurements with fbg sensors embedded in unidirectional composites,” *Polym. Test.*, vol. 32, no. 1, pp. 99–105, 2013, doi:10.1016/ j.polymertesting.2012.09.010.
 - [11] J. Frieden, J. Cugnoni, J. Botsis, T. Gmür, “Low energy impact damage monitoring of composites using dynamic strain signals from fbg sensors—part i: Impact detection and localization,” *Compos. Struct.*, vol. 94, no. 2, pp. 438–445, 2021, doi: 10.1016/j.compstruct.2021.08.003.
 - [12] J. Frieden, J. Cugnoni, J. Botsis, T. Gmür, “Low energy impact damage monitoring of composites using dynamic strain signals from fbg sensors— part ii: Damage identification,” *Compos. Struct.*, vol. 94, no. 2, pp. 593–600, 2012, doi: 10.1016/j.compstruct.2011.08.025.
 - [13] G. Cazzulani, S. Cinquemani, L. Comolli, A. Gardella, F. Resta, “Vibration control of smart structures using an array of fiber bragg grating sensors,” *Mechatron.*, vol. 24, no. 4, pp. 345–353, 2014, doi: 10.1016/j.mechatronics. 2013.07.014.
 - [14] Z.-S. Guo, “Strain and temperature monitoring of asymmetric composite laminate using fbg hybrid sensors,” *Struct. Health Monit.*, vol. 6, no. 3, pp. 191–197, 2007, doi:10.1177/14759217070060030201.
 - [15] V. Antonucci, M. Esposito, M. Ricciardi, M. Giordano, M. Zarrelli, “Strain monitoring of composite elements by fibre bragg grating sensors during a quasi-static indentation,” *Compos. B. Eng.*, vol. 56, pp. 34–41, 2014, doi: 10.1016/j.compositesb.2013.07.020.
 - [16] M. Basu, S. Ghorai, “Strain sensing in fiber-reinforced polymer laminates using embedded fiber bragg grating sensor,” *Fiber Integr. Opt.*, vol. 33, no. 4, pp. 279–298, 2014, doi:10.1080/01468030.2014.906686.
 - [17] A. Güemes, A. Fernández-López, P. F. Díaz-Maroto, A. Lozano, J. Sierra-Perez, “Structural health monitoring in composite structures by

- fiber-optic sensors," *Sensors*, vol. 18, no. 4, 2018, doi:10.3390/s18041094.
- [18] G. Rajan, M. Ramakrishnan, Y. Semenova, E. Ambikairajah, G. Farrell, G. Peng, "Experimental Study and Analysis of a Polymer Fiber Bragg Grating Embedded in a Composite Material," *J. Light. Technol.*, vol. 32, no. 9, pp. 1726–1733, May 1, 2014, doi:10.1109/JLT.2014.2311441.
 - [19] C. Jewart et al., "Sensitivity enhancement of fiber bragg gratings to transverse stress by using microstructural fibers," *Opt. Lett.*, vol. 31, no. 15, pp. 2260–2262, 2006, doi:10.1364/OL.31.002260.
 - [20] F. Bosia, P. Giaccari, J. Botsis, M. Facchini, H. G. Limberger, R. P. Sal-athé, "Characterization of the response of fibre bragg grating sensors subjected to a two-dimensional strain field," *Smart Mater. Struct.*, vol. 12, no. 6, 2003, doi:10.1088/0964-1726/12/6/009.
 - [21] G. Luyckx, E. Voet, N. Lammens, W. De Waele, J. Degrieck, "Residual strain-induced birefringent fbgs for multi-axial strain monitoring of cfrp composite laminates," *NDT E Int.*, vol. 54, pp. 142–150, 2013, doi: 10.1016/j.ndteint.2012.11.008.
 - [22] K. Shivakumar, and L. Emmanwori, "Mechanics of failure of composite laminates with an embedded fiber optic sensor," *J. Compos. Mater.*, vol. 38, pp. 669–679, 2004.
 - [23] P. Zhu, J. Wu, M. Huang, Y. Wang, P. Liu, and M. A. Soto, "Reducing Residual Strain in Fiber Bragg Grating Temperature Sensors Embedded in Carbon Fiber Reinforced Polymers," *J. Light. Technol.*, vol. 37, no. 18, pp. 4650–4656, 2019.
 - [24] K. Kalli et al., "Flat fibre and femtosecond laser technology as a novel photonic integration platform for optofluidic based biosensing devices and lab-on-chip applications: Current results and future perspectives," *Sens. Actuators B Chem.*, vol. 209, pp. 1030–1040, 2015, doi: 10.1016/j.snb.2014.12.003.
 - [25] G.-D. Peng, *Handbook of Optical Fibers*, Springer, 2019.
 - [26] K. D. Dambul et al., "Fabrication and characterization of ge-doped flat fibres," *J. Mod. Opt.*, vol. 66, no. 11, pp. 1219–1225, 2019, doi:10.1080/09500340.2019.1610518.
 - [27] F. R. M. Adikan et al., "Direct UV written optical waveguides in flexible glass flat fiber chips," *IEEE J. Sel. Top. Quantum Electron.*, vol. 18, no. 5, pp. 1534–1539, 2011, doi:10.1109/JSTQE.2011.2171921.

- [28] T. H. Loutas, A. Panopoulou, D. Roulias, V. Kostopoulos, “Intelligent health monitoring of aerospace composite structures based on dynamic strain measurements,” *Expert Syst. Appl.*, vol. 39, no. 9, pp. 8412–8422, 2012, doi: 10.1016/j.eswa.2012.01.179.
- [29] A. Propst et al., “Assessment of damage in composite laminates through dynamic, full-spectral interrogation of fiber bragg grating sensors,” *Smart Mater. Struct.*, vol. 19, no. 1, 2009, doi:10.1088/0964-1726/ 19/1/015016.
- [30] A. Papantoniou, G. Rigas, N. D. Alexopoulos, “Assessment of the strain monitoring reliability of fiber bragg grating sensor (FBGs) in advanced composite structures,” *Compos. Struct.*, vol. 93, no. 9, pp. 2163–2172, 2011, doi: 10.1016/j.compstruct.2011.03.001.
- [31] S. Minakuchi, Y. Okabe, T. Mizutani, N. Takeda, “Barely visible impact damage detection for composite sandwich structures by optical-fiber-based distributed strain measurement,” *Smart Mater. Struct.*, vol. 18, no. 8, 2009, doi:10.1088/0964-1726/18/8/085018.
- [32] E. Voet, G. Luyckx, W. De Waele, J. Degrieck, “Multi-axial strain transfer from laminated cfrp composites to embedded bragg sensor: II. experimental validation,” *Smart Mater. Struct.*, vol. 19, no. 10, 2010, doi: 10.1088/0964-1726/19/10/105018.
- [33] G. Luyckx, E. Voet, N. Lammens, J. Degrieck, “Strain measurements of composite laminates with embedded fibre bragg gratings: Criticism and opportunities for research,” *Sensors*, vol. 11, no. 1, pp. 384–408, 2011, doi:10.3390/ s110100384.
- [34] H.-S. Kim, S.-H. Yoo, S.-H. Chang, “In situ monitoring of the strain evolution and curing reaction of composite laminates to reduce the thermal residual stress using fbg sensor and dielectrometry,” *Compos. B. Eng.*, vol. 44, no. 1, pp. 446–452, 2013, doi: 10.1016/j.compositesb.2012. 04.021.
- [35] F. Anelli, A. Annunziato, A. Erario, C. Holmes, C. Ciminelli and F. Prudenzano, “Design of Microstructured Flat Optical Fiber for Multi-axial Strain Monitoring in Composite Materials,” in *J. Light. Technol.*, vol. 40, no. 17, pp. 5986-5994, 1 Sept.1, 2022, doi: 10.1109/JLT.2022.3186912.
- [36] C. Holmes et al., “Fabrication of Externally Microstructured Flat Optical Fibre for In-process Monitoring of Laminated Composite Structures,” 2023 Conference on Lasers and Electro-Optics Europe & European Quantum Electronics Conference (CLEO/Europe-EQEC),

- Munich, Germany, 2023, pp. 1-1, doi: 10.1109/CLEO/Europe-EQEC57999.2023.10232169.
- [37] A. Annunziato, F. Anelli, M. Godfrey, J. M. Barton, C. Holmes and F. Prudenzano, "Design of Flat Optical Fiber Sensor for Triaxial Strain Monitoring in Composite Laminates," 2021 AEIT International Annual Conference (AEIT), Milan, Italy, 2021, pp. 1-6, doi: 10.23919/AEIT53387.2021.9626867.
 - [38] J. Ge, A. E. James, L. Xu, Y. Chen, K. -W. Kwok and M. P. Fok, "Bidirectional Soft Silicone Curvature Sensor Based on Off-Centered Embedded Fiber Bragg Grating," *IEEE Photonics Technol. Lett.*, vol. 28, no. 20, pp. 2237-2240, 2016.
 - [39] D. Budnicki et al., "All-fiber vector bending sensor based on a multi-core fiber with asymmetric air-hole structure," *J. Light. Technol.*, vol. 38, no. 23, pp. 6685-6690, 2020.
 - [40] H. Wu, L. Liang, H. Wang, S. Dai, Q. Xu, and R. Dong, "Design and measurement of a dual FBG high-precision shape sensor for wing shape reconstruction," *Sensors*, vol. 22, no. 1, 2021.
 - [41] M. Rosenberger, H. Pauer, M. Girschikofsky, H. Woern, B. Schmauss, and R. Hellmann, "Flexible polymer shape sensor based on planar waveguide Bragg gratings," *IEEE Photonics Technol. Lett.*, vol. 28, no. 17, pp. 1898-1901, 2016.
 - [42] F. Attivissimo, A. Di Nisio, A.M.L. Lanzolla, M.A. Ragolia, "Analysis of position estimation techniques in a surgical EM Tracking System," *IEEE Sensors Journal*, vol. 21, no. 13, pp. 14389-14396, 2021.
 - [43] G. Brunetti, G. Marocco, A. Di Benedetto, A. Giorgio, M. N. Armenise, and C. Ciminelli, "Design of a large bandwidth 2×2 interferometric switching cell based on a sub-wavelength grating," *J. Opt.*, vol. 23, no. 8, 2021.
 - [44] E. Bertolesi, M. Fagone, T. Rotunno, E. Grande, and G. Milani, "Experimental characterization of the textile-to-mortar bond through distributed optical sensors," *Constr. Build. Mater.*, vol. 326, 2022.
 - [45] G. C. Righini, J. Krzak, A. Lukowiak, G. Macrelli, S. Varas, and M. Ferrari, "From flexible electronics to flexible photonics: A brief overview," *Opt. Mater.*, vol. 115, p. 111011, 2021.
 - [46] G. Macrelli, A. K. Varshneya, and J. C. Mauro, "Ultra-thin glass as a substrate for flexible photonics," *Opt. Mater.*, vol. 106, p. 109994, 2020.

- [47] A. Lukowiak, S. Jiang, M. Ferrari, "Foreword," *Opt. Mater.*, vol. 129, p. 112555, 2022.
- [48] T.N.L. Tran et al., "Rare-earth activated SnO₂ photoluminescent thin films on flexible glass: Synthesis, deposition and characterization," *Opt. Mater.*, vol. 124, p. 111978, 2022.
- [49] D. Feng, X. Qiao, and J. Albert, "Off-axis ultraviolet-written fiber Bragg gratings for directional bending measurements," *Opt. Lett.*, vol. 41, no. 6, pp. 1201-1204, 2016.
- [50] X. Chen, C. Zhang, D. J. Webb, K. Kalli, and G.-D. Peng, "Highly sensitive bend sensor based on Bragg grating in eccentric core polymer fiber," *IEEE Photon. Technol. Lett.*, vol. 22, no. 11, pp. 850–852, 2010.
- [51] W. Bao, Q. Rong, F. Chen, and X. Qiao, "All-fiber 3D vector displacement (bending) sensor based on an eccentric FBG," *Opt. Express*, vol. 26, no. 7, pp. 8619–8627, 2018.
- [52] L. Shao, L. Xiong, C. Chen, A. Laronche, and J. Albert, "Directional bend sensor based on re-grown tilted fiber Bragg grating," *J. Light. Technol.*, vol. 28, no. 18, pp. 2681–2687, 2010.
- [53] Y. Jin, C. Chan, X. Dong, and Y. Zhang, "Temperature-independent bending sensor with tilted fiber Bragg grating interacting with multi-mode fiber," *Opt. Commun.*, vol. 282, no. 19, pp. 3905–3907, 2009.
- [54] Y. P. Wang, and Y. J. Rao, "A novel long period fiber grating sensor measuring curvature and determining bend-direction simultaneously," *IEEE Sens. J.*, vol. 5, no. 5, pp. 839-843, 2005.
- [55] X. Xu et al., "A Vector Bending Sensor Based on a Core-Offset Long Period Fiber Grating Induced by an Arc-Discharge," *IEEE Sens. J.*, vol. 21, no. 21, pp. 24129-24133, 2021.
- [56] H. Jung et al., "Bending and strain sensitivities in a helicoidal long-period fiber gratings," *IEEE Photon. Technol. Lett.*, vol. 21, no. 17, pp. 1232-1234, 2009.
- [57] X. Zhong et al., "Bending characteristics of a long-period fiber grating in a hollow eccentric optical fiber," *Appl. Opt.*, vol. 54, no. 26, pp. 7879-7883, 2015.
- [58] Y. Tian et al., "Directional bending sensor based on a dual side-hole fiber Mach-Zehnder interferometer," *IEEE Photon. Technol. Lett.*, vol. 30, no. 4, pp. 375-378, 2017.

- [59] Y. Wu et al., "Highly sensitive curvature sensor based on asymmetrical twin-core fiber and multimode fiber," *Opt. Laser Technol.*, vol. 92, pp. 74-79, 2017.
- [60] A. Sun, and Z. Wu, "Multimode interference in single mode–multimode FBG for simultaneous measurement of strain and bending," *IEEE Sens. J.*, vol. 15, no. 6, pp. 3390-3394, 2014.
- [61] Q. Rong, X. Qiao, H. Yang, K. S. Lim, and H. Ahmad, "Fiber Bragg grating inscription in a thin-core fiber for displacement measurement," *IEEE Photon. Technol. Lett.*, vol. 27, no. 10, pp. 1108-1111, 2015.
- [62] A. Taghipour, A. Rostami, M. Bahrami, H. Baghban, and M. Dolatyari, "Comparative study between LPFG-and FBG-based bending sensors," *Opt. Commun.*, vol. 312, pp. 99-105, 2014.
- [63] M. Hou et al., "Two-dimensional vector bending sensor based on seven-core fiber Bragg gratings," *Opt. Express*, vol. 26, no. 18, pp. 23770-23781, 2018.
- [64] F. Khan, A. Denasi, D. Barrera, J. Madrigal, S. Sales and S. Misra, "Multi-Core Optical Fibers With Bragg Gratings as Shape Sensor for Flexible Medical Instruments," *IEEE Sens. J.*, vol. 19, no. 14, pp. 5878-5884, 2019.
- [65] D. Zheng, J. Madrigal, H. Chen, D. Barrera, and S. Sales, "Multicore fiber-Bragg-grating-based directional curvature sensor interrogated by a broadband source with a sinusoidal spectrum," *Opt. Lett.*, vol. 42, no. 18, pp. 3710-3713, 2017.
- [66] I. Floris, S. Sales, P.A. Calderón, and J.M. Adam, "Measurement uncertainty of Multicore Optical Fiber sensors used to sense curvature and bending direction," *Measurement*, vol. 132, pp. 35-46, 2019.
- [67] F. Anelli, A. Annunziato, M. Godfrey, A. M. Loconsole, C. Holmes and F. Prudenzano, "Effects of Curvature on Flexible Bragg Grating in Off-Axis Core: Theory and Experiment," *J. Light. Technol.*, vol. 41, no. 9, pp. 2904-2910, 1 May, 2023, doi: 10.1109/JLT.2023.3238427.
- [68] Andrea Annunziato, Mike Godfrey, Francesco Anelli, Janice Dulieu-Barton, Christopher Holmes, Francesco Prudenzano, "Flexible Photonic Sensors: Exploiting Ratiometric Power in Few-Mode Waveguides for Bending Inference," submitted to International Journal "Optics Express".
- [69] S. Dupont et al., "IR microscopy utilizing intense supercontinuum light source," *Opt. Express*, vol. 20, pp. 4887–4892, 2012.

- [70] E. Baudel et al.: Development of an evanescent optical integrated sensor in the mid-infrared for detection of pollution in groundwater or seawater, *Adv. Device Mater.*, vol. 3 pp. 23–29, 2017.
- [71] Y. Wang et al., “Mid-IR tunable CW and passively Q-switched laser operation of Dy-doped fluoride fiber,” *Opt. Mater. Express*, vol. 12 pp. 1502-1511, 2022.
- [72] B. Kuyken et al., “An octave-spanning mid-infrared frequency comb generated in a silicon nanophotonic wire waveguide,” *Nat. Commun.*, vol. 6 pp. 1-6, 2015.
- [73] M. C. Falconi et al., “Design of a Multi-Wavelength Fiber Laser Based on Tm:Er:Yb:Ho Co-Doped Germanate Glass,” *J. Light. Technol.*, vol. 38, no. 8, pp. 2406-2413, 2020.
- [74] A. M. Loconsole et al., “Design of a mid-IR laser based on a Ho:Nd-codoped fluoroindate fiber,” *J. Lightwave Technol.*, vol. 41, no. 2, pp. 702–708, 2023.
- [75] M. Churbanov et al., “Recent advances in preparation of high-purity glasses based on arsenic chalcogenides for fiber optics,” *J. Non-Cryst. Solids*, vol. 357 pp. 2352–2357, 2011.
- [76] D. Tran et al., “Heavy metal fluoride glasses and fibers: a review,” *J. Light. Technol.*, vol. 2 pp. 566–586, 1984.
- [77] L. N. Butvina et al., “Crystalline silver halide fibers with optical losses lower than 50 dB/km in broad IR region and their applications,” *Proc. SPIE* 4083, Advances in Fiber Optics, 2000.
- [78] M. Poulain et al., “Verres fluores au tetrafluorure de zirconium propriétés optiques d'un verre dope au Nd³⁺,” *Mater. Res. Bull.*, vol. 10 pp. 243–246, 1975.
- [79] C. A. Schäfer et al., “Fluoride-fiber-based side-pump coupler for high-power fiber lasers at 2.8 μm,” *Opt. Lett.*, vol. 43 pp. 2340-2343, 2018.
- [80] É. Ducharme et al., “Viscosity of fluoride glass fibers for fused component fabrication,” *Appl. Opt.*, vol. 61 pp. 5031-5039, 2022.
- [81] O. Benderov et al. “Broadband mid-IR chalcogenide fiber couplers,” *Appl. Opt.*, vol. 58 pp. 7222-7226, 2019.
- [82] B. Stepanov et al., “Chalcogenide optical fiber couplers made by FBT method,” *J. Non-Cryst. Solids*, vol. 480 pp. 23-27, 2018.
- [83] F. Tavakoli, A. Rekik, and M. Rochette, “Fused taper infrared optical fiber couplers in chalcogenide glass,” *J. Light. Technol.*, vol. 15 pp. 2242-2245, 1997.

- [84] R. R. Gattass et al., "Infrared Fiber N x 1 Multimode Combiner," *IEEE Photonics J.*, vol. 5 pp. 7100905–7100905, 2013.
- [85] R. R. Gattass et al., "Review of infrared fiber-based components," *Appl. Opt.*, vol. 54, 2015.
- [86] A. Annunziato et al., "Fused optical fiber combiner based on indium fluoride glass: perspectives for mid-IR applications," *Opt. Express*, vol. 30, pp. 44160-44174, 2022.
- [87] P. Baer et al., "Design and fabrication of a fused 7×1 35/50 μm into 125/250 μm fiber combiner," *OSA Contin.*, vol. 2 pp. 1106-1112, 2019.
- [88] F. Min et al., "Research on a 4×1 fiber signal combiner with high beam quality at a power level of 12kW," *Opt. Express*, vol. 29 pp. 26658-26668, 2021.
- [89] Y. Liu et al., "5-kW-Level Bi-Directional High-Efficiency Pump and Signal Combiner With Negligible Beam Quality Degradation," *IEEE Photonics Journal*, vol. 1 pp. 1-6, Feb. 2022.
- [90] D. Majumder, S. D. Chowdhury and A. Pal, "Mode-Field Matched Pump-Signal Combiner for High Power Fiber Laser in Advanced Manufacturing," *IEEE Journal of Selected Topics in Quantum Electronics*, vol. 27, no. 6, pp. 1-9, Nov.-Dec. 2021.
- [91] N. K. Fontaine et al. "Geometric requirements for photonic lanterns in space division multiplexing," *Opt. Express*, vol. 20, pp. 27123-27132, 2012.
- [92] J. J. Davenport et al., "Photonic lanterns: a practical guide to filament tapering," *Opt. Mater. Express*, 11(8), 2639-2649, (2021).
- [93] S. G. Leon-Saval, A. Argyros, J. Bland-Hawthorn, "Photonic lanterns: a study of light propagation in multimode to single mode converters," *Opt. Express*, vol. 18 pp. 8430-8439, 2010.
- [94] D. Noordgraaf et al. "Multi-mode to single mode conversion in a 61 port photonic lantern," *Opt. Express*, vol. 18, pp. 4673-4678, 2010.
- [95] Z. Li et al., "Fabrication of a side pump combiner and realization of a 2 kW single mode all-fiber laser oscillator," *OSA Continuum*, vol. 3 pp. 1240-1248, 2020.
- [96] M. Rezaei, and M. Rochette, "All-chalcogenide ring fiber laser," *Opt. Fiber Technol.*, vol. 71, no. 102900, 2022.
- [97] Q. Xiao, X. Chen, H. Ren, P. Yan, and M. Gong, "Fiber coupler for mode selection and high-efficiency pump coupling," *Opt. Lett.*, vol. 38, pp. 1170-1172, 2013.

- [98] V. Coudé du Foresto, and S. Ridgway, "FLUOR: a stellar interferometer using single-mode infrared fibers," High-resolution imaging by interferometry II eds. Beckers, J. and Merkle, F. (ESO, Garching, Germany), 731–740, 1991.
- [99] I. Tugendhaft, A. Bornstein, Y. Weissman, and A. A. Hardy, "Directional multimode fiber couplers in the mid-infrared," *Opt. Eng.*, vol. 34, no. 10, 1995.
- [100] F. Tavakoli, A. Rekik, and M. Rochette, "Broadband and Wavelength-Dependent Chalcogenide Optical Fiber Couplers," *IEEE Photon. Technol. Lett.*, vol. 29, no. 9, pp. 735-738, 2017.
- [101] M. Rezaei, and M. Rochette, "All-chalcogenide single-mode optical fiber couplers," *Opt. Lett.*, vol. 44, no. 21, pp. 5266-5269, 2019.
- [102] D. T. Schaafsma, J. A. Moon, J. S. Sanghera, and I. D. Aggarwal, "Fused taper infrared optical fiber couplers in chalcogenide glass," *J. Light. Technol.*, vol. 15, no. 12, pp. 2242-2245, Dec. 1997.
- [103] M. Rezaei, M. H. M. Shamim, M. E. Amraoui, Y. Messaddeq, and M. Rochette, "Nonlinear Optical Fiber Couplers Made of Chalcogenide Glass," Conference on Lasers and Electro-Optics, Technical Digest Series (Optica Publishing Group, 2022), paper ATh4C.7.
- [104] M. Rezaei, Md H. M. Shamim, M. El Amraoui, Y. Messaddeq, and M. Rochette, "Nonlinear chalcogenide optical fiber couplers," *Opt. Express*, vol. 30, no. 12, pp. 20288-20297, 2022.
- [105] S.T. Nicholls, and M. Scott, "Method of making fluoride glass optical coupler," U.S. patent US5139550 A, August 1992.
- [106] G. Stevens, and T. Woodbridge, "Mid-IR fused fiber couplers," Proc. SPIE 9730, Components and Packaging for Laser Systems II, 973007, 2016.
- [107] M. Rezaei, and M. Rochette, "Single-Mode ZBLAN Optical Fiber Couplers," in Optica Advanced Photonics Congress 2022, Technical Digest Series (Optica Publishing Group, 2022), paper ITh2B.3.
- [108] M. Rezaei, G. T. Zeweldi, M. H. M. Shamim, and M. Rochette, "Single Mode Optical Fiber Couplers Made of ZBLAN Glass," in CLEO 2023, Technical Digest Series (Optica Publishing Group, 2023), paper STh3G.3.
- [109] M. Rezaei, G. T. Zeweldi, Md H. M. Shamim, and M. Rochette, "Single-mode optical fiber couplers made of fluoride glass," *Opt. Express*, vol. 31, pp. 27183-27191, 2023.

- [110] L. Zhang, F. Guan, L. Zhang, Y. Jiang, "Next generation mid-infrared fiber: fluoroindate glass fiber," *Opt. Mater. Express*, vol. 12, no. 4, pp. 1683-1707, Mar. 2022.
- [111] Q. Luo, H. L. Xu, S. A. Hosseini, J.-F. Daigle, F. Théberge, M. Sharifi, S. L. Chin, "Remote sensing of pollutants using femtosecond laser pulse fluorescence spectroscopy," *Appl. Phys. B*, vol. 82, pp. 105-109, Nov. 2005.
- [112] S. B. Mirov, I. S. Moskalev, S. Vasilyev, V. Smolski, V. V. Fedorov, D. Martyshkin, J. Peppers, M. Mirov, A. Dergachev, V. Gapontsev, "Frontiers of Mid-IR Lasers Based on Transition Metal Doped Chalcogenides," *IEEE J. Sel. Top. Quantum Electron.*, vol. 24, no. 5, pp. Sep. 2018.
- [113] K. Wang, D.-W. Sun, H. Pu, "Emerging non-destructive terahertz spectroscopic imaging technique: Principle and applications in the agrifood industry," *Trends Food Sci. Technol.*, vol. 67, pp. 93-105, Sep. 2017.
- [114] Masahiro Kusano, et al. "Mid-infrared pulsed laser ultrasonic testing for carbon fiber reinforced plastics," *Ultrasonics*, vol. 84, pp. 310-318, 2018.
- [115] Masahiro Kusano, et al. "Mid-infrared laser ultrasonic testing for composite materials," 21st International Conference on Composite Materials, Xi'an, 20-25th August 2017.
- [116] E. A. Anashkina, "Laser Sources Based on Rare-Earth Ion Doped Tellu-rite Glass Fibers and Microspheres," *Fibers*, vol. 8, no. 30, pp. 1-17, May 2020.
- [117] M. C. Falconi, G. Palma, F. Starecki, V. Nazabal, J. Troles, J.-L. Adam, S. Taccheo, M. Ferrari, and F. Prudenzano, "Dysprosium-doped chalcogenide master oscillator power amplifier (MOPA) for mid-IR emission," *J. Lightw. Technol.*, vol. 35, no. 2, pp. 265–273, Jan. 2017.
- [118] M. R. Majewski, R. I. Woodward, J.-Y. Carrée, S. Poulain, M. Poulain, S. D. Jackson, "Emission beyond 4 μm and mid-infrared lasing in a dysprosium-doped indium fluoride (InF_3) fiber," *Opt. Lett.*, vol. 43, no. 8, pp. 1926-1929, 2018.
- [119] Y. Wang, F. Jobin, S. Duval, V. Fortin, P. Laporta, M. Bernier, G. Galze-rano, R. Vallée, "Ultrafast Dy^{3+} :fluoride fiber laser beyond 3 μm ," *Opt. Lett.*, vol. 44, pp. 395-398, Jan. 2019.

- [120] M. Saad, R. Pafchek, P. Foy, Z. Jiang, D. Gardner, P. Hawkins, “Indium Fluoride Glass Fibers for Mid-Infrared applications,” WSOF2015, Hong Kong, China, 4-6 Nov. 2015, paper WW4A.3.
- [121] J. Pisarska, “IR transmission and emission spectra of erbium ions in fluoroindate glass,” *J. Non-Cryst. Solids*, vol. 345-346, pp. 382-385, Oct. 2004.
- [122] V. A. Jerez, C. B. de Araujo, Y. Messaddeq, “Dynamics of energy transfer and frequency upconversion in Tm³⁺ doped fluoroindate glass,” *J. Appl. Phys.*, vol. 96, no. 5, 2530-2534, Sep. 2004.
- [123] L. J. Borrero-Gonzalez, G. Galleani, D. Manzani, L. A. O. Nunes, S. J. L. Ribeiro, “Visible to infrared energy conversion in Pr³⁺-Yb³⁺ codoped fluoroindate glasses,” *Opt. Mater.*, vol. 35, no. 12, pp. 2085-2089, Oct. 2013.
- [124] M. Kochanowicz, J. Zmojda, A. Baranowska, P. Miluski, M. Lesniak, M. Kuwik, J. Pisarska, W. A. Pisarski, J. Dorosz, D. Dorosz, “Near-IR and mid-IR luminescence end energy transfer in fluoroindate glasses co-doped with Er^{3+/-Tm³⁺,” *Opt. Mater. Express*, vol. 9, no. 12, Dec. 2019.}
- [125] M. Kochanowicz, J. Zmojda, P. Miluski, A. Baranowska, M. Kuwik, W. A. Pisarski, J. Pisarska, J. Dorosz, D. Dorosz, “Sensitization of Ho³⁺-doped fluoroindate glasses for near and mid-infrared emission,” *Opt. Mater.*, vol. 101, Mar. 2020, Art. no 109707.
- [126] Le Verre Fluoré, Catalog 2022, Bruz, Brittany, France. [Online]. Available:<https://leverrefluore.com/wp-content/uploads/2019/06/CatalogLVF-2019.pdf>
- [127] F. Maes, V. Fortin, S. Poulin, M. Poulin, J.-Y. Carrée, M. Bernier, R. Vallée, “Room-temperature fiber laser at 3.92 μm”, *Optica*, vol. 5, no. 7, pp. 761-764, Jul. 2018.
- [128] F. Zhou, J. Li, H. Luo, F. Quellette, Y. Liu, “Numerical Analysis of 3.92 μm Dual-Wavelength Pumped Heavily-Holmium-Doped Fluoroindate Fiber Lasers,” *J. Light. Technol.*, vol. 39, no. 2, pp. 633-645, Jan. 2021.
- [129] A. M. Loconsole, M. C. Falconi, V. Portosi, F. Prudenzano, “Numerical Design of a Gain-Switched Pulsed Laser at 3.92 μm Wavelength Based on a Ho³⁺-Doped Fluoroindate Fiber,” *J. Lightw. Technol.*, vol.39, no. 10, pp. 3276-3283, May 2021.

- [130] A. Florez, S. L. Oliveira, M. Florez, L. A. Gomez, L. A. O. Nunes, "Spec-troscopic characterization of Ho³⁺ ion-doped fluoride glass," *J. Alloys Compd.*, vol. 418, pp. 238–242, Feb. 2006.
- [131] S. Jia, Z. Jia, C. Yao, L. Zhang, Y. Feng, G. Qin, Y. Ohishi, W. Qin, "2875 nm Lasing From Ho³⁺-Doped Fluoroindate Glass Fibers," *IEEE Photon. Technol. Lett.*, vol. 30, no. 4, pp. 323-326, Feb. 2018.
- [132] K. S. Wu, D. Ottaway, J. Munch, D. G. Lancaster, S. Bennetts, S. D. Jackson, "Gain-switched holmium-doped fibre laser," *Optics Express*, vol. 17, no. 23, pp. 20872-20877, Nov. 2009.
- [133] J. Li, Y. Yang, D. D. Hudson, Y. Liu, S. D. Jackson, "A tunable Q-switched Ho³⁺-doped fluoride fiber laser," *Laser Phys. Lett.*, vol. 10, Feb. 2013.
- [134] M. C. Falconi, A. M. Loconsole, A. Annunziato, S. Cozic, S. Poulain, F. Prudenzano, "Design of an Er³⁺:InF₃ fiber laser pumped with red light," Proc. SPIE 12142, Fiber Lasers and Glass Photonics: Materials through Applications III, art. no. 121420Z, SPIE Europe 2022, 3-7 April 2022, Strasbourg, France.
- [135] Z. Zhang, R. Wang, M. Liu, S. Wang, J. Zhang, G. Brambilla, S. Jia, P. Wang, "Enhanced 3.9 μm emission from diode pumped Ho³⁺/Eu³⁺ cod-doped fluoroindate glasses," *Opt. Lett.*, vol. 46, no. 9, pp. 2031-2034, Apr. 2021.
- [136] P. Paradis, V. Fortin, Y. O. Aydin, R. Vallée, M. Bernier, "10 W-level gain-switched all-fiber laser at 2.8 μm," *Opt. Lett.*, vol. 43, no. 13, pp. 3196-3199, Jul. 2018.
- [137] N. Bawden, H. Matsukuma, O. Henderson-Sapir, E. Klantsataya, S. Tokita, and D. J. Ottaway, "Actively Q-switched dual-wavelength pumped Er^{3+**:ZBLAN fiber laser at 3.47 μm," *Opt. Lett.*, vol. 43, no. 11, pp. 2724–2727, Jun. 2018.}
- [138] F. Jobin, V. Fortin, F. Maes, M. Bernier, and R. Vallée, "Gain-switched fiber laser at 3.55 μm," *Opt. Lett.*, vol. 43, no. 8, pp. 1770–1773, Apr. 2018.
- [139] Wei-Ping Huang, "Coupled-mode theory for optical waveguides: an overview," *J. Opt. Soc. Am. A*, vol. 11, 963-983 (1994)
- [140] H. Haus, W. Huang, S. Kawakami and N. Whitaker, "Coupled-mode theory of optical waveguides," *J. Light. Technol.*, vol. 5, no. 1, pp. 16-23, January 1987, doi: 10.1109/JLT.1987.1075416.

- [141] A. Yariv, "Coupled-mode theory for guided-wave optics," in IEEE Journal of Quantum Electronics, vol. 9, no. 9, pp. 919-933, September 1973, doi: 10.1109/JQE.1973.1077767.
- [142] Markus J. Schmid and Mathias S. Müller, "Measuring Bragg gratings in multimode optical fibers," Opt. Express 23, 8087-8094 (2015)
- [143] Ho Sze Phing, Jalil Ali, Rosly Abdul Rahman, Bashir Ahmed Tahir, "Fiber Bragg grating modeling, simulation and characteristics with different grating lengths" *Journal of Fundamental Sciences*, Vol. 3, no. 2, (2007).
- [144] T. Erdogan, "Fiber grating spectra," *J. of Light. Technol.*, vol. 15, no. 8, pp. 1277-1294, Aug. 1997, doi: 10.1109/50.618322.
- [145] Nye JF. Physical properties of crystals. New York: Oxford University Press, May 1985.
- [146] Kim K-S, Ismail Y, Springer GS "Measurements of Strain and Temperature with Embedded Intrinsic Fabry-Perot Optical Fiber Sensors," *Journal of Composite Materials*, pp. 1663-1677, vol. 27, no. 17, 1993. doi:10.1177/002199839302701702
- [147] Kim K-S, Kollár L, Springer GS "A Model of Embedded Fiber Optic Fabry-Perot Temperature and Strain Sensors," *Journal of Composite Materials*, pp.1618-1662, vol. 27, no. 17, 1993. doi:10.1177/002199839302701701
- [148] H. R. Aleomohammad, E. Foroozmehr, B. S. Cotten and E. Toyserkani, "A Dual-Parameter Optical Fiber Sensor for Concurrent Strain and Temperature Measurement: Design, Fabrication, Packaging, and Calibration," *J. Light. Technol.*, vol. 31, no. 8, pp. 1198-1204, April 15, 2013, doi: 10.1109/JLT.2013.2240374.
- [149] R. T. Schermer, and J. H. Cole, "Improved bend loss formula verified for optical fiber by simulation and experiment," *IEEE J. Quantum Electron.*, vol. 43, no. 10, pp. 899-909, 2007.
- [150] A. M. Smith, "Birefringence induced by bends and twists in single-mode optical fiber," *Appl. Opt.*, vol. 19, pp. 2606-2611, 1980.
- [151] Y. Wu et al., "Highly sensitive curvature sensor based on asymmetrical twin core fiber and multimode fiber," *Opt. Laser Technol.*, vol. 92, pp. 74-79, 2017.
- [152] C. Liu, X. Yang, F. Laurell, and M. Fokine, "Fabrication of a widely tunable fiber Bragg grating filter using fused deposition modeling 3D printing," *Opt. Mater. Express*, vol. 9, no. 11, pp. 4409-4417, 2019.

- [153] J. Kong, X. Ouyang, A. Zhou, H. Yu, and L. Yuan, "Pure directional bending measurement with a fiber Bragg grating at the connection joint of eccentric-core and single-mode fibers," *J. Light. Technol.*, vol. 34, no. 14, pp. 3288-3292, 2016.
- [154] C. L. Tien, T. C. Cheng, L. C. Chen, G. R. Lin, and W. F. Liu, "Simultaneous measurement of bending curvature and axial stress using D-shaped fiber Bragg gratings," Proc. SPIE 7508, Shanghai, China, pp. 387-392, 2009.
- [155] I. Yokohama, K. Chida, and J. Noda, "Low excess loss conditions of polarization-maintaining fiber couplers," *Appl. Opt.*, vol. 27, no. 23, pp. 4807-4813, 1988.
- [156] J. D. Love, "Spot size, adiabaticity and diffraction in tapered fibres," *Electron. Lett.*, vol. 23, pp. 993–994.
- [157] L. S. Mendes, D. Pontes Nacaratti, R. E. Samad and C. Costa Motta, "Theoretical Analysis of the Efficiency of a 7×1 End-Pumped Power Combiner," 2021 SBMO/IEEE MTT-S International Microwave and Optoelectronics Conference (IMOC), pp. 1-3, 2021, doi: 10.1109/IMOC53012.2021.9624827.
- [158] D. Stachowiak, "High-power passive fiber components for all-fiber lasers and amplifiers application - Design and fabrication," *Photonics*, vol. 5, no. 4, 2018, doi: 10.3390/photonics5040038.
- [159] M. A. Chiapperino, O. Losito, T. Castellano, G. Venanzoni, L. Mescia, G. Angeloni, C. Renghini, P. Carta, P. Potenza, F. Prudenzano, "Dual-Band substrate integrated waveguide resonator based on sierpinski carpet," *Prog. Electromagn. Res. PIER*, vol. 57, pp. 1–12, Aug. 2015.
- [160] G. Venanzoni, D. Mencarelli, A. Morini, M. Farina, O. Losito, F. Prudenzano, "Compact double-layer substrate integrated waveguide magic Tee for X-band applications," *Microw. Opt. Technol. Lett.*, vol. 58, pp. 932–936, Feb. 2016.
- [161] H. Luyen, S.C. Hagness, N. Behdad, "A balun-free helical antenna for minimally invasive microwave ablation," *IEEE Trans. Antennas Propag.*, vol. 63, pp. 959 – 965, Mar. 2015.
- [162] P. Wang, J. Zhang, J. Zhang, S. Jia, L. Wang, Y. Ning, H. Peng, G. Farrell, S. Wang, and R. Wang, "3.5 μm emission in Er³⁺ doped fluoroindate glasses under 635 nm laser excitation," *J. Lumin.*, vol. 237, May 2021, Art. no. 118200, doi: 10.1016/j.jlumin.2021.118200.
- [163] A. Florez, Y. Messaddeq, O. L. Malta, and M. A. Aegegerter, "Optical transition probabilities and compositional dependence of Judd-Ofelt

- parameters of Er³⁺ ions in fluoroindate glass," *J. Alloys Compd.*, vol. 227, no. 2, pp. 135–140, Sep. 1995, doi: 10.1016/0925-8388(95)01613-9.
- [164] S. Sujecki, L. Sojka, A. B. Seddon, T. M. Benson, E. Barney, M. C. Falconi, F. Prudenzano, M. Marciak, H. Baghdasaryan, P. Peterka, and S. Taccheo, "Comparative modeling of infrared fiber lasers," *Photonics*, vol. 5, no. 4, Nov. 2018, Art. no. 48, doi: 10.3390/photonics5040048.
- [165] A. D'Orazio, M. De Sario, L. Mescia, V. Petruzzelli, F. Prudenzano, A. Chiasera, M. Montagna, C. Tosello, and M. Ferrari, "Design of Er³⁺ doped SiO₂-TiO₂ planar waveguide amplifier," *J. Non. Cryst. Solids*, vol. 322, no. 1, pp. 278–283, July 2003, doi: 10.1016/S0022-3093(03)00215-1.
- [166] L. Sojka, and L. Pajewski, S. Lamrini, M. Farries, T. M. Benson, A. B. Seddon, and S. Sujecki, "High peak power Q-switched Er:ZBLAN fiber laser," *J. Light. Technol.*, vol. 39, no. 20, pp. 6572–6578, Oct. 2021, doi: 10.1109/JLT.2021.3099498.
- [167] R. I. Woodward, M. R. Majewski, and S. D. Jackson, "Mode-locked dysprosium fiber laser: picosecond pulse generation from 2.97 to 3.30 μm", *APL Photonics*, vol. 3, no. 11, p. 116106, Nov. 2018, doi: 10.1063/1.5045799.
- [168] G. Fornarelli, L. Mescia, F. Prudenzano, M. De Sario, and F. Vacca, "A neural network model of erbium-doped photonic crystal fibre amplifiers," *Opt. Laser Technol.*, vol. 41, no. 5, pp. 580-585, July 2009, doi: 10.1016/j.optlastec.2008.10.010.
- [169] A. Öchsner and M. Öchsner, *The Finite Element Analysis Program MSC Marc/Mentat*, Springer, 2016.
- [170] R. Guan, F. Zhu, Z. Gan, D. Huang, and S. Liu, "Stress birefringence analysis of polarization maintaining optical fibers," *Opt. Fiber Technol.*, vol. 11, no. 3, pp. 240–254, 2005.
- [171] H. Alemohammad, *Opto-mechanical Fiber Optic Sensors*. Research, Technology, and Applications in Mechanical Sensing, Conner, 2018.
- [172] G. Rajan, R. Raju, S. Jinachandran, P. Farrar, J. Xi, and B. G. Prusty, "Polymerisation Shrinkage Profiling of Dental Composites using optical Fibre sensing and their Correlation with Degree of Conversion and Curing Rate," *Scientific Reports*, vol. 9, no. 1, p. 3162, 2019.
- [173] X. Zhang, R. Chen, A. Wang, Y. Xu, Y. Jiang, H. Ming, and W. Zhao, "Monitoring the failure forms of a composite laminate system by using

- panda polarization maintaining fiber Bragg gratings," *Opt. Express.*, vol. 27, no. 13, pp. 17571-17580, 2019.
- [174] X. Geng, M. Jiang, L. Gao, Q. Wang, Y. Jia, Q. Sui, L. Jia, and D. Li, "Sensing characteristics of FBG sensor embedded in CFRP laminate," *Measurement*, vol. 98, pp.199-204, 2017.
 - [175] Md. H. Ikbal, "Tensile properties of bidirectional glass-carbon hybrid composites: Part I," <http://textilefocus.com/tensile-properties-bidirectional-glass-carbon-hybrid-composites-part/>.
 - [176] F. Groh, E. Kappel, C. Huhne and F. Meyer, "Process-induced distortions of composite structures due to through-thickness fibre volume fraction gradients," in European Conference on Composite Materials, 2016, pp. 26-30.
 - [177] Z. Zhai, B. Jiang, and D. Drummer, "Tensile Creep Behavior of Quasi-Unidirectional E-Glass Fabric Reinforced Polypropylene Composite," *Polymers* vol. 10, no. 6, p. 661, 2018.
 - [178] W. Scarcia, G. Palma, M. C. Falconi, F. De Leonardi, V. M. N. Pasaro, and F. Prudenzano, "Electromagnetic Modelling of Fiber Sensors for Low-Cost and High Sensitivity Temperature Monitoring," *Sensors*, vol. 15, no. 12, pp. 29855-29870, 2015.
 - [179] L. Mescia, T. Palmisano, M. Surico, and F. Prudenzano, "Long-period gratings for the optimization of cladding-pumped microstructured optical fiber laser," *Opt. Mater.*, vol. 33, no. 2, pp. 236–240, 2010.
 - [180] F. Ren, T. Zhangsun, X. Huang, Y. Zhang, X. Fan, W. Chen, and J. Wang, "Design of 20-polarization-maintaining-mode “pseudo-rectangle” elliptical-core fiber for MIMO-less MDM networks," *Opt. Fiber Technol.*, vol. 50, pp. 87-94, 2019.
 - [181] Z. Han, N. Zhao, Z. Yang, and G. Li, "Error analyses for simultaneous measurement of temperature and strain based on polarization maintaining few-mode fibers," in Asia Communications and Photonics Conference, ed. IEEE, 2018.
 - [182] A. Annunziato, A. Erario, F. Anelli, G. Abbate, M. Godfrey, S. L. Jantzen, J. Gates, C. Holmes, C. Ciminelli and F. Prudenzano, "Structural Health Monitoring of Composite Laminae for Aerospace Applications via Embedded Panda Fiber Bragg Grating," in 2020 22nd International Conference on Transparent Optical Networks (ICTON), ed. IEEE, 2020.
 - [183] C. Zhang, W. K. Binienda, R. K. Goldberg, and L. W. Kohlman, "Meso-scale failure modeling of single layer triaxial braided

- composite using finite element method," *Compos. Part A: Appl. Sci. Manuf.*, vol. 58, pp. 36-46, 2014.
- [184] Z. Zhao, H. Dang, C. Zhang, G. J. Yun, and Y. Li, "A multi-scale modeling framework for impact damage simulation of triaxially braided composites," *Compos. Part A: Appl. Sci. Manuf.*, vol. 110, pp. 113-125, 2018.
- [185] M. P. Varnham, D. N. Payne, A. J. Barlow, and R. D. Birch, "Analytic solution for the birefringence produced by thermal stress in polarization-maintaining optical fibers", *J. Light. Technol.*, vol.1, no.2, pp. 332-339, 1983.
- [186] Y. H. Kim, H. Kwon, J. Kim, and K. Y. Song, "Distributed measurement of hydrostatic pressure based on Brillouin dynamic grating in polarization maintaining fibers", *Opt. Express*, vol. 24, no. 19, pp. 21399-21406, 2016.
- [187] J. L. Santos and F. Farahi, *Handbook of Optical Sensors* CRC press, 2018.
- [188] D. Kinet, P. Mégret, K. W. Goossen, L. Qiu, D. Heider and Christophe Caucheteur, "Fiber Bragg Grating Sensors toward Structural Health Monitoring in Composite Materials: Challenges and Solutions," *Sensors*, vol. 14, no.4, pp. 7394-7419, 2014.
- [189] Y. Okabe, S. Yashiro, T. Kosaka, N. Takeda, "Detection of transverse cracks in cfrp composites using embedded fiber bragg grating sensors," *Smart Mater. Struct.*, vol. 9, no. 6, 2000, doi:10.1088/0964-1726/9/6/313.
- [190] R. Potluri, "Mechanical properties evaluation of t800 carbon fiber reinforced hybrid composite embedded with silicon carbide microparticles: A micromechanical approach," *Multidiscip. Model. Mater. Struct.*, vol. 14, no. 29, 2018, doi:10.1108/MMMS-09-2017-0106.
- [191] M. Rodríguez, J. M. Molina-Aldareguía, C. González, J. LLorca, "A methodology to measure the interface shear strength by means of the fiber push-in test," *Compos. Sci. Technol.*, vol. 72, no. 15, pp. 1924–1932, 2012, doi: 10.1016/j.compscitech.2012.08.011.
- [192] L. St-Pierre, N. J. Martorell, S. T. Pinho, "Stress redistribution around clusters of broken fibres in a composite," *Compos. Struct.*, vol. 168, pp. 226–233, 2017, doi: 10.1016/j.compstruct.2017.01.084.
- [193] D. Chung, *Carbon fiber composites*. Elsevier, 2012.
- [194] T. Mawatari and D. Nelson, "A multi-parameter Bragg grating fiber optic sensor and triaxial strain measurement," *Smart Mater. Struct.*,

- vol. 17, no. 3, 2008, Art. no. 035033, doi: 10.1088/0964-1726/17/3/035033.
- [195] C. Sonnenfeld et al., “Microstructured optical fiber Bragg grating as an internal three-dimensional strain sensor for composite laminates,” *Smart Mater. Struct.*, vol. 24, no. 5, 2015, Art. no. 055003, doi: 10.1088/0964-1726/24/5/055003
 - [196] G. Luyckx, W. De Waele, J. Degrieck, W. Paepegem, J. Vlekken, S. Vandamme, K. Chah, “Three-dimensional strain and temperature monitoring of composite laminates,” *Insight: Non-Destr. Test. Cond. Monit.*, vol. 49, no. 1, pp. 10–16, 2007, doi:10.1784/insi.2007.49.1.10.
 - [197] W. Zhang, X. Lei, W. Chen, H. Xu, and A. Wang, “Modeling of spectral changes in bent fiber Bragg gratings,” *Opt. Lett.*, vol. 40, no. 14, pp. 3260-3263, 2015.
 - [198] M. Jang, J. S. Kim, S. H. Um, S. Yang, and J. Kim, “Ultra-high curvature sensors for multi-bend structures using fiber Bragg gratings,” *Opt. Express*, vol. 27, no. 3, pp. 2074-2084, 2019.
 - [199] J. H. Osório et al., “Bragg gratings in surface-core fibers: Refractive index and directional curvature sensing,” *Opt. Fiber Technol.*, vol. 34, pp. 86-90, 2017.
 - [200] C. Holmes, M. Godfrey, P. L. Mennea, S. Zahertar, and J. Barton, “Flexible photonics in low stiffness doped silica for use in fibre reinforced polymer composite materials,” *Opt. Mater.*, vol. 134, Part A, p. 113133, 2022,
 - [201] I. H. Malitson, “Interspecimen comparison of the refractive index of fused silica,” *J. Opt. Soc. Am.*, vol. 55, no. 10, pp. 1205-1208, 1965.
 - [202] Y. Wu, and K.S. Chiang, “Mode-selective coupling between few-mode fibers and buried channel waveguides,” *Opt. Express*, vol. 24, no. 16, pp. 30108-30123, 2016.
 - [203] A. Öchsner, Euler–Bernoulli Beam Theory, in Classical Beam Theories of Structural Mechanics, 1st ed., (Springer, Cham, 2021), pp. 7–66.
 - [204] P. Kiiveri et al., “Refractive index profiles and propagation losses in bent optical fibers,” *Opt. Eng.*, 61(12), (2022).
 - [205] C. Holmes et al., “Direct UV-written planar Bragg grating sensors,” *Meas. Sci. Technol.*, 26(11), 112001-112021 (2015).
 - [206] W. Zhou, Y. Zhou, X. Dong, L. -Y. Shao, J. Cheng and J. Albert, “Fiber-Optic Curvature Sensor Based on Cladding-Mode Bragg Grating

- Excited by Fiber Multimode Interferometer," *IEEE Photonics J.*, 4(3), 1051-1057 (2012).
- [207] C. Lei, Z. Chen, Y. Gu, H. Xiao, and J. Hou, "Loss mechanism of all-fiber cascaded side pumping combiner," *High Power Laser Sci. Eng.*, vol. 6, (2018).
- [208] S. Cozic, S. Boivinet, C. Pierre, J. Boulet, S. Poulain, and M. Poulain, "Splicing fluoride glass and silica optical fibers," EPJ Web of Conferences 215, 04003, (2019).
- [209] A. W. Snyder, "Coupled-Mode Theory for Optical Fibers," *J. Opt. Soc. Am.*, vol. 62, no. 11, pp. 1267-1277, 1972.
- [210] D. Donlogic, "In-line higher order mode filters based on long highly uniform fiber tapers," *J. Light. Technol.*, vol. 24, no. 9, pp. 3532-3539, 2006.
- [211] A. Florez, S. L. Oliveira, M. Florez, L. A. Gomez, L. A. O. Nunes, "Spectroscopic characterization of Ho³⁺ ion-doped fluoride glass," *J. Alloys Compd.*, vol. 418, pp. 238–242, Feb. 2006.
- [212] L. Gomes, V. Fortin, M. Bernier, R. Vallée, S. Poulain, M. Poulain, S. D. Jackson, "The basic spectroscopic parameters of Ho³⁺-doped fluoroindate glass for emission at 3.9 μm," *Opt. Mater.*, vol. 60, pp. 618-626, Sep. 2016.
- [213] R. Wang, J. Zhang, H. Zhao, X. Wang, S. Jia, H. Guo, S. Dai, P. Zhang, G. Brambilla, S. Wang, P. Wang, "3.9 μm emission and energy transfer in ultra-low OH-, Ho^{3+/-} Nd³⁺ co-doped fluoroindate glasses," *J. Lumin.*, vol. 225, Sep. 2020, Art. no. 117363.
- [214] Y. V. Orlovskii, R. J. Reeves, R. C. Powell, T. T. Basiev, K. K. Pu-khov, "Multiple-phonon non-radiative relaxation: Experimental rates in fluoride crystals doped with Er³⁺ and Nd³⁺ ions and theoretical model," *Phys. Rev. B*, vol. 49, n. 6, Feb. 1994.
- [215] L. de S. Menezes, G. S. Maciel, C. B. de Araújo, Y. Messaddeq, "Thermally enhanced frequency upconversion in Nd³⁺-doped fluoroindate glass," *J. Appl. Phys.*, vol. 90, no. 9, pp. 4498–4501, 2001.
- [216] M. C. Falconi, A. M. Loconsole, D. Laneve, L. Thi Ngoc Tran, L. Zur, A. Chiasera, R. Balda, J. Fernandez, P. Gluchowski, A. Lukowiak, M. Ferrari, and F. Prudenzano, "Design of active devices based on rare-earth-doped glass/glass ceramic: from the material characterization to the device parameter refinement," Proc. SPIE Fiber Lasers and Glass Pho-tonics: Materials through Applications II, Online Only (France), 6-10 Apr 2020.

- [217] T. Catunda, L. A. O. Nunes, A. Florez, Y. Messaddeq, and M. A. Aegerter, “Spectroscopic properties and upconversion mechanisms in Er³⁺-doped fluoroindate glasses,” *Phys. Rev. B*, vol. 53, no. 10, pp. 6065–6070, Mar. 1996, doi: 10.1103/PhysRevB.53.6065.
- [218] I. Chiamenti, T. Elsmann, A. Reupert, O. Kara, M. Becker, L. Wondraczek, M. Chernysheva, “First-order fiber Bragg grating inscription in indium fluoride fiber using a UV/Vis femtosecond laser and two-beam interferometry,” *Opt. Lett.*, vol. 46, no. 8, pp. 1816–1819, Apr. 2021, doi: 10.1364/OL.420264.
- [219] Z. Qin, Y. Zhou, G. Xie, P. Yuan, J. Ma, and L. Qian, “Red-diode-clad-pumped CW and mode-locked Er:ZBLAN fiber laser at 3.5 μm,” *Opt. Express*, vol. 30, no. 7, pp. 11174–11180, Mar. 2022, doi: 10.1364/OE.454521